Corrosion – Fouling on Heat Transfer Surfaces

by

Tyler James Stephenson

A thesis submitted in partial fulfillment of the requirements for the degree of

Doctor of Philosophy

in

Materials Engineering

Department of Chemical and Materials Engineering
University of Alberta

Abstract

This thesis presents a thorough examination of the corrosion and fouling behaviour of crude oil at refining conditions on industrially applicable heat transfer surfaces. The depletion of light sweet crude oil reserves means that the processing of ever heavier and more sour crude oils is inevitable. These less-ideal crude oils present a particularly challenging set of problems for a refinery. They often have a high asphaltene and sulfur content, which creates a very aggressive feedstock in terms of fouling and corrosion. Thermal processing is known to exacerbate the situation, however the inorganically driven fouling behaviour from corrosion of heat exchanger materials at high temperature is not well understood. An atmospheric bottoms fraction of crude oil (340 °C+) with an asphaltene content of 8.47 wt% and a sulfur content of 3.43 wt% was used in this thesis to evaluate its effects on high temperature corrosion and fouling of pure iron and 316 stainless steel. A surface temperature of 540 °C was chosen for this study, to approximate the conditions of a delayed coker heat exchanger.

The experiments were carried out using a stirred, batch-style fouling reactor that enabled the preferential resistive heating of a metallic wire, which was submerged in the test oil. The change in the fouling resistance (fouling factor) of the wire was measured with time. The behaviour of the fouling factor was found to be asymptotic with time, as the buildup of coke on the surface of the wire attenuated the surface corrosion reactions. This in turn reduced the amount of inorganic foulant being ejected into the foulant layer. The foulant was examined using

SEM-EDX, XRD, TEM, FIB, and AES. It was determined to be a mixture of organic carbonaceous coke, interspersed with an inorganic phase, which was found to be predominantly the pyrrhotite phase ($Fe_{(1-x)}S$) of iron sulfide.

Initially it was observed that the buildup of a thin iron sulfide layer occurred almost instantaneously, and preceded the formation of any surface coke. This led to the hypothesis that the iron sulfide is actually catalytic toward the formation of coke, alluding to the fact that it is a strong catalyst of dehydrogenation and condensation reactions. The attenuation of the fouling factor with time was attributed to the reduction in the amount of iron sulfide being ejected into the foulant layer and erupting at the foulant-oil interface.

Thiophene was also added to the oil bath to evaluate its effects on fouling. It was thought that the addition of a thermally stable, surface-active solvent would both solubilize the asphaltenes and reduce the interaction of corrosive species with the surface of the metal by blocking adsorption sites. The compound was added to the oil bath at concentrations of 0.5, 1.3, and 5.7 vol%. Fouling behaviour was evaluated for 250, 1000, and 1400 minutes of exposure at temperature. Thiophene was found to be very effective at reducing both the fouling factor, and the amount of surface corrosion on 316 stainless steel at all exposure levels and times.

Preface

Chapter 1 of this thesis embodies the introduction to the topic of corrosion and fouling as it pertains to the oil and gas industry. It outlines the methods as well as the reasons for choosing the experimental parameters of this study. It also outlines an explanation for the choice of the material in Chapter 4.

Material in Chapter 2 of this thesis has been published in the manuscript entitled; *Corrosion-Fouling of 316 Stainless Steel and Pure Iron by Hot Oil*, Energy & Fuels, 2011, 25, 4540-4551. I was the first author of this publication and was responsible for all facets of the laboratory work and composition.

Material in Chapter 3 of this thesis was published in the manuscript entitled; *Thiophene mitigates high temperature fouling of metal surfaces in oil refining*, Fuel, 2015, 139, 411-424. I was the first author of this publication and was again responsible for all aspects of the laboratory work and composition of the manuscript.

Material in Chapter 4 of this thesis was published in the manuscript entitled; *Lithium ion battery applications of molybdenum disulfide nanocomposites*, Energy and Environmental Science, 2014, 7, 209-231. I was the first author of this highly topical review article and was responsible for its entire composition.

Dedication

This thesis is dedicated to my Dad, Mike Stephenson, Mom, Lorna Stephenson, Sister, Ashley Stephenson, and Brother Jeffrey Stephenson. I am lucky to have the love and support of such a great family.

It is also dedicated to my one and only, Jenn Thompson, whom I could not have done this without.

To slake our thirst for knowledge is something which, over time, forces us to go the distance.

-

Acknowledgements

I would like to thank my supervisor, Dr. David Mitlin for all of his guidance throughout my program. Both Dr. Arno DeKlerk and Murray Gray deserve a heartfelt thank you and my continued gratitude for their mentorship. I would also like to express my appreciation for all the aid that the remaining members of my supervisory committee provided. Dr. Leijun Li, Dr. Dongyang Li, and Dr. Marc Secanell Gallart were all extremely helpful. Furthermore, thank you to Dr. Thomas Thundat for co-supervising me. Finally, thank you to Dr. David Xiulei Ji for agreeing to be my external examiner, and providing such constructive feedback regarding my thesis.

I would also like to thank Paul Concepcion, Martin Kupsta, Kai Cui, and Daniel Soloman for all of their help with the instruments at the National Institute for Nanotechnology. Lisa Brandt and Jeremiah Bryksa were instrumental in this thesis, and I will always be grateful for their continued help with various analytical techniques and instrument training. I would also like to express my gratitude towards the gentlemen at the Alberta Centre for Surface Engineering and Science, Dimitre Karpuzov, Anquang He, and Shihong Xu, for all of their expertise and excellent sample analysis.

The University of Alberta, and the faculty of graduate studies and research both deserve a great deal of praise for all of the financial assistance that they provided

to me throughout my program. Another thank you must be expressed to all of those individuals in the department of chemical and materials engineering who helped me with various technical and administrative problems along the way. In particular, thank you to Lily Laser, Matt Kloster, and Judy Powell. Lastly, I would like to thank my fellow group members Mike Hazelton, Chris Holt, Brian Olsen, Erik Luber, Ben Zahiri, Zhi Li, Li Zhang, Huanlei Wang, Peter Kalisvaart, Alan Kubis, Babak Shalchi, Mohsen Danaie, Justin Lepore, Elmira Memarzadeh Lotfabad, and Alireza Kohandehghan for all of their help with my work, and for their fellowship over the years. We got through it together.

Table of Contents

List of Figures

List of Tables

List of Equations

Abbreviations

FF	Fouling factor
FFF	Final fouling factor
TEM	Transmission electron microscopy
SAED	Selected area electron diffraction
HAADF	High angle annular dark field
HRTEM	High resolution transmission electron microscopy
EELS	Electron energy loss spectroscopy
SEM	Scanning electron microscopy
EDX	Energy dispersive X-ray analysis
XRD	X-ray diffraction
BCC	Body centred cubic
FCC	Face centred cubic
HCP	Hexagonal close-packed
AES	Auger electron spectroscopy
FIB	Focused ion beam
CNT	Carbon nanotube
MWCNT	Multi-walled carbon nanotube
TAN	Total acid number
TGA	Thermogravimetric analysis
CHNS	Carbon, hydrogen, nitrogen, sulfur analysis
HDS	Hydrodesulfurization
SARA	Saturates, aromatics, resins and asphaltenes

List of symbols

R_T	Fouling resistance or thermal resistance
R_{cond}	Thermal resistance to conduction
R_{conv}	Thermal resistance to convection
R_e	Electrical resistance to conduction
$\mathring{Q}_{clean}$	Heat generation in the clean state
$\mathring{Q}_{fouled}$	Heat generation in the fouled state
Q_{clean}	Heat transferred in the clean state
Q_{fouled}	Heat transferred in the fouled state
U_{clean}	Overall heat transfer coefficient in the clean state
U_{fouled}	Overall heat transfer coefficient in the fouled state
h	Convective heat transfer coefficient
T_{wire}	Temperature of the wire
T_{oil}	Temperature of the oil
ΔT	T_{wire} - T_{oil}
A_{wire}	Surface area of the wire
A_{clean}	Surface area of the clean wire (before fouling)
A_{fouled}	Surface area of the fouled wire (after fouling)
P	Power (watts) = V*I
PID	Proportional integral derivative control loop
R	Resistance (Ω) = V/I
σ	Electrical conductivity
k	Thermal conductivity
r_1	Radius of the wire
r_2	Radius of the wire plus the foulant

CHAPTER 1

Corrosion - Fouling in Context

1.1 Introduction

High temperature sulfidation and coking continues to exude a high economic impact on industrial equipment and environmental impact to the world. The exposure of hot metal surfaces to liquid and gaseous streams that are rich in sulfur containing species creates an environment that is incredibly aggressive towards their degradation. This thesis will focus on fouling and corrosion as it pertains to the oil and gas industry, where the problem is extremely costly and difficult to mitigate. Developing strategies to minimize the cost per barrel of finished products derived from crude oil is the current trend for oil processors. As such, the potential impact of research involving the elucidation and mitigation of petroleum fouling and corrosion is high. While the deposition of unwanted material is seen on exploration and production (E&P) infrastructure, transportation pipelines, and a multitude of refinery surfaces, this study will focus on the process conditions of delayed coking, where the problem is particularly detrimental.

Traditionally, fouling has been viewed as the homogeneous phase separation of crude oil resulting in the precipitation of asphaltene molecules, which stick to a surface and build up to form coke.[1] This precipitation can be brought about by turbulence, mixing incompatible oils and exposure to heat. These perturbations destabilize the colloidal structure of the oil mixture and cause asphaltenes to flocculate.[1] A theoretical asphaltene molecule is shown here in

Figure 1-1a[3], in conjunction with 1-1b, which is an idealized schematic of the colloidal structure of crude oil using the SaRA nomenclature (saturates, aromatics, resins and asphaltenes). The resin molecules, which have polar heads and apolar tails enhance the solubility of the polar asphaltenes in the apolar saturate and aromatic matrix.[1]

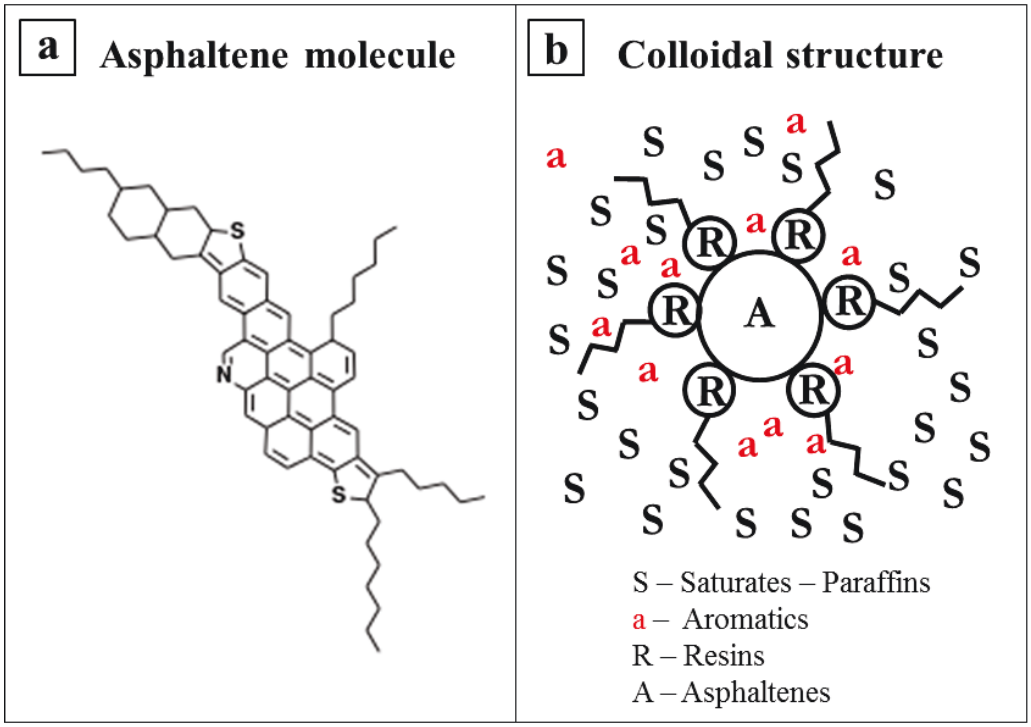

Figure 1-1: (a) Theoretical structure of an asphaltene molecule.[3] (b) Idealized colloidal structure of crude oil, showing the interaction of the SaRA constituents.

Wiehe has presented a large body of work regarding the precipitation of asphaltene molecules and their conversion to coke.[1] Since crude oil is an extremely complex mixture, it has been broken down into a series of solubility classes to aid researchers in its taxonomy. Coke is broadly categorized as the

only constituent of crude oil that is not soluble in toluene. Asphaltenes are characterized as toluene soluble, but heptane insoluble.[2] The saturates, aromatics, and resins are all heptane soluble, and can be separated via other techniques such as SaRA fractionation.[2] Wiehe heated a number of oil (residuum) mixtures with different amounts of asphaltenes to the cracking temperature for crude oil (400 °C) and measured the amount of coke that was formed as a function of time. A summary of his data is presented here as Figure 1-2.[1]

Figure 1-2a shows a sample that was 100% asphaltenes which began forming coke immediately upon heating. The 25% asphaltene mixture formed coke after an induction period of approximately 50 minutes, and the 0% asphaltene sample started forming coke after a period of approximately 90 minutes.[1] This work is widely accepted as an indication that the colloidal structure of the crude oil takes some time to become destabilized and liberate asphaltenes from the solution, hence the induction period. Furthermore, it is also an indication that asphaltenes and coke can be formed from the thermal processing of oils that contain none of these fractions, via cracking and condensation reactions of organic molecules.[1]

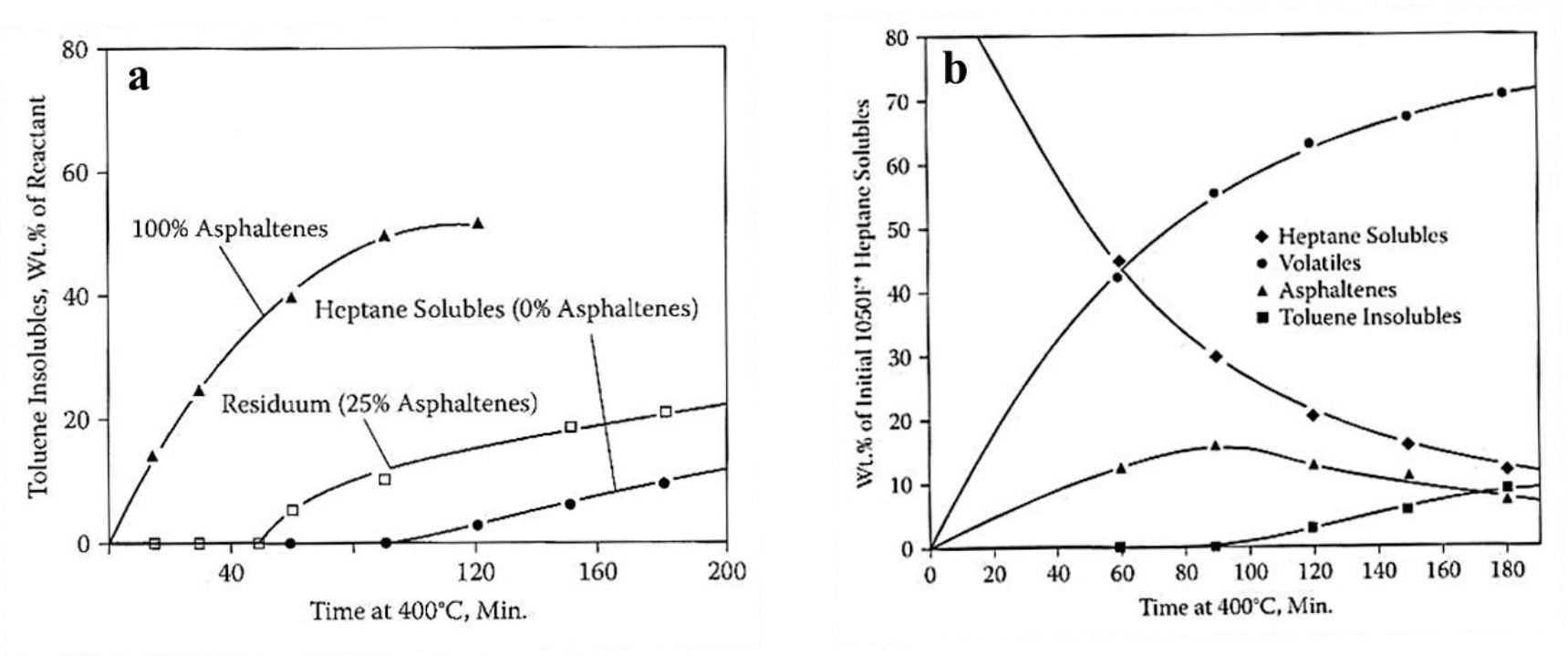

Figure 1-2: (a) Graph of coke formation with time as a function of asphaltene content of a crude oil mixture heated to 400 °C. (b) Graph of the conversion of the various constituents of crude oil with time at 400 °C.[1]

Figure 1-2b shows a graph of a 0% asphaltene sample that was heated to 400 °C and fractionated after different amounts of time. Here, the amount of the different crude oil constituents is observed to transform as the sample is held at temperature. Of particular note is that the asphaltene maximum corresponds with the end of the 90 minute coke induction period, and beginning of coke formation. Taken together, these two graphs represent the classical behaviour of crude oil samples during thermal processing, and elucidate the role of asphaltenes in fouling. The body of literature pertaining to fouling from homogeneous phase separation is large and well understood. However, the present study will provide evidence that there is a significant contribution to fouling from heterogeneous nucleation on the heat transfer surfaces in question, which is not well understood. In particular, the role of corrosion products forming on the heat transfer surfaces in coking will be explored, as it is hypothesized that these are catalytic towards coke formation.

A possible refinery schematic is presented here as Figure 1-3, where the delayed coking process has been highlighted in red.[4] Delayed coking is one of the most widely used methods of residua disproportionation. In this process, a solid carbon rich product is produced in conjunction with more hydrogen rich liquid and gaseous products from processed residue fractions of heavy oil. Places such as Western Canada, where there is no market for fuel oils, employ this technique for treating heavy residues.[3] A main difference from the schematic of Figure 1-3 in Alberta, is that bitumen commonly goes straight to vacuum distillation, as it is

often too heavy to be effectively processed by atmospheric distillation. However, at the point of delayed coking, the raw crude/bitumen has been exposed to atmospheric distillation, and/or vacuum distillation. This yields high boiling fraction residue that is rich in carbon, as well as impurities such as sulfur, nitrogen and heavy metals. These impurities will be partially removed by the delayed coking process. For the process of delayed coking to begin, the residue must be heated to destabilize the colloidal structures within the oil and start the precipitation of asphaltenes as coke. It is here that the temperature of the heat transfer surface is in excess of 550 °C. The combination of a hot aerobic environment, with high concentrations of sulfur species, produces a corrosion situation that is incredibly antagonistic. Furthermore, the buildup of unwanted material on the heat exchanger walls decreases thermal efficiency, causing a concomitant increase in fuel consumption to run the unit. Eventually the equipment must be shut down for cleaning, which is costly and causes unwanted downtime. While much of the open literature that will be discussed on the subject of fouling neglects the corrosion aspect, it is my hypothesis that these reactions are of paramount importance to the overall mechanism and morphology of the deposits produced. This will be explored in Chapters 2 and 3.

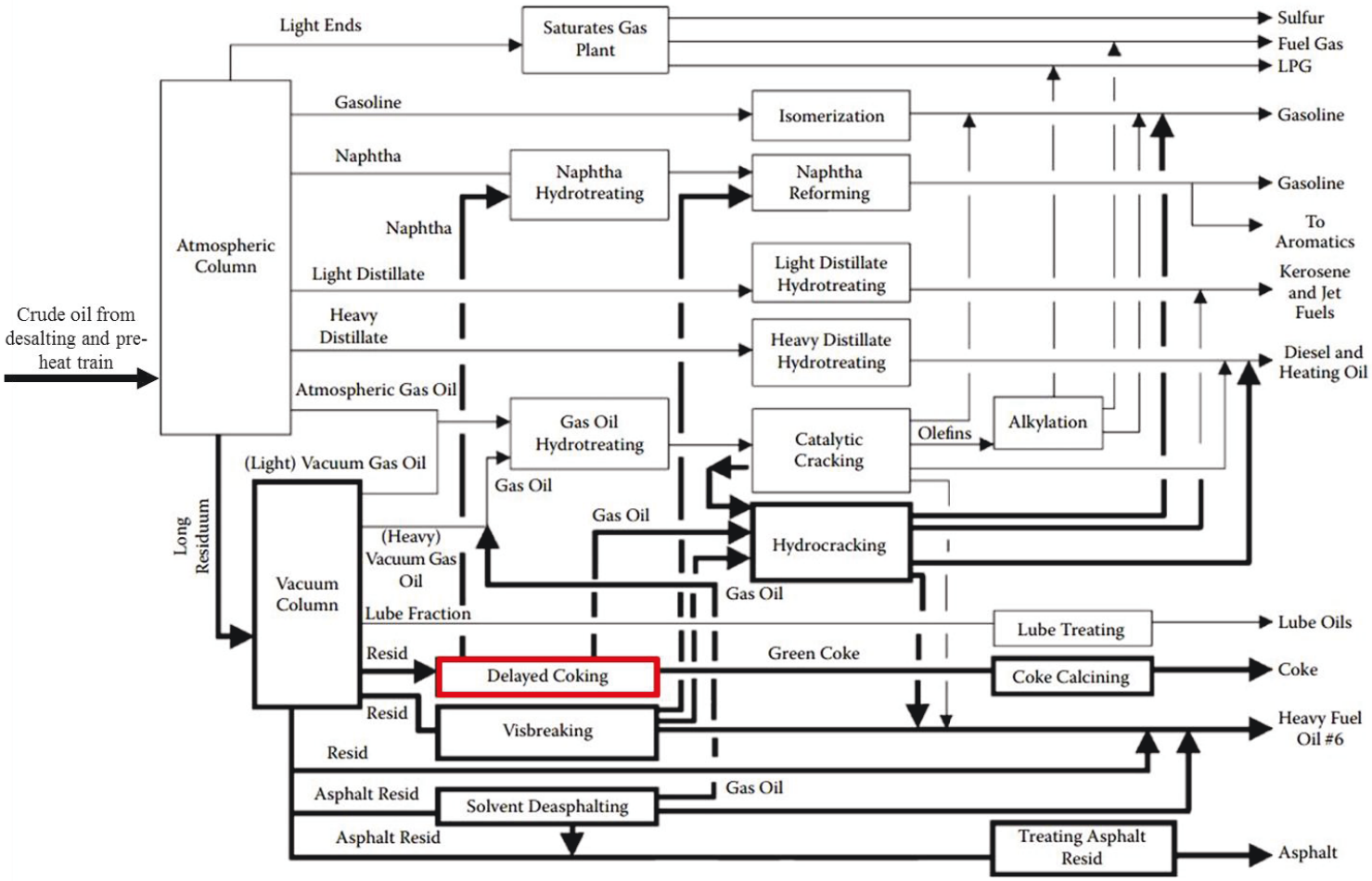

Figure 1-3: Schematic diagram of a typical refining process.[4]

In refining, catalysis is exploited to aid in the production of higher value products from lower value reactants.[5,6] Transition metal sulfide and oxide catalysts are favoured for processes such as heteroatom removal. In particular, the hydrodesulfurization (HDS) process is commonly catalyzed by a metal sulfide (usually molybdenum disulfide, MoS_2), which has been promoted with cobalt or nickel substitutional impurities and supported on a porous alumina pellet.[7-11] Thiophene is a model compound that is commonly used to study the efficacy of catalysts for HDS. The mechanism for the HDS of thiophene (C_4H_4S) is a multi-step process. First, the sulfur heteroatom adsorbs onto a sub-coordinated edge site of MoS_2, and this is followed by the scission of the C-S bonds.[7,8,10] A high partial pressure of hydrogen is critical to sustain the catalytic cycle and to liberate the adsorbed sulfur as H_2S.[5,7,12] Without hydrogen, the adsorbed organic sulfur atom is not released, and the catalytic site is blocked.

The nickel and cobalt promoter impurities provide local regions of enhanced electron density along the MoS_2 edges. This, in turn, results in the site-specific lowering of the binding energy and therefore higher activity for adsorption at the active site.[8,10,13] Iron has also been found to be an effective promoter impurity.[8,13] In addition, iron sulfide[14,15] coated stainless steel[16] as well as other metal surfaces have also been shown to exhibit catalytic activity for the HDS of thiophene.[17] However, this study will show that in the absence of hydrogen, thiophene is able to interact with heat transfer surfaces and remain thermally stable, even at high temperatures.

In catalytic upgrading it is well known that there are competitive reactions at work.[18,19] In general, the active site on a given catalyst can be poisoned by adsorbing polar species containing nitrogen or sulfur heteroatoms if there is not enough excess hydrogen to allow the catalytic cycle to continue.[18,20] Furthermore, it has been experimentally shown that the addition of thiophene and H_2S to a reactor has inhibitory effects on the catalytic cycle and the liberation of desired products.[18] Thus, I hypothesize that the addition of a polar solvent molecule such as thiophene will not only enhance the solubility of asphaltenes, but also inhibit the heat transfer surface from interacting with other organic molecules in the oil. This will reduce sulfidation, and coking.

It is also important for the reader to recognize a brief note on the layout and continuity of this thesis. I have completed an extensive amount of fouling and corrosion work to date which is presented in Chapters 1, 2, and 3. The initial fouling CRD grant was enough to generate the information presented in Chapter 2. After this, my research was focused on molybdenum disulfide in lithium ion batteries, as I was familiar with the concepts and chemistry associated with the sulfidation of transition metals. Also, molybdenum disulfide (MoS_2) is one of the main catalysts for catalytic cracking in refining. My research in this field culminated with a literature review on MoS_2 in lithium ion batteries and is presented as Chapter 4. However, the fouling project was eventually rejuvenated which allowed me to continue it as the main thrust of my work. Thus, the information presented in Chapter 3 is a direct result of this.

Chapter 4, a review of MoS_2 for lithium ion batteries, represents a seminal contribution to that field. At the time of its publication, there was a large debate in open literature regarding the lithiation mechanism and lithiation products of MoS_2 during charge/discharge cycling. A thorough study of open literature, combined with a small number of my own experiments (shown in Appendix B), revealed evidence which helped to elucidate the lithiation mechanism. This work has begun to change what was the minority view at the time, into the majority view. MoS_2 converts to lithium sulfide and molybdenum metal, and functions as a lithium sulfur battery after the first discharge cycle. Initially it was thought that the MoS_2 functions as an intercalation electrode over its full voltage range of 0-3V vs Li/Li^+. However, the MoS_2 actually decomposes after lithiation, and never re-forms in subsequent cycles. The paper presented as Chapter 4 was instrumental in bringing about that paradigm shift, and remains extremely well-received by the scientific community.

1.2 References

[1] Wiehe, I.A. *Process Chemistry of Petroleum Macromolecules.* CRC Press, Boca Raton Fl, USA, **2008**, 97-179.

[2] Pillon, L.Z. *Interfacial Properties of Petroleum Products*. CRC Press, Boca Raton Fl, USA, **2008**, 1-37, 123-149.

[3] Gray, M.R. *Upgrading Petroleum Residues and Heavy Oils.* Marcel Dekker Inc. New York, USA, **1994**, 237-260.

[4] Self, F. ; Ekholm, E. ; Bowers, K. *Refining Overview-Petroleum, Processes, and Products.* CD-Rom, AIChE – South Texas Section, **2000**.

[5] Rana, M.S. ; Samano, V. ; Ancheyta, J. ; Diaz, J.A.I. *Fuel*, **2007**, 86, 1216-1231.

[6] Speight, J.G. *The Chemistry and Technology of Petroleum*. 4th Ed. **2007**, CRC Press, Boca Raton, FL, 521-597.

[7] Cheng, F. ; Chen, J. ; Guo, X. *Adv. Mater.* **2006**, 18, 2561-2564.

[8] Moses, P.G. ; Hinnemann, B. ; Topsoe, H. ; Norskov, J.K. *J. Catal.* **2009**, 268, 201-208.

[9] Huang, Y. ; Zhou, Z. ; Qi, Y. ; Li, X. ; Cheng, Z. ; Yuan, W. *Chem. Eng. J.* **2011**, 172, 444-451.

[10] Castillo-Villalon, P. ; Ramirez, J. ; Castaneda, R. *J. Catal.* **2012**, 294, 54-62.

[11] Rao, B.G. ; Ramakrishna Matte, H.S.S. ; Chaturbedy, P. ; Rao, C.N.R. *ChemPlusChem*, **2013**, 78, 419-422.

[12] Menoufy, M.F. ; Ahmed, H.S. ; Betiha, M.A. ; Sayed, M.A. *Fuel*, **2014**, 119, 106-110.

[13] Thakur, D.S. *J. Catal.* **1985**, 94, 310-312.

[14] Embaid, B.P. ; Biomorgi, J.G. ; Gonzalez-Jimenez, F. ; Perez-Zurita, M.J. ; Scott, C.E. *Appl. Catal. A: General*, **2011**, 400, 166-170.

[15] Raje, A.P. ; Dadyburjor, D.B. *Ind. Eng. Chem. Res.* **1993**, 32, 1637-1644.

[16] Diaz, Y. ; Sevilla, A. ; Monaco, A. ; Mendez, F.J. ; Rosales, P. ; Garcia, L. ; Brito, J.L. *Fuel*, **2013**, 210, 235-248.

[17] Zaera, F. ; Kollin, E.B. ; Gland, J.L. *Langmuir*, **1987**, 3(4), 555-557.

[18] Dos Santos, N. ; Dulot, H. ; Marchal, N. ; Vrinat, M. *Appl. Catal. A*, **2009**, 352, 114-123.

[19] Li, Z. ; Wang, G. ; Liu, Y. ; Gao, J. ; Xu, C. ; Liang, Y. ; Wang, X. *Fuel Proc. Technol.* **2013**,115, 1-10.

[20] Valencia, D. ; Olivares-Amaya, R. ; Aburto, J. ; Garcia-Cruz, I. *Catal. Lett.* **2013**, 143, 1354-1361.

CHAPTER 2

Corrosion - Fouling of 316 Stainless Steel and Pure Iron by Hot Oil

Material in this chapter has been published in the journal article;

Corrosion-Fouling of 316 Stainless Steel and Pure Iron by Hot Oil, *Energy & Fuels*, **2011**, 25, 4540-4551.

Composed by;

Tyler Stephenson, Alan Kubis, Marzie Derakhshesh, Mike Hazelton, Chris Holt, Paul Eaton, Bruce Newman, Anne Hoff, Murray Gray, David Mitlin.

Abstract

In this chapter we will examine the fouling and corrosion that took place when 316 stainless steel and pure iron wires were electrically heated to 508-680 °C in a liquid bath of the atmospheric bottoms fraction of a crude oil. The foulant was determined to be heterogeneous, with a thick macro-scale outer layer of pitch, covering a micro-scale sheath of coke, which was in turn both covering and interspersed with a micro-scale layer of iron sulfide. This foulant was observed to delaminate from the wire surface, presumably both due to the generation of growth stresses and due to the action of gas bubbles that were evolved during the fouling process. Unexpectedly, but conclusively, it was observed that the underlying wire surface was heavily corroded. In the case of the stainless steel it was observed that a micro-scale chromium oxide layer separated the foulant from the underlying metal. This layer presumably reduced the rate of metal dissolution. The degree of corrosion was much higher in the pure iron samples where such a layer did not exist. The hypothesis is that there is a synergy between the measured macroscopic fouling and the underlying microscopic corrosion, where the iron from the wire reacts with the sulfur in the oil to build up the thick sulfide. The fouling factor of the iron specimens was approximately twice that of the 316 stainless steel (approximately 100 mm^2K/W versus 50 mm^2K/W respectively).

2.1 Introduction

The delayed coking process has emerged as the preferred technology for upgrading the residue fractions of heavy oil and bitumen. One significant drawback for this process is the fouling of the furnace that heats the feed. Deposits accumulate on the interior of the furnace tubes, requiring a gradual increase in furnace temperature and thus fuel consumption to run the unit, giving a concomitant increase in greenhouse gas emissions and cost.[1] Eventually, the deposits become thick enough that the furnace tubes must be cleaned or replaced. Similar problems are encountered in a variety of related applications where thick poorly heat conducting buildups occur and decrease thermal efficiency.[2-4] A schematic of the delayed coking process is shown in Figure A1 of Appendix A.

Recent work on fouling of bitumen furnaces includes research by Parker and MacFarlane.[5] The authors passed pigs through the tubes of a furnace which had been operating at 350–500 °C to recover samples of foulant material, which were washed, dried and analyzed. One key observation of that study was that the amount of iron and sulfur within the foulant increased significantly with the proximity to the furnace walls. The proposed mechanism was the migration of the iron sulfide in the liquid to the furnace walls followed by its deposition on the surfaces. They hypothesized that the iron would be present in the feed bitumen as soluble and colloidal corrosion products rendered from upstream handling and storage.[5] The exact mechanism was not established in the study and alternative hypotheses, such as the reaction of the sulfur in the bitumen with the furnace tube

walls remain plausible. The deposition may also include trapping of solid particles from oil in a sticky layer on the furnace tubes, giving rise to the accumulation of inorganic material or partly soluble asphaltene components.[6] These mechanisms are comparable to fouling of heat exchangers by crude oil at temperatures below 350 °C, except that the rates of chemical reaction are much higher at elevated furnace temperatures.[2]

Authors Eaton and Williams[7] have also proposed a possible mechanism involving a two-step coking process, whereby coke forms on a metal surface, then depending on the chemical state, becomes either oxidized, sulfided or inhibited which can accelerate or inhibit further coke growth.[7] The same authors showed that hydrochloric acid and subsequent application of neutralizers determine the formation of iron sulfide with consequent fouling,[8] and using heated metal wires, showed that fouling increased with iron vs. stainless steel, suggesting a corrosion mechanism.[9] Additionally, researcher Panchal[10] observed coke deposits which contained iron sulfide and postulated its formation was caused by corrosion of the metal surface in the presence of naphthenic acid and hydrogen sulfide.[10] Researchers Watkinson and Wilson[11] provided a review on chemical reaction fouling and concluded that while the effect of feedstock composition has been relatively well covered in literature, little is known regarding the chemical reactions occurring on the surfaces that lead to fouling deposits.[11] These authors also indicate that in fact the contribution to fouling from precipitation process versus from reaction processes is still to be elucidated.

Researchers Gentzis *et al.*[1] performed a microscopy study of the fouling deposits in bitumen furnaces heated to skin tube temperature as high as 630 °C.[1] One key observation to come out of the study was that the fouling layer directly adjacent to the furnace skin consisted of a thin continuous film of iron sulfide.[1] This was different from the iron sulfide observed within the bulk of the foulant, where it existed as particulates. The implication of this result is that there is a propensity of the sulfide to fully wet the steel walls and hence a strong chemical interaction between the two. Iron sulfide deposition has been shown to be an integral part of fouling in sour Canadian crudes in the surface skin temperature range of 300-380 °C.[12] One clear trend observed in this study was that fouling rates were the highest in the heaviest oil, which contained the most sulfur and iron. In a study of low temperature (100 °C) fouling of hydrotreater feed filters in an oxidative environment, authors Wu and Chung[13] concluded iron naphthenate – a byproduct of a corrosion reaction between naphthenic acid and the steel piping – had catalyzed the fouling reactions.[13] They went on to state that the replacement of mild steel components by stainless steel in vacuum distillation units mitigated the fouling problem.

Despite the numerous detailed studies on fouling mechanisms, there is still a need to better explain how the metallurgical corrosion reactions that take place at the oil-steel interface in the liquid phase, produce the elements found in the coke, at temperatures between 550-700 °C. This operating regime is the primary focus of this study. The hypothesis is that corrosion reactions are important at the

temperatures of interest (e.g. oil at 250-450 °C, metal surface in excess of 550 °C). In order to investigate the role of corrosion in a coking environment that is relevant to industrial furnaces, we submerged heated alloy and pure iron wires in a batch of crude oil under controlled conditions. The wires and the surface deposits were then characterized by a combination of surface and bulk analytical techniques. In addition to conventional techniques such as optical microscopy, X-ray diffraction analysis (XRD), energy dispersive X-ray analysis (EDX) and scanning electron microscopy (SEM), we employ focused ion beam analysis (FIB) to provide site-specific structural and analytical information about the corrosion-fouling reactions. We believe that the new fundamental insights coming out of this study will provide a rational basis for controlling fouling phenomena in a variety of environments in addition to an improved understanding of the mechanisms involved. A 316 stainless steel was chosen as a baseline alloy for the study, as it reflects the composition of one of the alloys used in industry for refinery process furnaces. Fouling of pure iron wires is also included in this study since it is expected to foul in a similar manner to conventional low-alloy steels also found in refineries.

2.2 Experimental Procedure

A stirred 2000 mL autoclave was equipped with a heated wire probe, as illustrated in Figure 2-1a.[14] The 316 stainless steel and iron wires were mounted in the probes and heated resistively with a constant electrical current. The reactor assembly allows for the immersion and resistive heating of wires in crude oil

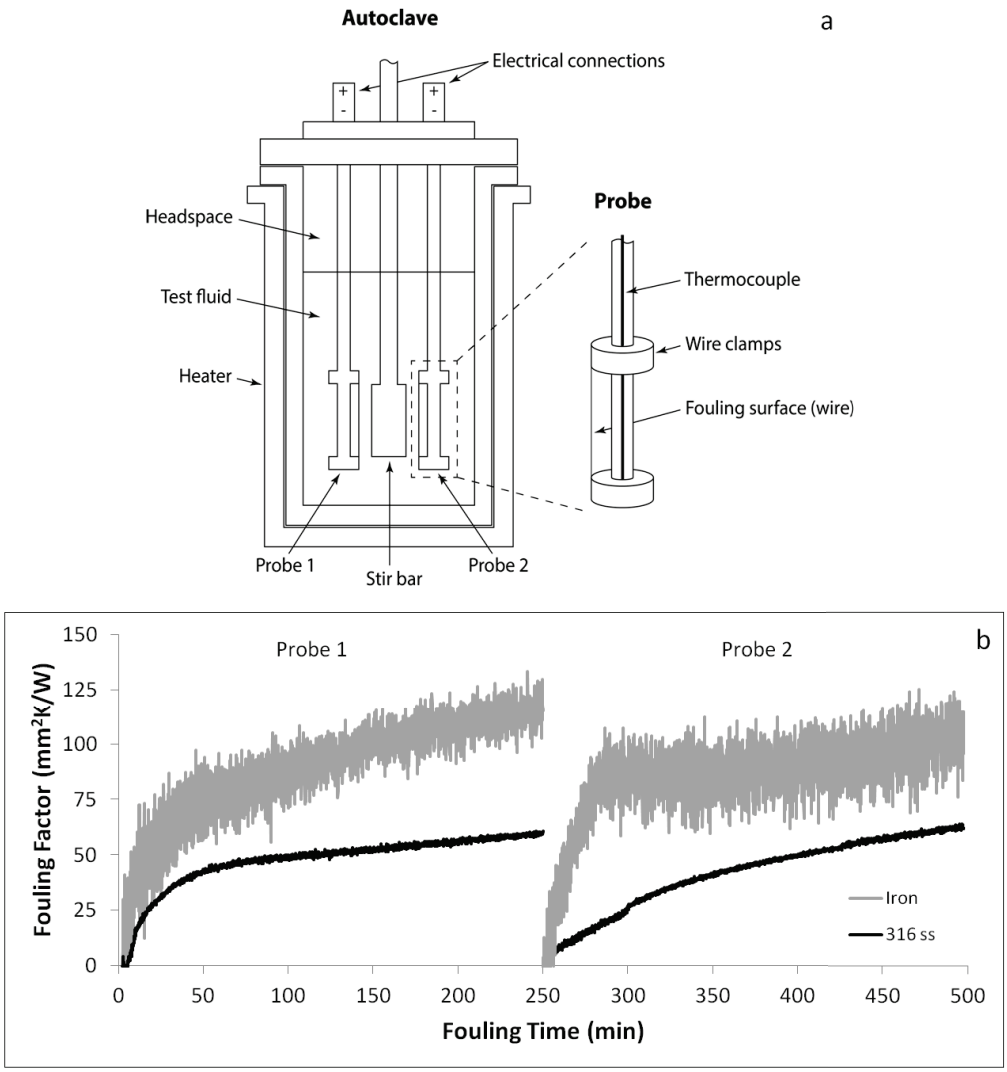

Figure 2-1: (a) Schematic diagram of the test autoclave. (b) Fouling factor curves generated for wire probes 1 and 2 using 316 stainless steel and iron. All wires were fouled at 5 A constant current.

under repeatable reactor conditions. The autoclave reactor was designed for batch operation, with a single charge of 1200 mL of crude oil. The crude oil in the autoclave was maintained at a constant temperature of 250 (±5) °C, using a thermocouple in a thermowell. The wire in the reactor probe could be heated resistively to a desired temperature above the bulk oil temperature via a constant

current input. Prior to testing, the reactor was sealed, purged with nitrogen, and pressurized to 8.84 atm. During testing the oil was stirred using a stirrer rotating at 300 RPM to ensure continuous delivery of crude oil to the surface of the heated wire.

The 316 stainless steel wires were fouled at 5 A constant current, which corresponded to a starting wire temperature of 540±9 °C. The iron wires were subjected to the same 5 A constant current, which produced a starting temperature of 508±12 °C. Each fouling run was conducted for 4.2 hours. The fouling factor (FF), or fouling resistance of the wire-oil interface is the inverse of its heat transfer coefficient: $FF = A_{wire}\ \Delta T / P$, where ΔT is $(T_{wire}-T_{oil})$, A is the heat transfer surface area of the wire and P is power output (derived from the product of voltage and current). During the constant current tests the voltage on the stainless steel and the iron wires increased by approximately 5 and 20% from their initial values, respectively. Here, the fouling factor was defined by the following overall equation, with the simplifying assumption of a constant heat transfer surface area;

$$FF = A\left[\left(\frac{\Delta T}{P}\right)_{fouled} - \left(\frac{\Delta T}{P}\right)_{clean}\right] \qquad \text{Eq. 2-1}$$

The temperature of the wire was determined by its resistance, where the measured resistance during the fouling run was compared with an ex-situ

temperature calibration plot generated by heating the wire externally within a quartz tube furnace and measuring its change in resistance with temperature. To generate this ex-situ plot, the probe was removed from the head of the fouling reactor and a wire was installed. The probe was then inserted into a 150 mm quartz tube furnace and heated from 25-400 °C at a rate of 1 °C/min. 0.2 A of current was passed through the wire to facilitate resistance measurement using a 1520 W DC power supply coupled with a data acquisition system. A plot of resistance with temperature was generated from the resulting data and used as a temperature calibration curve to estimate the temperature of the wire during fouling, using extrapolation. The wire temperatures were also verified ex-situ using temperature indicating liquids purchased from Tempil, and were found to agree within 5-10% of the extrapolated values. A more thorough derivation of fouling factor as well as the procedure for determining wire temperature is given in Figures A2, A3, and A4 of Appendix A. The correlation between wire resistance, temperature, fouling factor and foulant thickness is shown in Figure A5 of Appendix A.

The crude oil sample used for this study was an atmospheric bottoms fraction (nominally 340 °C+). Elemental analysis was conducted on the crude oil using a standard inductively coupled plasma mass spectrometry technique. The total acid number (TAN) of the crude oil was determined in accordance with ASTM standard D664-09a, using a Metrohm TIAMO 1.3 titration analyzer. Thermogravimetric (TGA) analysis of the crude oil and coke material was

conducted using a Thermo Cahn TherMax 300 TGA analyzer. Micro carbon residue content was determined in accordance with ASTM standard D4530. CHNS analysis of the crude oil and coke was completed using a Carlo Erba EA1108 elemental analyzer. Asphaltene content of the crude oil was determined via standard precipitation analysis using pentane mixed at a ratio of 40:1 and subsequent filtering and weighing of the asphaltene precipitates. The oil was 84.25 wt% carbon, 10.11 wt% hydrogen, 0.39 wt% nitrogen, and 3.43 wt% sulfur. The asphaltene content of the oil was 8.47 wt%, the micro carbon residue content was 6.45 wt%, the ash content was 0.02 wt%. The total acid number of the oil used for this study was 0.46±0.06 mg KOH/g crude oil. The concentration of chlorides in the oil was determined to be 9 ppm. The wires used to simulate the heat transfer surface were a standard (ASTM A-580) 316 austenitic stainless steel and a pure iron wire purchased from California Fine Wire Company. The composition of the 316 stainless steel wire (as reported by the manufacturer in wt%) was chromium (16-18), nickel (10-14), molybdenum (0-2), silicon (0-1), iron (balance). The diameter of the wires was 0.2 mm.

After removal from the reactor the wires were cleaned in two ways. Wires were soaked for 20 min in static xylene, or rinsed with xylene in a vortexer for approximately 30 s. The first cleaning technique allowed for imaging of the liquid pitch that coated the wire surface atop the coke. The second approach removed the pitch completely leaving the solid coke exposed. After cleaning in xylene, the wires were rinsed in acetone and isopropyl alcohol, and then dried

with a jet of compressed air for approximately 1 min. All fouled wires were stored in air at room temperature. For analysis of the mesophase, small flakes of the coke layer which covered the wires were broken off and placed into small plastic cups for mounting. The flakes were covered with epoxy and polished using standard metallographic techniques. The polished samples were analyzed using cross-polarized optical microscopy.

The wires were also mounted so that their cross-sections could be analyzed. Fouled wires were cut in half at their approximate center and oriented vertically using a small plastic mounting clip. They were then placed in a cylindrical mounting cup and covered with a conductive epoxy. The epoxy was mixed with a fine nickel powder (purchased from Buehler Canada) at a ratio of 1:1 by mass to make it conductive enough for imaging with an SEM. After hardening, the mounted wires were prepared using standard metallographic techniques. Wet grinding was conducted using SiC grinding papers of 180, 320, 600, 1200, 1800, 2000 and P-2400 grits. The total grinding time for each sample was approximately 1.5 hours. Grinding with P-2400 grit achieved an adequate surface smoothness for SEM imaging, however further improvement to the surface finish was achieved using a P-4000 grit SiC paper followed by a 0.05 μm alumina slurry and a napping cloth. Polishing with the slurry was conducted for approximately 2 hours and resulted in a mirror finish of the wire cross sections. The iron wires were thoroughly dried with air in between grinding steps to avoid

corrosion. They were not polished with slurry as it was found that this resulted in significant surface corrosion.

The wires were analyzed using a focused ion beam (FIB) microscope for micro cross-sectioning, conventional optical microscope, cross-polarized optical microscope, scanning electron microscope (SEM), X-ray diffraction (XRD) and energy dispersive X-ray analysis (EDX). Cross-polarized optical microscopy was performed using a Zeiss, Axio observer.D1m. XRD analysis was performed using a Bruker AXS D8 Discover diffractometer with a GADDS area detector. FIB analysis was performed using a Ziess NVision 40 dual beam system. The FIB uses a 30 kV Ga liquid metal ion source with ion currents of 0.15 pA-45 nA. The system is equipped with a vertical SEM column which is situated at 36° relative to the FIB column. For imaging of samples, the FIB SEM was operated at 3 kV to optimize surface sensitivity. For EDX area analysis, 15 kV electrons were used. Cross sections were milled with the FIB and then imaged with the SEM to minimize damage to the sample. EDX line scans were conducted using a Hitachi S-3000N SEM with an Oxford INCA EDX system. Scans and micrographs with this system were taken at 15 kV with a 58 μA saturated beam current.

2.3 Results

Figure 2-1b shows representative fouling factor versus time curves for 316 stainless steel and iron wires. Each fouling run was comprised of two probes

which were run in series as shown on the plot. Consistent results were obtained for each probe, indicating that the fouling behavior was the same at the geometrically opposing locations. Occasionally small random "jumps" were observed in the fouling curves generated by either probe. We believe that these were instrumentation artifacts due to the probe design. The concentric metal tubes within the probe expand due to heating. This causes an instantaneous change in resistance as the connections between the tubes are altered by this expansion. Such jumps did not affect the analysis. One immediately notices that the noise in the data is accentuated for the iron compared to the stainless steel. This is due to the fact that the resistivity of the pure iron wires is much lower than the stainless steel. Therefore, the overall resistance of the iron wires is closer to the resistance of the entire circuit, and the system picks up more noise in the measurements as a result. The temperature of the wires was observed to increase with time: The temperature of the 316 stainless steel and iron wires increased by 160 °C and 100 °C, respectively, over the full fouling run. As will be demonstrated in subsequent Figures, the temperature increase is caused by a buildup of the foulant on the wire surface, which impedes heat transfer as the layer thickens.

Figure 2-2a shows an FIB cross-section of the as-received 316 stainless steel wire. As expected, the nanoscale (typically < 5 nm in the as-received alloy) chromium oxide layer on the wire surface, which is always present on 316, was not visible even at a relatively high magnification. Some cracking and porosity

was observed at the surface of the wire, which was most likely due to shearing action and the removal of inclusions as a result of wire drawing. Figure 2-2b shows a polished and etched cross-section of the 316 stainless steel wire highlighting the grain size distribution in the alloy. The austenitic steel grains are approximately 5-25 μm in diameter.

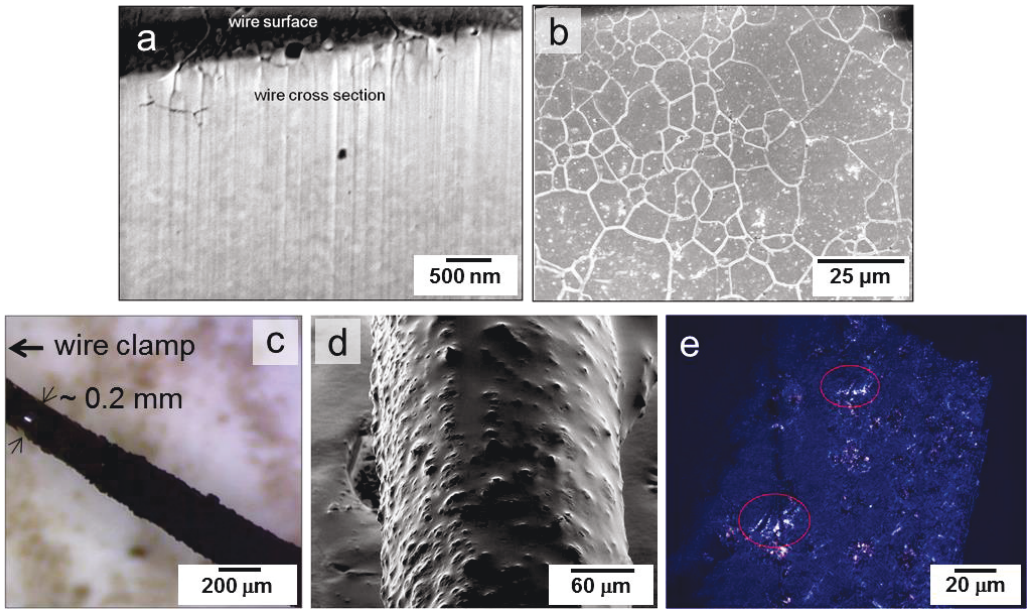

Figure 2-2: (a) FIB cross section of the as-received 316 stainless steel wire. (b) Polished and etched cross-section of the steel wire highlighting the grain size distribution in the alloy. (c) Optical microscope image of the surface of a 316 stainless steel wire fouled at 5 A constant current. Adjacent to the clamp the fouling layer is cracked, revealing the underlying metal. (d) SEM micrograph of a fouled 316 stainless steel wire. (e) Polished cross-section the foulant, analyzed under polarized light; the bright mesophase is highlighted by the circles.

Figure 2-2c shows an optical microscope image of the fouled 316 stainless steel wire. The wire was soaked in xylene to remove excess oil. A thick macroscopic fouling layer was observed to coat the entire length of the wire with an approximately uniform thickness. The fouled layer was not monolithic; rather

it was a composite consisting of a thick macroscopic outer layer of pitch coating a series of thinner layers that will be detailed in subsequent Figures. Below the pitch was a thick layer of coke (visible in 2-2c but detailed in subsequent Figures). The macroscopic coke was brittle, and had poor adhesion to the wire surface, being easily removed by bending, scraping or cutting. Figure 2-2d shows an SEM micrograph of a 316 stainless steel wire that was soaked in xylene for 20 minutes to expose the underlying pitch.

The composition of the coke was 61.4 wt% carbon, 1.73 wt% hydrogen, 1.31 wt% nitrogen, 13.67 wt% sulfur, with 21.9 wt% being iron sulfides. The elemental sulfur may be attributed to the high content of non-volatile sulfur in the asphaltenes that were the precursors to coke formation. The coke deposited on the wires was predominantly isotropic, based on examination under a microscope equipped with cross-polarizers, with a few domains of mesophase as illustrated in Figure 2-2e. The mesophase was observable as lightly-coloured and shiny domains within the body of the coke. Unfortunately the images do not reproduce well in photographs - they are clearer when directly examining the samples under the microscope. These domains are small and semi-spherical. The anisotropic matrix could also contain mineral matter, but the EDX shows that it is mainly carbon, sulfur and iron. These characteristics are comparable to deposits that were removed from industrial furnace tube walls in the study of Gentzis *et al*.[1] However in that work the furnace temperature was relatively lower, being in the 450-500 °C range. The other key difference compared to the present study is that

we fouled the wires for only 4.2 hours. Therefore our coke material was not subjected to as much ageing as their industrial samples.

Table 2-1 shows the results of the elemental analysis conducted on the crude oil before and after 50 fouling runs. Initial top and initial bottom pertains to the location within the reactor from which the oil was sampled prior to fouling. Fouled top and fouled bottom refer to the location of the sampled oil within the fouling reactor after the conclusion of the experiments. The analysis indicates fouling produces negligible change in the overall composition of the crude oil. In particular it is important to note that the iron content within the oil does not change at all after the fouling runs. As we will demonstrate, it is primarily the wires rather than the oil that is the source of the iron for the iron sulfide deposits that build up and spall off during fouling.

Table 2-1: Results of the elemental analysis of the crude oil before and after 50 fouling runs.

	Species (ppm)															
Sample	**Na**	**Al**	**P**	**Ti**	**V**	**Cr**	**Fe**	**Mn**	**Co**	**Ni**	**Cu**	**Zn**	**Sr**	**Mo**	**Ba**	**La**
Initial top	0.00	0.98	33.44	0.18	4.57	0.35	*61.89*	0.07	0.00	1.94	0.39	0.29	0.00	0.17	0.02	0.00
Initial bottom	1.38	1.12	32.61	0.30	10.53	0.35	*64.81*	0.08	0.00	6.00	0.00	0.38	0.00	0.22	0.04	0.00
Fouled top	0.00	1.45	33.74	0.46	16.90	1.03	*67.64*	0.17	0.00	8.82	0.84	0.90	0.04	0.30	0.03	0.00
Fouled bottom	2.67	1.56	30.16	0.61	22.55	1.03	*62.03*	0.18	0.04	12.68	0.56	0.73	0.05	0.23	0.05	0.04
Fouled bottom	2.14	1.77	31.05	0.54	23.23	1.07	*63.78*	0.18	0.04	13.09	0.58	0.72	0.05	0.26	0.04	0.05

Figure 2-3a shows the macrostructure of the iron sulfide and coke observed on a 316 stainless steel wire surface. The visible crystals are iron sulfide, which have a blocky-columnar morphology. The crystals begin at the wire surface and extend out from the wire by approximately 10-15 μm. The layer on top of the iron sulfide is coke. Figure 2-3b presents an XRD scan of the stainless steel wire with the deposit on it. The coke, which is mostly amorphous, does not present any clear Bragg peaks. Based on the thermodynamic properties of $Fe_{(1-x)}S$ at temperatures below approximately 700 °C, iron sulfide can exist as three phases, triolite, pyrrhotite and pyrite (FeS, $Fe_{(1-x)}S$ with x = 0.1 or less, and FeS_2 respectively) depending on its composition and thermal history.[15] The indexed XRD pattern shows well-defined Bragg peaks that are characteristic of the $Fe_{(1-x)}S$ form of iron sulfide, commonly known as pyrrhotite.[16] As will be demonstrated by the analytical results, the iron sulfide also contains nickel. This is expected since $Fe_{(1-x)}S$ and $Ni_{(1-x)}S$ are isostructural and fully soluble. For the purposes of brevity, we will refer to the phase as iron sulfide with implicit recognition that it is actually iron – nickel – sulfide.

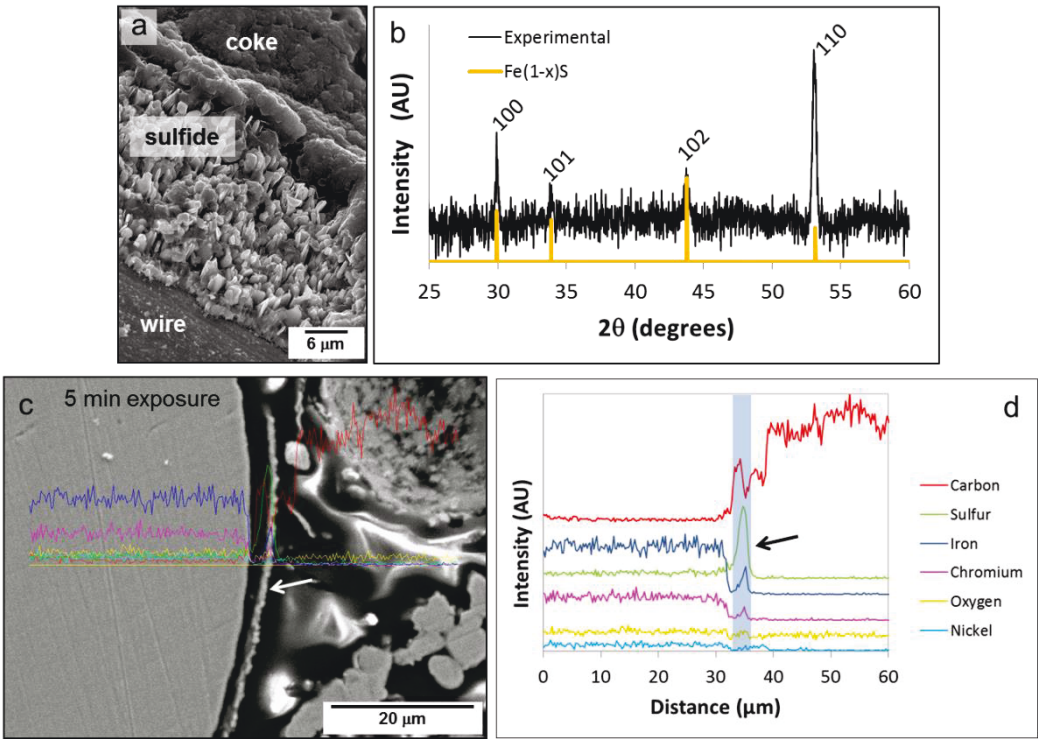

Figure 2-3: (a) SEM micrograph of the wire-sulfide-coke interface, representative of the foulant structure encountered everywhere on the 316 stainless steel wire surface. (b) XRD analysis of the coke layer showing that the FeS crystals underneath are primarily pyrrhotite $Fe_{(1-x)}S$. (c) and (d) Cross-sectional SEM micrograph and accompanying EDX line scan on the stainless steel wire after 5 minutes of fouling.

Figures 2-3c and 2-3d show a cross-sectional SEM micrograph and accompanying EDX line scans of the stainless steel wire after 5 minutes of fouling (3d expanded for clarity). The right half of the SEM micrograph shows the nickel-infused conductive epoxy used for mounting which helps to define the outer surface of the sulfide layer (arrowed). It can be seen that the spherical and nearly spherical nickel particles extend nearly all the way to the wire surface, indicating a negligible presence of coke. There is however, a thin layer of sulfide (arrowed in 2-3c) which has formed after only 5 minutes of fouling. This sulfide was observed as a thin and nearly continuous layer directly adjacent to the wire

surface. At this particular location, the sulfide appears to be partially detached from the wire, although one can't tell whether this occurred in-situ at temperature or during the cool down process due to the thermal expansion mismatch. The scan for carbon indicates that at some point during the fouling run, the sulfide layer delaminated, and allowed pitch to flow underneath. The EDX scans confirm an enhanced sulfur concentration (green line, arrowed in 2-3d) of the delaminated layer. Thus we can conclude that the sulfide layer is formed prior to coke deposition and that what is important is the wetting behavior of the coke on the sulfide rather than on the bare metal. We also see a small peak for chromium in the scan which indicates that to begin with, the sulfide layer on the stainless steel forms as a mixture of transition metal sulfides. Initially, the high surface concentration of chromium in the wire contributes a small amount of chromium sulfide to the surface sulfide scale. Over time, the concentration of chromium sulfide becomes diluted due to the dominant formation of iron sulfide, and the fact that chromium becomes immobilized as a surface oxide in the wire. At this point during the fouling, the native oxides on the wire, as well as any nickel sulfide which may have formed were below the detectable limits of this technique as shown by the negligible signal of their respective scans. We plan to conduct a more comprehensive analysis of the wire sub-surface in the follow-up study.

Figure 2-4 shows an SEM micrograph and EDX elemental maps of an end of a 316 stainless steel wire that has been severed using wire cutters. The brittle coke layer has been partially removed as a result of cutting, leaving the wire

surface exposed. The carbon scan confirms that the coke layer is of course carbonaceous. The presence of a sulfur-rich species on the surface of the wire is confirmed by EDX. Strong signals from chromium are detected on the surface of the wire where the coke has been removed. This indicates that the chromium layer is highly adherent to the wire, rather than to the coke. In the regions where the coke was still present on the surface, chromium signals were not detected. However the signal for nickel is present both on the bare wire surface and in the coke layer. Iron is similarly observed in both the coke layer and of course in the wire. The difference in the relative intensity of the nickel versus the iron in the coke layer may be explained by considering that the alloy concentration of the nickel in the bulk wire is relatively low.

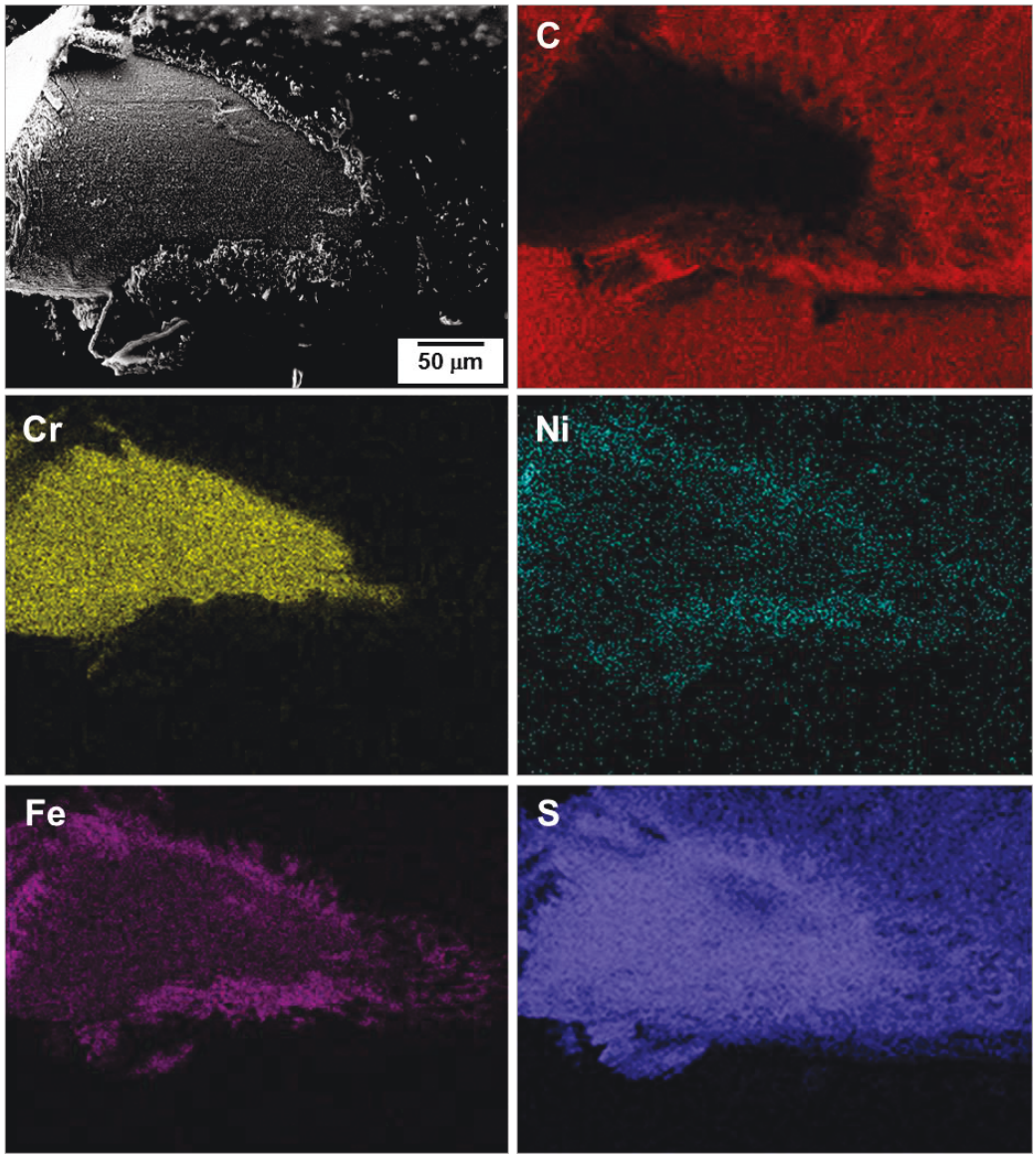

Figure 2-4: SEM micrograph and EDX elemental maps of a 316 stainless steel wire with the foulant partially removed.

Figure 2-5a shows an SEM micrograph of a fouled 316 stainless steel wire under low magnification. The surface of the coke is marked with gaseous exit craters (arrowed) thought to originate from the degassing associated with both the underlying corrosion reaction at the surface of the wire, as well as the formation

of the coke itself. Figure 2-5b shows a higher magnification image of such a crater. The presence of these craters indicates that the coke behaved as a viscous liquid during the fouling, being deformable enough to allow for bubble formation and transport, but stiff enough to resist collapse and facilitate pore formation. Figure 2-5c shows an SEM micrograph of an FIB cross section of the wire. Here, the coke layer is approximately 30-50 μm thick and forms a coating on the wire surface that contains some porosity. Figure 2-5d presents a higher magnification SEM micrograph of the FIB cross section that highlights the iron sulfide – wire surface interface. The two have mechanically separated. Between the bulk wire and the iron sulfide there is a micro-scale porous interface. Comparing this with the as-received FIB cross section of the stainless steel wire in Figure 2-2a we can see that no such porosity exists. The presence of such an interface in the fouled specimen is a direct indicator that corrosion of the wire has occurred concomitantly with the fouling.

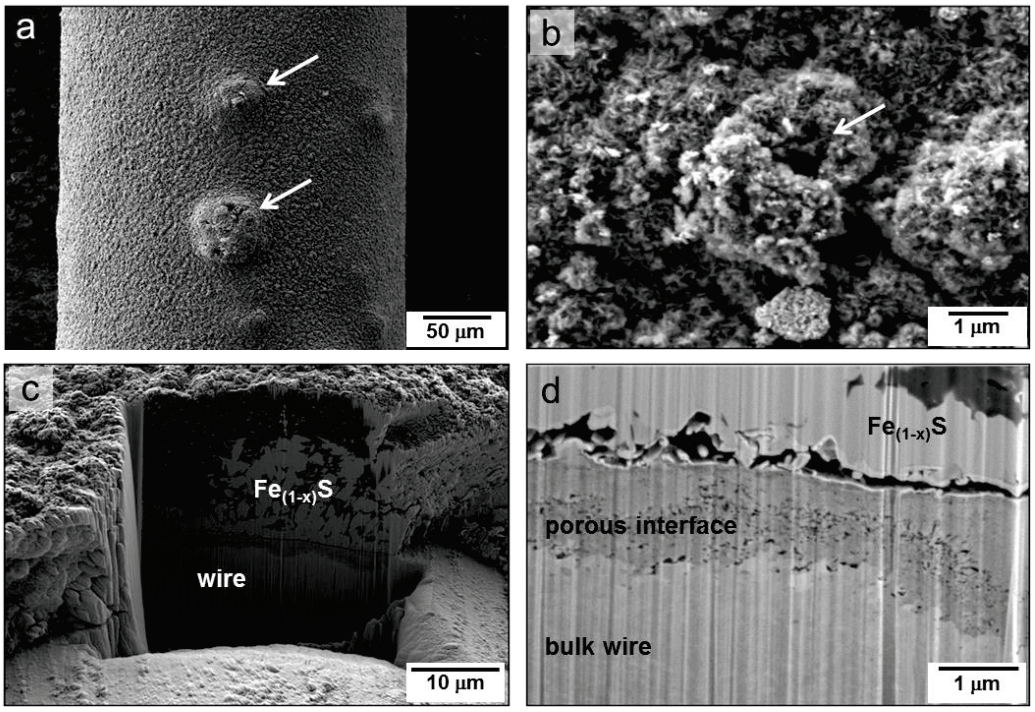

Figure 2-5: (a) SEM micrograph of the fouled 316 stainless steel wire surface highlighting the presence of gas-bubbles (arrowed) in the coke layer. (b) Higher-magnification micrograph highlighting the exit crater formed by a gas bubble in the coke. (c) FIB cross section highlighting the sulfide and coke composite fouling layer. (d) Magnified image of the delaminated wire-coke interface, highlighting the micro-scale composite structure of the fouled wire surface.

Figure 2-6 shows an SEM micrograph and EDX elemental maps of an FIB cross section taken through the foulant and the stainless steel wire. In the region shown, the sulfide layer has delaminated from the wire surface. Here the entire coke/sulfide layer has detached from the surface of the wire and has allowed pitch to flow in underneath. The detached foulant is identified as a combination of sulfide and coke. The scan for chromium indicates that it is heavily concentrated near the wire surface, with the concentration enhanced layer being micron-scale. There is also a secondary sulfur-rich layer in close proximity to the chromium-

rich layer. However, close inspection of the elemental maps reveals that the sulfur-rich and the chromium-rich regions of the wire are in fact separate, with the sulfur-rich layer being closer to the bulk.

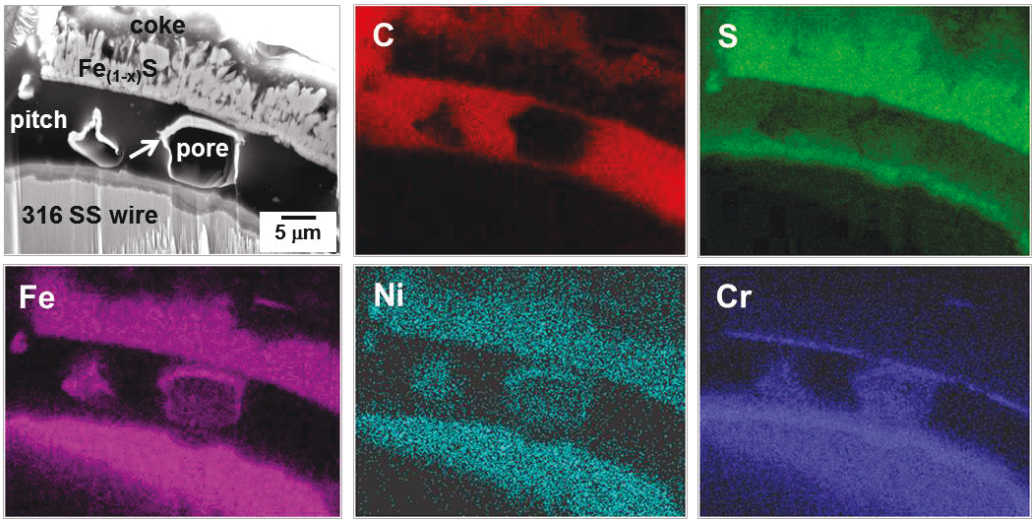

Figure 2-6: FIB cross section and EDX elemental maps of the pitch encapsulated by coke that has detached from the main wire. Adjacent regions (out of view) still have the sulfide connected to the wire surface. The underlying corroded wire surface is also shown. The metal present in the pore (arrowed) is an artifact of the milling process.

Figure 2-7 shows a higher magnification SEM micrograph and EDX elemental maps taken from the de-alloyed region of the same 316 stainless steel wire surface shown in Figure 2-6. The EDX scan for carbon helps to locate the wire surface in subsequent scans. The images highlight the chromium-rich and the sulfur-rich bi-layer surface corrosion products on the wire. The products can be seen to be iron-depleted. The chromium-rich portion of the bi-layer is also

clearly oxygen enriched. This oxide is most likely one or a combination of Cr_2O_3 and Cr_3O_4 oxides, both of which have appreciable solubility of iron and nickel.

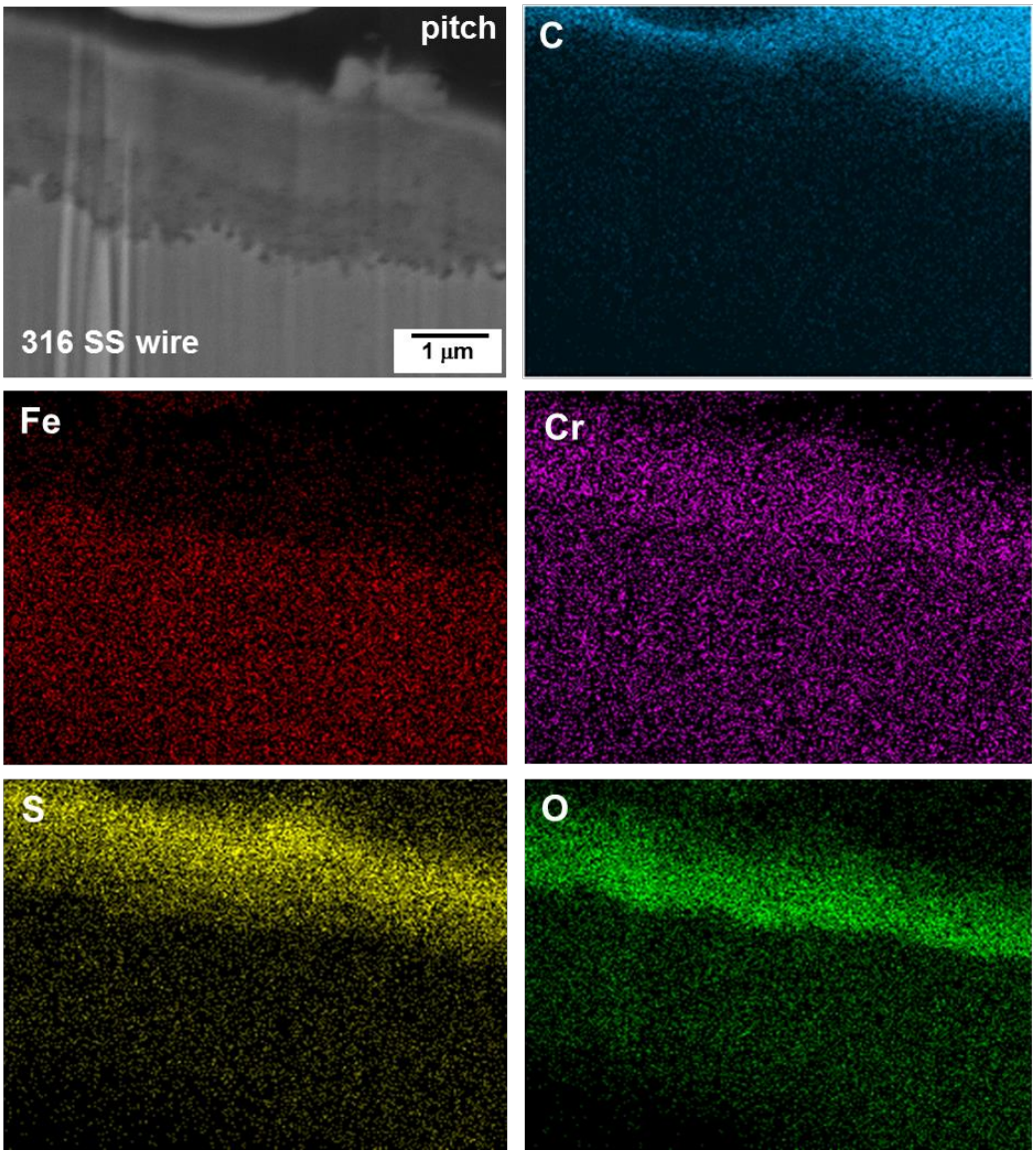

Figure 2-7: FIB micrograph and EDX elemental maps of the corroded 316 stainless steel wire surface, with the sulfide detached (top center of image).

Figure 2-8 highlights the pure iron wire. Figure 2-8a shows the extensive porosity that has evolved through the coke layer during fouling. The level of porosity in the coke was consistently higher than in the stainless steel specimens. Figure 2-8b shows an FIB cross-section of the fouled surface. The foulant was much thicker for the pure iron case and contained a higher fraction of iron sulfide. This is corroborated by the trend seen in Figure 2-1b, where the fouling factor for the iron wires is approximately double that of the 316 stainless steel. Figure 2-8c shows a high magnification image of the foulant near the wire surface, highlighting the predominance of iron sulfide.

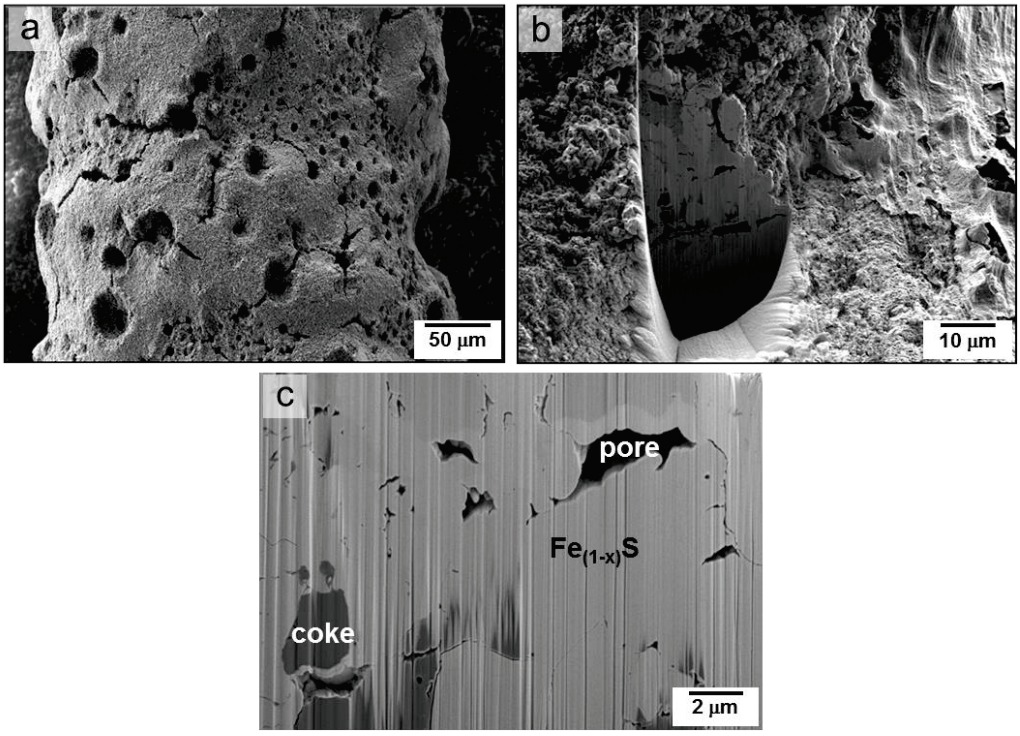

Figure 2-8: (a) SEM micrograph of pure iron wire fouled at 5 A constant current highlighting pores in the foulant. (b) FIB cross section through the iron wire and the foulant. (c) Magnified view of (b), highlighting the foulant structure.

Figure 2-9 shows an SEM micrograph and corresponding EDX elemental maps of a cross section from a fouled pure iron wire. Around the border of the SEM micrograph we can see the nickel-infused conductive epoxy used for mounting, which helps to define the outer surface of the coke layer in the carbon scan. The presence of a large quantity of iron sulfide is confirmed through the iron and sulfur elemental maps. The iron sulfide plumes originate from the iron wire surface and extend radially into the coke layer. Relative to the stainless steel, the levels of both fouling and corrosion to form iron sulfide are much higher. There is in fact a marked decrease in the cross section of the iron wire, which continuous to corrode as the iron sulfide is formed and then detaches. Samples fouled for longer times (not shown) actually corroded sufficiently to create an open circuit.

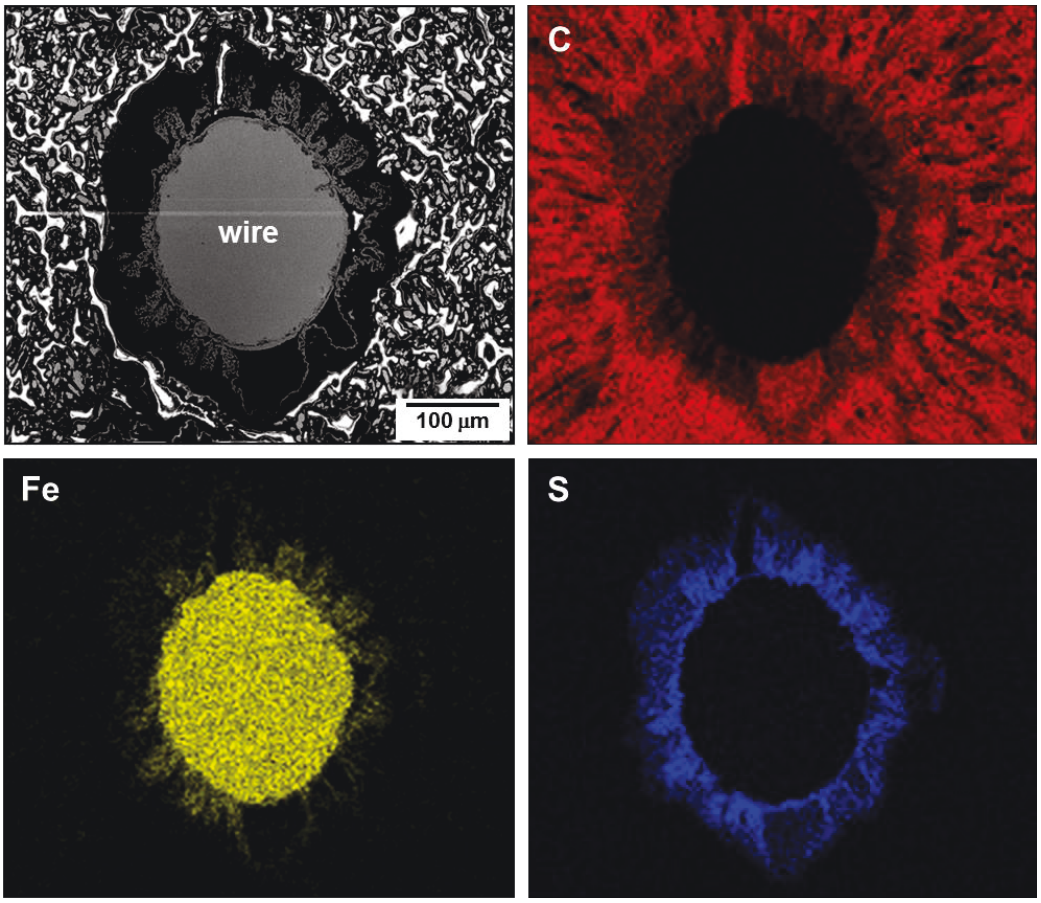

Figure 2-9: SEM micrograph and EDX elemental maps of the fouled pure iron wire mounted in nickel-infused epoxy.

2.4 Discussion

The experimental findings support a hypothesis that fouling is a combination of sulfidation and coking. Sulfur is among the most plentiful heteroatom species in heavy crude oils, and a portion of these components are reactive organic sulfides which will decompose at the temperatures of the wire surface in these experiments.[17] The precise reaction mechanisms of decomposition are complex, however the main product of the reaction is hydrogen sulphide, which would react to form iron sulfide as shown in equation 2-2;

$$Fe_{(s)} + H_2S_{(g)} \leftrightarrow FeS_{(s)} + H_{2(g)} \qquad \text{Eq. 2-2}$$

The evolution of hydrogen gas results from the sulfide-forming corrosion reaction, and other gases evolve from dehydrogenation and cracking reactions associated with coke formation. This creates the bubbles observed in the coke. In the case of pure iron there is more corrosion yielding more gaseous evolution, and hence the higher level of coke porosity observed (Figures 2-5a and 2-8a). However the gas evolved during coke formation is also important. Thermal decomposition of asphaltene species is accompanied by the removal of a range of volatile components, with boiling points ranging from close to the wire surface temperature down to that for methane. At some point, the concentration of dissolved gases and volatile components exceeds a critical saturation pressure, causing the formation of a bubble.[18,19] The bubbles then travel through the coke layer from the surface of the wire to the surrounding fluid. We suggest that this evolution of mixed gases, combined with stresses associated with thermal expansion and the volume change of forming iron sulfide, drives the delamination of the sulfide crystals in plumes or as layers. Thermophoretic motion could also contribute to the movement of particles down a thermal gradient, which extends from the wire surface into the coke.[20] The motion of heated particles due to thermal vibrations would presumably cause particles to dissociate away from the wire surface, where collisions would be most concentrated. After the sulfide layer

is dislodged from the wire surface, crude oil is then able to flow under the sulfide where the corrosion-fouling process begins again on fresh metal.

Historically, naphthenic acid corrosion has been of significant concern in refinery environments e.g.[21-24] Since naphthenic acids have a wide array of molecular sizes and structures, they will also have a range of decomposition temperatures, ranging from 200 °C to over 400 °C. At temperatures pertinent to this study, very limited acid components are expected to remain stable. The lower stability acid components will decompose to generate additional sulfur, which should react with hydrogen and feed the iron to iron sulfide corrosion reaction. While there may be other sulfur compounds present at the testing temperatures, H_2S is the key driver for the sulfide formation since it is both the most reactive and the most mobile of the sulfur species.

We will now consider the structure of the micro-scale surface corrosion product which remains attached to the wire surface. Afterwards we will revisit the mechanism by which the much thicker outer layer of sulfide - coke foulant is formed and continues to grow. The structure of the sub-surface scale in the 316 stainless steel may be considered in view of a competition between oxidation and sulfidation in this system. The water vapour present in the oil will stabilize the formation of oxides. Referring to the Ellingham diagram for 316 stainless steel presented by Ohmi *et al.* [25], we would expect an oxide multilayer composed of an outermost layer of Cr_2O_3, followed by Fe_3O_4, with mixed chromium-iron-nickel

oxide spinels adjacent to the unaffected metal.[25,26] The Ellingham diagram presented by Ohmi *et al.*[25] is shown in Figure A6 of Appendix A. However there is also H_2S in the system, which drives the formation of sulfides. Which phases will be sulfided and which ones will be oxidized can be estimated from considering their thermodynamics.[27] In this experimental setup it is impossible to provide a fully quantitative thermodynamic prediction. With the problem being that the activities of each gas (water and hydrogen sulfide) at the wire surface, and at the interfaces of the multiple and constantly evolving corrosion layers, are unknown. Though the activity of the gas components will certainly be smaller than in these calculations at standard conditions, the thermodynamic values should, however, still provide meaningful trends.

Table 2-2 summarizes thermodynamic data for the three principle transition metal oxides and sulfides that are prevalent in this experiment. Except for chromium sulfide, Fe_2S_3, Fe_3S_4, and nickel oxide, all data was gathered from the CRC handbook.[28] Chromium sulfide is a poorly characterized substance and the existing literature lacks reliable thermodynamic data. There have been no reports in open literature of Cr_2O_3 converting to a sulfide. Thermodynamic data for nickel oxide was taken from the data presented by Lee.[29] Thermodynamic data for Fe_2S_3 and Fe_3S_4 was taken from the data presented by researchers Waldner and Pelton.[15]

Table 2-2: Thermodynamic data for the principle metallurgical reactions during fouling.[15,28,29] na=not available

Reaction at 550 °C	$\Delta G_{(rxn)}$ (J/mol)
Oxidation of metals	
$2Cr_{(s)} + 3H_2O_{(g)} \leftrightarrow Cr_2O_{3(s)} + 3H_{2(g)}$	-298,500
$3Fe_{(s)} + 4H_2O_{(g)} \leftrightarrow Fe_3O_{4(s)} + 4H_{2(g)}$	-13,000
$2Fe_{(s)} + 3H_2O_{(g)} \leftrightarrow Fe_2O_{3(s)} + 3H_{2(g)}$	17,700
$Ni_{(s)} + H_2O_{(g)} \leftrightarrow NiO_{(s)} + H_{2(g)}$	42,300
Sulfidation of metals	
$Fe_{(s)} + H_2S_{(g)} \leftrightarrow FeS_{(s)} + H_{2(g)}$	-44,800
$Ni_{(s)} + H_2S_{(g)} \leftrightarrow NiS_{(s)} + H_{2(g)}$	-18,600
$Cr_{(s)} + H_2S_{(g)} \leftrightarrow CrS_{(s)} + H_{2(g)}$	na
Sulfidation of metal oxides	
$Fe_3O_{4(s)} + 4H_2S_{(g)} \leftrightarrow Fe_3S_{4(s)} + 4H_2O_{(g)}$	-118,100
$NiO_{(s)} + H_2S_{(g)} \leftrightarrow NiS_{(s)} + H_2O_{(g)}$	-60,900
$Fe_2O_{3(s)} + 3H_2S_{(g)} \leftrightarrow Fe_2S_{3(s)} + 3H_2O_{(g)}$	-98,000
$Cr_2O_{3(s)} + 3H_2S_{(g)} \leftrightarrow Cr_2S_{3(s)} + 3H_2O_{(g)}$	na

Free energy calculations reveal that chromium oxide will almost certainly remain stable, whereas iron and nickel sulfides will form preferentially over their most stable oxides at 550 °C. There is also a large thermodynamic driving force for the sulfidation of iron and nickel oxides, should they form. Taking into account these trends and referring to the sulfur and chromium scans in Figure 2-7, the 316 stainless steel sub-surface scale will be composed of Cr_2O_3 at the surface, with mixed sulfides underneath. Porosity is expected to develop in these oxide and sulfide layers due to unequal rates of outward diffusion. The presumably connected porosity in the chromia would allow for the counter diffusion of H_2S to the underlying mixed iron and nickel oxides, which convert to sulfides. The presence of chlorides in the oil may accelerate the H_2S ingress by reducing the structural integrity of the chromia.

Next we will reconsider the thick sulfide - coke layer that forms on the outer side of the chromia. Iron, and to a lesser extent nickel, are soluble in chromia.[30] At fouling temperatures both elements will diffuse outward through chromia (driven by the concentration gradient) and will be sulfided at the surface. The flux of the iron will be higher due to the higher solubility, concentration gradient, and perhaps due to a higher diffusion coefficient.[30] This should favour the formation of a mixed iron-nickel sulfide that is rich in iron. The iron sulfide that forms has a lower density than the parent metal (stainless steel); 4.7 versus 7.9 g/cm^3 respectively.[28,31] This results in compressive growth stresses in the thickening layers, which become particularly important for the much thicker and

unconstrained outer sulfide layer. As this sulfide grows to micro-scale dimensions the strain energy builds up as the logarithm of thickness.[32,33] This ultimately causes the sulfide layer to detach. Evolving gas bubbles generated due to the formation of hydrogen gas from corrosion at the wire surface would also cause delamination. As the layer detaches the stresses are eliminated and a new layer of sulfide initiates growth on the wire surface.

For the case of the stainless steel, at high temperatures the initially nanoscale chromia layer progressively thickens to the micro-scale dimensions. This adherent layer protects the underlying steel wire by increasing the diffusion distances for the iron and nickel to the surface. In the case of the pure iron wire, the chromia layer is absent, and the dissolution of the iron to form a sulfide continues unimpeded. It is unlikely that the usual Fe_2O_3 or the Fe_3O_4 passivating layers will be stable against their conversion to iron sulfide. The difference in the surface structure of the stainless steel versus that of the pure iron not only results in a variation of the corrosion rate, but in a subsequent variation in the fouling rate due to the much thicker sulfide/coke layer formed in the latter.

A summary of the proposed process for both materials is presented in Figure 2-10a and 2-10b. Though not explicitly emphasized in the schematic, we provide strong evidence that the sulfide layer forms first (Figures 2-3c and 2-3d). There should be a difference in the wetting behaviour of the coke sheath on the sulfide versus on an exposed metal surface, which contributes to the accelerated

fouling in the presence of the sulfide. We plan to investigate this effect in future studies.

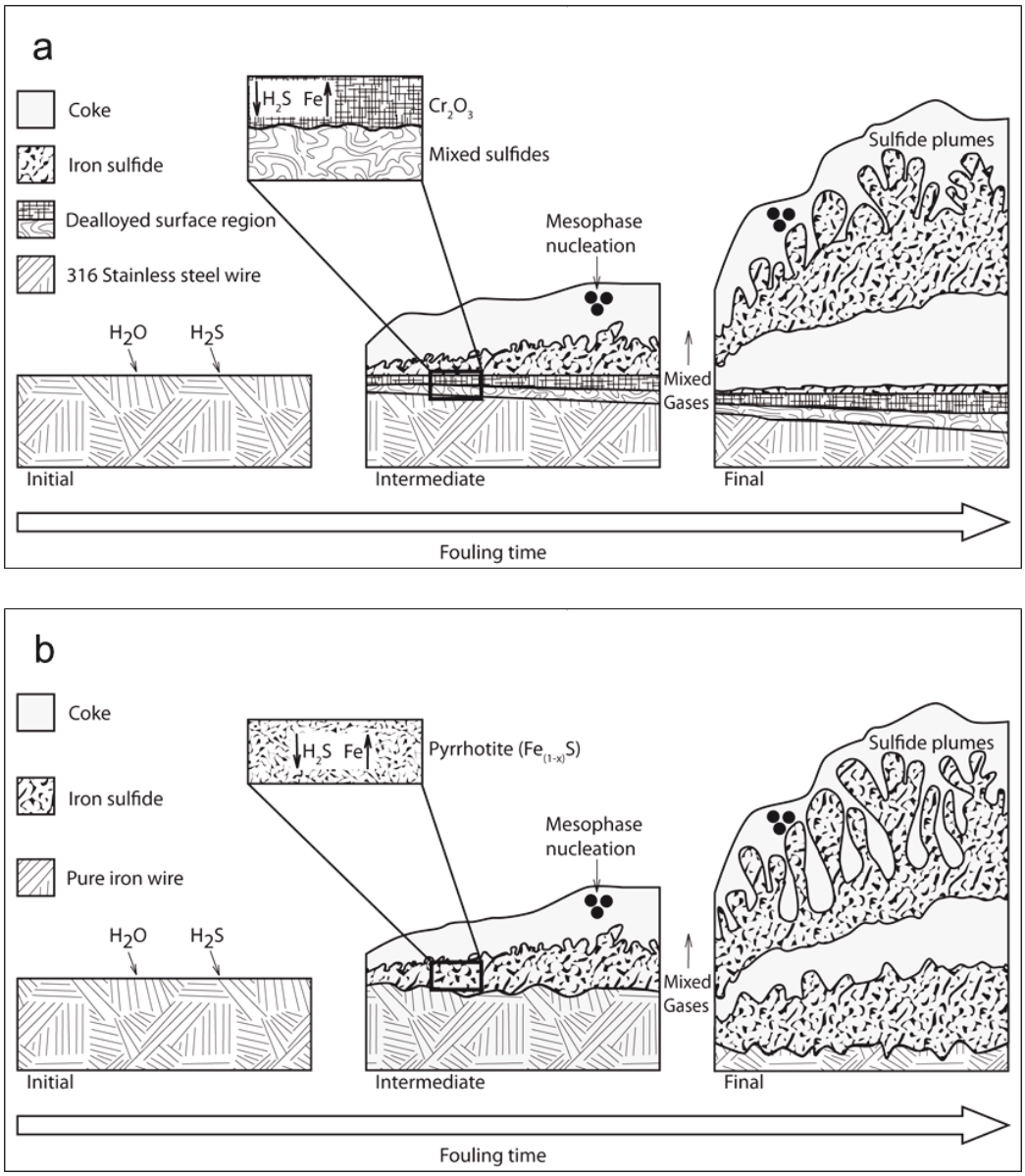

Figure 2-10: (a) Schematic highlighting the stages of fouling in the 316 stainless steel. (b) Schematic summarizing the fouling process for pure iron.

We would also like to emphasize that more work is needed. For example there is not yet a good quantitative understanding of the effect of fluid shear velocity on the rates/structure of the foulant build up for the current experimental configuration. We have some limited qualitative evidence of the expected inverse relation between the fouling rates and the fluid shear rates: Adjacent to the relatively bulky probe wire clamps, the fouling rates are locally higher. These would be the regions that experience reduced fluid velocities relative to the rest of the wire.

The fouling phenomenon that is detailed in this study is related to what is commonly termed "steady-state" or "chronic" fouling. We do expect that corrosion-related processes would also be active in parallel to the high-rate "catastrophic" fouling brought on by large-scale asphaltene flocculation in incompatible oil mixtures, nearly incompatible oil mixtures, and self-incompatible oils e.g.[34-36] However in those cases underlying metal corrosion should only have a secondary role in determining the net rate of deposit buildup. Additional research needs to be done in this area as well, employing our experimental system to study the more opportunity crudes.

2.5 Conclusions

An electrically heated wire probe in an autoclave reactor was utilized to foul 316 stainless steel and pure iron wires in a liquid bath of hot crude oil. Several analytical techniques, including focused ion beam analysis, scanning electron microscopy, optical microscopy, energy dispersive X-ray analysis, and X-ray diffraction, were combined to examine the structure of the macroscopic foulant layer.

The foulant was not monolithic. Rather it was a composite consisting of a thick macro-scale outer layer of pitch. Beneath the pitch we observed a sheath of coke, which was tens of microns in thickness. Inside and interspersed with the coke was iron sulfide. X-ray analysis revealed the majority phase of the sulfide to be of the pyrrhotite $Fe_{(1-x)}S$ structure. Analytical microscopy revealed that the sulfide phase also contained nickel in solid solution. These three layers - pitch, coke and sulfide - while adhering well to each other, had poor adhesion to the underlying corroded steel surface.

A corrosion-fouling mechanism was proposed, driven by H_2S, which generates at elevated temperatures. A synergy between fouling and corrosion results, since it is the H_2S driven corrosion process that creates the micro-scale foulant layers that ultimately reduce the thermal conductivity of the metal-oil interface in the furnace. In the case of 316 stainless steel, the high level of chromium in the alloy offers some protection from this process due to the in-situ

formation of a protective micro-scale chromia barrier. Such protection is not offered for pure iron which corrodes and fouls at much higher rates.

2.6 Acknowledgment

This work was supported by an NSERC CRD Grant: “Fundamentals of fouling of coker furnaces”. CRD Application Number 380110-08.

2.7 References

[1] Gentzis, T.; Parker, R. J.; McFarlane, R. A. *Fuel.* **2000**, 79, 1173-1184.

[2] Hong E.; and Watkinson A.P. *Heat Transf. Eng*. **2009**, 30, 786–793.

[3] Rabou, L.P.L.M.; Zwart, R.W.R.; Vreugdenhil B.J.; Bos L. *Energy Fuels.* **2009**, 23, 6189-6198.

[4] Frandsen, F.J.; Pedersen A.J.; Hansen J.; Madsen O.H.; Lundtorp K.; Mortensen L. *Energy Fuels.* **2009**, 23, 3490–3496.

[5] Parker, R.J.; McFarlane, R.A. *Energy Fuels.* **2000**, 14, 11-13.

[6] Falkler, T.J.; Stark, J.L. *Oil and Gas Journal.* **2004**, 102, 72-74.

[7] Eaton, P.E.; Williams, J., Delayed Coker Furnace Fouling Control – Laboratory Correlation to Field Experience. In *NACE*, paper 8670, **2008**, 1-7.

[8] Eaton, P.E.; Newman, B.; Gray, M. Kubis, A.; Derakhshesh, M.; Holt, C.; Mitlin, D. Furnace Coker Simulations in a Laboratory Apparatus. *PetroPhase Conference*, paper O30, **2010**.

[9] Eaton, P.E., Salt Hydrolysis in Crude & Bitumen Fouling. *AIChE,* Spring Meeting, paper 103d, **2006**.

[10] Panchal, C.B. Understanding the Mechanism of FeS induced Fouling in Upgrading. *AIChE,* Spring Meeting, paper 103f, **2006**.

[11] Watkinson, A.P.; Wilson, D.I. *Exp. Therm. and Fluid Sci.* **1997**, 14, 361-374.

[12] Srinivasan, M.; Watkinson, A. P. *Heat Transf. Eng.* **2005**, 26(1), 7-14.

[13] Wu, X.A.; Chung, K. *Energy Fuels* **2007**, 21, 1212-1216.

[14] Eaton, P. E. Method and Apparatus for Conducting Fouling Tests. US Patent #4,910,999, 1990.

[15] Waldner, P.; Pelton, A.D. *J. of Phase Equilib. and Diffus.* **2005**, 26(1), 23-38.

[16] Pareek, V.K.; Ramanarayanan, T.A.; Mumford, J.D. *Catal. Lett.* **1997**, 46, 223-228.

[17] Brons, G.; Yu, J.M. *Energy Fuels.* **1995**, 9, 641-647.

[18] Attar, A. *J. AIChE.* **1978**, 24(1), 106-115.

[19] Gray M.R.; Le, T.; McCaffrey, W.C. *Ind. Eng. Chem. Res.* **2001**, 40, 3317-3324.

[20] Piazza, R. ; Parola, A. *J. of Phys: Cond. Matt.* **2008**, 20, 1-19.

[21] Qu, D.R.; Zheng, Y.G.; Jing, H.M.; Yao, Z.M.; Ke, W. *Corrosion Science*, **2006**, 48, 1960-1985.

[22] Shi, Q.A.; Zhao, S.Q.; Xu, Z.M.; Chung, K.H.; Zhang, Y.H.; Xu, C.M. *Energy Fuels,* **2010**, 24, 4005-4011.

[23] Liu, P.; Shi, Q.A.; Chung, K.H.; Zhang, Y.H.; Pan, N.; Zhao, S.Q.; Xu, C.M. *Energ. Fuels,* **2010**, 24, 5089-5096.

[24] Babaiankibala, E.; Craig, H.L.; Rusk, G.L.; Blanchard, K.V.; Rose, T.J.; Uehlein, B.L.; Quinter, R.C.; Summers, M.A. *Materials Performance*, **1993**, 32, 50-55.

[25] Ohmi, T.; Nakagawa, Y.; Nakamura, M.; Ohki, A.; Koyama, T. *J. Vac. Sci. Tech.* **1996**, 14(4), 2505-2510.

[26] Cheng, S-Y.; Kuan, S-L.; Tsai, W-T. *Corr. Sci.* **2006**, 48, 634-649

[27] Davis, J.R. *Heat-Resistant Materials*. ASM International, Materials Park, OH, **1997**, 148-150, 159-166.

[28] Haynes, W.M. Ed. CRC Handbook of Chemistry and Physics, 91st Edition (Internet Version 2011), CRC Press/Taylor and Francis, Boca Raton, FL. **2011**, 5-4 – 5-42.

[29] Lee, H.G. *Chemical Thermodynamics for Metals and Materials.* Imperial College Press, London UK, **1999**, 279.

[30] Young, D. *High Temperature Oxidation and Corrosion of Metals.* Elsevier Ltd. Oxford, UK, **2008**, 326-331.

[31] Davis, J.R. *Stainless Steels.* ASM International, Materials Park, OH, **1997**, 10.

[32] Mitlin, D.; Misra, A.; Radmilovic, V.; Nastasi, M.; Hoagland, R.; Embury, D.J.; Hirth, J.P.; Mitchell, T.E. *Phil. Mag.* **2004**, 84(7), 719-736.

[33] Mitlin, D.; Misra, A.; Mitchell, T.E.; Hirth, J.P.; Hoagland, R.G. *Phil. Mag.* **2005**, 85(28), 3379-3392.

[34] Wiehe, I.A. *J. of Dispersion Sci. Technol.* **2004**, 25, 333-339.

[35] Wiehe, I.A.; Kennedy, R.J.; Dickakian, G. *Energy Fuels*, **2001**, 15, 1057-1058.

[36] Wiehe I.A.; Kennedy R.J. *Energy Fuels*, **2000**, 14, 60-63.

CHAPTER 3

Thiophene Mitigates High Temperature Fouling of Metal Surfaces in Oil Refining

Material in this chapter has been published in the journal article;

Thiophene mitigates high temperature fouling of metal surfaces in oil refining. *Fuel*, **2015**, 139, 411-424.

Composed by;

Tyler Stephenson, Mike Hazelton, Martin Kupsta, Justin Lepore, Einar Johan Andreassen, Anne Hoff, Bruce Newman, Paul Eaton, Murray Gray, David Mitlin.

Abstract

Inorganically driven fouling of metal heat-transfer surfaces employed in crude oil refining operations is not well understood. The object of this study was twofold: The first goal was to systematically elucidate the time-dependent mechanism of the interrelated carbonaceous and sulfidic build up that occurs at high temperatures on a metal surface (540 °C metal temperature, 250 °C oil bath temperature). Second, it was demonstrated that additions of 0.5, 1.3 and 5.7 vol% thiophene (C_4H_4S) cause a 2X, 10X, and 20X reduction in the fouling factor after a 1400 minute exposure. Analytical techniques including TEM, SEM - EDX, FIB, Auger electron spectroscopy and XRD were employed to detail the fouling phenomenology for a heated stainless steel wire immersed in an atmospheric bottoms fraction of crude oil (340 °C+), exposed for 1 to 1400 minutes. A key microstructural observation was the transformation of the wire's as-received near-surface textured austenitic grain structure into a micron scale (e.g. ~10 μm at 1400 minutes) highly porous inner-sulfide/chromium oxide bilayer composite. Additionally, significant localized sulfidic attack into the bulk of the metal was observed. During testing, an iron sulfide (pyrrhotite $Fe_{(1-x)}S$) corrosion product formed almost instantaneously at the metal surface, followed by coke formation around its periphery at longer times. This temporal sequence, combined with the observation that the thicker regions of the foulant were clearly associated with detached plumes of the sulfide, led to the argument that the sulfide is essential for promoting organic fouling. This is brought about by the sulfide's action as a potent dehydrogenation catalyst that drives the transformation of pitch to coke.

The hypothesis here is that the tremendous fouling inhibition effect of the thiophene originates from its adsorption onto the sulfide surfaces, thereby blocking the dehydrogenation reactions.

3.1 Introduction

The growth of thermally insulating foulant in crude oil preheat trains, heat exchangers, fractionators and reactor beds continues to exude a high economic, industrial health and safety and CO_2 emissions impact in the refining industry. While delayed coking is the preferred technology for upgrading residue fractions, the requirement of a hot metal surface in contact with the oil means that thermal cracking and fouling are inevitable.[1,2] With the depletion of light sweet crude reserves comes the recognition that this will exacerbate due to the necessity of processing more asphaltenic and/or higher-sulfur crudes. Crudes derived from the Canadian oil sands tend to demonstrate particularly severe fouling problems for refineries. Consequently asphaltene-flocculation driven fouling and coking behavior has been studied in great detail.[3-33] A schematic of the delayed coking process is shown in Figure A1, Appendix A.

High-rate “catastrophic” fouling is brought on by large-scale asphaltene flocculation in incompatible oil mixtures and has been discussed in literature by Wiehe and coworkers.[34-36] For instance, recently researchers have employed multifunctional polyisobutenyl oxazolidines as stabilizers for asphaltenes with a great positive effect.[37] The nominally slower "chronic" fouling involves a gradual

accumulation of organic and inorganic material on heated metal surfaces. This phenomenon may be broadly categorized into several mechanistic scenarios, which are not mutually exclusive. One scenario is particulate fouling by iron sulfide, where particles of sulfide form in the oil or boundary layer and deposit onto the hot metal surface, or into the coke layer. In this mechanism, the possibility of accelerated coking due to the presence of iron sulfide has been put forth.[8,22,28] The second mechanism is iron sulfide film fouling and involves the formation of an iron sulfide layer on the metal surface, followed by the deposition of coke.[11,22,28] Researchers have observed the presence of extensive iron sulfide in fouling deposits that were clearly not a result of particulate fouling.[1,13,18,29] The possibility of a catalytic effect of iron sulfide on coke formation is highly likely in either case. A third mechanism involves the formation of iron sulfide and coke simultaneously, brought about by the decomposition of the iron salts present in the oil.[1,18] The resultant carbonaceous deposit is observed to have a high concentration of iron sulfide particles throughout its bulk.[18] The contribution to fouling from in-situ chemical reaction processes still requires further elucidation.[7,18,25]

The use of catalysts for heteroatom removal from heavy oils and during the upgrading of resids is ubiquitous.[38,39] Presently we will provide evidence that a catalytic phase also plays an important role during fouling reactions. The hydrodesulfurization (HDS) process is commonly catalyzed by a metal sulfide (usually molybdenum disulfide, MoS_2), which has been promoted with cobalt or

nickel substitutional impurities and supported on a porous alumina pellet.[40-44] The mechanism for the HDS of thiophene (C_4H_4S) is a multi-step process involving the adsorption of the sulfur heteroatom onto a sub-coordinated edge site of MoS_2, followed by the scission of the C-S bonds.[40,41,43] A high partial pressure of hydrogen is critical to sustain the catalytic cycle and to liberate the adsorbed sulfur as H_2S.[38,40,45] Without hydrogen, the adsorbed organic sulfur atom is not released, and the catalytic site is blocked. The promoter impurities (nickel and/or cobalt) provide local regions of enhanced electron density along the MoS_2 edges, which result in lower binding energy and therefore higher activity for adsorption at the active site.[41,43,46] The role of iron as a promoter has also been characterized, and found to be effective, although much less so, than cobalt or nickel.[41,46] In addition to the effects of carbon supports on HDS[47], the efficacy of other catalysts such as iron sulfide[48,49] and coated stainless steel[50] have also been explored. Iron sulfide was proven to be an active catalyst for the HDS of thiophene, although much less effective than other sulfides such as MoS_2. Furthermore, it has been shown that metal surfaces[51], and an oxidized surface of a 304 stainless steel will embody some activity for the HDS of thiophene.[50] However, in the absence of hydrogen, thiophene is expected to be stable.

In catalytic upgrading it is well known that there are competitive reactions at work.[52,53] In general, the active site on a given catalyst can be poisoned by adsorbing polar species containing nitrogen or sulfur heteroatoms if there is not enough excess hydrogen to allow the catalytic cycle to continue.[52,54] These

species adsorb readily onto active catalytic sites due to the polar nature of the molecules. Furthermore, it has been experimentally shown that the addition of thiophene and H_2S to a reactor has inhibitory effects on the catalytic cycle and the liberation of desired products.[52] There has also been some work on the role of thiophene in inhibiting coke formation during steam cracking of hydrocarbons and naphtha pyrolysis.[55,56] For the former case, the authors examined the formation of coke at 820 °C in reformer raffinate without thiophene and with 0.05, 0.1, and 0.5 wt% thiophene. It was observed that with the increasing concentration of thiophene the rate of coking decreased significantly. The authors argued that thiophene both influences the radical conversion in the homogeneous phase and the surface reactions in the reactor, but this reaction mechanism was not proven. An early study by Taylor *et al.* demonstrated an inhibitory effect on foulant growth due to 3000 ppm (sulfur) of thiophene being added to deoxygenated jet fuel that was heated through a temperature range of 150 - 649 °C.[57] This was attributed to the thermal stability of the molecule, which resists pyrolysis and surface catalyzed decomposition reactions even at high temperatures.

Here we explore two key interrelated issues. First, the full phenomenology of chronic fouling in the absence of up-stream particulates is not yet entirely established. Evidence does exist that such chronic fouling is in fact a synergistic sulfidic corrosion-coke formation process.[29] However, factors like the evolution of both the foulant and of the underlying steel structure, as well as the

overall uniformity versus any site-specificity of the process, are poorly understood. Thus the first goal is to provide a detailed and comprehensive account of the key microstructural changes that occur both in the heated metal and in the organic/inorganic deposit through a broad spectrum of exposure times. Second, direct evidence that the addition of thiophene to the oil may be employed to mitigate chronic fouling will be presented. This observation should serve as a useful basis for improved fouling mitigation strategies and antifouling additives.

3.2 Experimental Procedure

A stirred 2000 mL autoclave was equipped with a heated wire probe. A detailed schematic is presented as Figure 3-1. The reactor assembly allows for the immersion and resistive heating of wires in crude oil under repeatable reactor conditions. The autoclave reactor was designed for batch operation, with a single charge of 1200 mL of crude oil. Thiophene (C_4H_4S) was introduced into the autoclave as an oil additive to evaluate its effects on fouling. In these tests, 6 mL (0.5 vol%), 16 mL (1.3 vol%) and 68 mL (5.7 vol%) of thiophene were added, with an equal amount of oil being removed from the reactor to ensure constant volume. The resulting oil sulfur content increased by approximately 7%, 20%, and 80%, respectively. Fouling runs with thiophene were conducted for up to 1400 minutes, with fresh oil being used for each run. Prior to testing, the reactor was sealed, purged with nitrogen, and pressurized to 8.84 atm. For all tests the autoclave temperature was held 250 °C, while the pressure was adjusted to 15 atm

prior to the start of the fouling run. During testing the oil was stirred using a stir bar rotating at 300 RPM.

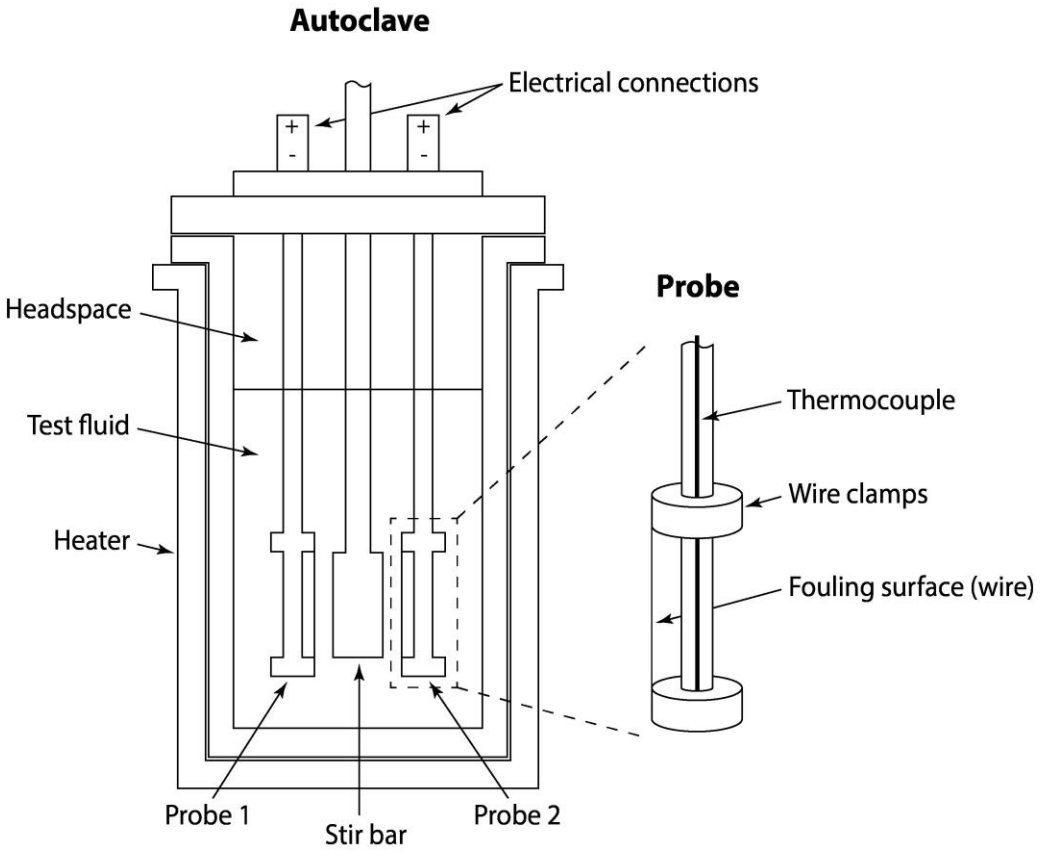

Figure 3-1: Schematic diagram of the test autoclave.

The crude oil sample used for this study was an atmospheric bottoms fraction (nominally 340 °C+). Elemental analysis was conducted on the crude oil using a standard inductively coupled plasma mass spectrometry technique. The total acid number (TAN) of the crude oil was determined in accordance with ASTM standard D664-09a, using a Metrohm TIAMO 1.3 titration analyzer.

Thermogravimetric (TGA) analysis of the crude oil and coke material was conducted using a Thermo Cahn TherMax 300 TGA analyzer. Micro carbon residue content was determined in accordance with ASTM standard D4530. CHNS analysis of the crude oil and coke was completed using a Carlo Erba EA1108 elemental analyzer. Asphaltene content of the crude oil was determined via standard precipitation analysis using pentane mixed at a ratio of 40:1 and subsequent filtering and weighing of the asphaltene precipitates. The oil was 84.25 wt% carbon, 10.11 wt% hydrogen, 0.39 wt% nitrogen, and 3.43 wt% sulfur. The asphaltene content of the oil was 8.47 wt%, the micro carbon residue content was 6.45 wt%, the ash content was 0.02 wt%. The total acid number of the oil used for this study was 0.46±0.06 mg KOH/g crude oil. The concentration of chlorides in the oil was determined to be 9 ppm.

A headspace gas analysis was conducted to help characterize the behaviour of thiophene in the system. Gas samples were collected into 1 litre Tedlar gas bags after the sampling line had been purged for 5 seconds with the analyte gas. Samples were taken (a) at room temperature before the initiation of the fouling run but after the reactor was purged with nitrogen; (b) before the initiation of the fouling run once the bath temperature had reached 250 °C; and (c) after the fouling run when the reactor had cooled back to ambient. Analysis of the gas was completed using an Agilent 3000A micro gas chromatograph. Gas was injected simultaneously into four separate columns for separation and detected using thermal conductivity detectors.

The wire used to simulate the heat transfer surface was a standard (ASTM A-580) 316 austenitic stainless steel purchased from California Fine Wire Company. The composition of the 316 stainless steel wire (as reported by the manufacturer in wt%) was chromium (16-18), nickel (10-14), molybdenum (0-2), silicon (0-1), iron (balance). The diameter of the wires was 0.2 mm. The fouling factor (FF), or fouling resistance of the wire-oil interface is the inverse of its heat transfer coefficient: FF = A_{wire} ΔT / P, where ΔT is (T_{wire}-T_{oil}), A is the heat transfer surface area of the wire and P is power output (derived from the product of voltage and current). To obtain a higher level of accuracy, a final fouling factor (FFF) was calculated by the following equation, which takes into account the increase in the heat transfer surface area.

$$FFF = \left| A_f \left(\frac{\Delta T}{P} \right)_{fouled} - A_c \left(\frac{\Delta T}{P} \right)_{clean} \right| \qquad \text{Eq. 3-1}$$

The area A_c is the initial "clean" surface area of the wire. The fouled surface area (A_f) is calculated using the diameter of the fouled wires. That diameter was obtained by SEM analysis of the fouled cross sections, with any remaining oil and pitch being first fully removed from the wire surface.

The 316 stainless steel wires in the reactor probes were heated resistively to a desired temperature above the bulk oil temperature via a constant current input. The wires were fouled at 5 A constant current, which corresponded to a

starting wire temperature of 540±9 °C. The crude oil in the autoclave was maintained at a constant temperature of 250±5 °C, using a PID control loop coupled to a heater. To facilitate the characterization of baseline foulant evolution with time, fouling runs were conducted for 1, 5, 10, 30, 60, 250, 480, 1000, and 1400 minutes. Runs with thiophene were conducted for 250, 1000, and 1400 minutes. The voltage (and thus the power output) of the stainless steel wires increased by approximately 5-10% of their initial values during the constant current tests. Thus, to a first approximation the system operated at constant heat output across the fouling surface.

The temperature of the wire was determined by its resistance. The measured resistance during the fouling run was compared with an ex-situ temperature calibration plot. The wire temperatures were also verified ex-situ using temperature indicating liquids purchased from Tempil, and were found to agree within 5-10% of the extrapolated values. The current in the wire was ramped at 0.05 A/s up to 5 A, which took 100 seconds. Fouling factor calculations were normalized to 150 seconds after the start of the fouling run, to allow the electrical measurements to reach steady state. While the presence of a small amount of sulfide was confirmed by Auger electron microscopy after 60 seconds, no carbonaceous foulant was observed even at 150 seconds. A thorough derivation of the fouling factor and determination of wire temperature is provided in Figures A2, A3 and A4 in Appendix A. Furthermore, the excellent correlation

between wire resistance, temperature, fouling factor and foulant thickness is also provided in Figure A5 of Appendix A.

After removal from the reactor, the wires were cleaned in xylene, acetone and isopropyl alcohol using a vortexer for approximately 30 seconds each. This approach removed the pitch completely leaving the solid coke exposed. After cleaning, the wires were dried in an oven at 90 ºC for 2 hours. All fouled wires were stored in air at room temperature prior to analysis. The wires were analyzed using focused ion beam (FIB) for micro cross-sectioning, Auger electron spectroscopy (AES), scanning electron microscope (SEM), X-ray diffraction (XRD), transmission electron microscopy, and SEM energy dispersive X-ray analysis (EDX). The XRD analysis was performed using a Bruker AXS D8 Discover diffractometer with a Histar GADDS area detector.

FIB analysis was performed using a Ziess NVision 40 dual beam system. The FIB uses a 30 kV Ga liquid metal ion source with ion currents of 0.15 pA-45 nA. The system is equipped with a vertical SEM column which is situated at 36° relative to the FIB column. For imaging of samples, the FIB SEM was operated at 3 kV to optimize surface sensitivity. Cross sections were milled with the FIB and then imaged with the SEM to minimize damage to the sample. For EDX area analysis, a 15 kV accelerating voltage was used on a Hitachi S-3000N SEM with an Oxford INCA EDX system. Here the working distance was set to 15 mm. The Auger measurements (with SEM) were carried out using JAMP-9500F Auger

microprobe (JEOL). The instrument is equipped with a Shottky field emitter that produces an electron probe diameter of about 3-8 nm at the sample surface. The accelerating voltage and emission current for both the SEM and Auger imaging were 10 kV and 8 nA, respectively. The working distance was 24 mm. TEM was performed using a JEOL JEM-2100. Selected area electron diffraction patterns (SAED) were processed using an open source software package that was developed in-house (Diffraction Ring Profiler version 1.7).[58] Since the foulant was rough and had an irregular outer surface, thickness measurements were conducted as follows: Quartz PCI software was used for the measurement on the SEM micrograph, and the foulant was measured radially at 8 places around the circumference of the wire cross section in increments of 45° starting at the 12 o'clock position. The thickness reported was the average of these values. The surface sulfide thickness was also measured in this manner.

Auger peaks of Fe LMM (700 eV), S LVV (140 eV), Cr LMM (526 eV), Ni LMM (844 eV), and O KLL (500 eV) were selected for the mapping. The intensity of each pixel in the Auger image was calculated by the (P – B)/B method, where P and B are the peak and background intensity, respectively. Such intensity definition helps to reduce signal differences because of sample roughness and height irregularities. An auto probe tracking technique was used to compensate for possible drifting of the image during the analysis as a result of power instabilities. The Auger samples were cleaned in-situ via sputtering with argon for 30 seconds prior to imaging to remove adsorbed surface contaminants.

3.3 Results and Discussion

Figure 3-2 shows TEM analysis of the as-received 316 stainless steel wire. Figure 3-2a shows a bright field micrograph highlighting the initial thickness of the passivating surface oxides, which is in the range of 10 nm. Referring to the Ellingham diagram for 316 stainless steel[59], we would expect an oxide multilayer composed of an outermost layer of corundum Cr_2O_3, followed by mixed chromium-iron-nickel oxide spinels of the prototype of Cr_3O_4.[59,60] The Ellingham diagram is provided as Figure A6 in Appendix A. Both oxides exhibit a wide range of solubilities for iron and the alloying elements present in the steel. This oxide multilayer is arrowed in 3-2a. Figure 3-2b shows an SAED pattern of the sample, and has been indexed to fcc iron. Figure 3-2c shows a dark field micrograph taken using a portion of the (111) and (200) rings (circled in 3-2b) and highlights the austenitic grain morphology that is typical of drawn wires. The metal adjacent to the surface is fully dense, with no porosity being detected. There are however, drawing defects in the form of cracks and pulled-out inclusions adjacent to the wire surface. These are arrowed in Figure 3-2d, which is an SEM micrograph of an FIB cross section of a 316 stainless steel wire. Both small (micro) cracks and metallurgical inclusions are typically encountered on the surfaces of drawn or otherwise mechanically processed steel structures, and should be present in pipes, rolled sheets, stamped or extruded sections, etc. As will be demonstrated, such defects may be an important source of sites for

initiation of highly localized sulfidic corrosion attack that is detected in addition to a more uniform sulfidation encountered on the majority of the surface.

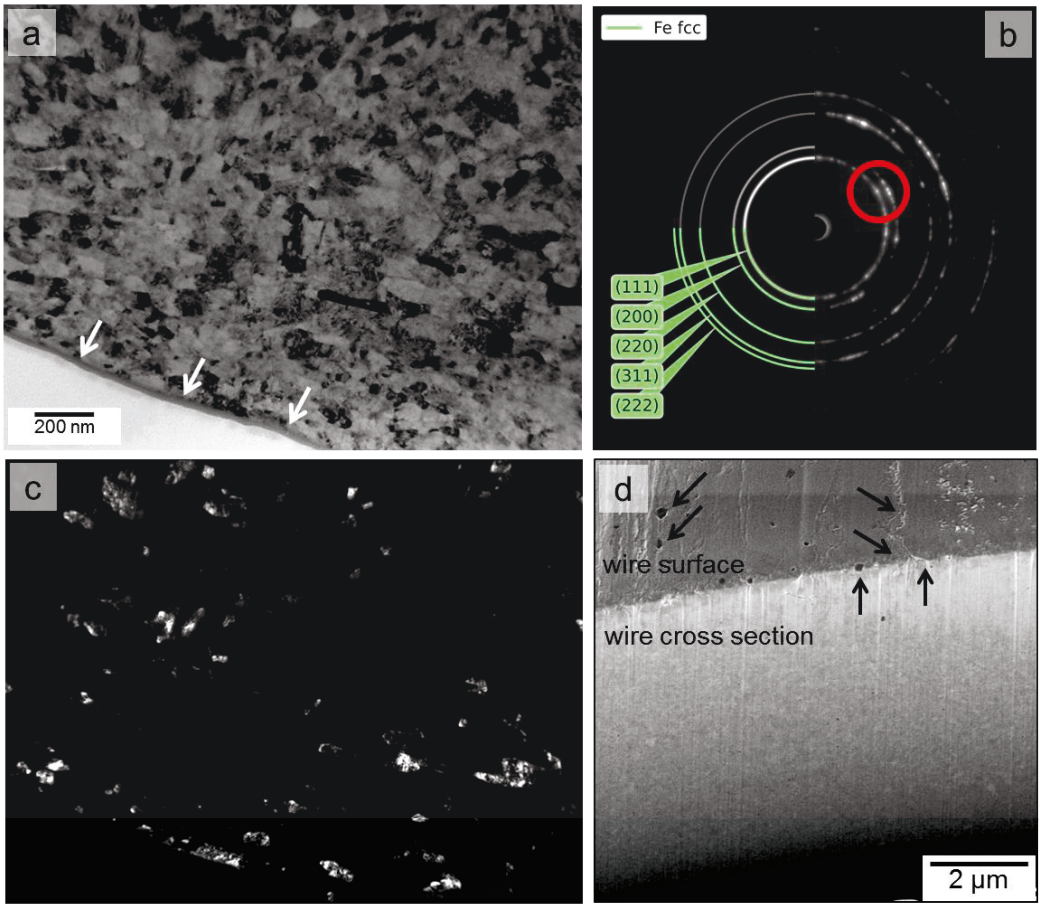

Figure 3-2: TEM analysis of an as-received 316 stainless steel wire. (a) Bright field micrograph highlighting the grain structure. The native surface oxide is arrowed. (b) Indexed SAED pattern of the austenitic grain structure. (c) Dark field micrograph highlighting typical grain morphology, taken using a portion of the (111) and (200) rings. (d) SEM micrograph of FIB cross section showing surface defects and cracks (arrowed).

Figure 3-3 shows a master plot of the final fouling factors (obtained from SEM analysis of the fouled wire cross sections to determine fouled surface area), analyzed at times of up to 1400 minutes, with and without the addition of

thiophene. The three volume fractions (0.5, 1.3, and 5.7 vol%) of thiophene were analyzed after 250, 1000, and 1400 minutes of fouling. Although the baseline (no thiophene) foulant thickness finally does asymptote, during the first 500 minutes the fouling rate is quite high. Conversely the fouling factors for the thiophene cases are much reduced at all times of analysis, with the 1.3 and 5.7 vol% samples undergoing minimal fouling even after the full duration of the experiment. After 1400 minutes the addition of 0.5 vol% thiophene reduces the final fouling factor from 1200 mm^2K/W to 500 mm^2K/W. Additions of 1.3 and 5.7 vol% further reduce it to 130 mm^2K/W and 60 mm^2K/W, respectively.

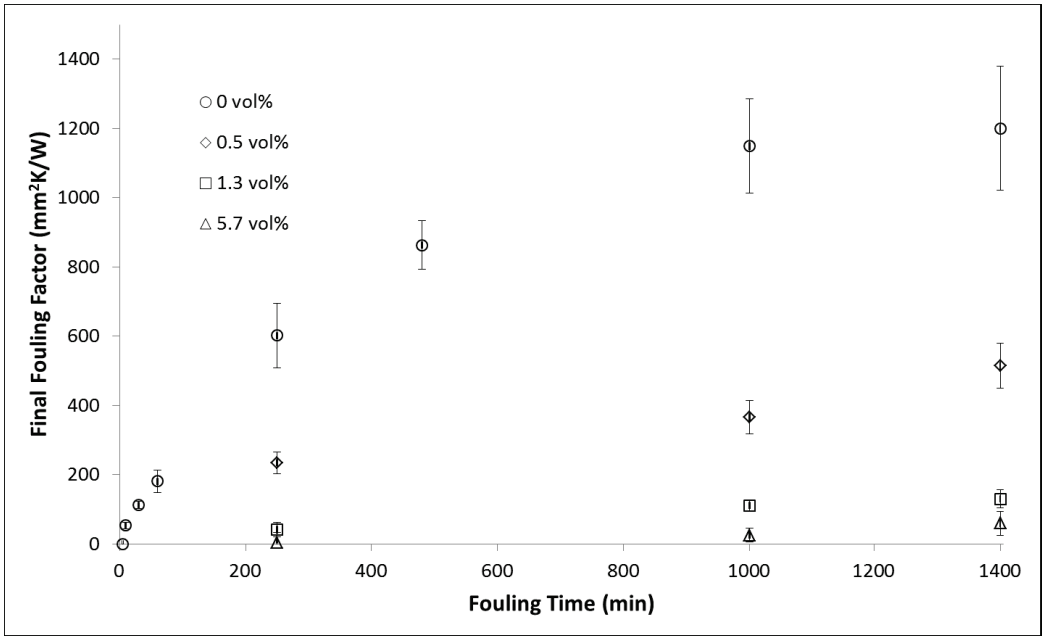

Figure 3-3: Final fouling factor for various times with no additive, and with three concentrations of thiophene. Error bars are one standard deviation of the average value obtained from multiple runs.

Figure 3-4 shows a series of SEM micrographs and EDX elemental maps of wire cross sections in the as received state, and fouled for 1 and 10 minutes.

Comparing Figures 3-4a-c, it is evident that the surface does roughen (i.e. corrode) prior to the development of a pronounced foulant deposit. Mass measurements completed with a Mettler Toledo XS205DU analytical balance with 0.01 mg resolution on wires fouled from 10 seconds to 10 minutes confirm the duration of the induction period, with minimal gain being detected.

A further examination of Figure 3-4 reveals some additional interesting points. Figure 3-4b shows a cross section of the fouled wire after 1 minute at temperature. The wires reach the target temperature after 100 seconds of ramping the current at 0.05 A/s. Figure 3-4c shows the cross section after 10 minutes of fouling. What is evident is the early formation of an iron sulfide (Fe and S analytical maps) prior to the onset of significant coking. In the case of the 1 minute test, no coke was detected on the wire surface, with the mounting epoxy being directly in contact with the sulfide. Note that the epoxy was filled with spherical and semi-spherical nickel microparticles to reduce charging during SEM analysis. These microparticles are visible in the epoxy and are easy to distinguish from the foulant.

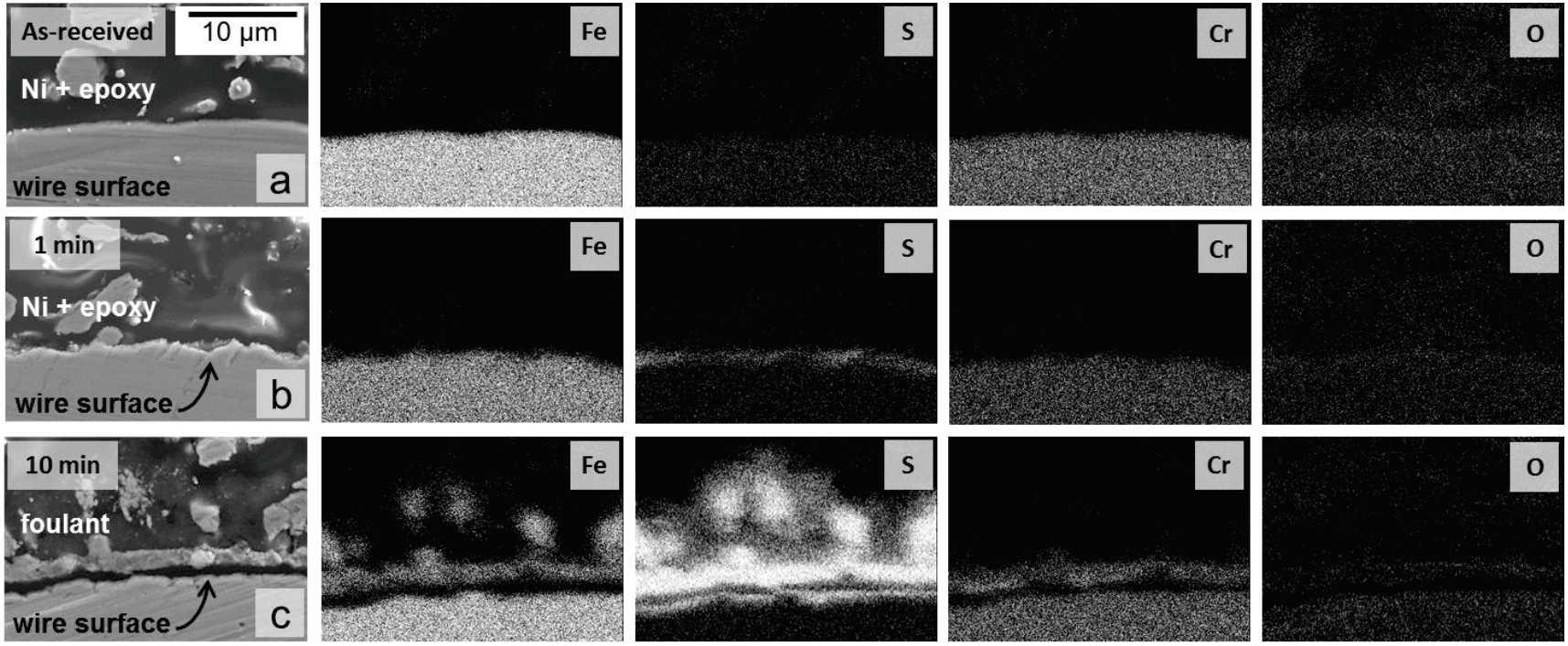

Figure 3-4: SEM micrograph and EDX elemental maps of fouled 316 stainless steel wire cross-sections at various times. (a) As-received. (b) After 1 minute of fouling. (c) After 10 minutes of fouling. For all experiments the initial wire temperature was 540 °C and the oil temperature was 250 °C. Note that the epoxy was filled with spherical and semi-spherical nickel microparticles to reduce charging during SEM analysis, which are visible in all the images of the epoxy and easy to distinguish from the foulant.

For the 10 minute test, the iron sulfide crystals were interspersed with coke, making a fouling layer that was approximately 10 microns thick. H_2S is a well-known decomposition product of high temperature hydrocarbon cracking reactions, especially with oils that are rich in sulfur such as the one employed here. Upon contact of H_2S with metals such as iron, nickel, molybdenum, etc. a sulfide is rapidly formed while hydrogen gas is generated as shown by the overall reaction in equation 3-2. The sulfide crystals are observed to detach and float into the coke layer, which would likely be a viscous fluid at the test temperature.[29]

$$Fe_{(s)} + H_2S_{(g)} \leftrightarrow FeS_{(s)} + H_{2(g)} \qquad \text{Eq. 3-2}$$

Figure 3-5 shows an SEM micrograph and AES elemental maps of the wire cross section after 10 minutes at temperature. At this exposure time, the foulant adjacent to the wire surface is primarily inorganic, being composed of an outer ~2 μm thick sulfide layer on top of one or a series of underlying oxides that are roughly 500 nm in total thickness (in the micrograph the fracture runs through the oxide layers). The phenomenology of the transition from a surface terminating 10 nm Cr_2O_3/Cr_3O_4 bilayer is analogous to what has been reported for elevated temperature corrosion scenarios in stainless steels, with H_2S being in the gas phase.[61-69]

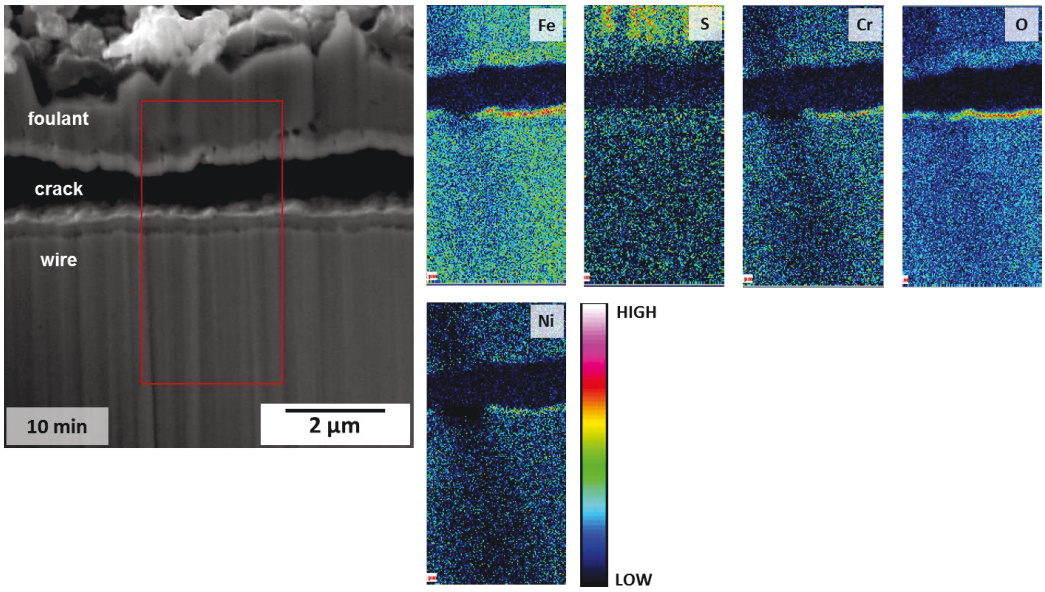

Figure 3-5: SEM micrograph and AES elemental maps of the wire cross section after 10 minutes of fouling, highlighting the structure of the foulant-wire delamination interface.

The "Cr_2O_3/Cr_3O_4" designation is used with the understanding that both the corundum and the spinel are heavily alloyed with iron, nickel, manganese, etc. In the case of high chromium alloys where the oxygen/water vapor partial pressure is non-negligible, a partially porous Cr_2O_3 layer grows. Despite extensive nitrogen sparging prior to each test run, some water from the upstream desalting operations, and some atmospheric oxygen may remain in the crude oil, with the water forming a vapor at temperature. A calculation for the amount of water that would be required to form a 500 nm Cr_2O_3 layer yielded 8 ppb by volume. Also, at the temperature of the wire surface any naphthenic acids will thermally decompose via a dehydration mechanism to generate water.[70] Above 500 °C both iron and nickel will readily move outward via bulk and grain boundary cation diffusion through both corundum and spinel. Ionic diffusion of

iron is known to be faster than that of nickel, leading to nickel enrichment in the near-surface wire metallurgy. Initially, at the Cr_2O_3 - oil interface, these elements will react with the H_2S to form mixed alloy iron-nickel sulfides that are iron-rich. While ultimately an inner sulfidation layer is also expected to develop due to inward H_2S diffusion through the intrinsic porosity of the chromium oxide[29], after 10 minutes it is not yet detected.

In the location where the image was taken, the foulant has separated from the wire surface. This may have happened at temperature, during the cool down process, or during the subsequent wire handling (which was quite carefully done). Regardless of when it happened, the fact that delamination occurred is indicative of the poor adhesion of the inorganic foulant to the metal surface. This observation is consistent with the work of Wang and Watkinson[71], who reported that foulant deposits that were primarily inorganic did not adhere as well as ones with a higher ratio of organic phase. In our findings, once a large amount of organic foulant had developed, it served to entrap the delaminating sulfide.

The AES plot shown in Figure 3-5 demonstrates that during the early stages, foulant delamination actually occurs through the oxide layer, rather than through the sulfide or at one of the interphase interfaces. This may be observed from the strong chromium, oxygen, iron and nickel signals on both sides of the fracture surface and a sulfur signal that is actually away from the crack. While sulfides are known to be relatively poor passivation barriers due to their high

porosity and poor mechanical strength, it is now evident that the chromia will also not be panacea for fouling-corrosion in heavy oils exposed to such elevated temperatures. The 9 ppm of chlorides contained in the as-received oil may be a contributor to the poor integrity of the oxide, though more experiments would be required to quantify this effect.

Figure 3-6 shows an SEM micrograph and the EDX elemental maps of the entire cross-section of a wire fouled for 60 minutes without thiophene. At this point the foulant structure has reached "steady-state" and remains analogous for the duration of the fouling times investigated. The foulant is a composite of coke and iron sulfide, with sheets or plumes of sulfide being released into the fluid coke. For a more thorough determination of relative amounts of coke and sulfide, see Figure A7 in Appendix A.

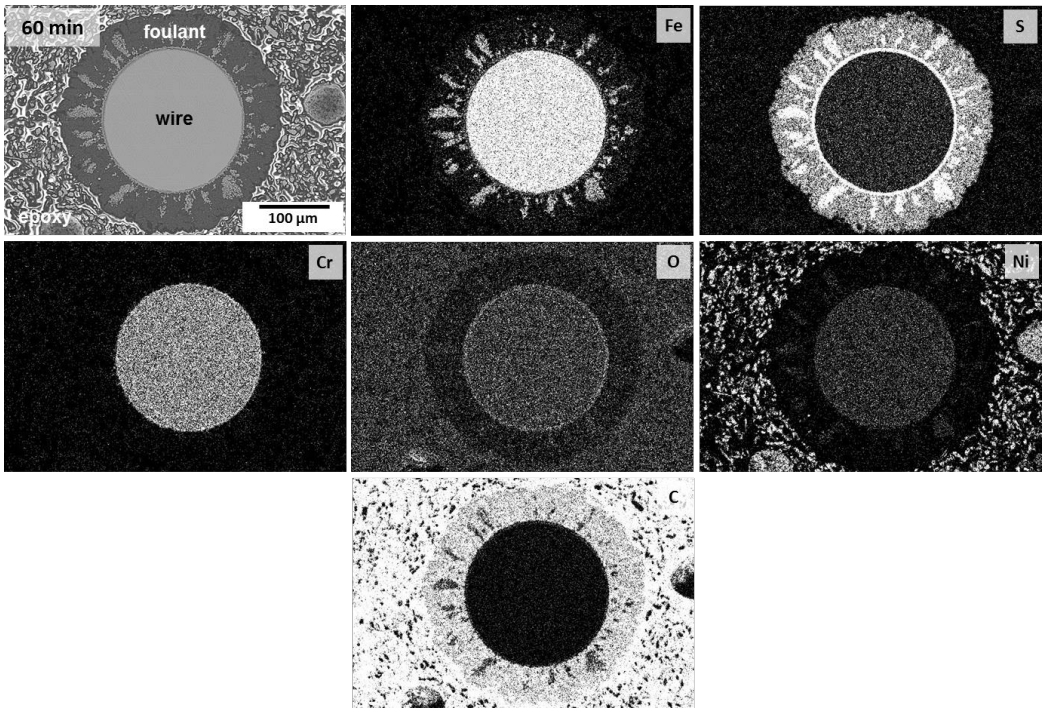

Figure 3-6: SEM micrograph and EDX elemental maps showing an entire cross section of a wire fouled for 60 minutes.

Figure 3-7 shows SEM and EDX scans of the same wire at a higher magnification, where the sulfide can be seen delaminating from the wire surface in plumes. The sulfides are less dense than the underlying metal, which will impart a compressive stress onto the films as they grow on the wire surface. This stress combined with the pressure due to the hydrogen bubbles that are generated during sulfidation of the metal surface and from other gases evolved during pyrolysis will drive the sulfide layers away from the wire surface. Fluid convection and thermophoretic motion will also contribute. However, rather than drifting entirely away from the wire into the surrounding uncracked oil, much of the sulfide will be captured by the viscous fluid-like coke that surrounds the wire. As may be seen from the bright field SEM micrographs (Figures 3-6 and 3-7), the

majority of the foulant by volume is organic coke. See Figure A7 in Appendix A for more information on the coke:sulfide ratio. However due to the higher atomic mass of the sulfide vs. carbon, the analytical maps show pronounced iron and sulfur signal. Nickel is also present in the sulfide though to a lesser extent.

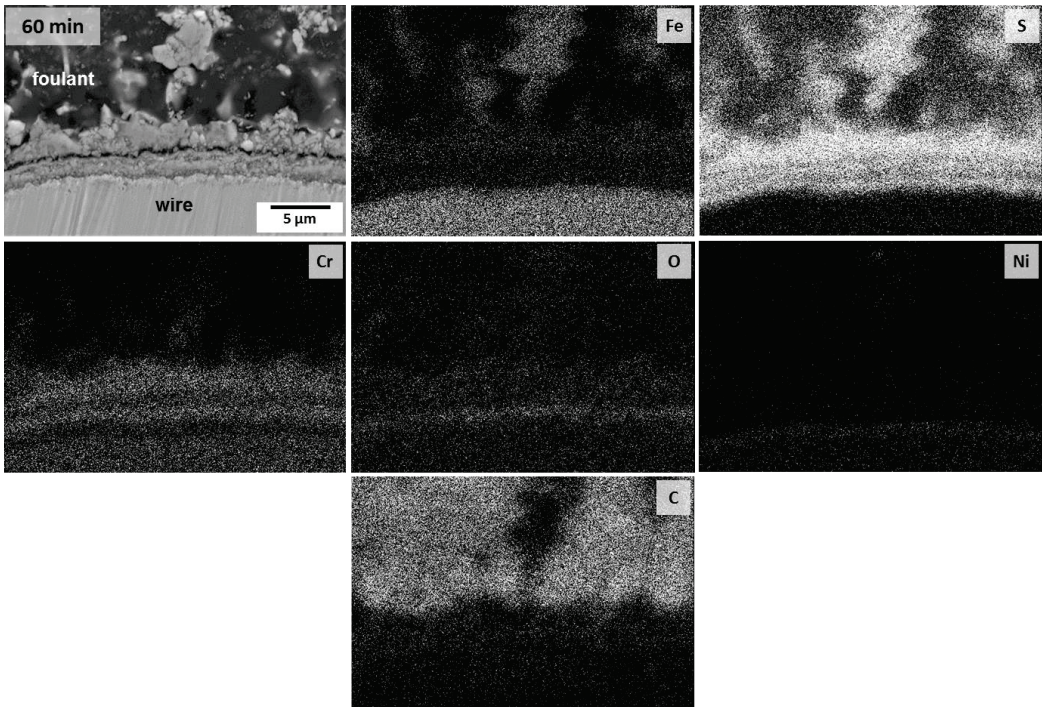

Figure 3-7: SEM micrograph and EDX elemental maps showing a magnified portion of the cross section of a wire fouled for 60 minutes.

At the wire temperature (540 °C), the foulant behaves as a viscous fluid and is expected to be minimally effective in protecting the underlying base metal from further sulfur attack.[29] Transition-metal sulfides are known to be good dehydrogenation catalysts, and are therefore expected to promote coking reactions on their surfaces.[22,72] Moreover as was shown in Figures 3-4 and 3-5, the sulfide forms first prior to any growth of organic foulant. We do not believe that for the

experimental system employed in this study, where an initial ΔT of approximately 300 °C exists between the wire surface and the oil reservoir, that homogenous coke formation in the bulk of the oil has an appreciable contribution to the measured fouling rates. Visual examination of the reactor walls even after 1400 minute tests did not reveal coke buildup, as would be expected if homogeneous reactions in the bulk of the oil were significant. Rather, fouling is a heterogeneous process initiated on the heated wire surface, which from the onset, is covered by preferential catalytic sites i.e. the sulfides.

The decreasing fouling rate with time may be understood by considering the distribution of iron sulfide in the foulant. If the sulfide particulates are indeed preferential sites for dehydrogenation, condensation, and desulfurization of the depositing asphaltenes, their decreasing volume fraction at the foulant-oil interface, with increasing foulant thickness, will lead to the process transitioning from catalytic to pyrolytic. Further support for this claim can be seen in Figure A7 in Appendix A. Fan and Watkinson[19] as well as Wilson *et al*.[25] have reported that the thermal conductivity of an ageing fouling deposit can slowly improve as the layer becomes more dense, resulting in a gradual decrease in fouling resistance. This may also contribute to the decaying fouling rate. The fouling rate decay is not an artifact of a decreasing surface to oil heat output, since tests were run at approximately constant power rather than at a constant wire temperature.

Figure 3-8 shows an SEM micrograph and EDX elemental maps of a wire fouled for 250 minutes without thiophene. It may be seen that coke formation around the wire is non-uniform, with arrows on the micrograph pointing to locations where foulant protrusions are correlated with a high content of iron sulfide. This supports our argument that the formation of the organic foulant is catalyzed by the presence of the heated sulfide particles that extend into the bulk oil.

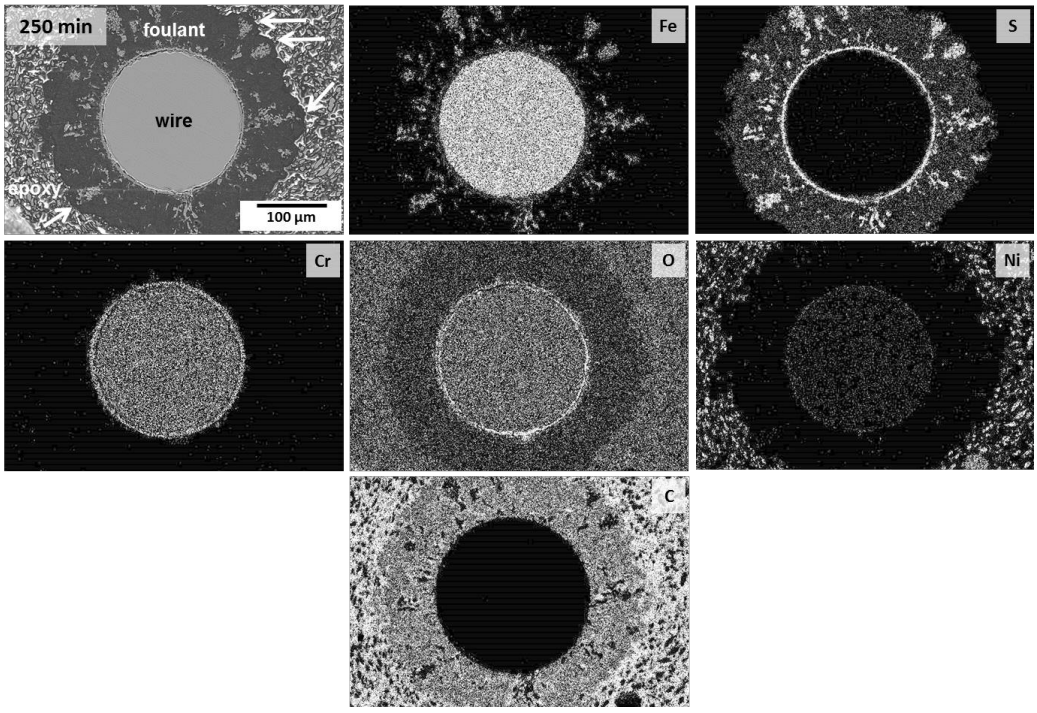

Figure 3-8: SEM micrograph and EDX elemental maps showing an entire cross section of a wire fouled for 250 minutes.

Figure 3-9 shows a high magnification SEM micrograph and EDX maps of the 250 minute specimen. The sulfide is observed to contain small amounts of nickel, and large amounts of iron.

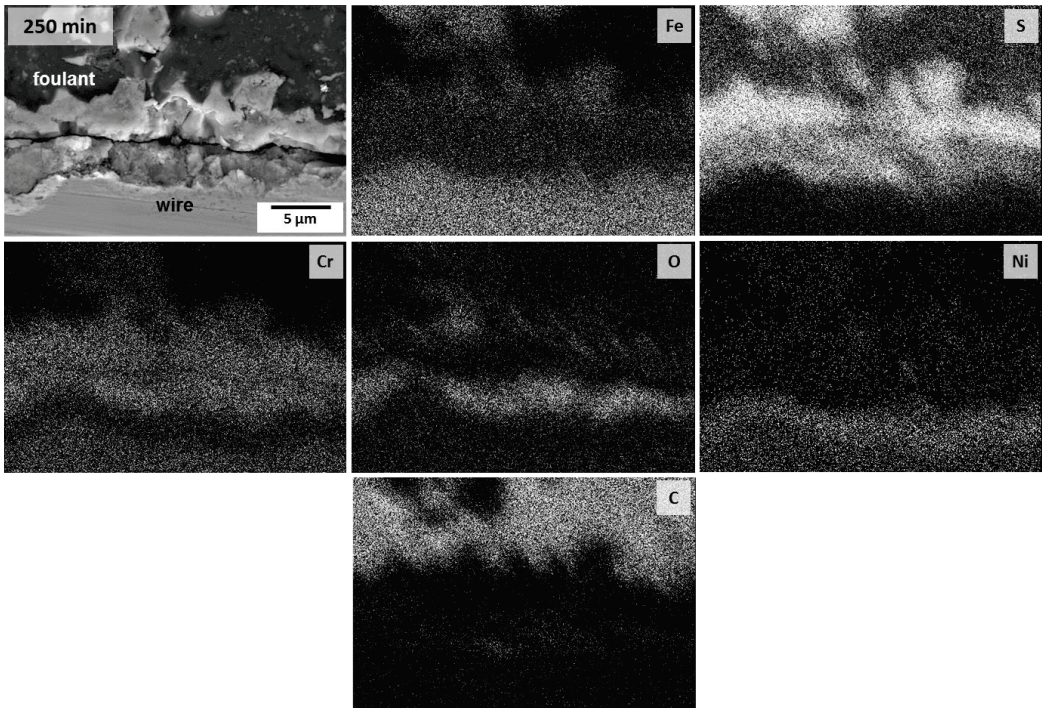

Figure 3-9: SEM micrograph and EDX elemental maps showing a magnified portion of the cross section of a wire fouled for 250 minutes.

Fouled wire cross sections often exhibited regions of extended local corrosion attack into the wire surfaces and spatially correlated sulfide plumes in the coke. An example of this is shown in Figure 3-10, which shows a micrograph of a wire cross section which was fouled for 250 minutes. The localized corrosion attack and resulting sulfide plumes are arrowed in black and white respectively. Localized sulfidic attack is often reported in alloy steel, stainless steel, and nickel based alloys.[61-69] Its origin is attributable to both microstructural

and macroscopic/mechanical defects. Microstructural defects include sensitized grain boundaries terminating at the metal surface, with these chromium-depleted regions being preferentially sulfided deep into the bulk metal.

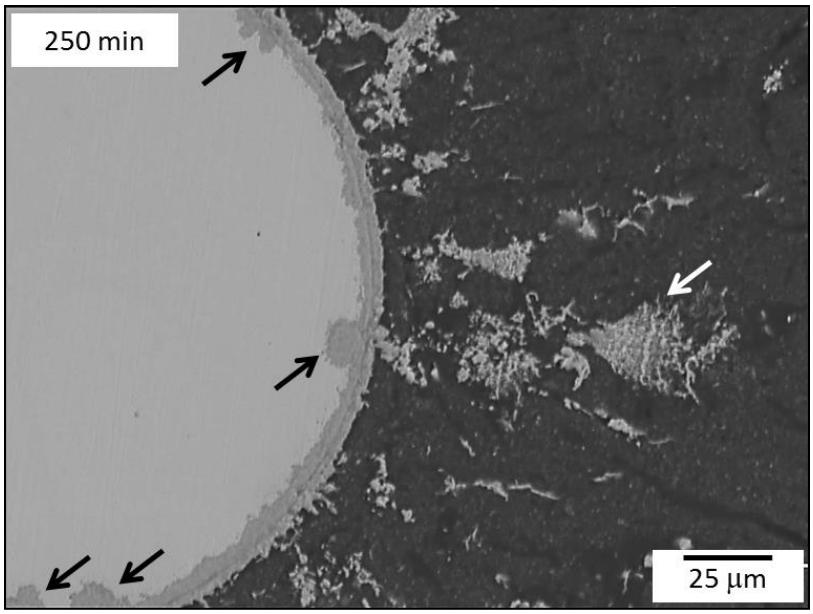

Figure 3-10: SEM micrograph of the cross section of a 316 stainless steel wire fouled for 250 minutes. The black arrowed locations are defect sites where localized corrosion attack has resulted in accelerated fouling. The white arrowed location shows a sulfide plume which is spatially correlated with a region of localized corrosion.

Locally highly deformed regions, containing a high density of dislocations, would similarly offer less resistance towards sulfidation than the bulk alloy. Surface terminating pores, regions containing loosely bound or torn out inclusions left over from the steel making process, and surface cracks caused by metal forming operations would also offer regions of preferential H_2S attack. Examining the cross-section of the as-received wire surface (Figure 3-2d) it is evident that wire drawing induced surface cracks, and that surface pores associated with pulled-out

inclusions are present. It is reasonable to assume that these would be the sites for localized attack. We should also point out that there is no such thing as a perfectly pristine metal surface (be it formed or cast) and analogous defects would be observed in pipes, flanges, joints, etc. employed in refining operations.

Figure 3-11 highlights cross-sectional TEM analysis of the wire fouled for 250 minutes. The bright field image (3-11a) illustrates the porosity (white regions) of the inner sulfide which forms between the base metal and the surface oxide bilayer. Figure 3-11b shows an indexed SAED pattern corresponding to pyrrhotite $Fe_{(1-x)}S$ while Figure 3-11c shows an SAED pattern corresponding to the base metal. SAED patterns from the oxide beginning in the top view of the micrograph were not obtained. From this image it is evident that these interfacial layers are sufficiently porous that H_2S ingress to the underlying base metal should be facile even at higher inner sulfide - oxide thicknesses. In addition, such a porous barrier is not expected to provide good mechanical integrity and will ultimately fracture/delaminate during prolonged exposure.

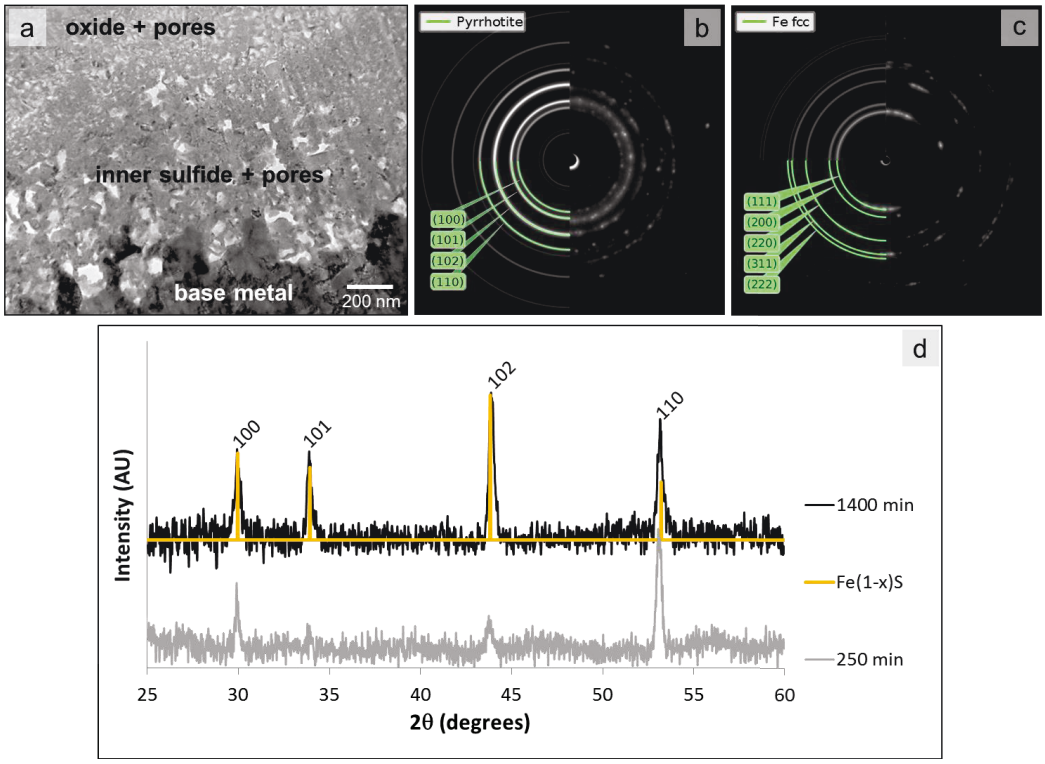

Figure 3-11: (a) Bright field TEM micrograph of a 316 stainless steel wire fouled for 250 min, highlighting the highly porous (white regions) layer formed at the bulk metal – sulfide interface and the non-uniform penetration of corrosion into the metal surface. (b) SAED pattern with pyrrhotite simulation of the region in (a) labelled "inner sulfide + pores". (c) SAED pattern with Fe fcc simulation of the region in (a) labelled "base metal". (d) XRD data showing that the pyrrhotite $Fe_{(1-x)}S$ phase is retained after 1400 minutes of fouling.

Figure 3-12 shows this effect experimentally. Here the base metal - foulant interface is highly fractured around the wire circumference. Also in Figure 3-12, we see that the thickening of the interfacial inner sulfide - oxide structure is not continuous. The interfacial inner sulfide - oxide in the wire tested for 1800 minutes is approximately half the thickness as it is in the wire tested for 1000 minutes. It also contains large circumferential cracks. Such a phenomenology is analogous to what has been observed for "runaway" sulfidic gas corrosion, where there is a transition from the decaying ($\sim t^{1/2}$) time

dependence of the corrosion rate to something more linear.[69] This transition has been previously attributed to the localized growth of an inner sulfide, followed by localized cracking.

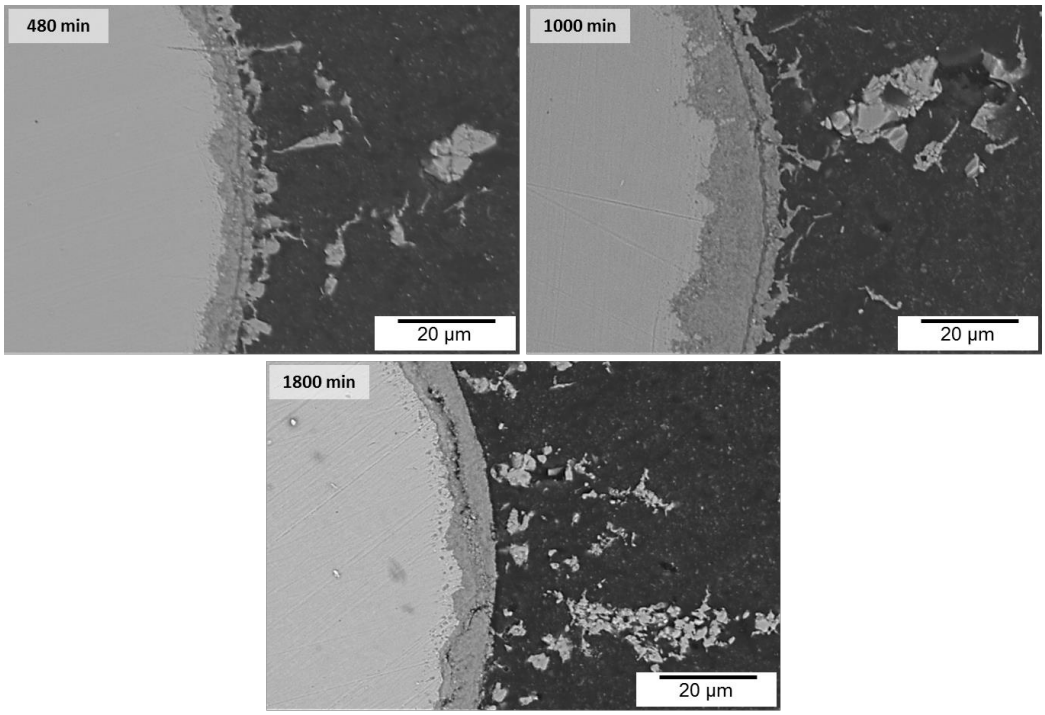

Figure 3-12: SEM micrographs of wire cross sections fouled at various times highlighting the spallation of the barrier bilayer, which is not a self-terminating or passivating process.

Figure 3-11d shows a glancing angle XRD scan taken from the wire surfaces after 250 and 1400 minutes of fouling. Here we see that the pyrrhotite structure of the outer iron sulfide foulant is retained. From Figures 3-11a and 3-11d it may be concluded that both the inner and the outer sulfide are isostructural. This is reasonable as one would expect a similar activity of H_2S at both surfaces.

Figures 3-13 and 3-14 show low and high magnification SEM images and EDX elemental maps of a wire that was fouled for 1000 minutes. After this prolonged exposure, the inner sulfide - outer Cr_2O_3 bilayer is of considerable thickness (~10 μm) and is granular and porous. The two phases are sufficiently interspersed that it is not possible to resolve them in the analytical maps shown in Figure 3-14.

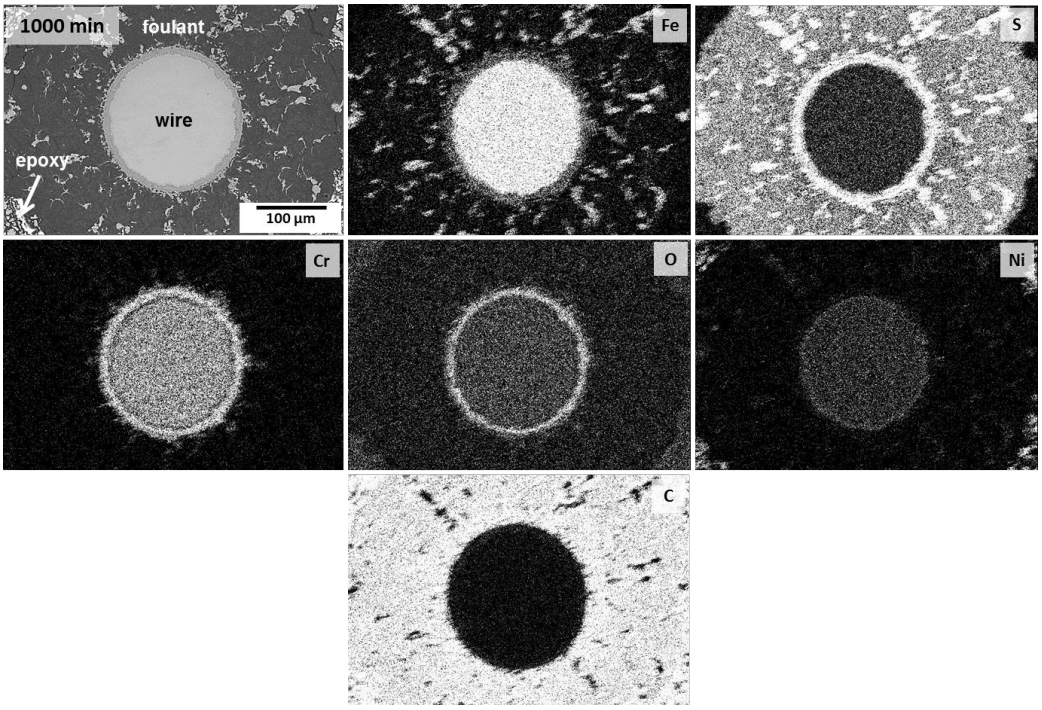

Figure 3-13: SEM micrograph and EDX elemental maps showing an entire cross section of a wire fouled for 1000 minutes.

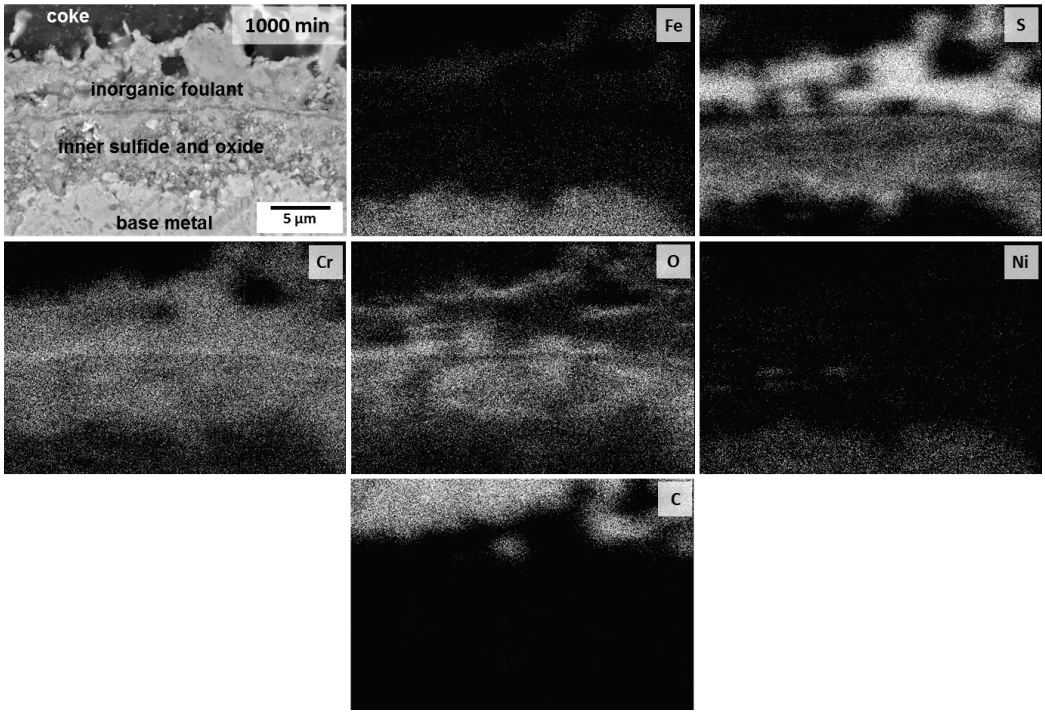

Figure 3-14: SEM micrograph and EDX elemental maps showing a magnified portion of the cross section of a wire fouled for 1000 minutes.

Figure 3-15 shows a summary of the baseline fouling behaviour through a series of fouled wire cross sections taken at various fouling times. The surrounding epoxy mounting material has been masked for clarity. The rapid initial deposition rates are apparent from the development of the deposit thickness from 10 to 60 minutes. Regions where sulfide plumes have reached the foulant-oil interface and stimulated accelerated fouling from organic species are now clearly visible at all exposure times. From Figures 3-15d-f we can clearly see the non-uniform corrosion attack on the wire surfaces.

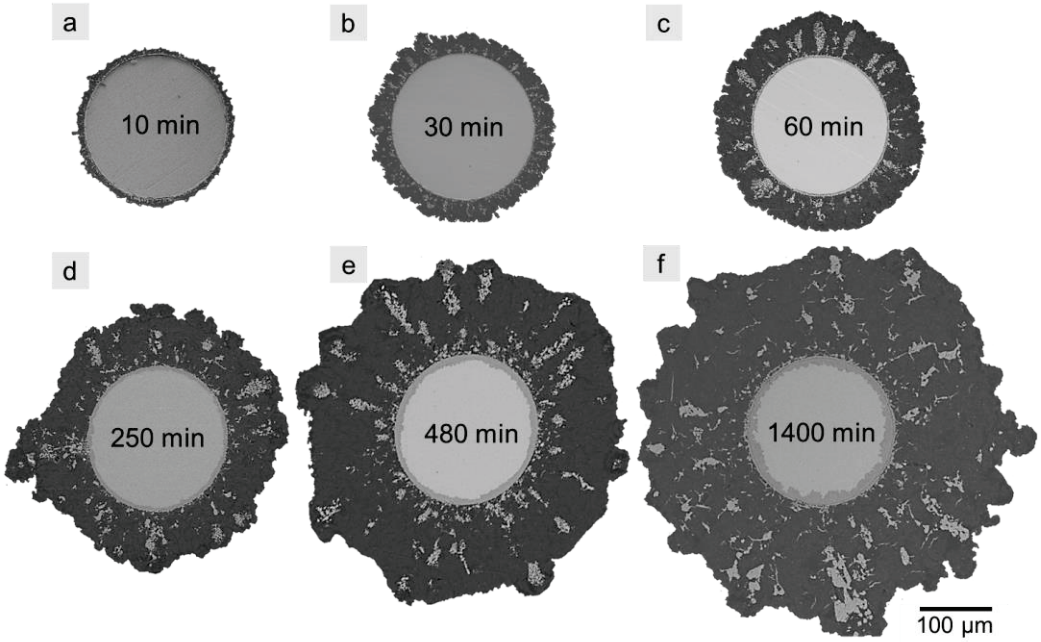

Figure 3-15: SEM micrographs of 316 stainless steel wires fouled at various fouling times. Epoxy material surrounding the wires has been masked for clarity.

As shown in Figure 3-3, the addition of thiophene drastically reduces the final fouling factor. Even with a 0.5 vol% addition, the fouling factor and thus the fouling rate were significantly decreased at all exposure times. When 1.3 vol% and 5.7 vol% of thiophene were added, the fouling rate was minimal at all the exposure times. Figure 3-16 provides an SEM and EDX comparison of wire cross sections fouled for 1400 minutes with and without the thiophene. Here we can see direct evidence corroborating the trend observed in Figure 3-3. All three concentrations of thiophene led to reduced amounts of sulfide plumes as compared to the baseline and too much less coke.

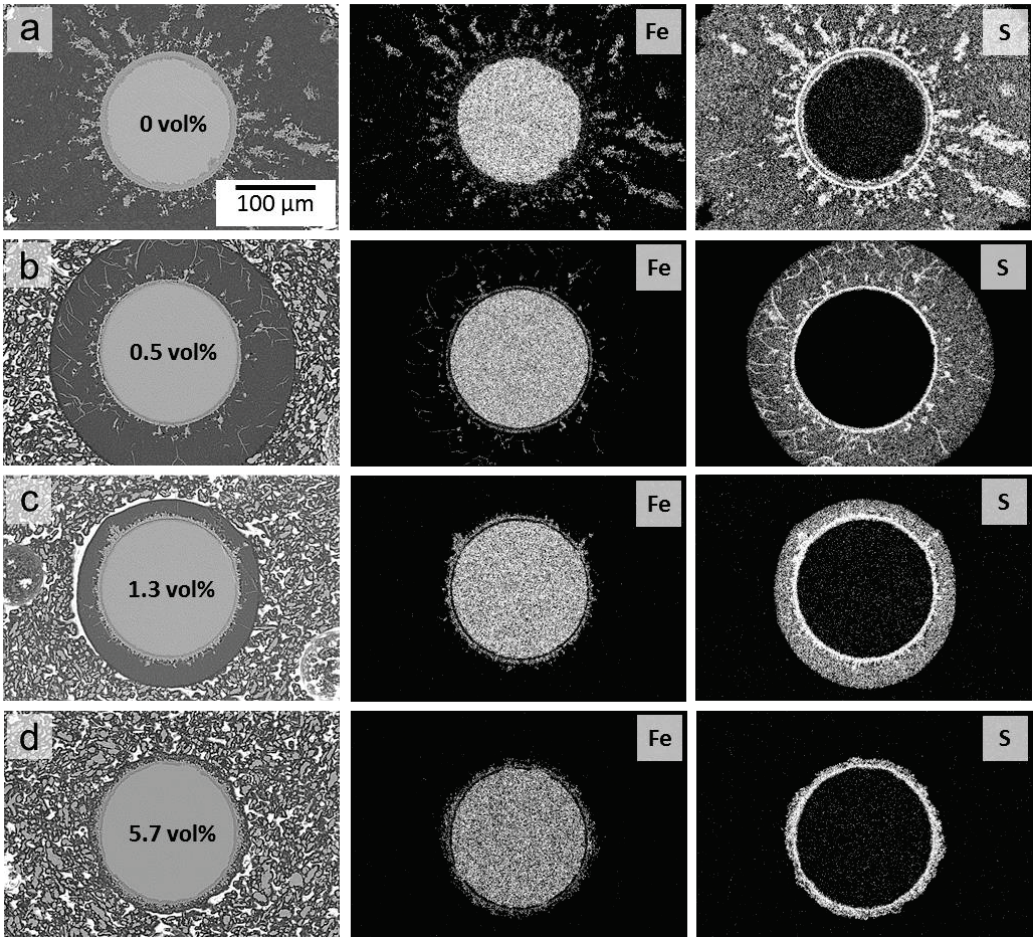

Figure 3-16: SEM micrographs and accompanying EDX elemental maps of 316 stainless steel wire cross sections fouled for 1400 minutes, showing the effect of thiophene as an oil additive. (a) No additive. (b) 0.5 vol% thiophene. (c) 1.3 vol% thiophene. (d) 5.7 vol% thiophene.

Figure 3-17 shows the 250 and 1000 minute samples with thiophene, where the same trend is present. Figure 3-18a shows a plot of the average foulant thickness versus fouling time, while 3-18b shows a plot of the outer sulfide thickness at the surface of the wire versus fouling time. Both figures show the results with and without the thiophene. While the trend in the surface sulfide thickness (Figure 3-18b) is less pronounced, its thickness is still reduced by the addition of thiophene.

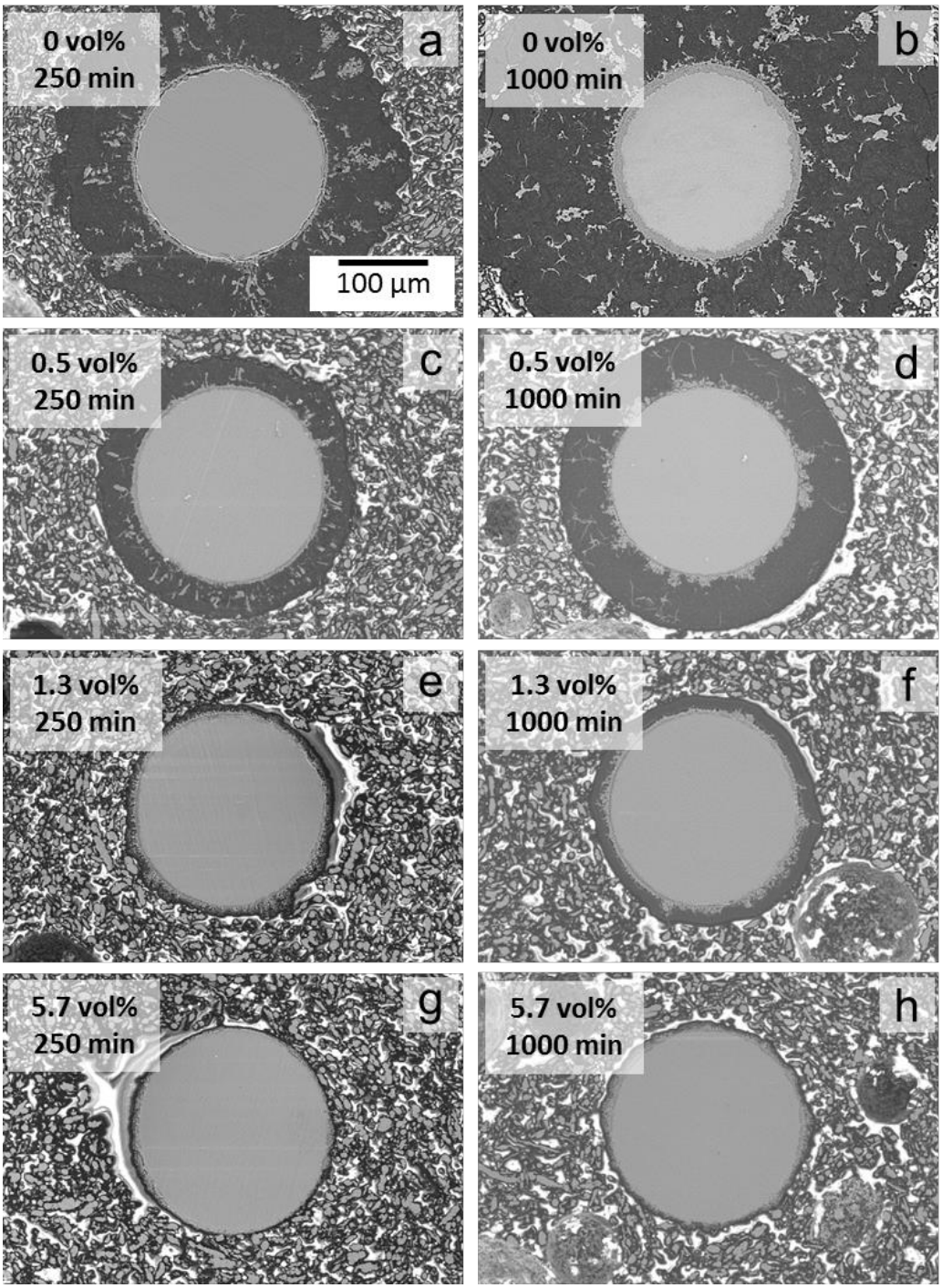

Figure 3-17: SEM micrographs of wire cross-sections after 250 and 1000 minutes of fouling with various concentrations of thiophene. (a,b) No additive. (c,d) 0.5 vol%. (e,f) 1.3 vol%. (g,h) 5.7 vol% thiophene.

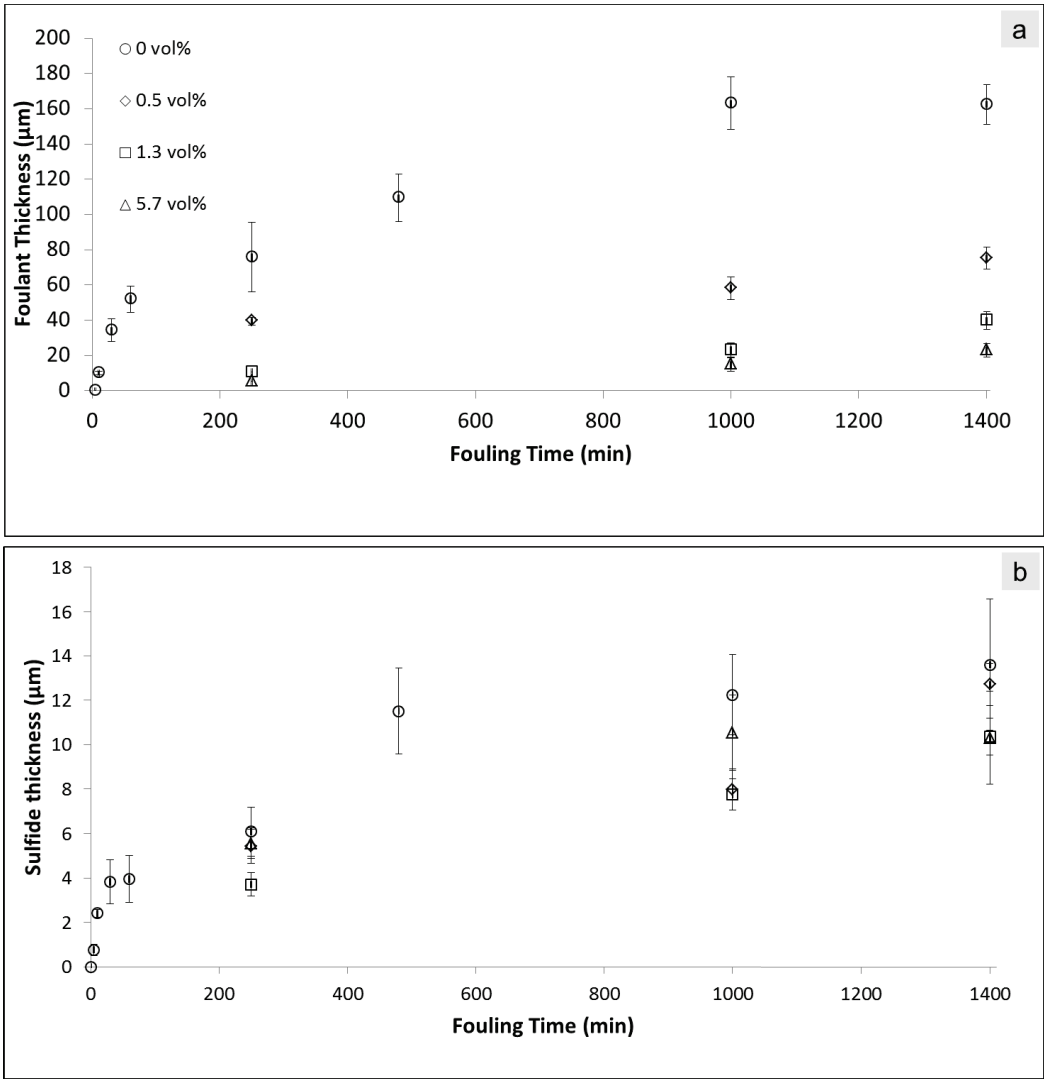

Figure 3-18: (a) Average foulant thickness versus time, with and without thiophene additions. (b) Average sulfide thickness at the surface of the wire. Error bars are one standard deviation of the average thickness.

Figure 3-19 shows a series of higher magnification SEM micrographs and EDX elemental maps of the samples in Figure 3-16, fouled for 1400 minutes. Comparing the elemental maps of these figures reveals some interesting results. First, it appears that the sulfidic corrosion of the wire has been partially inhibited in the 1.3 and 5.7 vol% thiophene cases (3-19c and d), since there is less iron

depletion at the wire surface compared to the baseline. This observation will be discussed later. Comparing these cases at 1400 minutes it may be concluded that thiophene has a tremendous positive effect on reducing the fouling rate, with the foulant in the 5.7 vol% thiophene specimen being effectively negligible compared to the baseline. Figure 3-20 shows SEM micrographs of the wire surfaces that further corroborate this observation.

Figure 3-20a shows the surface of a wire fouled for 250 minutes without additive. Figure 3-20b shows the surface of a wire fouled for 250 minutes with 5.7 vol% thiophene. The micrographs were taken near the center of the wires and are representative of the deposit found everywhere on the surface. EDX analysis (not shown) of the baseline wire surfaces (not cross sections) detected primarily carbon, while for the cases of thiophene it was iron and sulfur. This is indicative of the much thicker coke layer in the baseline oil, with the beam not penetrating deep enough to generate an appreciable signal from the underlying sulfide. Figures 3-20c and 3-20d show the surface foulant morphology after 1400 minutes, with and without thiophene.

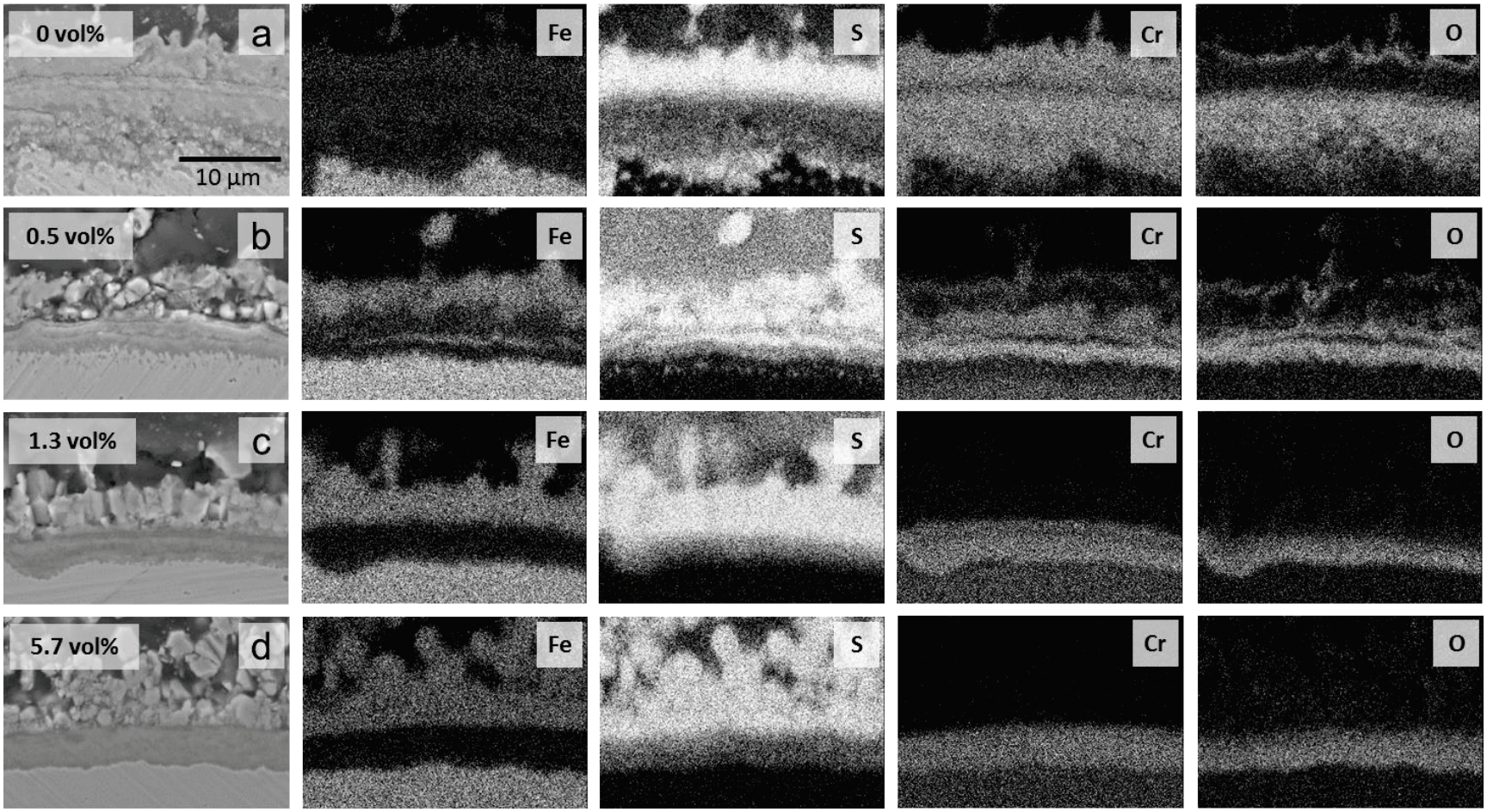

Figure 3-19: SEM micrographs and accompanying EDX elemental maps of 316 stainless steel wire cross sections fouled for 1400 minutes, showing the effect of thiophene as an oil additive. (a) No additive. (b) 0.5 vol% thiophene. (c) 1.3 vol% thiophene. and (d) 5.7 vol% thiophene.

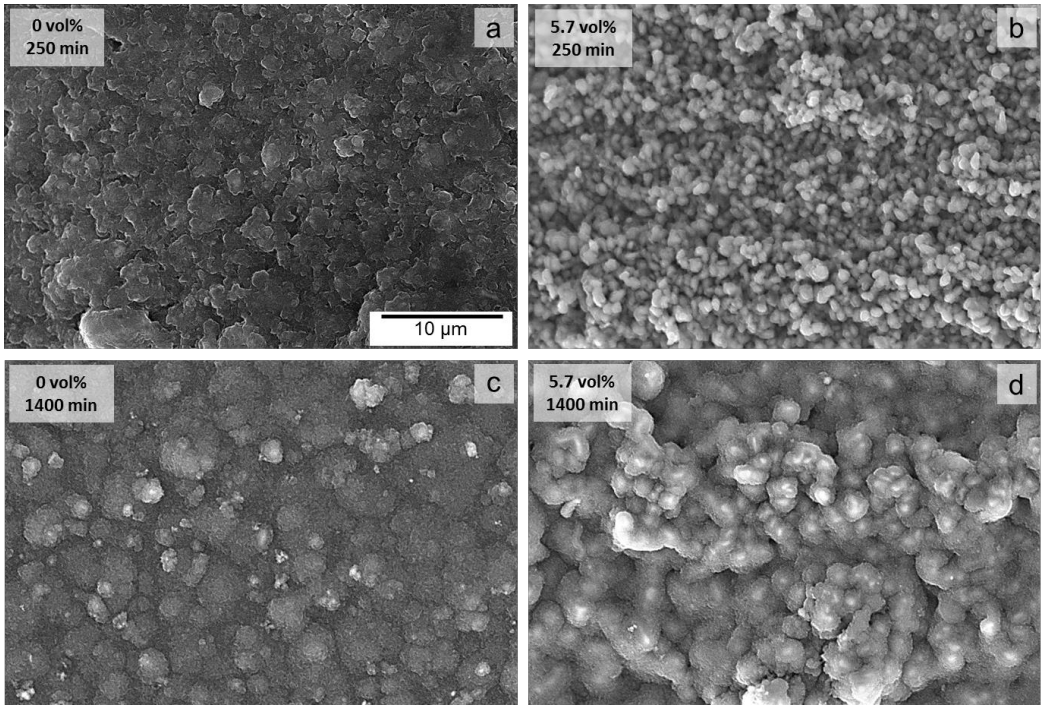

Figure 3-20: SEM micrographs of the surfaces of fouled wires taken along the length, near the center of the wires after 250 and 1400 minutes of fouling. (a) No additive, 250 minutes. (b) 5.7 vol% thiophene, 250 minutes. (c) No additive, 1400 minutes. (d) 5.7 vol% thiophene, 1400 minutes. The images are representative of the deposit found everywhere on the surface of the wire. EDX elemental maps (not shown) confirmed that the dominant phase was carbon in (a,c) and iron and sulfur in (b,d).

Table 3-1 shows the results of a headspace gas analysis that was conducted to help characterize the behaviour of the thiophene additive in the system. Samples were taken (a) at room temperature before the initiation of the fouling run but after the reactor was purged with nitrogen; (b) before the initiation of the fouling run but once the bath temperature had reached 250 °C; and (c) after the fouling run when the reactor had reached room temperature again (20 °C).

The addition of thiophene resulted in an increase to the concentration of H_2S in the system in all cases. While there is some decomposition of thiophene in

the system via HDS and thermal mechanisms, these are generally inhibited by a lack of excess hydrogen. We can see from the overall reaction shown as equation 3-3 that a large amount of hydrogen is needed to sustain the breakdown of thiophene.

$$C_4H_4S_{(g)} + 4H_{2(g)} \leftrightarrow C_4H_{10(g)} + H_2S_{(g)} \qquad \text{Eq. 3-3}$$

Table 3-1 shows that hydrogen was either not detected, or detected in very small quantities at all sampling points during the fouling runs. Also, if one assumes that all of the thiophene-related molecules present on the table were derived directly from thiophene decomposition, the volume percent of these gaseous products are actually quite small (less than 1 vol% when we sum the values on the table from H_2S to *cis*-2-butene). Furthermore, in our reactor, the addition of 5.7 vol% thiophene meant that 2.5 moles of the substance was introduced. This amount, if fully decomposed, would liberate 2.5 moles of H_2S by equation 3-3. However we can clearly see from the table that only fractions of a volume percent were actually detected after each run. Considering the run in which 0.608 vol% H_2S was detected, this would correspond to 0.0023 moles of the gas at the reactor conditions (considering it as an ideal gas) and therefore 0.0023 moles of thiophene consumed. Consequently, the headspace gas analysis supports the claim that thiophene is quite stable in the reactor. There is also a cornucopia of other gaseous species present after fouling that could not have come from the decomposition of thiophene.

Table 3-1: Headspace gas analysis of runs with and without thiophene. All data is reported in vol%.

Species	Before 0 vol% (20 °C)	Before 0 vol% (250 °C)	Before 0 vol% (250 °C)	After 0 vol% (20 °C) 250 min	After 0 vol% (20 °C) 1400 min	Before 5.7 vol% (20 °C)	Before 5.7 vol% (250 °C)	After 1.3 vol% (20 °C) 1400 min	After 5.7 vol% (20 °C) 250 min	After 5.7 vol% (20 °C) 1400 min
Hydrogen	0	0	0	0.011	0.317	0	0	0.165	0.108	0.140
Oxygen	0	1.650	0	1.688	0	0	0	0	0	0
Nitrogen	99.951	98.312	99.967	98.217	98.989	99.964	99.120	98.713	98.948	98.589
Methane	0	0	0	0	0	0	0	0.170	0.094	0.228
Carbon Dioxide	0.049	0.038	0.025	0.041	0.099	0.034	0.042	0.053	0.039	0.057
Ethylene	0	0	0	0	0.039	0	0.010	0.023	0.011	0.016
Ethane	0	0	0	0	0.211	0	0.032	0.087	0.050	0.034
Hydrogen Sulfide	***0***	***0***	***0***	***0.038***	***0.251***	***0***	***0.158***	***0.542***	***0.404***	***0.608***
n-Propane	0	0	0	0	0.043	0	0.188	0.060	0.032	0.021
Propylene	0	0	0	0	0.033	0	0.041	0.040	0.023	0.027
iso-Butane	0	0	0	0	0	0	0.002	0.003	0.001	0.003
n-Butane	0	0	0	0	0.019	0	0.024	0.045	0.028	0.029
t-2-Butene	0	0	0	0	0	0	0.009	0	0.007	0.015
1-Butene	0	0	0	0	0	0	0.009	0.014	0.010	0.006
iso-Butene	0	0	0	0	0	0	0.008	0.014	0.008	0.014
c-2-Butene	0	0	0	0	0	0	0.004	0	0	0.009
iso-Pentane	0	0	0	0	0	0	0.009	0	0.009	0.017
n-Pentane	0	0	0	0	0	0	0.013	0.016	0.017	0.024
Hexanes	0	0	0.008	0.005	0	0.002	0.322	0.055	0.208	0.163
Heptanes	0	0	0	0	0	0	0.011	0	0.003	0

We argue that the key role of thiophene is to poison the active sites on the catalytic iron sulfide, which have been associated with desulfurization and dehydrogenation of the crude oil.[52-54] While the high surface temperature of the wire will facilitate many rapid adsorption and desorption events, thiophene will continuously compete with other molecules for interaction with sulfide active sites. Being less sterically hindered than larger polyaromatic molecules such as asphaltenes, it will remain the dominantly adsorbed species. Thus the thiophene molecules will site-specifically moderate the production of coke by inhibiting key reactions associated with its catalytic formation. Lacking enough excess hydrogen to decompose, these adsorbed molecules are expected to be stable over time.

The addition of a higher concentration of thiophene yields more of all gaseous species, not just the C4's. This behaviour is consistent with enhanced pyrolysis of the oil although not to its full completion to form solid coke. The presence of more H_2S in the headspace due to thiophene, when combined with a lessening of iron sulfide on the wire surface, means that thiophene adsorbs on the base metal and acts as an H_2S corrosion inhibitor. It does so by preventing H_2S adsorption and consequent reaction with the iron. With less H_2S being tied up as a solid sulfide, more H_2S is detected in the headspace. In parallel with fewer sulfides being generated from the corroding wire surface, the rate of coke formation is suppressed. If our hypothesis is correct, H_2S corrosion inhibition and fouling inhibition are synergistic and interrelated.

In Figure 3-21 we present a schematic summarizing the corrosion fouling process with and without thiophene. Without the additive, the process proceeds unmitigated, with preferential corrosion taking place at metallurgical defects. The film stress and the ejection of gas from the corrosion reaction and from cracking reactions cause the eventual detachment of sulfide plumes, which erupt at the foulant surface and catalyze further coke deposition. The delamination of sulfide also exposes fresh metal and the process of sulfidation and coking continues. With thiophene, the deactivation of catalytic sites on the iron sulfide suppresses dehydrogenation and desulfurization reactions thereby subduing catalytic coke formation in favor of a slower thermally driven process. In parallel, sulfidic corrosion is reduced.

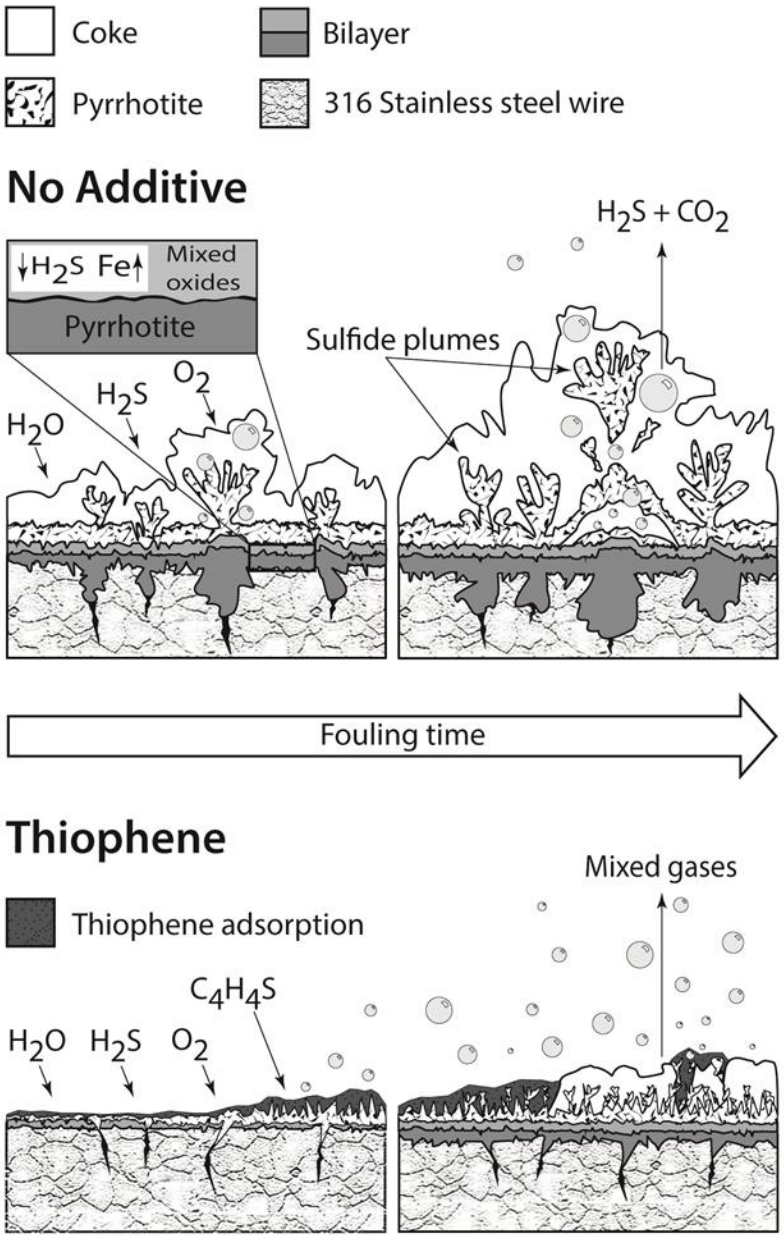

Figure 3-21: Schematic diagram showing the corrosion - fouling behaviour with and without thiophene.

3.4 Conclusions

An electrically heated wire probe in an autoclave reactor was utilized to study the high temperature (540 °C) fouling behaviour of the atmospheric bottoms fraction of a crude oil. The addition of thiophene as an antifouling additive resulted in a major reduction in the fouling rate, with the final fouling factor at 1400 minutes dropping from 1200 mm^2K/W in the baseline to below 60 mm^2K/W. Based on the experimental results, the hypothesis was that thiophene adsorbs onto catalytic sites of the iron sulfide layer, effectively passivating them and suppressing further dehydrogenation and desulfurization reactions of other species in the oil. Thiophene also inhibits sulfidic corrosion of the base metal, presumably though a similar mechanism of preferential adsorption. The propensity of the thiophene to act as a solvent for asphaltenes was not decoupled from the overall mechanism and remains an area for further study. However, it is unlikely that the thiophene would have been effective at reducing surface corrosion on the wires if its efficacy was derived from an asphaltene solvency effect alone.

Analysis by TEM, AES, SEM, EDX and XRD of the thiophene-free baseline demonstrated that the corrosion-fouling process has the following key features: The foulant was observed to grow asymptotically, reaching a thickness of approximately 160 μm after 1400 minutes. The initiation of organic foulant is preceded by the formation of an inorganic iron-nickel sulfide corrosion product on the metal surface, which forms almost instantaneously. Coke formation around the wire is non-uniform, with foulant protrusions into the surrounding

pitch/oil being well correlated with detached plumes of the sulfide. The near-surface metal transforms from the as-received microstructure of fully dense textured austenitic grains to a highly porous bilayer composite (inner sulfide and chromium oxide) that grows to over 10 microns thick after 1400 minutes of exposure. Significant localized sulfidation attack was also observed at exposure times as short as 250 minutes. This is likely related to accelerated H_2S corrosion at pre-existing defects on the metal surface.

3.5 References

[1] Gentzis, T.; Parker, R. J.; McFarlane, R. A. *Fuel,* **2000**, *79(10)*, 1173-1184.

[2] Ebrahimi, S. ; Moghaddas, J.S. ; Aghjeh, M.K.R. *Fuel*, **2008**, *87*, 1623-1627.

[3] Wiehe, I.A. *Ind. Eng. Chem. Res.* **1993**, *32*, 2447-2454.

[4] Reyniers, M.-F.S.G. ; Froment, G.F. *Ind. Eng. Chem. Res.* **1995**, *34*, 773-785.

[5] Acevedo, S. ; Ranaudo, M.A. ; Escobar, G. ; Gutierrez, L. ; Ortega, P. *Fuel*, **1995**, *74(4)*, 595-598.

[6] Brons, G.; Yu, J.M. *Energ. Fuel.* **1995**, *9*, 641-647.

[7] Watkinson, A.P.; Wilson, D.I. *Exp. Therm. and Fluid Sci.* **1997**, *14*, 361-374.

[8] Lemke, H.K. ; Stephenson, W.K. *Petrol. Sci. Technol.* **1998**, *16(3)*, 335-360.

[9] Crittenden, B.D. ; Kolaczkowski, S.T. ; Phillips, D.Z. *Chemical Reaction Fouling.* 91-103. In *Understanding Heat Exchanger Fouling and its Mitigation*: Proceedings of an International Conference on Understanding Heat Exchanger Fouling and Its mitigation. Castelvecchio Pascoli, Italy, 1997. Ed. Bott, T.R. ; Melo, L.F. ; Panchal, C.B. Somerscales, E.F.C. Begell House Publishers Inc. Redding Connecticut, USA, **1999**.

[10] Parker, R.J.; McFarlane, R.A. *Energ. Fuel.* **2000**, *14*, 11-13.

[11] Costulchi, A. ; Garciafigueroa, E. ; Mar, B. ; Garcia-Borquez, A. ; Lara, V.H. ; Bosch, P. *Fuel*, **2002**, *81*, 413-421.

[12] Wang, J. ; Anthony, E.J. *Chem. Engg. Sci.* **2003**, *58*, 157-162.

[13] Gentzis, T. ; Rahimi, P.M. *Fuel*, **2003**, *82*, 1531-1540.

[14] Hong, E. ; Watkinson, P. *Fuel*, **2004**, *83*, 1881-1887.

[15] Falkler, T.J.; Stark, J.L. *Oil and Gas J.* **2004**, *102*, 72-74.

[16] Srinivasan, M.; Watkinson, A. P. *Heat Transf. Eng.* **2005**, *26(1)*, 7-14.

[17] Eaton, P.E., Salt Hydrolysis in Crude & Bitumen Fouling. *AIChE,* Spring Meeting, paper 103d, **2006**.

[18] Panchal, C.B. Halpern, Y. ; Kuru, W.C. ; Miller, G. *Mechanisms of Iron Sulfide Formation in Refining Processes.* 1-8. In: Proceedings of the Engineering Foundation Conference. *Understanding of Heat Exchanger Fouling and its Mitigation.* Lucca, Italy, **1997**.

[19] Fan, Z. ; Watkinson, A.P. *Ind. Eng. Chem. Res.* **2006**, *45*, 6104-6110.

[20] Silva, C.C. ; Machado, J.P.S.E. ; Sobral-Santiago, A.V.C. ; de Sant'Ana, H.B. ; Farias, J.P. *J. Petrol. Sci. Engg.* **2007**, *59*, 219-225.

[21] Wu, X.A.; Chung, K. *Energ. Fuel.* **2007**, *21*, 1212-1216.

[22] Wiehe, I.A. *Process Chemistry of Petroleum Macromolecules*; CRC Press: Boca Raton, FL, **2008**, Vol. 121, 296-298.

[23] Eaton, P.E.; Williams, J., Delayed Coker Furnace Fouling Control – Laboratory Correlation to Field Experience. In *NACE*, paper 8670, **2008**, 1-7.

[24] Hong E.; and Watkinson A.P. *Heat Transf. Eng*. **2009**, *30*, 786–793.

[25] Wilson, D.I. ; Ishiyama, E.M. ; Paterson, W.R. ; Watkinson, A.P. *Ageing: Looking back and looking forward.* 221-230. In: Procedings of International Conference on Heat Exchanger Fouling and Cleaning VIII. Ed: Muller-Steinhagan, H. ; Malayeri, M.R. ; Watkinson, A.P. Schladming, Austria. **2009**.

[26] Fan, Z. ; Rahimi, P. ; McGee, R. ; Wen, Q. ; Alem, T. *Energy Fuels*, **2010**, *24*, 6110-6118.

[27] Eaton, P.E.; Newman, B.; Gray, M. Kubis, A.; Derakhshesh, M.; Holt, C.; Mitlin, D. Furnace Coker Simulations in a Laboratory Apparatus. *PetroPhase Conference*, paper O30, **2010**.

[28] Wang, W. ; Watkinson, A.P. *Iron sulphide and coke fouling from sour oils: Review and initial experiments.* 23-30. In: Proceedings of International Conference on Heat Exchanger Fouling and Cleaning. Ed: Malayeri, M.R. ; Muller-Steinhagen, H. ; Watkinson, A.P. Crete Island, Greece. **2011**.

[29] Stephenson, T. ; Kubis, A. ; Derakhshesh, M. ; Hazelton, M. ; Holt, C. ; Eaton, P. ; Newman, B. ; Hoff, A. ; Gray, M. ; Mitlin, D. *Energ. Fuel.* **2011**, *25*, 4540-4551.

[30] Derakhshesh, M. ; Eaton, P. ; Newman, B. ; Hoff, A. ; Mitlin, D. ; Gray, M.R. *Energ. Fuel.* **2013**, 27, 1856.

[31] Yang, M. ; Wood, Z. ; Rickard, B. ; Crittenden, B. ; Gough, M. ; Droegemueller, P. ; Higley, T. *Appl. Thermal Eng.* **2013**, 54, 516-520.

[32] Muller-Steinhagen, H. ; Malayeri, M.R. ; Watkinson, A.P. *Heat Trasf. Eng.* **2013**, 34(8-9), 653-654.

[33] Petkovic, B. ; Watkinson, A.P. *Heat Trasf. Eng.* **2014**, 35(3), 302-310.

[34] Wiehe, I.A. ; Kennedy R.J. *Energ. Fuel.* **2000**, 14, 60-63.

[35] Wiehe, I.A. ; Kennedy, R.J.; Dickakian, G. *Energ. Fuel.* **2001**, 15, 1057-1058.

[36] Wiehe, I.A. *J. Disper. Sci. Technol.* **2004**, *25*, 333-339.

[37] Mena-Cervantes, V.Y. ; Hernandez-Altamirano, R. ; Buenrostro-Gonzalez, E. ; Beltran, H.I. ; Zamudio-Rivera, L.S. *Fuel*, **2013**, 110, 293-301.

[38] Rana, M.S. ; Samano, V. ; Ancheyta, J. ; Diaz, J.A.I. *Fuel*, **2007**, 86, 1216-1231.

[39] Speight, J.G. *The Chemistry and Technology of Petroleum*. 4th Ed. **2007**, CRC Press, Boca Raton, FL, 521-597.

[40] Cheng, F. ; Chen, J. ; Guo, X. *Adv. Mater.* **2006**, 18, 2561-2564.

[41] Moses, P.G. ; Hinnemann, B. ; Topsoe, H. ; Norskov, J.K. *J. Catal.* **2009**, 268, 201-208.

[42] Huang, Y. ; Zhou, Z. ; Qi, Y. ; Li, X. ; Cheng, Z. ; Yuan, W. *Chem. Eng. J.* **2011**, 172, 444-451.

[43] Castillo-Villalon, P. ; Ramirez, J. ; Castaneda, R. *J. Catal.* **2012**, 294, 54-62.

[44] Rao, B.G. ; Ramakrishna Matte, H.S.S. ; Chaturbedy, P. ; Rao, C.N.R. *ChemPlusChem*, **2013**, 78, 419-422.

[45] Menoufy, M.F. ; Ahmed, H.S. ; Betiha, M.A. ; Sayed, M.A. *Fuel*, **2014**, 119, 106-110.

[46] Thakur, D.S. *J. Catal.* **1985**, 94, 310-312.

[47] Yu, Z. ; Fareid, L.E. ; Molijord, K. ; Blekkan, E.A. ; Walmsley, J.C. ; Chen, D. *Appl. Catal. B: Environ.* **2008**, 84, 482-489.

[48] Embaid, B.P. ; Biomorgi, J.G. ; Gonzalez-Jimenez, F. ; Perez-Zurita, M.J. ; Scott, C.E. *Appl. Catal. A: General*, **2011**, 400, 166-170.

[49] Raje, A.P. ; Dadyburjor, D.B. *Ind. Eng. Chem. Res.* **1993**, 32, 1637-1644.

[50] Diaz, Y. ; Sevilla, A. ; Monaco, A. ; Mendez, F.J. ; Rosales, P. ; Garcia, L. ; Brito, J.L. *Fuel*, **2013**, 210, 235-248.

[51] Zaera, F. ; Kollin, E.B. ; Gland, J.L. *Langmuir*, **1987**, 3(4), 555-557.

[52] Dos Santos, N. ; Dulot, H. ; Marchal, N. ; Vrinat, M. *Appl. Catal. A*, **2009**, 352, 114-123.

[53] Li, Z. ; Wang, G. ; Liu, Y. ; Gao, J. ; Xu, C. ; Liang, Y. ; Wang, X. *Fuel Proc. Technol.* **2013**,115, 1-10.

[54] Valencia, D. ; Olivares-Amaya, R. ; Aburto, J. ; Garcia-Cruz, I. *Catal. Lett.* **2013**, 143, 1354-1361.

[55] Bajus, M. ; Vesely, V. ; Baxa, J. ; Leclercq, P.A. ; Rijks, J.A. *Ind. Eng. Chem. Prod. Res. Dev.* **1981**, 20, 741-745.

[56] Sahu, D. Kunsru, D. *Can. J. Chem. Eng*. **1988**, 66, 808-816.

[57] Taylor, W.F. *Ind. Eng. Chem. Prod. Res. Dev.* **1976**, 15(1), 64-68.

[58] Zhang, L. ; Holt, CMB. ; Luber, E.J. ; Olsen, B.C. ; Wang, H. ; Danaie, M. ; Cui, X. ; Tan, X. ; Lui, V. ; Kalisvaart, P. ; Mitlin, D. *J. Phys. Chem. C*, **2011**, 115, 24381-24393.

[59] Ohmi, T.; Nakagawa, Y.; Nakamura, M.; Ohki, A.; Koyama, T. *J. Vac. Sci. Tech.* **1996**, *14(4)*, 2505-2510.

[60] Cheng, S-Y. ; Kuan, S-L.; Tsai, W-T. *Corr. Sci.* **2006**, *48*, 634-649.

[61] Li, H. ; Chen, W. *Oxid. Met.* **2012**, 78, 103-122.

[62] Gesmundo, F. ; Viani, F. ; Znamirowski, W. ; Godlewski, D. ; Bregani, F. *Mater. Corr.* **1992**, 43, 83-85.

[63] Orchard, J.P. ; Young, D.J. *J. Electrochem. Soc*. **1986**, 133, 1734-1741.

[64] Lobnig, R.E. ; Grabke, H.J. *Corr. Sci.* **1990**, 30, 1045-1071.

[65] Baxter, D.J. ; Natesan, K. *Oxid. Met*. **1989**, 31, 305-322.

[66] Wilson, D.F. ; Devereux, O.F. *J. Electrochem. Soc.* **1991**, 138, 2168-2176.

[67] Farrell, D. ; Roberts, L. NACE Conference, *Corrosion*, **2010**, paper 10358, 1-11.

[68] Gutzeit, J. *High Temperature Sulfidic Corrosion in Steels*, in Process Industries Corrosion-The Theory and Practice, NACE, **1986**, 367-372.

[69] Lai, G.Y. *High-Temperature Corrosion and Materials Applications*, ASM International, Ohio, **2007**, 201-231.

[70] Nguyen, M.T. ; Sengupta, D. ; Raspoet, G. ; Vanquickenborne, L.G. *J. Phys. Chem.* **1995**, 99, 11883-11888.

[71] Wang, W. ; Watkinson, A.P. *Deposition from a sour heavy oil under incipient coking conditions: Effects of surface material and temperature*. 9-17. In: Proceedings ofInternational Conference on Heat Exchanger Fouling and Cleaning. Budapest, Hungary. **2013**.

[72] Lacroix, M. ; Marrakchi, H. ; Calais, C. ; Breysse, M. ; Forquy, C. *Stud. Surf. Sci. Catal.* **1991**, 59, 277-285.

CHAPTER 4

Lithium Ion Battery Applications of Molybdenum Disulfide (MoS_2) Nanocomposites

Material in this chapter has been published in the journal article;

Lithium ion battery applications of molybdenum disulfide (MoS_2) nanocomposites. *Energy & Environmental Science*. **2014**, 7, 209-231.

Composed by;

Tyler Stephenson, Zhi Li, Brian Olsen, and David Mitlin.

Abstract

This chapter will present the first targeted review of the synthesis - microstructure - electrochemical performance relations of MoS_2 - based anodes and cathodes for secondary lithium ion batteries (LIBs). Molybdenum disulfide is a highly promising material for LIBs that compensates for its intermediate insertion voltage (~ 2 V vs. Li/Li^+) with a high reversible capacity (up to 1290 mAh/g) and an excellent rate capability (e.g. 554 mAh/g after 20 cycles at 50 C). Several themes emerge when surveying the scientific literature on the subject: First, we argue that there is excellent data to show that truly nanoscale structures, which often contain a nanodispersed carbon phase, consistently possess superior charge storage capacity and cycling performance. We provide several hypotheses regarding why the measured capacities in such architectures are well above the theoretical predictions of the known MoS_2 intercalation and conversion reactions. Second, we highlight the growing microstructural and electrochemical evidence that the layered MoS_2 structure does not survive past the initial lithiation cycle, and that subsequently the electrochemically active material is actually elemental sulfur. Third, we show that certain synthesis techniques are consistently demonstrated to be the most promising for battery applications, and describe these in detail. Fourth, we present our selection of synthesis methods that we believe to have a high potential for creating improved MoS_2 LIB electrodes, but are yet to be tried.

4.1 Introduction

In this chapter we focus on synthesis - microstructure - electrochemical performance relationships for MoS_2 - based electrodes for secondary lithium ion batteries (LIBs). The use of MoS_2 is discussed both in terms of its application for LIB anodes (where most work has been done) and for cathodes (an emerging and highly promising area). We treat these aspects in detail, while avoiding discussions regarding other dichalcogenides. We present a detailed and critical review regarding what is known about the lithiation/delithiation mechanism in MoS_2; a topic that is currently under significant debate in the energy storage community. The outline of this review is as follows: Section 4.2 presents other applications of MoS_2 beyond rechargeable batteries. Section 4.3.1 outlines the long and rich history of MoS_2 in the battery field, including its commercial applications in the 1980's by *Moli Energy*. Section 4.3.2 contrasts the scope and the aims of this article with those of several other recent reviews that adopt a broader context for the various energy and non-energy applications of dichalcogenides. Section 4.4 provides an overview of MoS_2 in the LIB material landscape, contrasting its electrochemical performance to that of other promising electrode materials. Section 4.5 details the structure and bonding of MoS_2. In Section 4.6 we discuss the lithiation mechanisms of MoS_2, which are in fact highly dependent on the cut-off voltage at discharge. Section 4.7 presents a detailed discussion on MoS_2 nanocomposites for LIBs. Here we consider the interrelation between the various synthesis approaches that have been employed for creating nanostructured MoS_2. In addition we examine the resultant

microstructures that often contain a secondary nanodispersed carbon phase, and the several criteria used to judge electrochemical cycling performance (e.g. maximum reversible capacity, cycle 1 and steady-state cycling coulombic efficiency, cycling capacity retention, and rate capacity retention). Finally in Section 4.8, we present an overview of what we believe are the additional promising approaches for achieving MoS_2 - based nanomaterials for lithium storage, but which have not been investigated to date. Section 4.9 contains the concluding remarks.

4.2 Applications of MoS_2

Molybdenum disulfide exhibits a remarkably diverse range of unique properties, many of which are effectively summarized by the reviews of Strano *et al*.[1] and Zhang *et al*.[2] Due to these properties MoS_2 is currently the focus of research groups across a broad range of disciplines. In the field of tribology, MoS_2 is often referred to as a super lubricant. The material has long been recognized for its exceptional lubricity, owing to the weak van der Waals bonds between S-Mo-S layers, and to the relative inertness of the sulfur basal planes.[3] It has been a favored dry lubricant for aerospace applications due to its excellent lubricity *in vacuo* and under high load.[4,5] MoS_2 is also a key additive in many types of commercial lubricating fluids and greases. More recently, a fascinating negative compressibility effect for MoS_2 under conditions of dynamic shear has revealed a new property of the interlayer glide mechanism.[6] MoS_2 is also making an impact in the field of chemical sensing. Owing to the variance in reactivity

between basal and edge sites, functionalized MoS_2 nanosheets have been used to immobilize DNA strands and immunoglobins for biosensing applications.[7,8] Additionally, flexible MoS_2 based thin film transistors have successfully been used to detect minute changes in nitrogen oxide (NO)[9], and nitrogen dioxide (NO_2)[10] concentrations under ambient conditions. This type of sensor is highly sought after in the field of toxic gas detection.

The tunable direct band gap and highly deformable nature of a monolayer of MoS_2 has led many researchers to consider it as a viable material for photovoltaic applications.[11-15] In addition to this, the use of MoS_2 in catalysis is widespread due again to its band gap (which couples well with the solar spectrum), as well as the catalytic activity of its edge sites.[16,17] As a photocatalyst for the oxidation of environmental contaminants, MoS_2 is frequently coupled with an additional semiconducting phase (such as TiO_2) as a nanocomposite with great positive effect.[18,19] Its catalytic effects for hydrodesulfurization in oil refining are well known.[20] MoS_2 has also been shown as a synergistic catalytic support for gold nanoparticles[21] as well as for a nickel-iron alloy used in the electrooxidation of hydrazine, an important fuel.[22] Furthermore, many groups are exploring the catalytic effect of MoS_2 for hydrogen evolution.[23-28] Finally, methods are being elucidated to employ MoS_2 nanocomposites as flexible and rewritable memory diodes.[29] While this article will focus on the application of MoS_2 to the field of energy storage in lithium ion batteries, the material remains exquisitely versatile.

4.3 History

4.3.1 Background and Motivation

Efficient energy storage is a long-standing technological and scientific problem that has global implications for all of humanity. The requirements of progressively smaller scale and larger capacity for a wide range of portable, automotive and stationary systems continue to be strong driving forces for the development of advanced lithium ion batteries. Though lithium has been incorporated into battery systems since the late 1950's[30-32], commercial secondary lithium ion batteries remain a challenge for many applications requiring capacity retention over thousands of cycles and progressively higher energy storage densities. Early work revealed the propensity of mixed valence state transition metal dichalcogenides to intercalate alkali metal ions.[33-35] These studies led to various commercial primary lithium battery systems in the 1970's. Of these, lithium sulfur dioxide (Li/SO_2), lithium thionylchloride ($Li/SOCl_2$), and lithium sulfurylchloride (Li/SO_2Cl_2) were influential. In addition, the viability of molybdenum and other disulfides was also explored.[36-43]

Given the emergence of nanostructured materials, MoS_2 is once again becoming the subject of significant attention as a battery anode material.[44,45] The material is quite promising as a negative electrode, since its capacity can be three and a half times that of commercial graphite anodes (372 mAh/g). For example, reversible values as high as 1290 mAh/g have been reported for nanostructured MoS_2-graphene composite electrodes.[46] Moreover, compared to other emerging negative electrode materials, such as silicon or germanium, MoS_2 generally

displays much better rate capability and lower rates of cycling induced degradation. While silicon anodes possess initial capacities around 3500 mAh/g when tested at low rates such as 0.1 or 0.2 C, they retain minimal capacity at rates of 10 C and higher, e.g.[47] Conversely, as will be discussed later, properly designed MoS_2 electrodes are capable of being cycled at high current densities, retaining a capacity of 554 mAh/g after 20 cycles at a rate of 50 C.[48] From a practical battery design perspective, MoS_2 electrodes are also quite attractive since they possess significantly less volumetric expansion upon lithiation compared to some other conversion materials. For example, while silicon expands 280% upon full lithiation ($Li_{15}Si_4$), the conversion reaction of MoS_2 to Li_2S and molybdenum yields "only" 103% expansion.

A key disadvantage of employing MoS_2 based anodes is their intermediate lithiation voltages (1.1-2.0 V vs Li/Li^+, depending on the degree of lithiation), which substantially narrows the voltage window and hence the net energy density of a full cell LIB. While one can argue that a higher potential versus lithium makes MoS_2 safer than graphite due to a reduction in the driving force for lithium dendrite formation, there is always a trade-off.[49] Moreover, recent studies by Cui *et al*.[50] and Xie *et al*.[51] have demonstrated that by employing heteronanostructures that can accommodate the volume expansion, the cyclability of silicon may be substantially improved. As is going to be documented in this review, nanostructured MoS_2-based anodes are also highly stable during cycling. However a polysulfide shuttling problem, well known for Li-S batteries, may

cause premature electrode failure via electrochemical degradation of the active material.

In addition, the intermediate voltage profile versus Li/Li^+ has led researchers to consider MoS_2 as a positive electrode, with the system often being pre-lithiated prior to device assembly. The application of MoS_2 as a cathode was patented in 1980[52] and has since been explored by others.[53-57] Similar to the case of using MoS_2 as an anode, the intermediate voltage of MoS_2 is generally viewed as a disadvantage for its use as a cathode. The cathodic voltage of $LiMoS_2$ is lower than other commercial cathode materials such as lithium cobalt oxide ($LiCoO_2$) and related four and five component oxides (2.5-4.5 V vs. Li/Li^+).[58-61] However in some applications this may be compensated by the higher charge storage capacity of $LiMoS_2$ to yield energy densities on par or even higher than $LiCoO_2$ and related materials (for example 1.5 V*1000 mAh/g vs. 3.5 V*150 mAh/g).[62,63] Secondary lithium metal batteries using MoS_2 as a cathode and lithium as an anode were commercialized in the early 1980's by *Moli Energy*. However these batteries were prone to the growth of lithium dendrites from the anode which resulted in poor cycle life and safety concerns due to short circuiting.

Archer *et al*.[64] have recently shown that this effect can be mitigated by the use of carefully selected ionic liquid electrolytes. These researchers constructed a half cell of MoS_2 and lithium, using an electrolyte consisting of a blend of silica nanoparticles with 1-methyl-3-propylimidazolium bis(trifluoromethanesulfone)

and propylene carbonate (SiO2-IL-TFSI/PC). The cell retained a reversible capacity of 750 mAh/g after 15 cycles. Moreover, the use of their hybrid electrolyte prolonged short circuit times by an order of magnitude compared to a "standard" electrolyte of ethylene carbonate and dimethyl carbonate. This achievement should provide a research path forward to optimize pre-lithiated MoS_2-based microstructures for positive electrode applications. Not only would the revival of the lithium-metal battery solve electrode compatibility issues, it would enable the use of a wider range of high capacity cathodic materials. The emergence of nanostructured materials has led to a performance enhancement of a number of traditional lithium ion battery materials. As a result, molybdenum disulfide is presently being re-explored as an advanced lithium ion battery material and will hence be the focus of this article.

4.3.2 Related reviews

Recently there have been several high quality review articles on the synthesis and structure of a variety of sulfides which include their general application in a multitude of functional and energy storage fields. The relatively broad and excellent review by Chen *et al*.[65] discussed a wide range of sulfides and chalcogenides, including MoS_2. This review gave a comprehensive description of chalcogenide properties including optical, magnetic, electrical, field-emission, photoelectric, thermoelectric, and photocatalytic activity. In addition to the energy storage applications of these materials (lithium ion batteries), the authors

discussed a wide range of others including fuel cells, solar cells, and electrical nanogenerators.

The comprehensive article by Yu *et al.*[66] provides another exceptional discussion on a wide variety of nanostructured metal chalcogenides, including sulfur, selenium and tellurium compounds, for energy conversion and storage. The thrust of their work is to summarize and critically compare winning synthesis and modification strategies across a range of energy related applications, making the review highly pertinent across those fields. Emphasis is placed on methods for creating a wide array of nanomaterials, including discussions of an array of liquid-phase synthesis methodologies and strategies for modification of metal chalcogenide nanomaterials. A diverse range of synthesis methods are covered including liquid exfoliation, hot-injection, mixed solvent, microwave, Kirkendall-effect-induced and photochemical. Modification of metal chalcogenide nanomaterials with carbon, noble metals, metal oxides and with other metal chalcogenides is also discussed in detail. The applications covered include fuel cells, water splitting, supercapacitors and solar cells, in addition to lithium ion batteries.

The highly relevant review by Zhang *et al.*[67] focuses on metal dichalcogenide (mostly MoS_2) nanosheets, and covers a broad array of synthesis methods, properties and applications. The section on preparation methods emphasizes the optimum approaches for yielding such morphologies as 2D

graphene-like single and multi-layers. Moreover this particular article offers a uniquely in-depth discussion of device and sensor applications of MoS_2. The authors begin with the synthesis approach that really began the "graphene revolution" i.e. mechanical cleavage, and demonstrate how it has been applied to a variety of materials such as sulfides, nitrides, selenides, and oxides. The review then covers synthesis by electrochemical lithium intercalation, exfoliation, and sonication in various solvents as well as CVD growth. The authors provide a critical review of MoS_2 crystal structure (structures 2H and 1T are emphasized), mechanical properties, electronic structure and optical properties. In the Applications section the review provides a detailed discussion regarding the use of MoS_2 nanosheets for electronic devices, optoelectronic devices, sensing platforms, and energy storage devices that includes both electrochemical supercapacitors and lithium ion batteries.

Researchers focused a state-of-the-art review on several highly technologically promising two-dimensional layered nanomaterials: molybdenum trioxide (MoO_3), disulphide (MoS_2), diselenide ($MoSe_2$) and ditelluride ($MoTe_2$). [68] Their manuscript provides an accurate overview of the crystal structure and bonding of the oxide and of each dichalcogenide, and explains and contrasts their electronic band structure, electrical, optical, mechanical, thermal and magnetic properties. Synthesis methods for layered crystals including vapor phase deposition (PVD and CVD methods), liquid phase deposition and solid state reactions are discussed. Moreover this review offers a detailed section

discussing methods for layer exfoliation and identification. Approaches such as mechanical exfoliation, liquid exfoliation, laser thinning, as well as AFM and optical methods for thickness and layer number identification are examined. The authors span numerous application fields by discussing uses of these materials as lubricants, in electrochromic systems, in electronic devices, in battery electrodes, as catalysts, in optical devices, in sensors and in superconductors.

The key aspect differentiating this review from others is that while being quite comprehensive, we focus almost entirely on synthesis - microstructure - electrochemical performance relationships of MoS_2 - based electrodes. These are discussed in terms of their application to anodes and cathodes in LIBs. We treat these aspects in substantial detail, and keep our focus relegated to MoS_2. We limit our discussion of the synthesis methods to those approaches that have either been demonstrated to be optimum for LIBs or to those that in our opinion have much promise. Moreover, a substantial portion of this manuscript contains a critical discussion regarding the ambiguity in the battery literature concerning the actual lithiation sequence of MoS_2, with and without the addition of nanostructured carbons.

4.4 MoS_2 in the LIB material landscape

While bulk MoS_2 offers little in the way of exciting electrochemical properties for lithium storage, its nanostructured counterparts are the focus of much attention. The nanostructuring of materials for lithium ion batteries

embodies a number of well-known advantages and disadvantages.[44,69-71] The trend that nanostructured analogues routinely outperform their bulk equivalents in terms of capacity and cycle life has been demonstrated in many other emerging negative electrode materials. As such, there exists a wide range of nanostructured materials that provide a highly competitive landscape in terms of electrochemical performance in LIBs. Compared to these, MoS_2 stacks up well in terms of experimental reversible specific capacity, and values as high as 1290 mAh/g have been reported for nanostructured MoS_2-graphene composite electrodes.[46] While there are a few materials with higher theoretical capacity, such as certain nanostructured carbons, silicon[72], tin[73,74], and tin dioxide (SnO_2)[75,76], MoS_2 is advantageous in terms of rate capability and capacity retention, as well as cost (e.g. sub-micron MoS_2 powder retails for dollars/kg).

Nanostructured carbons show significantly higher lithium storage capacity than bulk graphite, especially at high current densities.[77,78] Single-walled carbon nanotubes exhibit a range of capacities between 400-460 mAh/g, while multi-walled carbon nanotubes have a capacity of 340 mAh/g, similar to graphite (372 mAh/g).[79-81] Reversible capacities from 540-780 mAh/g have achieved for graphene, which can be further enhanced by forming mixtures with other carbon allotropes such as carbon nanotubes and fullerenes.[82-84] Furthermore, an impressive 800 mAh/g specific capacity was reported for oxidized graphene nanoribbons.[85] More recently, researchers often employ graphene as a nanocomposite additive with great positive effect.[86] However, the low packing

density of carbons, especially for the nanostructured variety limits their volumetric energy density, one of the most important parameters for portable applications.[77, 87] Also, the high surface area often leads to the excessive formation of solid electrolyte interphase (SEI) which results in large irreversible capacities and capacity fading.[77,88] In addition, most varieties of nanostructured carbons, such as graphene and carbon nanotubes, remain far too expensive for commercial electrode applications.

Among the other emerging anode materials, nanostructured metal oxides remain attractive in terms of capacity, though they generally fall short in their rate capability, significant overpotential, and capacity retention. For example, SnO_2 can exhibit a large specific capacity (~800 mAh/g) when coupled with carbon.[89] However, similar to what is found for most conversion oxides, poor cycling performance has impeded tin dioxide's usefulness. Cobalt oxide (Co_3O_4) is also promising owing to its large theoretical specific capacity (890 mAh/g).[90] However it too demonstrates poor cycling stability. There are some general exceptions to the rule that oxides cycle poorly, and have poor rate performance. Some notable cases are the insertion electrodes based on TiO_2 nanostructures.[91-94] However, the capacity of TiO_2 (250 mAh/g) is less than that of graphite. Molybdenum dioxide (MoO_2) graphene nanocomposites (there is some debate concerning whether these are conversion or insertion electrodes) have been reported to retain 675 mAh/g after 100 cycles.[95] Recently, an MoO_2 nanocomposite with multiwalled carbon nanotubes was reported to have a

reversible capacity of 1144 mAh/g after 200 cycles.[96] MoO_2 has also been successfully employed as a single component anode demonstrating a simple, low cost fabrication process.[97] Other materials, such as nickel oxide (NiO) also exhibit enhanced performance (1031 mAh/g after 40 cycles) when formed as a nanocomposite with graphene.[98-100]

Other materials which exhibit high capacities for lithium storage include silicon and sulfur compounds. Silicon nanoparticles in a composite with graphene, as well as aluminum coated silicon nanowires have been shown to exhibit large reversible capacities of 1866 mAh/g [101] and 3300 mAh/g [102] respectively. However the majority of silicon nanostructures are prone to rapid capacity degradation due to volumetric expansion upon lithium intercalation which pulverizes the electrode.[103-106] The samples in [102] suffered a 25% capacity degradation after 50 cycles. Tin disulfide (SnS_2) is also being considered as a replacement for the commercial graphite anode. SnS_2 nanoplates were shown to retain a capacity of 583 mAh/g after 30 cycles but did not survive for longer durations.[107,108] Elemental sulfur has long been recognized for its large theoretical specific capacity of 1675 mAh/g.[109] Unfortunately, lithium-sulfur batteries suffer from poor rate capability (due to poor electrical conductivity of sulfur) and dissolution of lithium-sulfur compounds. Promising efforts are underway to stabilize these compounds (usually with a carbon phase) and capacities as high as 455 mAh/g after 50 cycles at higher current densities have been reported.[110] These materials, as well as others are effectively summarized in recent reviews.[111-121]

Table 1 provides a summary of the electrochemical performance of various LIB electrode materials. From the comparison, we can see that MoS_2 is a highly competitive LIB material in terms of charge capacity, rate capability and cycle life. The main disadvantage of MoS_2 is the intermediate voltage of 2.0 V that prevents it from coupling well with other materials in a full cell. Reported voltages vs. Li/Li^+ are experimentally measured values.

Table 4-1: Summary of electrochemical performance data for various LIB electrode materials.[a]

Anode Materials	Theoretical Specific Capacity (mAh/g)	Voltage vs. Li/Li+	First Discharge Capacity (mAh/g)	First Charge Capacity (mAh/g)	Reversible Capacity after (W) cycles (mAh/g)	Coulombic Efficiency after (X) cycles (%)	Current Density	Reversible Capacity (mAh/g) after (Y) cycles at (Z) Current Density	Reference
MoS_2	*669-1675*	*2.0*	*1062*	*917*	*907 (50)*	*98* (50)*	*1 C*	*554 (20) (50 C)*	48
MoS_2-GNS	*669-1675*	*2.0*	*1300*	*2200*	*1290 (50)*	*99.2 (50)*	*100 mA/g*	*1050 (5) (1000 mA/g)*	46
MoO_2-MWCNT	840	1.6	2270	1243	1144 (200)	99 (200)	100 mA/g	408 (5) (1 A/g)	96
TiO_2	335	1.5	334	245	243 (30)	98.7 (30)	66 mA/g	6 (10) (6.67 A/g)	91
Co_3O_4	890	1.2	1285	1108	1004 (50)	98 (50)	50 mA/g	790 (5) (1 A/g)	90
Sn-C	994	0.6	490*	350*	510* (200)	99* (200)	0.8 C	200 (10) (5 C)	74
SnO_2-GNS	790	0.6	1875*	1120*	872 (200)	99.5 (200)	100 mA/g	519 (10) (2 A/g)	75,76
SiNW-Al	4200	0.5	3347	3105	1300 (100)	98.8 (100)	0.1 C	1300 (100) (0.1 C)	102
NiO-GNS	718	0.5	1600*	1056	1031 (40)	98 (40)	0.1 C	460* (5) (5 C)	98,99
Graphene	372-1116	0.5	945	650	460 (100)	99* (100)	1 C	460 (100) (1 C)	82-84
Graphite	372	0.3	320*	320*	240 (20)	99* (1)	50 mA/g	240 (20) (50 mA/g)	84
Li	3600	0.0	-	-	-	-	-	-	111
Cathode Materials									
$Li\ Ni_{0.5}Mn_{1.5}O_4$	331	4.6	311	367	294 (80)	99* (80)	0.3 C	245* (30) (7 C)	58
$LiCoO_2$	272	4.5	190	153	110* (14)	-	47 mA/g	110* (14) (47 mA/g)	62,63
Sulfur	1675	2.0	960	830*	650 (40)	95 (30)	0.2 C	350 (45) (1 C)	109

[a]* - Indicates a value estimated from a published graph

4.5 Structure and bonding of MoS_2

A considerable amount of work has been done to characterize the electronic, optical and physical properties of molybdenum disulfide.[122-145] It is known to be a polytypic material[125,127,130], and along with a myriad of higher order sulfides[125], three main structural polytypes of the material have been identified: 2H-MoS_2, 3R-MoS_2, and 1T-MoS_2. Figure 4-1 shows idealized molecular models of these structures, as well as their lithiated counterparts. Figures 4-1a and 4-1b show the neat and the lithiated 2H-MoS_2 structures, with a 5% lattice expansion in the c-direction and a-direction due to lithium intercalation. Figure 4-1c shows the lithiated 1T-MoS_2, with the lithium ions occupying octahedral interstices. Figure 4-1d shows 3R-MoS_2 while Figure 4-1e shows Li_2S, which will be pertinent when discussing the lithiation-cycled structures. Of these, the 2H and 3R polytypes have been found to be naturally occurring (the 2H is found in much higher quantities) and thus their structures are very well characterized.[124] The 1T polytype is a synthetic material, and as a result, there is some disagreement in open literature regarding its structure. The 2H and 3R polytypes exhibit stacking sequences of ABA, and ABC respectively, with the molybdenum cations having trigonal prismatic coordination.[123,142] Figure 4-1a shows the stable 2H structure (space group P63/mmc), with lattice parameters of a = 3.16 Å, c = 12.29 Å and Wyckoff positions of molybdenum and sulfur atoms being: 2 Mo at ±(⅓,⅔,¼) and 4 S at ±(⅓,⅔,z and ⅓,⅔,½-z) with z = 0.621.[122,130] Figure 4-1d shows the 3R structure which is of the R3m space group, with lattice parameters of a = 3.16 Å

and c = 18.37 Å.[131] Here, Wyckoff positions of molybdenum and sulfur were reported as Mo at (⅔,⅓,0), and S at (0,0, ±z) with z = (⅔ x 0.127).[131]

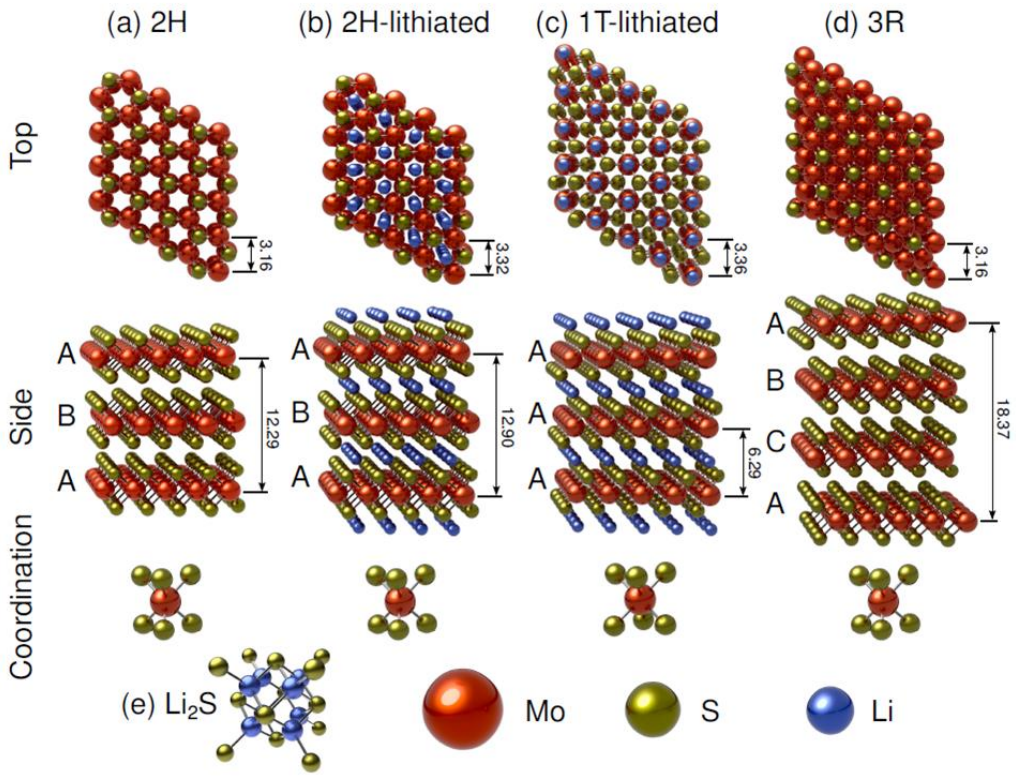

Figure 4-1: Molecular models of (a) 2H-MoS_2. (b) Lithiated 2H-MoS_2 showing a 5% lattice expansion in the c-direction and a-direction due to intercalation. (c) Lithiated 1T-MoS_2 showing lithium ions occupying octahedral interstices. (d) 3R-MoS_2 (e) Li_2S (domains of this phase would be interspersed with molybdenum nanoparticles). Dimensions are shown in Angstroms.

While theory predicts the trigonal (1T) polytype of MoS_2, its unstable nature has made it difficult to characterize.[126,127,130] In literature pertaining to lithium ion batteries, the 1T polytype is only observed after lithiation. We employed the crystallographic data from the study by Py and Haering to construct Figure 4-1c.[146] The lattice parameters for the 1T polytype are reported as a = 3.36

Å and c = 6.29 Å.[146] The model in Figure 4-1c was constructed using the space group P1, a = b = 3.36 Å, c = 6.29 Å, α = β = 90°, γ = 120°, with Wyckoff positions of Li at (0,0,½), Mo at (0,0,0) and S at (⅓,⅔,¾) and (⅔,⅓,¼).

As a layered transition metal dichalcogenide the electrical, optical, and physical properties of MoS_2 are extremely anisotropic.[123] Electrical and thermal conductivities are orders of magnitude smaller in the direction perpendicular to the basal plane, and thermal expansion is an order of magnitude greater.[123] The layered hexagonal crystal structure is formed by strong Mo-S covalent bonds in the layers, and weak van der Waals forces between S-Mo-S layers.[122,129] The van der Waals gap has been measured at approximately 3.49 Å via XRD.[123,130,143] Within the S-Mo-S layers, the intermediate difference in electronegativities between sulfur and molybdenum lead to covalent bonds that are partially polarized. The molybdenum cations give up (primarily d-band) valence electrons to the sulfur anions and are left in an oxidation state of (4+) while the oxidation state of the sulfur anions becomes (2-).[123] However, within the layer, each molybdenum atom is coordinated with six sulfur atoms while each sulfur atom becomes coordinated with three molybdenum atoms to give the hexagonal unit cell of 2H-MoS_2, as shown in Figure 4-1a. Looking in the direction perpendicular to the basal plane, the molybdenum and sulfur atoms are arranged in hexagonal sheets.[123]

The trigonal prismatic coordination of the molybdenum atoms gives rise to six equivalent cylindrical bond functions. These are a combination of the 4d, 5s, and 5p orbitals.[129,133,134,143] This type of orbital combination has been described as d^4sp hybridization by the work of Pauling[147] and Hultgren.[148] On the molybdenum atom, four valence electrons primarily from the 4d orbital are responsible for the bonding to the sulfur atoms, and the remaining two valence electrons of molybdenum reside in non-bonding orbitals. Each sulfur atom achieves coordination to three molybdenum atoms via hybridization of 3p and 3d orbitals. The van der Waals bonding between S-Mo-S sandwiches is a result of the interaction between saturated sulfur 3s subshells, which extend perpendicular to the basal plane.[123,129] The weak inter-layer van der Waals bonding allows for expansion of the bulk structure in the c-direction upon intercalation.

4.6 Lithiation mechanism of MoS_2

4.6.1 Lithiation of MoS_2 from 3.0 to 1.1 V

Intercalation of lithium into MoS_2 is known to occur within the voltage range of 3-0 V with a significant change in lithiation mechanism occurring below approximately 1.1 V versus Li/Li^+. In the range of 3 through 1.1 V, lithium ion insertion is fully reversible which is shown as reaction 4-1 and idealized in Figure 4-1b. A qualitative schematic of the charge/discharge process for MoS_2 half cells is shown in Appendix B. This sequence, which is well agreed upon in literature, is commonly observed up to the voltage plateau occurring at approximately 1.1 V during initial discharge. Here, x is in the range of $0 \leq x \leq 1$.

$$MoS_2 + xLi^+ + xe^- \rightarrow Li_xMoS_2 \quad (\sim 1.1 \text{ V vs. } Li/Li^+) \qquad \text{Eq. 4-1}$$

The theoretical specific charge capacity of this reaction is 167 mAh/g, corresponding to the intercalation of one lithium ion per molybdenum atom.[146] At voltages below this plateau there appears to be one or several disproportionation reactions as well as the presence of intermediate metastable sulfide species. These reactions have been suspected since early work on Li-MoS_2 was conducted[36], and were partially clarified in the late 1980's when Selwyn *et al.*[149] published seminal work on the decomposition of molybdenum and tungsten dichalcogenides during lithiation. The exact potential onset as well as the nature of these reactions have only recently been elucidated, and are still not fully understood. These will be discussed in the next section of the review.

Since then, lithium intercalation into molybdenum disulfide has been studied in detail by various groups.[53,142,150-154] More recent work has also been instrumental in the understanding of the complex mechanisms involved in lithium intercalation into molybdenum disulfide host lattices.[155-159] Various methods were employed to study the insertion of lithium into molybdenum disulfide. These include physical vapor deposition (PVD) of lithium onto cleaved MoS_2 in high vacuum[150], liquid phase intercalation by immersion of MoS_2 in n-butyl lithium (C_4H_9Li)[40,42,156,157], and intercalation via electrochemical methods.[36-43,55,151,158] Intercalated samples were characterized via X-ray diffraction (XRD),

X-ray photoelectron spectroscopy (XPS), nuclear magnetic resonance (NMR), transmission electron microscopy (TEM), and scanning electron microscopy (SEM).

Below approximately $x = 1$, intercalation of lithium into molybdenum disulfide is commonly described as an ion/electron transfer topotactic reaction producing a metallic paramagnetic product.[36,38,155] For lithium atoms, the occupied valence electron states have a higher energy than the unoccupied conduction band states of the molybdenum cations in MoS_2 (primarily the 4d bands), and so electron transfer results upon intercalation.[155] The weak van der Waals forces that hold the S-Mo-S layers together in 2H-MoS_2 allow for the insertion of lithium between them. As intercalation proceeds, lithium diffuses between the MoS_2 planes and occupies vacant octahedral interstices in the hexagonal crystal lattice as shown in Figure 4-1b. It has been suggested that the diffusion of lithium ions involves tetragonal interstices in the van der Waals gap, alluding to the fact that these ions are fast diffusers.[36,39,43,153,160] The occupation of tetragonal interstices is however, less likely, since the energy to occupy a tetrahedral site is larger. Alkali ion conductivity in transition metal sulfides is due to a number of factors.[43] First, there is a high concentration of potential charge carriers. Second, there is a high concentration of vacancies and interstitial sites, and third, the activation energy for ionic hopping to adjacent sites is relatively low (on the order of the formation enthalpy for the ternary compound Li_xMX_2).[43] Diffusion of lithium ions takes place primarily in two-dimensional intercalation

planes in the van der Waals gap.[41] For Li^+ ions in MoS_2 this occurs primarily between octahedral interstices parallel to the basal plane.[161]

Below approximately $x = 0.1$, intercalation proceeds into the 2H-MoS_2 lattice with little disruption. The host lattice supplies intercalation sites and redox centers, but otherwise assumes a passive role in the reaction. As the lithium concentration increases in the 2H-MoS_2 lattice, the addition of 1 or more electrons to the host phase, creating $[MoS_2]^-$, leads to the formation of a distorted octahedral environment for the metal cations, which experience substantial alterations in electronic band structure and electrochemical potentials.[38-40,142] Researchers have commonly observed a lithium superlattice forming in the van der Waals gap as the lithium concentration rises in the range of approximately $0.1 \leq x \leq 1$.[157,160-164] This superlattice, described as $2a_o x 2a_o$, is an ordering of lithium ions in the van der Waals gap, which occupy octahedral and then tetrahedral interstices above the saturation limit. This effects a phase change in which the coordination of the molybdenum atoms shifts from trigonal prismatic in the 2H phase, to octahedral in the 1T phase. This phase change is associated with the voltage plateau that is commonly observed around 1.1 V vs. Li/Li^+ in galvanostatic cycling. The mechanism of this phase change, as explained by the work of Py and Haering[146], is described as a glide process between the molybdenum and sulfur planes. A similar process has been observed in the lithiation of graphitic carbons.[165] Mulhern[166] has gone on to demonstrate that the resulting intercalated phase of MoS_2 is highly distorted, and undergoes

appreciable lattice expansion. Intercalation-induced lattice strain in the basal plane causes the formation of dislocations, which fragment the lattice and may create diffusion pathways for lithium ions, allowing them to penetrate further into the host material.[160] Furthermore, this fragmentation may lead in part to the disproportionation reaction associated with the formation of lithium sulfide (Li_2S) and molybdenum metal particles that will be outlined in the next section.

An examination of 2H-MoS_2 octahedral site radius and lithium ionic radius indicates that the two are approximately 0.7 Å.[167] Here we consider that the van der Waals gap in 2H-MoS_2 is approximately 3.49 Å and the sulfur atom covalent radius is 1.04 Å.[167] Therefore, it can be inferred that lithium intercalation should proceed into molybdenum disulfide without any appreciable change in host lattice parameters. However experimentally we know this is not the case. XRD studies of intercalated MoS_2 indicate that there is an approximate 4-6% lengthening of the c-axis and a-axis in the hexagonal unit cell upon intercalation with lithium ions as shown in Figures 4-1b and 4-1c.[36,38,146,160] While it is true that a portion of this expansion in the c-direction is attributed to the co-intercalation of solvent molecules (most of the intercalation studies are done using n-butyl lithium solutions in hexane), there is still appreciable expansion that results from lithium ion insertion.

Nuclear magnetic resonance studies have shown that lithium atoms can vary in size based on their ionic character (having a fully ionized radius of

approximately 0.7 Å and a neutral radius of approximately 1.4 Å).[40] It is thought that the ionicity of the lithium decreases, as its concentration in the host lattice rises.[38,40] Therefore, the ionicity will have an effect on the lattice strain being exerted by the lithium ions. The first lithium atoms to intercalate each donate an electron to the empty 4d band of the molybdenum cations and are thus stored in a completely ionized state. However, it has been shown that as the lithium ion concentration increases, their ionicity decreases, and the ions themselves are thought to undergo a slight increase in ionic radius. This brings about an expansion of the lattice in the c-direction.[36-39,146] In MoS_2, lattice expansion in the a-direction is partially attributed to alterations in the electronic band structure of the host as intercalation continues.[150] It is known that the transition metal dichalcogenides have strong overlap-covalency interactions between the metal d-bands, and the chalcogen s-p bands.[143] Therefore, as intercalation continues, the sulfur atoms in MoS_2 experience a slight increase in atomic radius as the electron density in the host lattice rises.[40,143] These affects, along with solvent co-intercalation, are the likely source of the observed increase in the lattice parameters of MoS_2 during intercalation (Figure 4-1b).

4.6.2 Lithiation of MoS_2 from 1.1 to 0 V

More recently, an increasing number of authors are validating the existence of one, or a series of decomposition reactions when MoS_2 cells are discharged below 1.1 V vs. Li/Li^+.[46,168-182] Furthermore, since these decomposition reactions all yield a lithium sulfide product, an examination of some of the more prevalent

lithium sulfur (Li-S) battery literature provides us with some clarification of the reaction mechanisms. For this system the formation of polysulfides and the sulfide shuttling effect are well characterized.[183-193] For the more "bulk-like" structures of MoS_2, significant voltage plateaus are observed upon the first discharge at approximately 1.1 and 0.6 V vs. Li/Li^+, although the exact values vary by study.[46,168 -182]

For the case of truly nanoscale structures the five issues that arise when interpreting or even comparing the charging profiles are: First, the morphology of the nanostructured MoS_2 electrodes deviates significantly from bulk, for example possessing much larger interlayer spacing and surface area to volume ratio, and/or a much higher defect density.[168,180,181,194-198] For the case of interlayer spacing, it has been shown that MoS_2 nanostructures with a wider spacing resulted in enhancements in electrochemical performance in terms of the initial lithiation kinetics and the charge storage capacity.[168,177,180-182] Here, the effect is attributed to the increased volume associated with the layer expansion leading to faster ionic diffusion and better material utilization during the initial lithiation. The effect of enhanced lithium storage in a wider van der Waals gap has also been conclusively demonstrated with graphene.[82,84,101, 199] The increased surface area effect is expected to remain influential during the life of the material. However, effects due to the non-equilibrium spacing of the basal planes in MoS_2 or high defect content will become unimportant after the structure irreversibly decomposes to molybdenum and Li_2S.

Interestingly, an examination of literature pertaining to MoS_2 nanostructures as hydrodesulfurization (HDS) catalysts leads to some useful information regarding point defects in the material.[200-204] The structure of HDS catalysts must be well characterized, as it is usually defect sites on the crystal that lead to the bonding of the sulfur functional group (or sulfur-containing groups) in organic compounds. Using techniques such as scanning tunneling microscopy (STM), the morphology of these MoS_2 nanostructures (such as nanosheets and fullerenes) have been meticulously characterized by these researchers. In the nanostructures, they see a much higher defect density in the form of vacancies (mainly sulfur edge vacancies) that lead to sub-coordinated molybdenum centers, and have concluded that they exhibit increased reactivity due to the presence of dangling bonds. It seems plausible that these same sites could act as adsorption sites for lithium ions, and may help to explain the elevated lithium storage capacities that are so often observed in the MoS_2 nanostructures during the first cycle.[157] Also, the presence or creation of point defects along the sulfur basal plane may serve as nucleation points for the formation of the lithium superlattice that has been observed to develop in the van der Waals gap.[157,160,162,164] Researchers are therefore encouraged to attempt atomic force microscopy and STM studies on lithiated MoS_2 samples to observe lithiation patterns, similar to what was done by Kalinin *et al*.[205]

Second, the structures often contain significant amounts of carbon-based phases, which are electrochemically active towards lithium.[170,172,174,181,182] For example Archer *et al*.[172] describe a system with 22 wt.% carbon that had the best electrochemical performance. In many studies, the authors employ carbon nanostructures that possess charge storage capacities well in excess of graphite's 372 mAh/g.[77,78,82-85] Materials like multilayer "graphene", highly graphitic nanoparticles, or carbon nanotubes bind lithium via adsorption, pore filling, and intercalation, routinely yielding capacities as high as 650 mAh/g. Were the carbons to also contain substantial amounts of nitrogen heteroatoms, reversible capacities as high as 1780 mAh/g are possible.[88,206] In the authors' opinion the coaptation of an active material with carbons goes a long way towards accounting for the tremendously enhanced capacity of the nanocomposites, since in general this contribution is neglected in the calculations.

Third, in nanoscale materials, the formation of an SEI layer (commonly described as a gel-like polymeric layer) can also have a significant contribution to the overall voltage profile.[170] Such capacity contribution is of course detrimental, resulting in poor coulombic efficiency of the electrodes. Fourth, it is likely that similar to the lithium-sulfur battery, full charging-discharging for the Li-MoS_2 system involves intermediate "molecular" polysulfides. For the Li-S system these reactions are well characterized[183-193], however their exact nature remains to be elucidated in the Li-MoS_2 system.[177-182] Fifth, it is therefore plausible that the surfaces of molybdenum nanoparticles present after full discharge have dangling

bonds that will attract and immobilize polysulfides, and could serve as adsorption sites for lithium ions in subsequent cycles. As a corollary, sub-coordinated molybdenum centers have been shown to have a high affinity for sulfur-containing molecules.[200] However molybdenum metal nanoparticles are generally X-ray amorphous and are thus difficult to track during the lithiation studies.[181]

The lower voltage plateau evident upon first discharge, occurring at approximately 0.6 V vs. Li/Li^+, has been attributed to either the reversible conversion reaction of MoS_2 to Li_2S and metallic molybdenum through reactions 4-1 and then 4-2[46,168-176], or the irreversible decomposition with the same redox chemistry, followed by cycling between Li_2S (Figure 4-1e) and elemental sulfur (reaction 4-3).[177-182] The theoretical specific charge capacity of reaction 4-1 is 167 mAh/g, while the theoretical capacity of MoS_2 lithiating by reactions 4-1 and then by 4-2 (i.e. full discharge) is 669 mAh/g.

$$Li_xMoS_2 + (4-x)Li^+ + (4-x)e^- \rightarrow Mo + 2Li_2S \ (\sim 0.6 \text{ V vs. } Li/Li^+) \qquad \text{Eq. 4-2}$$

The reaction of elemental sulfur and lithium may be described by reaction 4-3, which yields a theoretical capacity of 1675 mAh/g if the weight of the molybdenum is *not* taken into account.

$$S + 2Li^+ + 2e^- \rightarrow Li_2S \ (\sim 2.2 \text{ V vs. } Li/Li^+) \qquad \text{Eq. 4-3}$$

Though the majority of open literature favors the reversible conversion reaction sequence, recent detailed XRD studies indicated that upon delithiation, MoS_2 was no longer detectable.[177-181] This may be due to an amorphization of the electrode materials. However since both the 1.1 and the 0.6 V plateaus are observed only during the first lithiation, we believe that the irreversible decomposition of MoS_2 is more likely. At room temperature solid-state sulfidation reactions are quite sluggish, so it is unlikely that MoS_2 would re-form especially at higher charging rates. This conclusion is also based on a recent TEM study of post-cycled MoS_2 electrodes (Figure S8 in their Supplemental section).[182] The authors conclusively detected metallic molybdenum in the delithiated state. One difficulty in characterizing the cycle 1 discharge plateaus for the MoS_2 half-cell (vs. Li/Li^+) is that the plateau at 0.6 V is difficult to distinguish from the one attributed to SEI formation. Unfortunately, the formation of an SEI layer occurs in most battery anodes during the first discharge cycle around 0.6 V. In fact it may be very difficult to separate the two processes for high surface area electrodes where substantial capacity is lost due to SEI formation, while the initial lithiation reaction irreversibly alters the lithium active phases. However extensive microstructural evidence, discussed in this manuscript, supports the formation of metallic molybdenum during discharge cycle 1. Moreover low surface area "bulk" MoS_2, where the total irreversible capacity due to SEI should be relatively low, clearly demonstrates the 0.6 V plateau (as seen by the CV peak at ~0.6 V in Figure 4-2a).[170]

The irreversibility of the MoS_2 decomposition reaction upon initial discharge is further supported by the trends observed in cyclic voltammetry (CV). Figures 4-2a[170] and 4-2d[179] highlight CV curves for commercial MoS_2 powders in different voltage ranges (scan rates 0.5 and 0.05 mV/s respectively). Figure 4-2b[170] shows a typical CV curve for an MoS_2/graphene nanocomposite (scan rate 0.5 mV/s). Figure 4-2c[172] is a CV curve for an amorphous carbon-MoS_2 nanocomposite (scan rate 0.2 mV/s). Figure 4-2e[207] is a CV curve for a typical lithium-sulfur redox couple, shown for comparison (scan rate 0.05 mV/s). In Figure 4-2e, the two cathodic peaks at ~2.3 and ~2.1 V are attributed to the stepwise reduction of sulfur to Li_2S. The first step (~2.3 V) involves the reduction of sulfur to intermediate lithium polysulfides (Li_2S_n, $2<n<8$) and the second step (~2.1 V) is attributed to the reduction of higher order polysulfides to Li_2S.[109,118] The dominant oxidation peak at 2.4 V is recognized as the conversion of all lithium polysulfides to S_8^{2-} accomplished by facile charge transfer kinetics.[109] This CV plot also demonstrates the excellent reversibility of the lithium-sulfur redox couple.

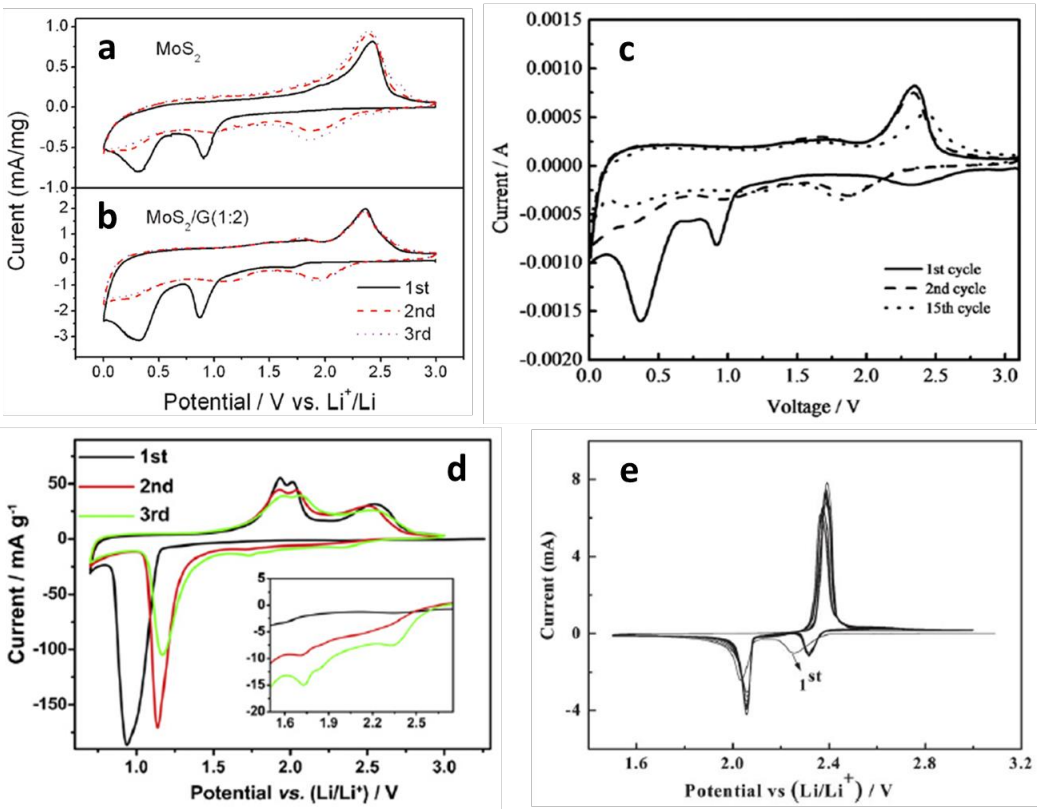

Figure 4-2: Cyclic voltammograms for (a) MoS_2 powder.[170] (b) MoS_2-graphene nanocomposite (scan rate 0.5 mV/s).[170] (Copyright 2011 American Chemical Society) (c) MoS_2-amorphous carbon nanocomposite (scan rate 0.2 mV/s).[172] (d) Commercial MoS_2 powder in a smaller voltage window (scan rate 0.05 mV/s).[179] (Copyright 2012 Elsevier Ltd.). (e) Sulfur (scan rate 0.05 V).[207] Adapted from Refs. 170 (DOI: 10.1021/nn200659w), 172 (DOI: 10.1039/c2jm32468g), 179 (DOI: 10.1016/j.electacta.2012.07.020), and 207 (DOI: 10.1039/c2jm15041g) with permission.

Figures 4-2a - 4-2c show similar trends in all cathodic and anodic sweeps. In the first cathodic sweep, peaks at approximately 1.0 V are observed on all plots and attributed to the formation of Li_xMoS_2 and the resulting 2H to 1T phase transition.[170,177] This peak is also observed in 2d, although here, the authors only discharge to 0.8 V in an attempt to investigate the reversibility of reaction [1] in this voltage range. The large cathodic peak at approximately 0.4 V (Figures 4-2a - 4-2c) is attributed to the conversion reaction of MoS_2 to Li_2S and molybdenum

(reaction [2]). The irreversibility of this reaction is supported by the disappearance of these peaks in subsequent reduction cycles. Instead, a dominant cathodic peak at approximately 2.0 V (consistent with 4-2e) is observed in Figures 4-2a - 4-2c, while the peaks at 1.0 V and 0.4 V previously discussed are greatly diminished in subsequent cycles. The dominant cathodic peak forming at ~2.0 V is well known in lithium-sulfur battery systems and is attributed to the formation of Li_2S.[109,186,188,208] Upon recharging, Figures 4-2a - 4-2c show two anodic peaks (one shallow peak at ~1.7 V and a large peak at ~2.4 V). The first shallow anodic peak is likely due to the delithiation of residual Li_xMoS_2 which has not undergone conversion. The dominant anodic peak at ~2.4 V is due to the conversion of Li_2S to S_8^{2-} consistent with Figures 4-2d and 4-2e.[110,187,208-210]

The material in Figure 4-2d[179] was discharged too deeply to demonstrate full reversibility of reaction 4-1. However by initiating it in a stepwise manner the MoS_2 conversion reaction was successfully observed. This is similar to the results obtained by Py and Haering[146], where the formation of Li_xMoS_2 was conclusively identified with the long voltage plateau at 1.1 V. In Figure 4-2d, the first discharge to 0.8 V[179] allowed the conversion of MoS_2 to Li_2S and molybdenum metal, but not completely. The first anodic sweep reveals the delithiation of Li_xMoS_2 (the doublet centered at 2.0 V) as well as a large broad peak at ~2.5 V, which is attributed to the formation of sulfur (similar to Figure 4-2e). With subsequent cycling the anodic doublet centered around 2.0 V and the dominant cathodic peak at around 1.0 V both get weaker. This indicates the

consumption of the active materials initially present, i.e. Li_xMoS_2 and MoS_2. Such cycling induced degradation has also been observed in other studies[172,178] and attests to the instability of the Li_xMoS_2 compound, and its tendency to decompose at higher values of x. By the third cycle, two small cathodic peaks at 1.75 and 2.34 V appear (shown inset in Figure 2d), which are likely due to the reduction of higher order lithium polysulfides.[109] Based upon the trends observed in literature, the pertinent redox reaction after first discharge involves lithium and sulfur as the electro-active species (reaction 4-3).

Figure 4-3 presents recent XRD data that further supports the argument regarding a lithiation sequence that involves the irreversible formation of molybdenum.[172,177] Figure 4-3a shows an XRD scan of an MoS_2 electrode in the as-received state (bottom) and after it was discharged to 0.01 V (top).[172] The as-received material is clearly 2H-MoS_2, while the discharged material is Li_2S and molybdenum metal. Figure 4-3b shows an XRD pattern of a commercial MoS_2 powder after the first discharge to 0.01 V.[177] Again, there is strong evidence that Li_2S and molybdenum are the dominant phases. Figure 4-3c shows the Li_2S + molybdenum composite (material analyzed in Figure 3b) after it was recharged to 3.0 V. While there is substantial peak broadening due to partial amorphization and/or nanocrystallization, elemental sulfur and molybdenum metal are definitively present in the charged state. This also indicates that the material was not fully lithiated, consistent with it being a micro-scale powder rather than a nanocomposite. In-situ XRD studies of MoS_2 have been performed, though no

study has done this across the entire voltage range of 0.01 to 3 V.[146,179] The elucidation of the microstructural evolution in MoS_2 based electrodes during cycling would benefit greatly from an in-situ XRD study throughout the entire voltage range. XRD and FTIR have been used by others to track the lithiation of MoS_2, with the results being in agreement with the trends discussed here.[179,181]

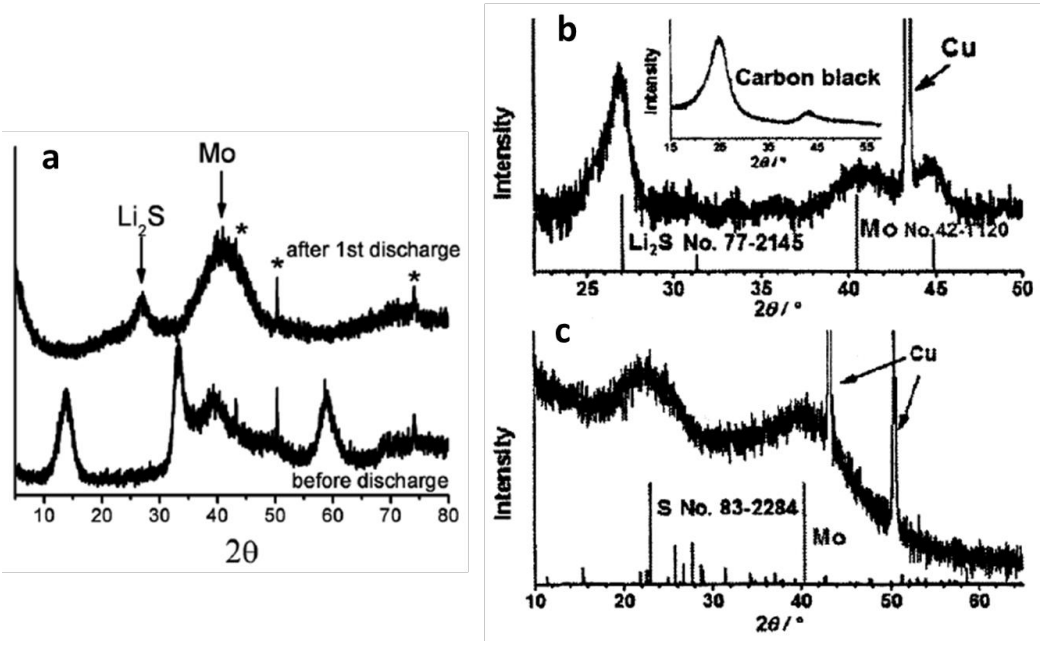

Figure 4-3: XRD scans of MoS_2 electrode at various states of charge. (a) (bottom) as received, and (top) after discharge to 0.01 V. Peaks marked by * are from the copper current collector.[172] (b) After discharge to 0.01 V.[177] (c) After recharge to 3.0 V.[177] (Copyright 2012 Wiley-VHC Verlag GmbH &Co, KGaA, Weinheim) Adapted from Refs. 172 (DOI: 10.1039/c2jm32468g), and 177 (DOI: 10.1002/asia.200100796) with permission.

It appears that after the first discharge, the molybdenum nanoparticles may have a multifunctional beneficial role: First, the particles serve to enhance the electrical conductivity of the Li_2S matrix, which partially alleviates the poor electrical conductivity concern associated with both the sulfur and Li_2S phases.

Second, the nanoparticles may serve as pinning sites for soluble polysulfides, preventing their dissolution, and thus mitigating the shuttling effect that causes electrochemical degradation of lithium-sulfur batteries. While the first effect is quite reasonable and should be expected were the MoS_2 to irreversibly decompose, the second effect is hypothetical and requires substantial experimental evidence before being considered a real benefit. Authors have argued that it may be the carbon that in fact pins the soluble polysulfide anions.[186,187,191]

The theoretical specific capacity of reaction 4-2 is 669 mAh/g while that of reaction 4-3 is 1675 mAh/g. Therefore reaction 4-2 does not fully explain the enhanced specific capacities well in excess of 700 mAh/g that are commonly observed in the Li-MoS_2 system.[46,169-182] While reaction 4-3 is quite likely, it can only follow reaction 4-2, which means the mass of molybdenum must also be taken into account. Therefore in the authors' opinion, reactions 4-2 and 4-3 do not fully capture the complexity of the charging/discharging process in the MoS_2-based system. We believe that there are three additional, and by no means mutually exclusive, contributions to the net charge storage: First, nanostructured molybdenum particles may also participate to some extent in the lithiation reaction, serving as physical adsorption sites for the Li^+ ions. Bulk molybdenum is inactive towards lithiation, so any binding would have to be at or near the surface.[211] Reports in literature are consistent in showing a much higher capacity for materials that are nanoscale rather than their bulk

counterparts.[170,174,180,181,185,212-214] Researchers have characterized these effects well for a variety of transition metal nanoparticles formed from oxide conversion electrodes.[215-218] These authors comment on the various charge storage mechanisms in conversion electrodes and allude to enhancements from capacitive effects brought about by the high surface area metallic nanoparticles. Authors also point out that there may be a contribution to the reversible capacity from the polymeric SEI layer that forms around the metallic nanoparticles.[215] However in our opinion such reactions would be either fully irreversible or very poorly reversible, and would only adversely affect the coulombic efficiency without boosting the reversible capacity. Another possibility is that more than two lithium ions react per sulfur atom in reaction 4-3. We believe that this is unlikely since no analogue has been reported for the well-characterized Li-S system.

The present authors believe that much of the capacity enhancement beyond 669 mAh/g is largely due to the presence of a nanostructured carbon phase whose contribution to the total electrode capacity is either underappreciated or perhaps not accounted for at all. As was discussed previously, many of the carbon allotropes interspersed with MoS_2 possess quite a high lithium storage capability that well-exceeds that of carbon black and even that of graphite. There is also a likely synergy between the two nanodispersed phases that cannot be captured by a standard rule of mixtures calculation even when the capacity of each phase is obtained separately. The enhancement of lithium capacity by carbon phases is routinely demonstrated in MoS_2 and Li-S literature, though the exact mechanism

remains unclear.[46,169,170,172,180-182,185,187,193] Further evidence supporting the electrochemical decomposition of MoS_2 to molybdenum metal and Li_2S upon lithiation is shown in Appendix B.

4.7 MoS_2 nanocomposites in LIBs

With the development of nanostructured materials, there is a resurgence of synthesis research directed at creating MoS_2-based nanocomposite structures for lithium ion battery applications. The effort is primarily directed at utilizing MoS_2 as an anode material to be used against a pre-lithiated cathode. A particle size refinement of MoS_2 down to the nanoscale greatly shortens the lithium ion diffusion distances, providing a substantial boost in the rate-dependent capacity retention as compared to the more "micro" MoS_2 counterparts.[44,46,159,172,174,180,182] In addition, it is consistently demonstrated that it is the hybrid MoS_2-carbon systems, in particular the ones with nanoscale structure, that offer the optimum combination of energy density, cycling stability, and high rate capability.[190,219-229]

There are several microstructural scenarios during the conversion reaction, where nanostructured carbon would enhance electrode performance. These include one or a combination of a) carbon acting as a binder between the S/Li_2S and the molybdenum nanoparticles; b) carbon encapsulating both phases providing an electrically conductive path down the current collector; c) carbon acting as a "skeleton" which provides both an electrically conductive pathway down to the current collector and prevents material agglomeration during cycling.

The possibility of a) vs. b) vs. c) would also depend on the type of carbon added. It is intuitive that crystalline/particulate phases like carbon nanotubes or graphene nanoflakes would be more effective in providing a skeleton, while materials like amorphous carbon would be more effective as coatings and/or binder. At this point in the case of MoS_2 there is not enough microstructural evidence to conclusively identify such enhancement mechanisms. There exists a wide range of techniques by which to synthesize electrode-grade molybdenum disulfide of various morphologies. Among these, hydrothermal, assisted hydrothermal, solvothermal, and template assisted techniques are the most successfully employed and will be presently discussed.

4.7.1 MoS_2 nanostructures by hydrothermal techniques

A significant portion of the recent published work uses carbon-templated hydrothermal synthesis to create nanocomposite structures of MoS_2 dispersed in a conductive matrix such as graphene, carbon nanotubes (CNTs) or amorphous carbon. The key advantage of hydrothermal methods is that they may be employed to create commercial or near commercial mass loadings (~10 mg/cm^2) on the electrodes.[230] Electrically conducting multiwalled carbon nanotubes, possessing large open specific surface areas and excellent chemical and thermal stabilities, are perhaps the most widely employed nanometer-sized templates.[190,219-224] Graphene is also becoming a popular choice of support, progressively gaining greater scientific attention as compared to CNTs.[225-229] The rationale for this stems from a real cost and scalability advantage of wet methods

used to synthesize graphene/graphene oxide versus chemical vapor deposition generally employed to fabricate CNTs.[231-233]

It is well known that, similar to graphene, exfoliated MoS_2 often exists in the form of nanosheets due to its layered structure. The presence of 2D graphene sheets in the hydrothermal process could further guide the formation of MoS_2 sheets and generate a sheet-on-sheet structure. Despite common literature claims of such structures possessing a long-term benefit (i.e. over numerous charge/discharge cycles), there is little microstructural or electrochemical evidence that suggests they survive past the initial lithiation step. Nevertheless the increased interfacial contact between carbon and Mo/S would promote cycling stability by reducing the rates of material aggregation. Graphene, CNTs and related materials are known to template the growth of various sulfides and oxides from solution, resulting in orders of magnitude reduction in particle sizes as compared to the non-templated baselines.[228,234] Since such nanocarbons are very effective in refining the as-synthesized microstructure and hence shortening the lithium diffusion distances, they substantially improve the rate dependent capacity retention. It has also been suggested that during cycling, the electrochemically active surface area of these electrodes can increase due to a gradual breakdown of the graphene and resulting introduction of defect sites.[228] These sites serve to trap more lithium ions during intercalation and could explain the gradual increase in specific capacity that is often observed. A highly interspersed carbon phase

would also substantially improve the electrical conductivity of the electrode down to the current collector, regardless of the lithium-active phases present.

By introducing graphene nanosheets into the hydrothermal synthesis process for MoS_2, authors were able to create a true nanocomposite.[46] Figures 4-4a and 4-4b highlight the resulting as-synthesized microstructure, which exhibits significantly improved electrochemical performance over the graphene-free baseline.[46] Figures 4-4c and 4-4d show the cycling results, demonstrating a stable reversible capacity of approximately 1290 mAh/g and an excellent rate capability. The capacity retention of this material was 99.2% after 50 cycles (current density 100 mA/g). This is among the best performance, in terms of capacity and cycling stability, reported in literature for an MoS_2-based anode. The graphene additive has significantly decreased the size of the MoS_2 nanosheets, which likely led to better material utilization during the conversion to Li_2S and molybdenum. Authors elaborated upon the synergistic behavior of MoS_2 and graphene, and provide a detailed investigation of the electronic and atomic structure of the nanocomposite.[235] The work provides evidence that the creation of a graphene-MoS_2 nanocomposite improves the overall electrical conductivity of the electrode. Furthermore, the authors discuss the weak van der Waals and electrostatic interactions of the two materials, which would allow for facile expansion at the graphene-MoS_2 interface during initial lithiation.[235] This may actually influence the subsequent cycling behavior in terms of allowing all the MoS_2 to be converted. In contrast, studies repeatedly show that for micro-scale MoS_2 much

of the material does not react with lithium during the first cycle or afterwards (capacities well below 669 mAh/g).

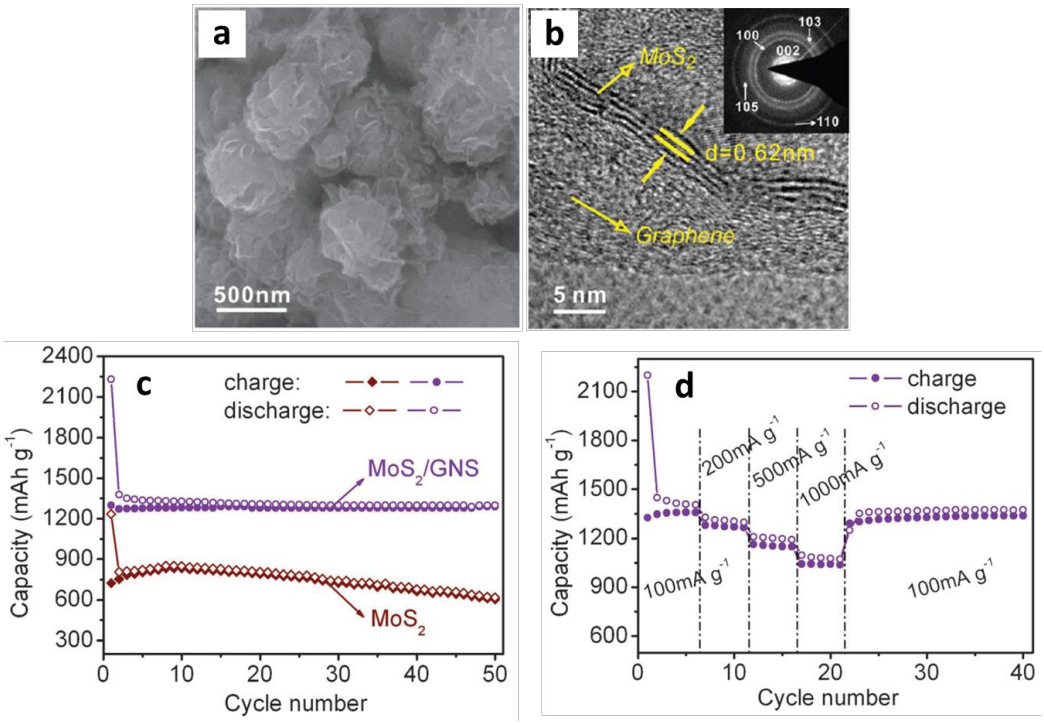

Figure 4-4: As-synthesized MoS_2-graphene nanocomposite. (a) and (b) SEM and TEM micrographs respectively. (c) Cycling behavior of the nanocomposite (with graphene-free MoS_2 as the baseline). (d) Cycling behaviour of MoS_2-graphene nanocomposite at various current densities. Adapted from Ref. 46 (DOI: 10.1039/c1cc10631g) with permission.

Amorphous carbons formed during the hydrothermal synthesis of MoS_2 can also increase the electrode performance. Authors prepared amorphous carbon-MoS_2 nanostructures via a hydrothermal/carbonization technique.[172] Figures 4-5a and 4-5b display SEM and TEM micrographs of the as-prepared MS-22 nanostructures (MoS_2 + 22 wt.% carbon). Figure 4-5c shows that the capacity retention of this composite had a very strong carbon loading dependence. At a

carbon loading of 22 wt.%, the stable capacity was approximately 875 mAh/g for over 100 cycles. The authors attributed this stability to the MoS_2 being fully coated with carbon, which allowed for full material utilization during electrochemical cycling. Moreover, the carbon coating may mitigate the SEI layer formation, though more evidence is needed for this hypothesis. Figure 4-5d shows capacity-voltage profiles for charging and discharging, which are typical of MoS_2-carbon composites. Here, the first discharge exhibits plateaus at approximately 1.1 and 0.6 V, indicative of the 2H to 1T MoS_2 (~1.1 V) phase transformation, and subsequent conversion to Li_2S and molybdenum metal (~0.6 V). These disappear in subsequent cycles, indicating that this reaction is irreversible. XRD scans from this material (shown in Figure 4-3a) suggested the presence of Li_2S and molybdenum metal after first discharge. Moreover, the discharge (~2.0 V) and charging (~2.3 V) voltage plateaus for the 100th cycle are indicative of the lithium-sulfur redox couple.[186,188,210]

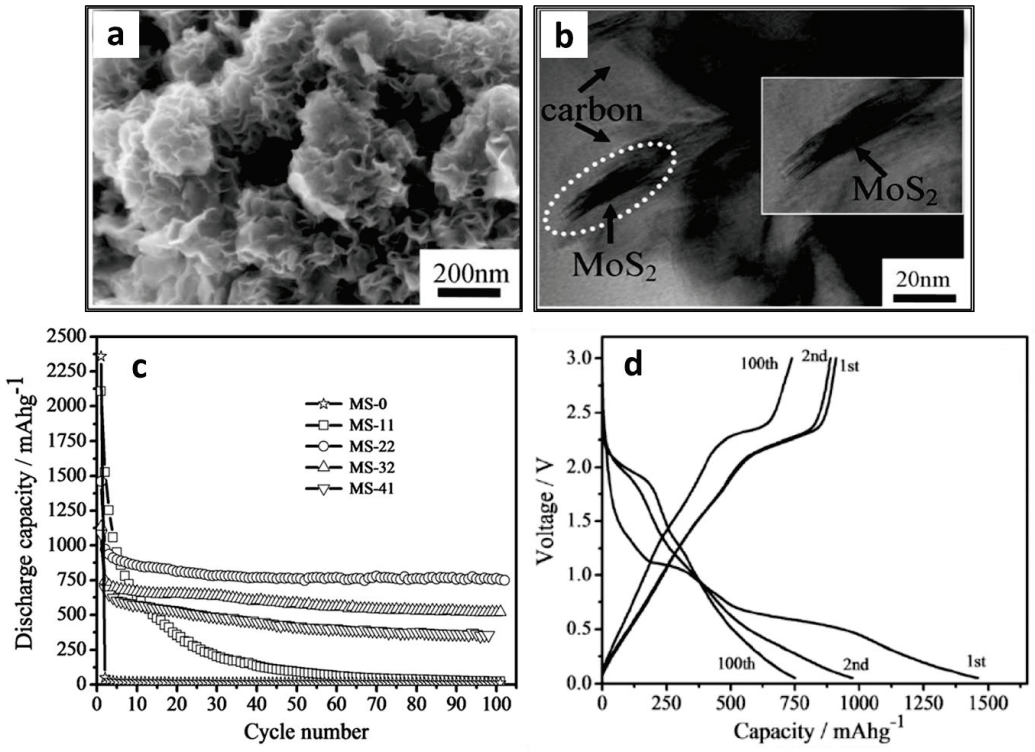

Figure 4-5: Hydrothermally synthesized MoS_2-amorphous carbon nanocomposite. (a) and (b) SEM and TEM micrographs of MS-22 (MoS_2 + 22wt.% C). (c) Cycling stability of pure MoS_2 and various MoS_2–carbon composites, MS-X stands for MoS_2 with X wt.% C. (d) Voltage capacity profiles for MS-22 (current density 100 mA/g). Adapted from Ref. 172 (DOI: 10.1039/c2jm32468g) with permission.

Researchers have employed polystyrene microspheres to tailor the dispersion and the microscopic assembly of MoS_2 nanosheets (MoS_2-NS).[174] Through a post hydrothermal synthesis annealing treatment in an inert atmosphere, the template polystyrene microspheres were decomposed. The resultant ultrathin MoS_2 nanosheet assemblies assumed microsphere morphologies with a wide spacing between the layers. This material had a BET surface area of 36 m^2/g, with a primarily mesoporous structure due to the stacking of the individual nanosheets. The hierarchical structure of the MoS_2-NS

microspheres was quite advantageous for battery applications: The high surface area of the nanosheets increased the overall charge storage capacity, while the void space buffered the volumetric changes allowing for facile lithiation/delithiation. Figures 4-6a and 4-6b show TEM micrographs of these resultant hierarchical structures.[174] Figures 4-6c and 4-6d show the cycling performance of the baseline MoS_2 flakes (I) and the MoS_2-NS microspheres (II) at a current density of 100 mA/g (4-6c) and at various current densities (4-6d). The MoS_2-NS microspheres consistently outperformed the baseline in terms of overall capacity, cycling capacity retention and rate capability, supporting the authors' argument regarding the essential role of polystyrene microsphere assisted synthesis.

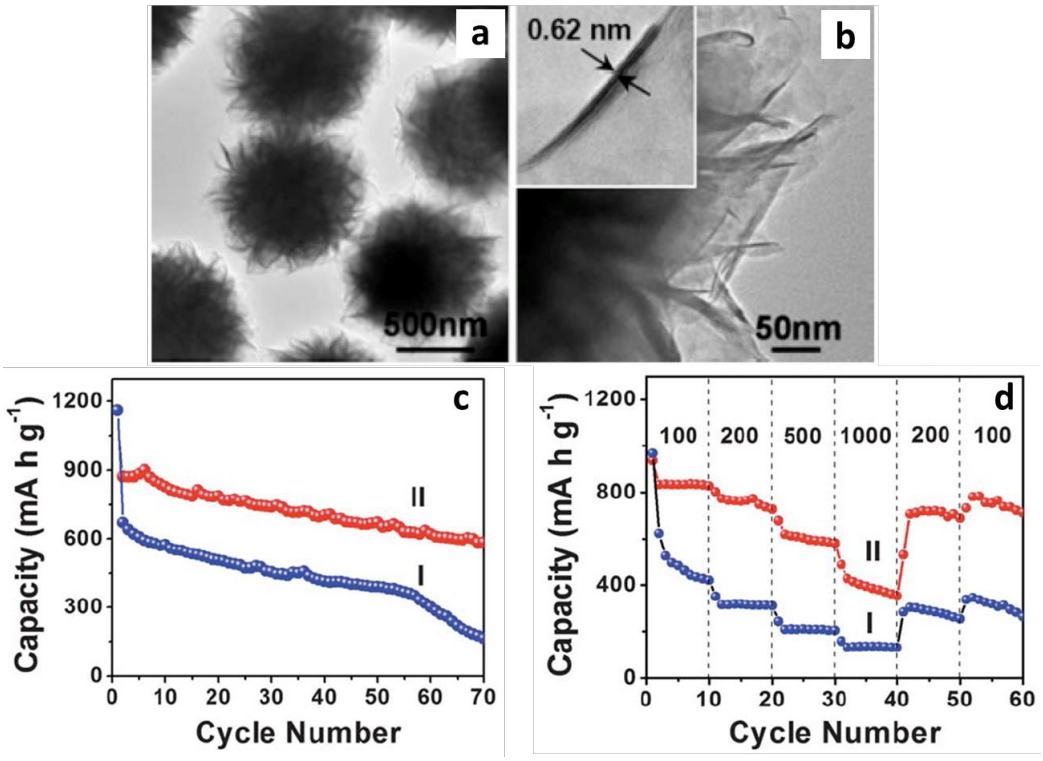

Figure 4-6: MoS_2-nanosheet microspheres. (a) TEM micrograph of as-synthesized MoS_2 nanosheet microspheres. (b) HRTEM image of several MoS_2 nanosheets; the inset shows an HRTEM image of a single MoS_2 nanosheet. (c) Cycling performance of MoS_2 flakes (I) and MoS_2-NS microspheres (II) at a current density of 100 mA/g. (d) Cycling performance of MoS_2 flakes (I) and MoS_2-NS microspheres (II) at different current densities (mA/g). Adapted from Ref. 174 (DOI: 10.1039/c1nr11552a) with permission.

This group also reported similar results using glucose as an additive in the presence of CNTs during hydrothermal synthesis.[175] This was shown to significantly decrease the thickness of the MoS_2 nanosheets. The glucose adsorbed on the surface of the CNT@MoS_2 was further converted into a thin amorphous carbon layer during the calcination process, and hence acted as an additional conductive and perhaps protective coating. The BET surface area was reported at 30 m^2/g. The glucose-assisted material consistently outperformed the glucose-free baseline (in terms of capacity retention and rate capability). The

capacity of the glucose-assisted CNT@MoS_2 was nearly 1000 mAh/g, decreasing to approximately 800 mAh/g after 60 cycles.[175]

Further to their previous work[46], authors present a study on L-cysteine assisted hydrothermal synthesis of MoS_2 graphene nanocomposites.[170] While biomolecular-assisted synthesis methods have been employed to create other types of sulfide nanostructures, this was the first study of its kind for MoS_2. The electrochemical results were very promising. The synthesized materials were true graphene-MoS_2 nanocomposites and possessed a synergistic charge capacity of nearly 1200 mAh/g which was shown to be dependent on the graphene-MoS_2 ratio (optimal was 2:1). The strong dependence of the electrode capacity on the amount of graphene added substantiates the argument that it is a major contributor to the net charge storage. The fact that there is an optimum ratio of graphene to MoS_2 does not need to be rationalized in terms of any profound electronic effects or a fundamental modification of the MoS_2 structure (it does not exist past cycle 1). Rather it can be explained by correlating this ratio to the best microstructural dispersion of the two phases, i.e. a mixture that is the most "nano". Unfortunately there are no existing literature reports where authors have demonstrated the variations in the key microstructural parameters (i.e. MoS_2 crystallite and particle size, total porosity and pore size distribution, electrical conductivity of the composite, degree of encapsulation by the carbon of the MoS_2 particles, etc.) with the loading of a given carbon phase. However it is quite reasonable to expect a "volcano" type of electrochemical performance curve versus carbon mass loading,

with the peak corresponding to the optimum overall capacity retention and rate capability (e.g. in Figure 4-7f). At lower carbon loadings the dispersion would not be optimized due to an insufficient amount of the carbon phase, while at higher mass loading agglomeration would reduce the amount of electrochemically accessible material and drive up the electrode resistivity.

Figure 4-7 shows SEM and TEM micrographs of their baseline material (4-7a) which was nearly monolithic, and their 2:1 graphene-MoS_2 nanocomposite (4-7b and 4-7c).[170] Though the two materials appear to be well interspersed, further evidence in terms of analytical mapping, Z-contrast imaging, HRTEM, etc. would have been useful. Electrochemical tests (Figures 4-7d, 4-7e, and 4-7f) highlight the significant differences between the baseline MoS_2 and the various nanocomposites that were analyzed. Figure 4-7f shows that the total capacity and the cycling stability are much better for the 2:1 nanocomposite (marked 3) as compared to the graphene-free MoS_2 baseline (marked 1). The 1:1 graphene/MoS_2 (marked 2) and 4:1 graphene/MoS_2 (marked 4) nanocomposites are both inferior to the 2:1, likely for the reasons previously discussed. There are also significant differences in the voltage-capacity profiles for the baseline (Figure 4-7d) and the 2:1 nanocomposite (Figure 4-7e). The previously described plateaus at ~1.1 and 0.6 V vs. Li/Li^+ during the first discharge of MoS_2 were much less conspicuous for the nanocomposite (Figure 4-7e). It is difficult to quantitatively compare the voltage-capacity profiles for the two materials during subsequent cycling, since neither possesses well-defined plateaus. However one

can qualitatively state that the voltage profiles did vary with the graphene content, supporting the argument that it had a substantial contribution to the net capacity. Furthermore, the lack of discernible voltage plateaus in subsequent cycles indicates that both materials went through similar phase changes as a result of their initial lithiation. The stable cycling capacity of nearly 1200 mAh/g after 100 cycles is among the highest reported in literature for any MoS_2-based electrodes. The 2:1 graphene-MoS_2 nanocomposite not only displayed over twice the capacity of the MoS_2 baseline but was also much more stable. This is shown in Figure 4-7f.

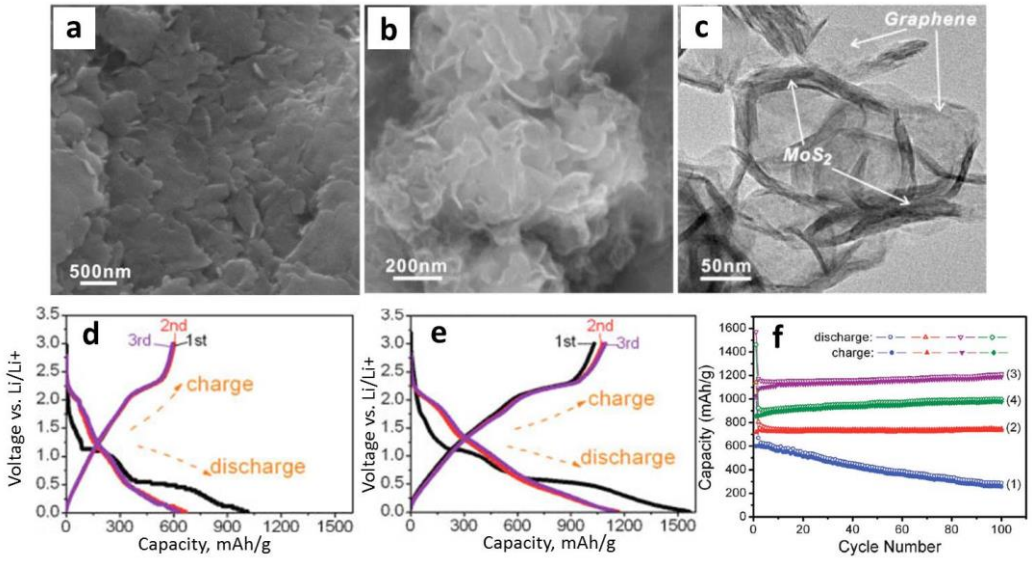

Figure 4-7: L-cysteine assisted hydrothermal synthesis of graphene-MoS_2 nanocomposites. (a) SEM micrograph of the MoS_2 baseline. (b) and (c) SEM and TEM micrographs of the 2:1 by weight graphene-MoS_2 nanocomposite. (d) and (e) Charge-discharge curves for the baseline MoS_2 and for the 2:1 nanocomposite, respectively. (f) Cycling stability of the nanocomposites: (1) MoS_2 (2) G/MoS_2 (1:1) (3) G/MoS_2 (2:1) (4) G/MoS_2 (4:1). Adapted from Ref. 170 (DOI: 10.1021/nn200659w) with permission from the American Chemical Society, Copyright 2011.

It is also important to note that additives such as ionic liquids, glucose and biomolecular compounds show a strong impact on the morphologies of hydrothermally synthesized MoS_2. Similar effects have been demonstrated in the hydrothermal synthesis of metal oxides[236-239], where the solution-phase interactions are generally better understood. Hence any comparisons with the carbon-free baselines are further obscured since not only is the resultant carbon content and dispersion different, but also the morphology of the MoS_2 phase. Varying the relative amount of precursor would also have an effect on the microstructure of MoS_2. For instance, in the previous study[170] the microstructure of MoS_2 would not only differ between the graphene-free MoS_2 baseline and the graphene-MoS_2 samples, but also between the 1:1, 2:1 and 4:1 specimens. These types of questions would be better resolved through the application of more robust microscopy analysis on the as-synthesized and post cycled specimens.

4.7.2 MoS_2 prepared by solvothermal synthesis

Despite the success of the MoS_2 electrode in a half-cell configuration, published work on a full cell is limited. Cho *et al*.[48] are one of the only groups to successfully test and publish results on such a cell, using a lithium cobalt oxide cathode and an anode consisting of graphene-like MoS_2 nanoplates. The nanoplates were synthesized via a liquid phase solvothermal reaction of molybdenum hexacarbonyl ($Mo(CO)_6$) and sulfur in xylene. Figures 4-8a and 4-8b display SEM and TEM images of the synthesized nanostructures, respectively. The SEM images indicate that the particulate size of the MoS_2 is sub-100 nm

scale, while the TEM micrographs indicate that the structure is highly disordered. Examining the published micrograph one observes a structure that is quite heterogeneous even on the sub – 5 nm scale (dimension of the scale marker), with both crystalline and amorphous regions being present throughout. For the crystalline sections, a variety of contrast fringe spacings are observed. These may not actually be conclusively ascribed to any given set of interplanar spacings due to an unknown orientation of the polycrystalline specimen relative to the electron beam. Moreover some regions of the micrograph show contrast synonymous with Moiré patterns, which are caused by overlapping crystallites. It is not clear as to what kind of feature the marker showing 0.69 nm spacing is referring too, though we believe it to be a Moiré fringe.

Figures 4-8c and 4-8d show the potential-capacity curves and cycling stability results for the half-cell, which are very impressive. The dominant discharge (~2.0 V) and charge (~2.3 V) plateaus are consistent with other work[172] and are indicative of the lithium-sulfur redox couple. The authors correctly point out that larger interlayer spacing in their nanostructured MoS_2 would alter the intercalation thermodynamics and kinetics. However, this effect will only be realized during the first lithiation and cannot contribute to the electrochemical performance in the subsequent cycles. The charge storage capacities are in excess of the theoretical value. Though the authors argued that the structure is only porous MoS_2, the residual presence of a substantial amount of carbon from the molybdenum hexacarbonyl precursor cannot be ruled out. Neither TEM nor XRD

analysis presented by the authors was sufficiently detailed to negate that possibility. Given the reported surface area of 80 m^2/g, there may also be a contribution to the net capacity due to the surface adsorption of lithium on metallic molybdenum after the conversion reaction (in addition to the almost certain adsorption of lithium on any residual carbon). The authors' rate dependence results in Figure 4-8d (nearly 800 mAh/g at 30 C and 700 mAh/g at 50 C) may only be realized with a high charge transfer surface area and extremely short diffusion distances, implying that the very fine, high surface area microstructure remains stable throughout the cycling.

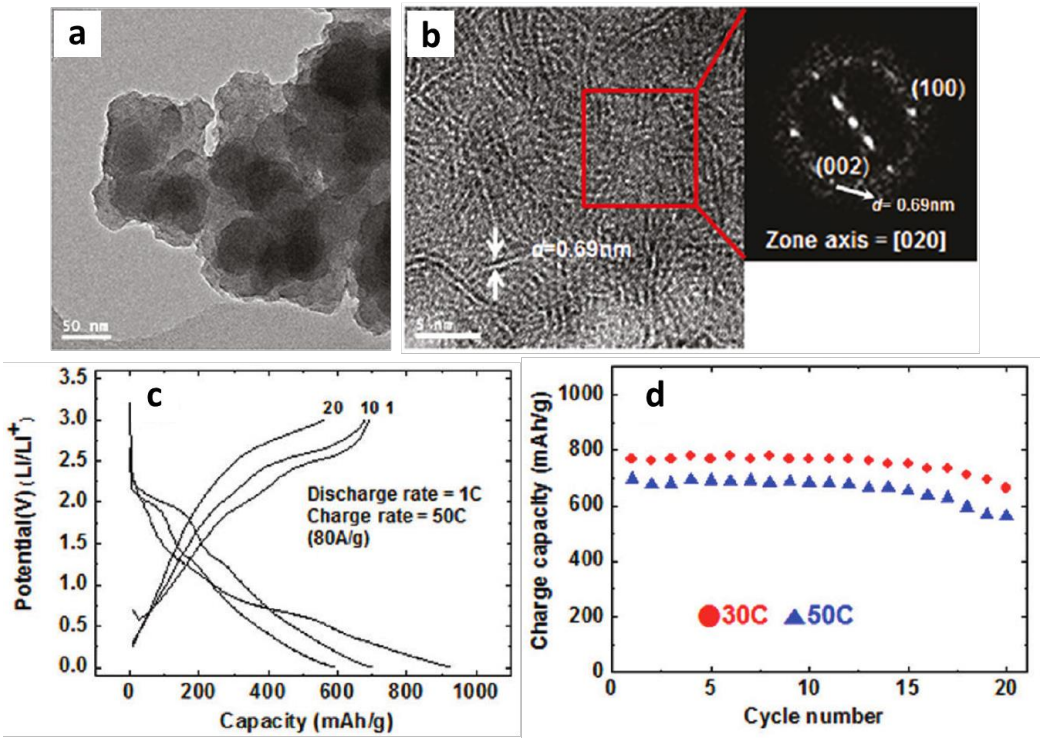

Figure 4-8: Disordered graphene-like MoS_2 achieved via liquid phase solvothermal technique. (a) and (b) SEM and TEM (with FFT insert) images of the synthesized nanostructures. (c) and (d) Charging-discharging curves and cycling stability results for the half-cell. Adapted from Ref. 48 (DOI: 10.1021/nl202675f) with permission from the American Chemical Society, Copyright 2011.

4.7.3 Ordered mesoporous MoS_2 through templating

The use of hard templates has been recently and successfully employed to synthesize highly porous MoS_2 nanostructures with high surface areas. The surface areas of these materials are large enough to justify lithium ion surface adsorption and lithium metal pore filling (nanoplating) as an important secondary contributor to the net charge storage.[177,182,240] In such cases a charge storage capacity beyond 669 mAh/g is expected analogous to the high surface area/high porosity carbons that exceed 372 mAh/g. Figure 4-9 highlights one of the more interesting and better performing examples of such an approach.[240] The specific surface area and pore volume of mesoporous MoS_2 were calculated to be 130 m^2/g and 0.24 cm^3/g, and are expected to further increase after the first lithiation. Figure 4-9a shows a low magnification SEM image revealing macroscopic clusters of rod-like interconnected MoS_2 nanowires. The mesoporous channels are partially revealed by the TEM micrograph in Figure 4-9b, with SAED inset indexed to 2H-MoS_2. Figure 4-9c shows the excellent cycling stability of the material, retaining a reversible capacity of 876 mAh/g after 100 cycles at a current density of 0.1 A/g. Figure 4-9d shows the exceptional rate capability, and capacity recovery of the material, even after cycling at a current density of 10 A/g. This capability was attributed to the large electrode/electrolyte interface allowed by the mesoporous channels (which had a narrow size distribution). This led to ultrafast lithium intercalation over a large surface area. Similar results have also been obtained for other mesoporous materials.[241] The authors comment that the high rate capability is also due to the enhanced layer spacing of their MoS_2,

however this is doubtful after the first cycle. The high rate capability could only be realized in a highly conductive matrix which suggests the presence of a finely dispersed metallic phase. The authors employed an excessive amount of carbon black in their electrode recipe (70:20:10, active material : carbon black : PVDF binder) which may partially account for the capacity enhancement, though in this case we believe that it is a secondary issue relative to the porosity effect.

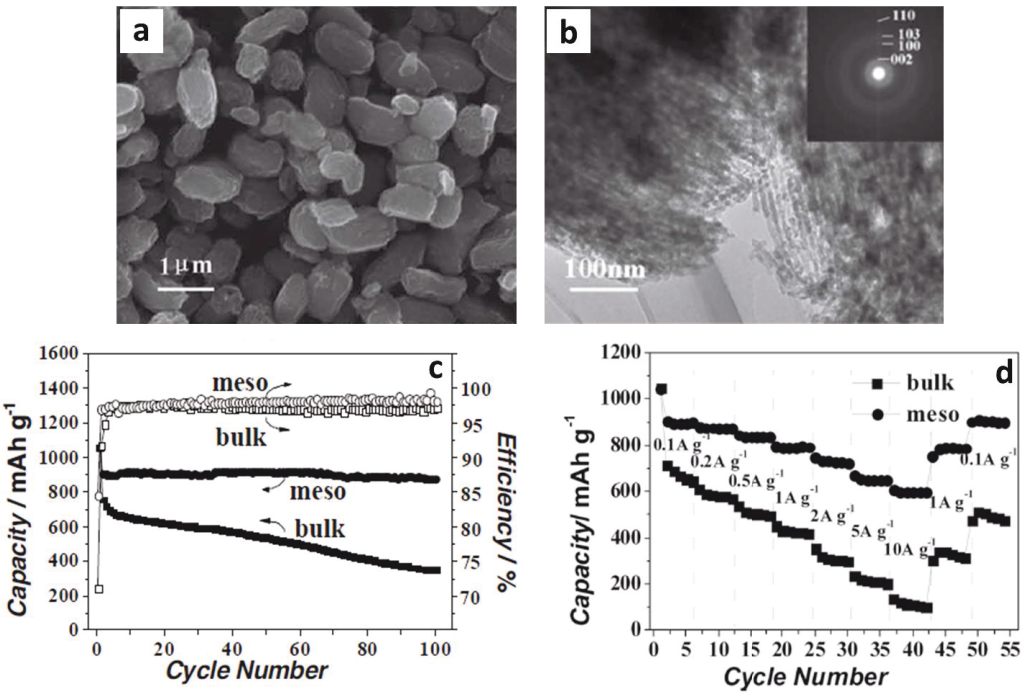

Figure 4-9: Templated mesoporous MoS_2. (a) Low magnification SEM image revealing MoS_2 microstructures. (b) TEM micrograph (with SAED inset) revealing the mesoporosity of MoS_2 crystallites and wire-like arrays. (c) Cycling performance at a current density of 0.1 A/g. (d) Cycling performance at different current densities. Adapted from Ref. 240 (DOI: 10.1002/aenm.201200087) with permission from Wiley-VHC Verlag GmbH &Co, KGaA, Weinheim, Copyright 2012.

One would expect that the high surface area would lead to excessive SEI layer formation, however the templated electrode is shown to remain quite stable

with good coulombic efficiency (97 - 98%) throughout cycling. This agrees with what is commonly reported in literature for templated carbons with highly ordered porosity, which are also stable upon cycling and demonstrate good coulombic efficiency.[206] Apparently after the first cycle, SEI formation is at least partially inhibited. While no post-cycled TEM was completed in this work, others have shown SEI formation on mesoporous MoS_2 with partial retention of the mesoporous structure after initial charge and discharge.[178] For this material, the pore volume is also expected to accommodate the volume expansions and distortions associated with lithiation and the conversion reaction. The stability of the material suggests that the mesoporous structure may have been partially retained after many cycles, however this was not proven.

Table 4-2 provides a summary of the electrochemical data from the various literature sources. As can be seen there is a substantial variation not only in the charge storage capacities but also in the coulombic efficiencies between the studies. Interestingly, nominally similar techniques, e.g. hydrothermal synthesis, can result is radically different electrochemical performance outcomes. The implication of this is that both subtle changes in the experimental synthesis parameters, the electrode/cell fabrication techniques, and the morphology of the as-synthesized material can all play a major role in determining how well the battery performs.

Table 4-2: Summary of recent electrochemical data collected for MoS_2. In all cases electrodes were tested in a half-cell configuration versus Li/Li^+ and fully cycled across a voltage window of ~0.01-3 V.[a]

Material	Synthesis Method	First Discharge Capacity (mAh/g)	First Charge Capacity (mAh/g)	Reversible Capacity after (X) cycles (mAh/g)	Coulombic Efficiency after (Y) cycles (%)	Current Density	Highest Current Density tested	Reference
MoS_2-PEO (plate-like particles)	Exfoliation/ hydrolysis	1131	822*	890 (50)	95* (50)	50 mA/g	50 mA/g	180
MoS_2-GNS-PEO (nanoparticles)	Exfoliation/ hydrolysis	1130	830*	1000 (180)	93* (180)	50 mA/g	10 A/g	181
MoS_2 - GNS (nanoparticles)	*Hydrothermal*	*2200**	*1300*	*1290 (50)*	*99.2 (50)*	*100 mA/g*	*1000 mA/g*	*46*
MoS_2 - GNS (nanoparticles)	Hydrothermal	1571	1031	1187 (100)	99* (100)	100mA/g	1000 mA/g	170
MoS_2 - CNTs (nanosheets)	Hydrothermal	1434	862	698 (60)	94 (3)	100 mA/g	1000 mA/g	174
MoS_2 - CNTs (nanosheets)	Hydrothermal	710*	390*	390 (50)	98 (50)	0.6 mA/cm^2	0.6 mA/cm^2	171
MoS_2-amC (nanosheets)	Hydrothermal	1175	870*	852 (40)	94* (40)	60 mA/g	60 mA/g	159
MoS_2-amC (nanoparticles)	Hydrothermal	1340*	869	633 (50)	65 (1)	100 mA/g	400 mA/g	173
MoS_2-amC (nanoparticles)	Hydrothermal	1160	791	585 (70)	95 (3)	100 mA/g	1000 mA/g	174
MoS2-amC (nanoparticles)	Hydrothermal	2100*	930*	912 (100)	99* (100)	100 mA/g	100 mA/g	169
MoS_2-amC (nanowires)	Template-assisted	880	625	630 (20)	98.5 (20)	33 mA/g	669 mA/g	177
MoS_2@CMK-3 (nanorods)	Template-assisted	1056	824	602 (100)	97* (100)	250 mA/g	2000 mA/g	182
MoS_2-AB (nanorods)	Template-assisted	1060*	1052	876 (100)	98* (100)	100 mA/g	10 A/g	240
MoS_2-amC (nanoparticles)	*Solvothermal*	*1062*	*917*	*907 (50)*	*87 (1)*	*1062 mA/g*	*53.1 A/g*	*48*

[a]* - Indicates a value estimated from a published graph.

4.8 Promising MoS_2 nanomaterials not investigated for lithium storage

As a nanostructured material, MoS_2 can exist in a diverse range of morphologies and microstructures. These include fullerene-like MoS_2 (layered onion-like nanospheres)[200,201,242-247], MoS_2 nanotubes[194,195,196,248-252], MoS_2 nanowires with various stoichiometries[253-255], nanoribbons and nanosheets.[256-262] As summarized in previous review papers[197,263,264], these nanostructures can be synthesized via a wide range of methods. At this stage the vast majority of these structures have not been investigated as electrode materials for lithium storage. We believe that these MoS_2 nanostructures could hold great promise for electrode applications as many of the synthesis techniques offer opportunities for nanoscale carbon incorporation. In this section, we will give a brief overview of the nanostructures achieved using two of the most scalable methods: template-assisted and gas-phase synthesis techniques. These techniques are already widely utilized in sectors such as microelectronics and thin films coatings for various industrial applications, making the technology mature and transferrable to the energy storage sector. Moreover the described approaches yield arrays of interconnected nanostructures that offer direct electron conductions paths down to the current collectors; a key advantage over techniques that result in isolated crystallites or particles.

4.8.1 Various MoS_2 nanostructures synthesized through templating

Many MoS_2 nanostructures can be synthesized through the templating strategy. Authors performed seminal work on template-assisted synthesis of monodispersed microscale MoS_2 nanofibers and nanotubes.[265] They utilized thermal decomposition of two different ammonium thiomolybdate precursors within the confines of a porous aluminum oxide template. Their technique resulted in a dense fibrous network of MoS_2 nanotubes that extended parallel to the substrate. This is appealing for lithium storage due to the high degree of interconnectivity and potential for flexibility.[266] Additional work describe routes to MoS_2 nanotube and fullerene synthesis.[267,268] Authors describe a procedure to synthesize MoS_2 nanotubes of different chiralities, similar to carbon nanotubes.[267] While drawing comparisons the authors mentioned that the unique sandwich-like structure of MoS_2 may offer greater resistance to nanotube buckling and kinking than for CNTs. This fact may prove useful for the creation of flexible lithium ion batteries that can withstand large amounts of deformation.

Researchers have also developed an alternate template-assisted technique to create a coaxial-binary system of graphene and MoS_2 nanotubes.[269] Since it is known that a capacity enhancement is accompanied by the coordination of graphene with MoS_2 nanosheets, the creation of a coaxial-binary system of MoS_2 and carbon nanotubes may exhibit excellent electrochemical performance. Additionally, a template-assisted method using silica for producing mesoporous MoS_2 has also been successfully completed.[270] Here, the authors have developed

a method of synthesizing tubular mesoporous domains of MoS_2 which are highly layered and nanoscale. They go on to describe a dimensional tunability, which is difficult to achieve with other synthesis techniques and could therefore be useful for creating MoS_2 nanostructures with controllable size for lithium storage. This technique may be useful for quantifying the dimensional effect of MoS_2 on charge capacity.

4.8.2 MoS_2 nanostructures synthesized through gas-phase techniques

Gas-phase synthesis techniques are amongst the most intriguing since they yield a wide range of unique microstructures and offer a high degree of versatility. Authors describe methods which involve aerosol assisted CVD processes that form MoS_2 via the decomposition of a single source precursor gas.[271,272] These methods have led to some very distinctive MoS_2 microstructures, which exhibit a plate-like morphology that was found to vary with annealing temperature. Although complex, the result was the deposition of nanoscale MoS_2 structures over centimeter square areas which may be useful for conformal coatings on complex geometries.[271] Additionally, researchers also report on a novel CVD method of synthesizing MoS_2 monolayers over large areas.[273] These procedures are advantageous since many of the methods previously discussed yield interconnected particulates of MoS_2 that are difficult to deposit as large-area coatings. While these coatings are usually evaluated for anti-friction applications, their adaptation for lithium storage on complex geometries could be beneficial, since electrode templates often have intricate, high surface area morphologies.

Authors have shown that it is also possible to synthesize high surface area molybdenum disulfide nanotubes directly from a reaction of molybdenum metal and sulfur powder together with iodine flakes reacted in a glass ampoule at 850 °C.[274] In their method, C_{60} was added at 5 wt.% and used as a growth catalyst in their reactions but was removed in subsequent processing steps. Others have reported an electrochemical enhancement by adding C_{60}.[84] These tubes were observed to have a high defect density along their length and be of relatively uniform diameter. Furthermore, they demonstrate that it is possible to grow vertically aligned MoS_2 nanotube forests across a substrate surface, similar to CNTs.[263]

Researchers have achieved physical vapor deposition of MoS_2 thin films using reactive magnetron sputtering of a solid molybdenum target and magnetron sputtering a solid MoS_2 target.[198,275] In this work the authors noticed that a significant portion of crystallites would form with their c-axis parallel to the substrate, which would present dangling bonds in the form of edge vacancies to the outer surface as well as provide potential inter-planar diffusion pathways to incident lithium ions. Authors describe a technique for the synthesis of MoS_2 nanoparticles using pulsed laser ablation.[276] Here pure, fullerene-like nanoparticles with a very uniform size distribution were synthesized by the ablation of a target in water. This technique could be adapted as a simple way to fabricated nanocomposites with carbon, via carbon incorporation into the pressed

molybdenum disulfide target pellet. The propensity for unique facile nanostructures involving carbon encapsulation and incorporation seems plausible with this technique.

4.9 Concluding thoughts

While $LiMoS_2$ cathodes may offer little in the way of capacity enhancement compared to $LiCoO_2$, the material is still worth considering due to its exceptional rate performance and cycling stability. As an anode, the capacity enhancement of MoS_2 over graphite has been well demonstrated. There is still significant debate regarding the actual lithiation reaction sequence during charging/discharging. However, there is progressively more evidence to support what is currently the minority view, that the primary lithium active phase is elemental sulfur beyond the first cycle. Metallic molybdenum appears to have a secondary albeit very important role of both enhancing the electrical conductivity of the electrode and perhaps stabilizing the shuttling of polysulfides that are known to be the source of premature failure in Li-S batteries. However for the case of Li-MoS_2, the role of polysulfides and their interaction both with the molybdenum and the various nanocarbon phases interspersed within the electrodes remains quite poorly understood.

This brings up the second outstanding scientific issue: The experimentally reported reversible charge storage capacities for MoS_2-based architectures are consistently above the theoretical capacity of the literature-proposed lithiation

conversion reactions. These involve either MoS_2 or sulfur (keeping in mind the weight contribution of the "inactive" molybdenum). While scenarios such as nanoscale molybdenum actually being electro-active towards lithium are possible and should be further explored, we believe that the charge capacity of the nanodispersed carbons present in the composites is often underestimated.

4.10 References

[1] Wang, Q.H. ; Kalantar-zadeh, K. ; Kis, A. ; Coleman, J.N. ; Strano, M.S. *Nat. Nanotechnol.* **2012**, 7, 699.

[2] Chhowalla, M. ; Shin, H.S. ; Eda, G. ; Li, L.-J. ; Loh, K.P. ; Zhang, H. *Nat. Chem.* **2013**, 5, 263.

[3] Rapoport, L. ; Fleischer, N. ; Tenne, R. *J. Mater. Chem.* **2005**, 15, 1782.

[4] Le Mogne, T. ; Donnet, C. ; Martin, J.M. ; Tonck, A. ; Millard-Pinard, N. *J. Vac. Sci. Technol. A.* **1994**, 12(4), 1998.

[5] Wang, H.W. ; Skeldon, P. ; Thompson, G.E. *Surf. Coat. Technol.* **1997**, 91, 200.

[6] Barboza, A.P.M. ; Chacham, H. ; Oliveira, C.K. ; Fernandes, T.F.D. ; Ferreira, E.H.M. ; Archanjo, B.S. ; Batista, R.J.C. ; de Oliveira, A.B. ; Neves, B.R.A. *Nano Lett.* **2012**, 12, 2313.

[7] Zhang, H. ; Loh, K.P. ; Sow, C.H. ; Gu, H. ; Su, X. ; Huang, C. ; Chen, Z.K. *Langmuir*, **2004**, 20, 6914.

[8] Zhu, C. ; Zeng, Z. ; Li, H. ; Li, F. ; Fan, C. ; Zhang, H. *J. Am. Chem. Soc.* **2013**, 135, 5998.

[9] Li, H. ; Yin, Z. ; He, Q. ; Li, H. ; Huang, X. ; Lu, G. ; Fam, D.W.H. ; Tok, A.L.Y. ; Zhang, Q. ; Zhang, H. *Small*, **2012**, 8(1), 63.

[10] He, Q. ; Zeng, Z. ; Yin, Z. ; Li, H. ; Wu, S. ; Huang, X. ; Zhang, H. *Small*, **2012**, 8(19), 2994.

[11] Barreau, N. ; Bernede, J.C. *J. Phys. D: Appl. Phys.* **2002**, 35, 1197.

[12] Feng, J. ; Qian, X. ; Huang, C.-W. ; Li, J. *Nat. Photonics,* **2012**, 6, 866.

[13] Liu, C.-J. ; Tai, S.-Y. ; Chou, S.-W. ; Yu, Y.-C. ; Chang, K.-D. ; Wang, S. ; Chien, F.S.-S. ; Lin, J.-Y. ; Lin, T.-W. *J. Mater. Chem.* **2012**, 22, 21057.

[14] Tai, S.-Y. ; Liu, C.-J. ; Chou, S.-W. ; Chien, F.S.-S. ; Lin, J.-Y. ; Lin, T.-W. *J. Mater. Chem.* **2012**, 22, 24753.

[15] Shanmugam, M. ; Bansal, T. ; Durcan, C.W. ;Yu, B. *Appl. Phys. Lett.* **2012**, 100, 153901.

[16] Kibsgaard, J. ; Chen, Z. ; Reinecke, B.N. ; Jaramillo, T.F. *Nat. Mater.* **2012**, 11, 963.

[17] Hansen, L.P. ;Ramasse, Q.M. ; Kisielowski, C. ; Brorson, M. ; Johnson, E. ; Topsoe, H. ; Helveg, S. *Angew. Chem. Int. Ed.* **2011**, 50, 10153.

[18] Wilcoxon, J.P. *J. Phys. Chem. B.* **2000**, 104, 7334.

[19] Ho, W. ; Yu, J.C. ; Lin, J. ; Yu, J. ; Li, P. *Langmuir*, **2004**, 20, 5865.

[20] Han, W. ; Yuan, P. ; Fan, Y. ; Shi, G. ; Liu, H. ; Bai, D. ; Bao, X. *J. Mater. Chem.* **2012**, 22, 25340.

[21] Chu, X. ; Yao, G. ; Wee, A.T.S. ; Wang, X.-S. *Nanotechnology,* **2012**, 23, 375603.

[22] Zhong, X. ; Yang, H. ; Guo, S. ; Li, S. ; Guo, G. ; Niu, Z. ; Dong, Z. ; Lei, Y. ; Jin, J. ; Li, R. ;Ma, J. *J. Mater. Chem.* **2012**, 22, 13925.

[23] Merki, D. ; Fierro, S. ; Vrubel, H. ; Hu, X. *Chem. Sci.* **2011**, 2, 1262.

[24] Laursen, A.B. ; Kegnaes, S. ; Dahl, S. ; Chorkendorff, I. *Energy Environ. Sci.* **2012**, 5, 5577.

[25] Wang, T. ; Liu, L. ;Zhu, Z. ; Papakonstantinou, P. ; Hu, J. ; Liu, H. ; Li, M. *Energy Environ. Sci.* **2013**, 6, 625.

[26] Yan, Y. ; Xia, B. ; Qi, X. ; Wang, H. ; Xu, R. ; Wang, J.-Y. ; Zhang, H. ; Wang, X. *Chem. Commun.* **2013**, 49, 4884.

[27] Laursen, A.B. ; Vesborg, P.C.K. ; Chorkendorff, I. *Chem. Commun.* **2013**, 49, 4965.

[28] Huang, X. ; Zeng, Z. ; Bao, S. ; Wang, M. ; Qi, X. ; Fan, Z. ; Zhang, H. *Nat. Commun.* **2013**, 4, 1444.

[29] Liu, J. ; Zeng, Z. ; Cao, X. ; Lu, G. ; Wang, L.H. ; Fan, Q.L. ; Huang, W. ; Zhang, H. *Small*, **2012**, 8(22), 3517.

[30] van Schalkwijk, W.A. (Ed.) ; Scrosati, B. (Ed.), *Advances in Lithium-Ion Batteries*, Klumer Academic Publishers, New York USA, **2002**, 1-5.

[31] Gabano, J.P. (Ed.) *Lithium Batteries*, Academic Press, New York USA, **1983**, 1-12.

[32] Linden, D. (Ed.) ; Reddy, T.B. (Ed.) *Linden's Handbook of Batteries.* McGraw Hill, NewYork USA, **2011**, 27.1-26.28

[33] Harris, W.S. Ph.D. Thesis, UCRL-8381, University of California, Berkeley, **1958**, 1-37.

[34] Rudorff, W. *Angew. Chem.* 71, **1959**, 487.

[35] Rudorff, W. ; Sick, H.H. *Angew. Chem.* 71, **1959**, 127.

[36] Whittingham, M.S. ; Gamble Jr. F.R. *Mat. Res. Bull.* **1975**, 10, 363.

[37] Whittingham, M.S. *Science*. **1976**, 192, 1126.

[38] Whittingham, M.S. *J. Electrochem. Soc.* **1976**, 123(3), 315.

[39] Whittingham, M.S. *Prog. Solid St. Chem.* **1978**, 12, 41.

[40] Silbernagel, B.G. ; Whittingham, M.S. *J. Chem. Phys.* **1976**, 64(9), 3670.

[41] Farrington, G.C. ; Briant, J.L. *Science*, **1979**, 204, 1371.

[42] Dines, M.B. *Mat. Res. Bull.* **1975**, 10, 287.

[43] Goodenough, J.B. *Proc. R. Soc. Lond.* **1984**, A 393, 215.

[44] Xie, Y. ; Wu, C. *Dalton Trans.* **2007**, 45, 5235.

[45] Wang, Y. ; Li, H. ; He, P. ; Hosono, E. ; Zhou, H. *Nanoscale*, **2010**, 2, 1294.

[46] Chang, K. ; Chen, W. *Chem. Commun.* **2011**, 47, 4252.

[47] Kohandehghan, A. ; Kalisvaart, P. ; Kupsta, M. ; Zahiri, B. ; Amirkhiz, B.S. ; Li, Z. ; Memarzadeh, E.L. ; Bendersky, L.A. ; Mitlin, D. *J. Mater. Chem. A.* **2013**, 1, 1600-1612.

[48] Hwang, H. ; Kim, H. ; Cho, J. *Nano Lett.* **2011**, 11, 4826.

[49] Yang, Z. ; Zhang, J. ; Kintner-Meyer, M.C.W. ; Lu, X. ; Chio, D. ; Lemmon, J.P. ; Liu, J. *Chem. Rev.* **2011**, 111, 3577.

[50] Cui, L.-F. ; Hu, L. ; Choi, J.W. ; Cui, Y. *ACS Nano*, **2010**, 4(7), 3671.

[51] Xie, J. ; Yang, X. ; Zhou, S. ; Wang, D. *ACS Nano,* **2011**, 5(11), 9225.

[52] Haering, R.R. ; Stiles, J.A.R. ; Brandt, K. US Patent No. 4,224,390, Sept. 23, **1980**.

[53] Julien, C. ; Saikh, S.I. ; Nazri, G.A. *Mater. Sci. Eng.* **1992**, B15, 73.

[54] Miki, Y. ; Nakazato, D. ; Ikuta, H. ; Uchida, T. ; Wakihara, M. *J. Power Sources*, **1995**, 54, 508.

[55] Yufit, V. ; Nathan, M. ; Golodnitsky, D. ; Peled, E. *J. Power Sources.* **2003**, 122, 169.

[56] Murugan, A.V. ; Quintin, M. ; Delville, M.-H. ; Campet, G. ; Gopinath, C.S. ; Vijayamohanan, K. *J. Power Sources*, **2006**, 156, 615.

[57] Shembel, E. ; Apostolova, R. ; Kirsanova, I. ; Tysyachny, V. *J. Solid State Electrochem.* **2008**, 12, 1151.

[58] Kim, M.G. ; Jo, M. ; Hong, Y.-S.; Cho, J. *Chem. Commun.* **2008**, 219.

[59] Chen, H. ; Qiu, X. ; Zhu, W. ; Hagenmuller, P. *Electrochem. Commun.* **2002**, 4, 488.

[60] Xia, L. ; Li, S.-L. ; Ai, X.-P. ; Yang, H.-X. ; Cao, Y.-L. *Energy Environ. Sci.* **2011**, 4, 2845.

[61] Hong, Z. ; Zheng, X. ; Ding, X. ; Jiang, L. ; Wei, M. ; Wei, K. *Energy Environ. Sci.* **2011**, 4, 1886.

[62] Koksbang, R. ; Barker, J. ; Shi, H. ; Saidi, M.Y. *Solid State Ionics*, **1996**, 84, 1.

[63] Chen, Z. ; Dahn, J.R. *Electrochim. Acta*, **2004**, 49, 1079.

[64] Lu, Y. ; Das, S.K. ; Moganty, S.S. ; Archer, L.A. *Adv. Mater.* **2012**, 24, 4430.

[65] Lai, C.-H. ; Lu, M.-Y. ; Chen, L.-J. *J. Mater. Chem.* **2012**, 22, 19.

[66] Gao, M.-R. ; Xu, Y.-F. ; Jiang, J. ; Yu, S.-H. *Chem. Soc. Rev.* **2013**, 42, 2986.

[67] Huang, X. ; Zeng, Z. ; Zhang, H. *Chem. Soc. Rev.* **2013**, 42, 1934.

[68] Balendhran, S. ; Walia, S. ; Nili, H. ; Ou, J.Z. ; Zhuiykov, S. ; Kaner, R.B. ; Sriram, S. ; Bhaskaran, M. ; Kalantar-zadeh, K. *Adv. Funct. Mater.* **2013**, 23, 3952.

[69] Wang, Y. ; Li, H. ; He, P. ; Hosono, E. ; Zhou, H. *Nanoscale*, **2010**, 2, 1294.

[70] Manthiram, A. ; Murugan, A.V. ; Sarkar, A. ; Muraliganth, T. *Energy Environ. Sci.* **2008**, 1, 621.

[71] Balaya, P. *Energy Environ. Sci.* **2008**, 1, 645.

[72] Fan, X. ; Zhang, H. ; Du, N. ; Wu, P. ; Xu, X. ; Li, Y. ; Yang, D. *Nanoscale*, **2012**, 4, 5343.

[73] Lim, A.-H. ; Shim, H.-W. ; Seo, S.-D. ; Lee, G.-H. ; Park, K.-S. ; Kim, D.-W. *Nanoscale,* **2012**, 4, 4694.

[74] Derrien, G. ; Hassoun, J. ; Panero, S. ; Scrosati, B. *Adv. Mater*. **2007**, 19, 2336.

[75] Ding, S. ; Lou, X.W. *Nanoscale*, **2011**, 3, 3586.

[76] Pabakar, S.J.R. ; Hwang, Y.-H. ; Bae, E.-G. ; Shim, S. ; Kim, D. ; Lah, M.S. ; Sohn, K.-S. ; Pyo, M. *Adv. Mater*. **2013**, 25, 3307.

[77] Sun, D.S. ; Schlogl, R. *Chem. Sus. Chem.* **2010**, 3, 136.

[78] Song, R. ; Song, H. ; Zhou, J. ; Chen, X. ; Wu, B. ; Yang, H.Y. *J. Mater. Chem.* **2012**, 22, 12369.

[79] Frackowiak, E. ; Gautier, S. ; Gaucher, H. ; Bonnamy S. ; Beguin F. *Carbon*, **1999**, 37, 61.

[80] Landi, B.J. ; Ganter, M.J. ; Cress, C.D. ; DiLeo, R.A. ; Raffaelle, R.P. *Energy Environ. Sci.* **2009**, 2, 638.

[81] Chen, J. ; Wang, J.Z. ; Minett, A.I. ; Liu, Y. ; Lynam, C. ; Liu, H. ; Wallace, G. *Energy Environ. Sci.* **2009**, 2, 393.

[82] Pan, D. ; Wang, S. ; Zhao, B. ; Wu, M. ; Zhang, H. ; Wang, Y. ; Jiao, Z. *Chem. Mater.* **2009**, 21, 3136.

[83] Wang, G. ; Shen, X. ; Yao, J. ; Park, J. *Carbon*, **2009**, 47, 2049.

[84] Yoo, E. ; Kim, J. ; Hosono, E. ; Zhou, H.S. ; Kudo, T. ; Honma, I. *Nano Lett.* **2008**, 8(8), 2277.

[85] Bhardwaj T. ; Antic, A. ; Pavan, B. ; Barone, V. ; Fahlman, B.D. *J. Am. Chem. Soc.* **2010**, 132, 12556.

[86] Pumera, M. *Energy Environ. Sci.* **2011**, 4, 668.

[87] Zu, C.-X. ; Li, H. *Energy Environ. Sci.* **2011**, 4, 2614.

[88] Li, Z. ; Xu, Z. ; Tan, X. ; Wang, H. ; Holt, C.M.B. ; Stephenson, T. ; Olsen, B.C. ; Mitlin, D. *Energy Environ. Sci.* **2013**, 6, 871.

[89] Wu, P. ; Du, N. ; Zhang, H. ; Yu, J. ; Qi, Y. ; Yang, D. *Nanoscale,* **2011**, 3, 746.

[90] Choi, B.G. ; Chang, S.-J. ; Lee, Y.B. ; Bae, J.S. ; Kim, H.J. ; Huh, Y.S. *Nanoscale*, **2012**, 4, 5924.

[91] Das, S.K. ; Darmakolla, S. ; Bhattacharyya, A.J. *J. Mater. Chem.* **2010**, 20, 1600.

[92] Han, H. ; Song, T. ; Bae, J.-Y. ; Nazar, L.F. ; Kim, H. ; Paik, U. *Energy Environ. Sci.* **2012**, 4,4532.

[93] Yang, Z. ; Du, G. ; Meng, Q. ; Guo, Z. ; Yu, X. ; Chen, Z. ; Guo, T. ; Zeng, R. *J. Mater. Chem.* **2012**, 22, 5848.

[94] Zhu, G.-N. ; Wang, Y.-G. ; Xia, Y.-Y. *Energy Environ. Sci.* **2012**, 5, 6652.

[95] Xia, F. ; Hu, X. ; Sun, Y. ; Luo, W. ; Huang, Y. *Nanoscale*, **2012**, 4, 4707.

[96] Bhaskar, A. ; Deepa, M. ; Rao, T.N. *Appl. Mater. Inferfaces*. **2013**, 5, 2555.

[97] Sun, Y. ; Hu, X. ; Yu, J.C. ; Li, Q. ; Luo, W. ; Yuan, L. ; Zhang, W. ; Huang, Y. *Energy Environ. Sci.* **2011**, 4, 2870.

[98] Huang, X.H. ; Tu, J.P. ; Zhang, C.Q. ; Chen, X.T. ; Yuan, Y.F. ; Wu, H.M. *Electrochim. Acta,* **2007**, 52, 4177.

[99] Zou, Y. ; Wang, Y. *Nanoscale*, **2011**, 3, 2615.

[100] Liu, H. ; Yang, W. *Energy Environ. Sci.* **2011**, 4, 4000.

[101] Zhou, X. ; Yin, Y.-X. ; Wan, L.-J. ; Guo, Y.-G. *Chem. Commun.* **2012**, 48, 2198.

[102] Memarzadeh, E.L. ; Kalisvaart, W.P. ; Kohandehghan, A. ; Zahiri, B. ; Holt, C.M.B. ; Mitlin, D. *J. Mater. Chem.* **2012**, 22, 6655.

[103] Ji, L. ; Zhang, X. *Energy Environ. Sci.* **2010**, 3, 124.

[104] Szczech, J.R. ; Jin, S. *Energy Environ. Sci.* **2011**, 4, 56.

[105] Du, C. ; Gao, C. ; Yin, G. ; Chen, M. ; Wang, L. *Energy Environ. Sci.* **2011**, 4, 1037.

[106] Nguyen, H.T. ; Zamfir, M.R. ; Duong, L.D. ; Lee, Y.H. ; Bondavalli, P. ; Pribat, D. *J. Mater. Chem.* **2012**, 22, 24618.

[107] Seo, J.-W. ; Jang, J.-T. ; Park, S.-W. ; Kim, C. ; Park, B. ; Cheon, J. *Adv. Mater.* **2008**, 20, 4269.

[108] Luo, B. ; Fang, Y. ; Wang, B. ; Zhou, J. ; Song, H. ; Zhi, L. *Energy Environ. Sci.* **2012**, 5, 5226.

[109] Ji, X. ; Nazar, L.F. *J. Mater. Chem.* **2010**, 20, 9821.

[110] Cai, K. ; Song, M.-K. ; Cairns, E.J. ; Zhang, Y. *Nano Lett.* **2012**, 12, 6474.

[111] Arico, A.S. ; Bruce, P. ; Scrosati, B. ; Tarascon, J.-M. ; Schalkwijk, W.V. *Nat. Mater.* **2005**, 4, 366.

[112] Tarascon, J.-M. ; Armand, M. *Nature*, **2001**, 414, 359.

[113] Whittingham, M.S. *Chem. Rev.* **2004**, 104, 4271.

[114] Marom, R. ; Amalraj, S.F. ; Leifer, N. ; Jacob, D. ; Aurbach, D. *J. Mater. Chem.* **2011**, 21, 9938.

[115] Cabana, J. ; Monconduit, L. ; Larcher, D. ; Palacin M.R. *Adv. Energ. Mater.* **2010**, 22, E170.

[116] Liu, X.H. ; Huang, J.Y. *Energy Environ. Sci.* **2011**, 4, 3844.

[117] Etacheri, V. ; Marom, R. ; Elazari, R. ; Salitra, G. ; Aurbach, D. *Energy Environ. Sci.* **2011**, 3243.

[118] Scrosati, B. ; Hassoun, J. ; Sun, Y.-K. *Energy Environ. Sci.* **2011**, 4, 3287.

[119] Manthiram, A. *J. Phys. Chem. Lett.* **2011**, 2, 176.

[120] Liwen, J. ; Lin, Z. ; Alcoutlabi, M. ; Zhang, X. *Energy Environ. Sci.* **2011**, 4, 2682.

[121] Wu, H.B. ; Chen, J.S. ; Hng, H.H. ; Lou, X.W. *Nanoscale*, **2012**, 4, 2526.

[122] Dickinson, R.G. ; Pauling, L. *J. Amer. Chem. Soc.* **1923**, 45, 1466.

[123] Bell, R.E. ; Herfert, R.E. *J. Am. Chem. Soc.* **1957**, 79(13), 3351.

[124] Traill, R.J. *Can. Mineral*, **1963**, 7, 524.

[125] Wildervanck, J.C. ; Jellinek, F. *Z. Anorg. Allg. Chem.* **1964**, 328, 309.

[126] Takeuchi, Y. ; Nowacki, W. *Schweiz. Mineral. Petrogr. Mitteil.* **1964**, 44, 105.

[127] Wickman, F.E. ; Smith, D.K. *Am. Mineral.* **1970**, 55, 1843.

[128] Wilson, J.A. ; Yoffe, A.D. *Advan. Phys.* **1969**, 18, 193.

[129] Connell, G.A.N. ; Wilson, J.A. ; Yoffe, A.D. *J. Phys. Chem. Solids*, **1969**, 30, 287.

[130] Newberry, R.J.J. *Am. Mineral.* **1979**, 64, 758.

[131] Schonfeld, B. ; Huang, J.J. ; Moss, S.C. *Acta Cryst.* **1983**, B39, 404.

[132] Bronsema, K.D. ; De Boer, J.L. ; Jellinek, F. *Z. Anorg. Allg. Chem.* **1986**, 540/541, 15.

[133] Fleischauer, P.D. ; Lince, J.R. ; Bertrand, P.A. ; Bauer, R. *Langmuir*, **1989**, 5, 1009.

[134] Didziulis, S.V. ; Lince, J.R. ; Shuh, D.K ; Durbin, T.D. ; Yarmoff, J.A. *J. Electron Spec. Rel. Phenom.* **1992**, 60, 175.

[135] Wypych, F. ; Schollhorn, R. *J. Chem. Soc. Chem. Commun.* **1992**, 19, 1386.

[136] Rovira, C. ; Whangbo, M.-H. *Inorg. Chem.* **1993**, 32, 4094.

[137] Goodenough, J.B. ; Dutta, G. ; Manthiram, A. *Phys. Rev. B.* **1991**, 43, 10170.

[138] Guay, D. *Chem. Mater.* **1994**, 6, 614.

[139] El Beqqali, O. ; Zorkani, I. ; Rogemond, F. ; Chermette, H. ; Ben Chaabane, R. ; Gamoudi, M.; Guillaud, G. *Synth. Met.* **1997**, 90, 165.

[140] Wypych, F. ; Weber, Th. ; Prins, R. *Chem. Mater.* **1998**, 10, 723.

[141] Wypych, F. ; Solenthaler, C. ; Prins, R. ; Weber, Th. *J. Solid State Chem.* **1999**, 144, 430.

[142] Benavente, E. ; Santa Ana, M.A. ; Mendizabal, F. ; Gonzalez, G. *Coordin. Chem. Rev.* **2002**, 224, 87.

[143] Mattheiss, L.F. *Phys. Rev. B.* **1973**, 8, 3719.

[144] Lu, P. ; Wu, X. ; Guo, W. ; Zeng, X.C. *Phys. Chem. Chem. Phys.* **2012**, 14, 13035.

[145] Zhou, Y. ; Yang, P. Zu, H. ; Gao, F. ; Zu, X. *Phys. Chem. Chem. Phys.* **2013**, 15, 10385.

[146] Py, M.A. ; Haering, R.R. *Can. J. Phys.* **1983**, 61, 76.

[147] Pauling, L. *J. Am. Chem. Soc.* **1931**, 53, 1367.

[148] Hultgren, R. *Phys. Rev.* **1932**, 40, 891.

[149] Selwyn, L.S. ;McKinnon, W.R. ; von Sacken, U. ; Jones, C.A. *Solid State Ionics.* **1987**, 22, 337.

[150] Papageorgopoulos, C.A. ; Jaegermann, W. *Surf. Sci.* **1995**, 338, 83.

[151] Imanishi, N. ; Toyoda, M. ; Takeda, Y. ; Yamamoto, O. *Solid State Ionics.* **1992**, 58, 333.

[152] Gonzalez, G. ; Santa Ana, M.A. ; Benavente, E. ; Donoso, J.P. ; Bonagamba, T.J. ; Mello, N.C. ; Panepucci, H. *Solid State Ionics*, **1996**, 85, 225.

[153] Dungey, K.E. ; Curtis, M.D. ; Penner-Hahn, J.E. *Chem. Mater.* **1998**, 10, 2152.

[154] Zak, A. ; Feldman, Y. ; Lyakhovitskaya, V. ; Leitus, G. ; Popovitz-Biro, R. ; Wachtel, E. ; Cohen, H. ; Reich, S. ; Tenne, R. *J. Am. Chem. Soc.* **2002**, 124, 4747.

[155] Tonti, D. ; Pettenkofer, C. ; Jaegermann, W. *J. Phys. Chem. B.* **2004**, 108, 16093.

[156] Chen, J. ; Tao, Z.-L. ; Li, S.-L. *Angew. Chem, Int. Ed.* **2003**, 42, 2147.

[157] Julien, C.M. *Mater. Sci. Eng.* **2003**, R40, 47.

[158] Kim, Y. ; Goodenough, J.B. *J. Phys. Chem. C.* **2008**, 112, 15060.

[159] Feng, C. ; Ma, J. ; Li, H. ; Zeng, R. ; Guo, Z. ; Liu, H. *Mat. Res. Bull.* **2009**, 44, 1811.

[160] Chrissafis, K. ; Zamani, M. ; Kambas, K. ; Stoemenos, J. ; Economou, N.A. ; Samaras, I. ; Julien, C. *Mat. Sci. Eng.* **1989**, B3, 145.

[161] Li, Y. ; Wu, D. ; Zhou, Z. ; Cabrera, C.R. ; Chen, Z. *J. Phys. Chem. Lett.* **2012**, 3, 2221.

[162] Yang, D. ; Sandoval, S.J. ; Divigalpitiya, W.M.R. ; Irwin, J.C. ; Frindt, R.F. *Phys. Rev. B.* **1991**, 43(14), 12053.

[163] Zubavichus, Y.V. ; Slovokhotov, Y.L.; Schilling, P.J. ; Tittsworth, R.C. ; Golub, A.S. ; Protzenko, G.A. ; Novikov, Y.N. *Inorg. Chim. Acta*, **1998**, 280, 211.

[164] Heising, J. ; Kanatzidis, G. *J. Am. Chem. Soc.* **1999**, 121, 11720.

[165] Dahn, J.R. ; Zheng, T. ; Liu, Y. ; Xue, J.S. *Science*, **1995**, 270, 590.

[166] Mulhern, P.J. *Can. J. Phys.* **1989**, 67, 1049.

[167] Hayes, W.M. (Ed.) ; Lide, D.R. (Ed.). *CRC Handbook of Chemistry and Physics, Internet Version,* **2012***,* 92nd Ed. CRC Press: Boca Raton, Florida, pp. 9-50, 12-11.

[168] Du, G. ; Guo, Z. ; Wang, S. ; Zeng, R. ; Chen, Z. ; Liu, H. *Chem. Comm.* **2010**, 46, 1106.

[169] Chang, K. ; Chen, W. ; Ma, L. ; Li, H. ; Li, H. ; Huang, F. ; Xu, Z. ; Zhang, Q. ; Lee, J.-Y. *J. Mater. Chem.* **2011**, 21, 6251.

[170] Chang, K. ; Chen, W. *ACS Nano*, **2011**, 5(6), 4720.

[171] Wang, Q. ; Li, J. *J. Phys. Chem. C.* **2007**, 111, 1675.

[172] Das, S.K. ; Mallavajula, R. ; Jayaprakash, N. ; Archer, L.A. *J. Mater. Chem.* **2012**, 22, 12988.

[173] Li, H. ; Li, W. ; Ma, L. ; Chen, W. ; Wang, J. *J. Alloys and Compounds,* **2009**, 471, 442.

[174] Ding, S. ; Zhang, D. ; Chen, J.S. ; Lou, X.W. *Nanoscale.* **2012**, 4, 95.

[175] Ding, S. ; Chen, J.S. ; Lou, X.W. *Chem. Eur. J.* **2011**, 17, 13142.

[176] Kwon, J.-H. ; Ahn, H.-J. ; Jeon, M.-S. ; Kim, K.-W. ; Ahn, I.-S. ; Ahn, J.-H. ; Wang, G. ; Ryu, H.-S. *Res. Chem. Intermed.* **2010**, 36, 749.

[177] Fang, X. ; Guo, X. ; Mao, Y. ; Hua, C. ; Shen, L. ; Hu, Y. ; Wang, Z. ; Wu, F. ; Chen, L. *Chem. Asian J.* **2012**, 7, 1013.

[178] Fang, X. ; Yu, X. ; Liao, S. ; Shi, Y. ; Hu, Y.S. ; Wang, Z. ; Stucky, G.D. ; Chen, L. *Micropor. Mesopor. Mat.* **2012**, 151, 418.

[179] Fang, X. ; Hua, C. ; Guo, X. ; Hu, Y. ; Wang, Z. ; Gao, X. ; Wu, F. ; Wang, J. ; Chen, L. *Electrochim. Acta.* **2012**, 81, 155.

[180] Xiao, J. ; Choi, D. ; Cosimbescu, L. ; Koech, P. ; Liu, J. ; Lemmon, J.P. *Chem. Mater.* **2010**, 22, 4522.

[181] Xiao, J. ; Wang, X. ; Yang, X.Q. ; Xun, S. ; Liu, G. ; Koech, P.K. ; Liu, J. ; Lemmon, J.P. *Adv. Funct. Mater.* **2011**, 21, 2840.

[182] Zhou, X. ; Wan, L.-J. ; Guo, Y.-G. *Nanoscale*, **2012**, 4, 5868.

[183] Rauh, R.D.; Abraham, K.M.; Pearson, G.F.; Surprenant, J.K.; Brummer, S.B. *J. Electrochem. Soc.* **1979**, 126, 523.

[184] Yamin, H. ; Peled, E. *J. Power Sources,* **1983**, 9, 281.

[185] Liang, C. ; Dudney, N.J. ; Howe, J.Y. *Chem. Mater.* **2009**, 21, 4724.

[186] Ji, X. ; Lee, K.T. ; Nazar, L.F. *Nat. Mater.* **2009**, 8(6), 500.

[187] Zhang, B. ; Qin, X. ; Li, G.R. ; Gao, X.P. *Energy Environ. Sci.* **2010**, 3, 1531.

[188] Gao, X.-P. ; Yang, H.-X. *Energy Environ. Sci.* **2010**, 3, 174.

[189] Ellis, B.L. ; Lee, K.T. ; Nazar, L.F. *Chem. Mater.* **2010**, 22, 691.

[190] Chen, J.-J. ; Zhang, Q. ; Shi, Y.-N. ; Qin L.-L. ; Cao, Y. ; Zheng, M.-S. ; Dong, Q.-F. *Phys. Chem. Chem. Phys.* **2012**, 14, 5376.

[191] Park, M.S. ; Yu, J.-S. ; Kim, K.J. ; Jeong, G. ; Kim, J.-H. ; Jo, Y.-N. ; Hwang, U. ; Kang, S. ; Woo, T. ; Kim, Y.-J. *Phys. Chem. Chem. Phys.* **2012**, 14, 6796.

[192] Dorfler, S. ; Hagen, M. ; Althues, H. ; Tubke, J. ; Kaskel, S. ; Hoffmann, M.J. *Chem. Commun.* **2012**, 48, 4097.

[193] Ahn, W. ; Kim, K.-B. ; Jung, K.-N. ; Shin, K.-H. ; Jin, C.-S. *J. Power Sources*, **2012**, 202, 394.

[194] Enyashin, A.N. ; Ivanovskii, A.L. *Semicond.* **2007**, 41(1), 81.

[195] Deepak, F.L. ; Jose-Yacaman, M. *Isr. J. Chem.* **2010**, 50, 426.

[196] Pan, H. ; Zhang, Y.-W. *J. Mater. Chem.* **2012**, 22, 7280.

[197] Enyashin, A. ; Gemming, S.; Seifert, G. *Eur. Phys. J. Special Topics.* **2007**, 149, 103.

[198] Weiss, W. ; Bohne, W. ; Rohrich, J. ; Strub, E. ; Bloeck, U. ; Sieber, I. ; Ellmer, K. ; Mientus, R. ; Prosch, F. *J. Appl. Phys.* **2004**, 95(12), 7665.

[199] Chan, Y. ; Hill, J.M. *Nanoscale Res. Lett.* **2011**, 6, 203.

[200] Kibsgaard, J. ; Lauritsen, J.V. ; Laegsgaard, E. ; Clausen, B.S. ; Topsoe, H. ; Besenbacher, F. *J. Am. Chem. Soc.* **2006**, 128, 13950.

[201] Enyashin, A.N. ; Bar-Sadan, M. ; Sloan, J. ; Houben, L. ; Seifert, G. *Chem. Mater.* **2009**, 21, 5627.

[202] Tuxen, A. ; Kibsgaard, J. ; Gobel, H. ; Laegsgaard, E. ; Topsoe, H. ; Lauritsen, J.V. ; Besenbacher, F. *ACS Nano.* **2010**, 4(8), 4677.

[203] Castro-Guerrero, C.F. ; Deepak, F.L. ; Ponce, A. ; Cruz-Reyes, J. ; Valle Granados, M.D. ; Fuentes-Moyado, S. ; Galvan, D.H. ; Jose Yacaman, M. *Catal. Sci. Technol.* **2011**, 1, 1024.

[204] Kochubei, D.I. ; Rogov, V.A. ; Babenko, V.P. ; Bogdanov, S.V. ; Zaikovskii, V.I. *Kinet. Catal.* **2003**, 44, 135.

[205] Balke, N. ; Jesse, S. ; Morozovska, A.N. ; Eliseev, E. ; Chung, D.W. ; Kim, Y. ; Adamczyk, L. ; Garcia, R.E. ; Dudney, N. ; Kalinin S.V. *Nature Nanotech.* **2010**, 5, 749.

[206] Mao, Y. ; Duan, H. ; Xu, B. ; Zhang, L. ; Hu, Y. ; Zhao, C. ; Wang, Z. ; Chen, L. ; Yang, Y. *Energy Environ. Sci.* **2012**, 5, 7950.

[207] Wang, Y.-X. ; Huang, L. ; Sun, L.-C. ; Xie, S.-Y. ; Xu, G.-L. ; Chen, S.-R. ; Xu, Y.-F. ; Li, J. T. ; Chou, S.-L. ; Dou, S.-X. ; Sun, S.-G. *J. Mater. Chem.* **2012**, 22, 4744.

[208] Elazari, R. ; Salitra, G. ; Garsuch, A. ; Panchenko, A. ; Aurbach, D. *Adv. Mater.* **2011**, 23, 5641.

[209] Su, Y.-S. ; Manthiram, A. *Chem. Comm.* **2012**, 48, 8817.

[210] Li, X. ; Cao, Y. ; Qi, W. ; Saraf, L.V. ; Xiao, J. ; Nie, Z. ; Mietek, J. ; Zhang, J.-G. ; Schwenzer, B. ; Liu, J. *J. Mater. Chem.* **2011**, 21, 16603.

[211] Jamnik, J. ; Maier, J. *Phys. Chem. Chem. Phys.* **2003**, 5, 5215.

[212] Yang, Y. ; McDowell, M.T. ; Jackson, A. ; Cha, J.J. ; Hong, S.S. ; Cui, Y. *Nano Lett.* **2010**, 10, 1486.

[213] Li, Y. ; Tan, B. ; Wu, Y. *Nano Lett.* **2008**, 8, 265.

[214] Qie, L. ; Chen, W.-M. ; Wang, Z.-H. ; Shao, Q.-G. ; Li, X. ; Yuan, L.-X. ; Hu, X.-L. ; Zhang, W.-X. ; Huang, Y.-H. *Adv. Mater.* **2012**, 24, 2047.

[215] Laruelle, S. ; Grugeon, S. ; Poizot, P. ; Dolle, M. ; Dupont, L. ; Tarascon, J.-M. *J. Electrochem. Soc.* **2002**, 149(5), A627.

[216] Dedryvere, R. ; Laruelle, S. ; Grugeon, S. ; Poizot, P. ; Gonbeau, D. ; Tarascon, J.-M. *Chem. Mater.* **2004**, 16, 1056.

[217] Shi, Y. ; Guo, B. ; Corr, S.A. ; Shi, Q. ; Hu, Y.-S. ; Heier, K.R. ; Chen, L. ; Seshardri, R. ; Stucky, G.D. *Nano Lett.* **2009**, 9(12), 4215.

[218] Balaya, P. ; Li, H. ; Kienle, L. ; Maier, J. *Adv. Funct. Mater.* **2003**, 13(8), 621.

[219] Zhai, C. ; Du, N. ; Zhang, H. ; Yu, J. ; Wu, P. ; Xiao, C. ; Yang, D. *Nanoscale*, **2011**, 3, 1798.

[220] Bindumadhavan, K. ; Srivastava, S.K. ; Mahanty, S. *Chem. Commun,* **2013**, 49, 1823.

[221] Marschilok, A. ; Lee, C.-Y. ; Subramanian, A. ; Takeuchi, K.J. ; Takeuchi, E.S. *Energy Environ. Sci.* **2011**, 4, 2943.

[222] Zhou, G. ; Wang, D.-W. ; Hou, P.-X. ; Li, W. ; Li, N. ; Liu, C. ; Li, F. ; Cheng, H.-M. *J. Mater. Chem.* **2012**, 22, 17942.

[223] Park, S.-K. ; Yu, S.-H. ; Woo, S. ; Quan, B. ; Lee, D.-C. ; Kim, M.K. ; Sung, Y.-E. ; Piao, Y. *Dalton Trans.* **2013**, 42, 2399.

[224] Lee, S.W. ; Gallant, B.M. ; Byon, H.R. ; Hammond, P.T. ; Shao-Horn, Y. *Energy Environ. Sci.* **2011**, 4, 1972.

[225] Cao, X. ; Shi, Y. ; Shi, W. ; Rui, X. ; Yan, Q. ; Kong, J. ; Zhang, H. *Small,* **2013**, 9(20), 3433.

[226] Xi, J. ; Long, M.L. ; Tang, L. ; Wang, D. ; Shuai, Z. *Nanoscale,* **2012**, 4, 4348.

[227] Jia, X. ; Campos-Delgado, J. ; Terrones, M. ; Meunier, V. ; Desselhaus, M.S. *Nanoscale*, **2011**, 3, 86.

[228] Zhou, X. ; Wan, L.-J. ; Guo, Y.-G. *Chem. Commun.* **2013**, 49, 1838.

[229] Chang, K. ; Geng, D. ; Li, X. ; Yang, J. ; Tang, Y. ; Cai, M. ; Li, R. ; Sun, X. *Adv. Funct. Mater.* **2013**, 3, 839.

[230] Wang, H. ; Holt, C.M.B. ; Li, Z. ; Tan, X. ; Amirkhiz, B.S. ; Xu, Z. ; Olsen, B.C. ; Stephenson, T. ; Mitlin, D. *Nano Research*, **2012**, 5, 605-617.

[231] Hummers, W.S. ; Offeman, R.E. *J. Am. Chem. Soc.* **1958**, 80(6), 1339.

[232] Chen, W. ; Zhu, Z. ; Li, S. ; Chen, C. ; Yan, L. *Nanoscale*, **2012**, 4, 2124.

[233] Malik, S. ; Vijayaraghavan, A. ; Erni, R. ; Arida, K. ; Khalakhan, I. ; Hill, J.P. *Nanoscale*, **2010**, 2, 2139.

[234] Xu, Z. ; Li, Z. ; Tan, X. ; Holt, C.M.B. ; Zhang, L. ; Shalchi-Amirkhiz, B. ; Mitlin, D. *RSC Advances*, **2012**, 2, 2753.

[235] Ma, Y. ; Dai, Y. ; Guo, M. ; Niu, C. ; Huang, B. *Nanoscale*, **2011**, 3, 3883.

[236] Jiang, H. ; Zhao, T. ; Yan, C. ; Ma, J. ; Li, C. *Nanoscale*, **2010**, 2, 2195.

[237] Cao, F.-F. ; Guo, Y.-G. ; Wan, L.-J. *Energy Environ. Sci.* **2011**, 4, 1634.

[238] Jung, H.-G. ; Myung, S.-T. ; Yoon, C.S. ; Son, S.-B. ; Oh, K.H. ; Amine, K. ; Scrosati, B. ; Sun, Y.-K. *Energy Environ. Sci.* **2011**, 4, 1345.

[239] Lei, D. ; Zhang, M. ; Qu, B. ; Chen, L. ; Wang, Y. ; Zhang, E. ; Xu, Z. ; Li, Q. ; Wang, T. *Nanoscale,* **2012**, 4, 3422.

[240] Liu, H. ; Su, D. ; Zhou, R. ; Sun, B. ; Wang, G. ; Qiao, S.Z. *Adv. Energy Mater.* **2012**, 2, 970.

[241] Saravanan, K. ; Ananthanarayanan, K. ; Balaya, P. *Energy Environ. Sci.* **2010**, 3, 939.

[242] Srolovitz, D.J. ; Safran, S.A. ; Homyonfer, M. ; Tenne, R. *Phys. Rev. Lett.* **1995**, 74(10), 1779.

[243] Xiong, Y. ; Xie, Y. ; Li, Z. ; Li, X. ; Zhang, R. *Chem. Phys. Lett.* **2003**, 382, 180.

[244] Alexandrou, I. ; Sano, N. ; Burrows, A. ; Meyer, R.R. ; Wang, H. ; Kirkland, A.I. ; Kiely, C.J. ; Amaratunga, G.A.J. *Nanotech.* **2003**, 14, 913.

[245] Bar-Sadan, M. ; Enyashin, A.N. ; Gemming, S. ; Popovitz-Biro, R. ; Hong, S.Y. ; Prior, Y. ; Tenne, R. ; Seifert, G. *J. Phys. Chem. B.* **2006**, 110, 25399.

[246] Chang, L. ; Yang, H. ; Fu, W. ; Zhang, J. ; Yu, Q. ; Zhu, H. ; Chen, J. ; Wei, R. ; Sui, Y. ; Pang, X. ; Zou, G. *Mater. Res. Bull.* **2008**, 43, 2427.

[247] Li, T. ; Galli, G. *J. Phys. Chem. C.* **2007**, 111, 16192.

[248] Frey, G.L. ; Tenne, R. *J. Mater. Res.* **1998**, 13(9), 1998, 2412.

[249] Seifert, G. ; Terrones, H. ; Terrones, M. ; Jungnickel, G. ; Frauenheim, T. *Phys. Rev. Lett.* **2000**, 85(1), 146.

[250] Tenne, R. ; Rao, C.N.R. *Phil. Trans. R. Soc. Lond. A.* **2004**, 362, 2099.

[251] Tenne, R. ; Seifert, G. *Annu. Rev. Mater. Res.* **2009**, 39, 387.

[252] Zibouche, N. ; Kuc, A. ; Heine, T. *Eur. Phys. J. B.* **2012**, 85(49), 1.

[253] Hassanien, A. ; Tokumoto, M. ; Mrzel, A. ; Mihailovic, D. ; Kataura, H. *Physica E.* **2005**, 29, 684.

[254] Hassanien, A. ; Leintschnig, G. ; Mrzel, A. ; Tokumoto, M. ; Kataura, H. *Surf. Interface Anal.* **2006**, 38, 1530.

[255] Kibsgaard, J. ; Tuxen, A. ; Levisen, M. ; Laegsgaard, E. ; Gemming, S. ; Seifert, G. ; Lauritsen, J.V. ; Besenbacher, F. *Nano Lett.* **2008**, 8(11), 3928.

[256] Heising, J. ; Kanatzidis, M.G. *J. Am. Chem. Soc.* **1999**, 121, 638.

[257] Li, Q. ; Newberg, J.T. ; Walter, E.C. ; Hemminger, J.C. ; Penner, R.M. *Nano Lett.* **2004**, 4(2), 277.

[258] Li, Y. ; Zhou, Z. ; Zhang, S. ; Chen, Z. *J. Am. Chem. Soc.* **2008**, 130, 16739.

[259] Brivio, J. ; Alexander, D.T.L. ; Kis, A. *Nano Lett.* **2011**, 11, 5148.

[260] Wang, Z. ; Li, H. ; Liu, Z. ; Shi, Z. ; Lu, J. ; Suenaga K. ; Joung, S.-K. ; Okazaki, T. ; Gu, Z. ; Zhou, J. ; Gao, Z. ; Li, G. ; Sanvito, S. ; Wang, E. ; Iijima, S. *J. Am. Chem. Soc.* **2010**, 132, 13840.

[261] Matte, H.S.S.R. ; Gomathi, A. ; Manna, A.K. ; Late, D.J. ; Datta, R. ; Pati, S.K. ; Rao, C.N.R. *Angew. Chem. Int. Ed.* **2010**, 49, 4059.

[262] Balendhran, S. ; Ou, J.Z. ; Bhaskaran, M. ; Sriram, S. ; Ippolito, S. ; Vasic, Z. ; Kats, E. ; Bhargava, S. ; Zhuiykov, S. ; Kalatar-zadeh, K. *Nanoscale*, **2012**, 4, 461.

[263] Remskar, M. ; Mrzel, A. ; Skraba, Z. ; Jesih, A. ; Ceh, M. ; Demsar, J. ; Stadelmann, P. ; Levy, F. ; Mihailovic, D. *Science.* **2001**, 292, 479.

[264] Terrones, H. ; Terrones, M. *New J. Phys.* **2003**, 5, 126.1.

[265] Zelenski, C.M. ; Dorhout, P.K. *J. Am. Chem. Soc.* **1998**, 120, 734.

[266] Jia, X. ; Chen, Z. ; Suwarnasarn, A. ; Rice, L. ; Wang, X. ; Sohn, H. ; Zhang, Q. ; Wu, B.M. ; Wei, F. ; Lu, Y. *Energy Environ. Sci.* **2012**, 5, 6845.

[267] Hsu, W.K. ; Chang, B.H. ; Zhu, Y.Q. ; Han, W.Q. ; Terrones, H. ; Terrones, M. ; Grobert, N. ; Cheetham, A.K. ; Kroto, H.W. ; Walton, D.R.M. *J. Am. Chem. Soc.* **2000**, 122, 10155.

[268] Feldman, Y. ; Frey, G.L. ; Homyonfer, M. ; Lyakhovitskaya, V. ; Margulis, L. ; Cohen, H. ; Hodes, G. ; Hutchison, J.L. ; Tenne, R. *J. Am. Chem. Soc.* **1996**, 118, 5362.

[269] German, C.R.S. ; Santiago, P. ; Ascencio, J.A. ; Pal, U. ; Perez-Alvarez, M. ; Rendon, L. ; Mendoza, D. *J. Phys. Chem. B.* **2005**, 109, 17488.

[270] Shi, Y. ; Wan, Y. ; Liu, R. ; Tu, B. ; Zhao, D. *J. Am. Chem. Soc.* **2007**, 129, 9522.

[271] Adeogun, A. ; Afzaal, M. ; O'Brien, P. *Chem. Vap. Deposition*. **2006**, 12, 597.

[272] Zhang, J. ; Soon, J.M. ; Loh, K.P. ; Yin, J. ; Ding, J. ; Sullivian, M.B. ; Wu, P. *Nano Lett.* **2007**, 7(8), 2370.

[273] Lee, Y.H. ; Zhang, X.-Q. ; Zhang, W. ; Chang, M.-T. ; Lin, C.-T. ; Chang, K. D. ; Yu, Y.-C. ; Wang, J.T.-W. ; Chang, C.-S. ; Li, L.-J. ; Lin, T.-W. *Adv. Mater.* **2012**, 24, 2320.

[274] Remskar, M. ; Mrzel, A. ; Virsek, M. ; Godec, M. ; Krause, M. ; Kolitsch, A. ; Singh, A. ; Seabaugh, A. *Nanoscale Res. Lett.* **2011**, 6(26), 1.

[275] Fleischauer, P.D. *Thin Solid Films*, **1987**, 154, 309.

[276] Wu, H. ; Yang, R. ; Song, B. ; Han, Q. ; Li, J. ; Zhang, Y. ; Fang, Y. ; Tenne, R. ; Wang, C. *ACS Nano.* **2011**, 5(2), 1276.

Concluding remarks

A range of interesting topics have been covered in this thesis, and we have learned a great deal about corrosion, fouling and lithium ion batteries. In Chapter 2 we explored the fouling behaviour of 316 stainless steel and pure iron when they were exposed to a high temperature sulfidic environment with a high fouling propensity. The atmospheric resid (340 °C+) used in those experiments was seen to produce a great deal of foulant at the testing temperatures of 316 stainless steel and pure iron (540±9 °C and 508±12 °C respectively). The foulant was observed to be a combination of coke and sulfide. The sulfide was shown to be delaminating from the metal surfaces in plumes and as layers. This was indicative of its formation at the surface of the metal, via an overall corrosion mechanism in which H_2S was the primary species attacking the metal surface, producing mixed metal sulfides. XRD data revealed that the sulfide phase was primarily pyrrhotite ($Fe_{(1-x)}S$).

In this work, the link between sulfidation and coking was elucidated. The sulfide that is produced from corrosion at the metal surface is a well-recognized catalyst for a number of reactions known to be involved in the coking process. ie: dehydrogenation, desulfurization and condensation reactions. Together, these processes form a foulant on the heat transfer surface that is a mixture of an organic phase (carbonaceous in nature) and an inorganic phase (primarily sulfide). The pure iron wires fouled approximately twice as much as the 316 stainless steel

as expected. Fouling factors of approximately 100 mm^2K/W and 50 mm^2K/W were measured respectively after 250 minutes at temperature.

In Chapter 3 the link between corrosion and fouling was further elucidated, and a mitigation strategy was applied. The corrosion and fouling behaviour was evaluated out to a fouling time of 1400 minutes for 316 stainless steel, and the fouling behaviour was asymptotic in nature. Sulfide plumes were observed to form, and protrude radially from the heat transfer surface. The foulant reached a thickness of 160 μm at 1400 minutes, and the corresponding final fouling factor was approximately 1200 mm^2K/W.

Thiophene was added to the oil in an attempt to mitigate fouling. Since iron sulfide is known to catalyze a range of reactions that are significant to the formation of organic foulant, the hypothesis was that adding a species that would interact with the catalyst preferentially, should reduce foulant formation. The addition of 5.7 vol% thiophene reduced the fouling factor from 1200 mm^2K/W in the baseline, to below 60 mm^2K/W after 1400 minutes at temperature. The mechanism proposed was the preferential adsorption of thiophene at catalytic sites on the heat transfer surface. The thermal stability of thiophene allowed the molecule to remain intact even at temperatures in excess of 540 °C. By competing with surface adsorption sites, thiophene was able to reduce the frequency of other reactants forming coke products at the heat transfer surface.

It should be mentioned that thiophene is a small aromatic molecule that will also act as a solvent for asphaltenes in the oil mixture. As previously explained in Chapter 1, resins and aromatics are considered responsible for the solubility of asphaltene agglomerates. Therefore, adding thiophene to the oil likely improved the solubility of asphaltenes, and attenuated fouling in this way. In this work, the added solvency effect of thiophene on the fouling behaviour was not decoupled from the overall mechanism. This remains a possible area for further study. However, it was clearly seen in the experimental results that thiophene had the effect of attenuating not only the amount of organic foulant, but also the amount of inorganic foulant. The reduction in surface corrosion in the thiophene samples was a direct indication that thiophene is a surface active compound that blocks adsorption sites. If the sole mechanism of foulant attenuation was from a solubility effect, it is highly unlikely that any reduction in surface corrosion would have been observed in the wires. Thiophene was seen as effective at reducing surface corrosion, presumably by competing with the adsorption of H_2S at the wire surface.

Chapter 4 provided an in depth look at lithium ion batteries and provided a summary of what is known about the charge/discharge mechanisms of molybdenum disulfide. The incorporation of a carbon phase with MoS_2 to form a nanocomposite material was shown to greatly enhance the electrochemical properties of the electrode. It was also shown that there is significant debate in the scientific community regarding the charge/discharge behaviour of MoS_2.

However, a careful examination of the literature revealed a considerable amount of evidence to support what is currently the minority view about the mechanism. After the first discharge cycle, MoS_2 decomposes into metallic molybdenum and lithium sulfide. After this decomposition, the battery functions as a lithium-sulfur system, with the molybdenum metal particles enhancing the conductivity of the active material. My own experiments were also shown to support this finding (Appendix B).

The theoretical capacity of MoS_2 was also discussed, as experimental values are often reported in excess of the theoretical value. It may be that the theoretical capacity of the composite electrode has been underestimated, as there are phases present that could contribute to the capacity but are not accounted for in the calculations. While the exact reason for this remains to be proven, the large capacity of the active material is likely a linear combination of some fraction of Li_2S, a nanodispersed carbon, and nanoparticles of molybdenum metal.

References

Chapter 1

[1] Wiehe, I.A. *Process Chemistry of Petroleum Macromolecules.* CRC Press, Boca Raton Fl, USA, **2008**, 97-179.

[2] Pillon, L.Z. *Interfacial Properties of Petroleum Products*. CRC Press, Boca Raton Fl, USA, **2008**, 1-37, 123-149.

[3] Gray, M.R. *Upgrading Petroleum Residues and Heavy Oils.* Marcel Dekker Inc. New York, USA, **1994**, 237-260.

[4] Self, F. ; Ekholm, E. ; Bowers, K. *Refining Overview-Petroleum, Processes, and Products.* CD-Rom, AIChE – South Texas Section, **2000**.

[5] Rana, M.S. ; Samano, V. ; Ancheyta, J. ; Diaz, J.A.I. *Fuel*, **2007**, 86, 1216-1231.

[6] Speight, J.G. *The Chemistry and Technology of Petroleum*. 4th Ed. **2007**, CRC Press, Boca Raton, FL, 521-597.

[7] Cheng, F. ; Chen, J. ; Guo, X. *Adv. Mater.* **2006**, 18, 2561-2564.

[8] Moses, P.G. ; Hinnemann, B. ; Topsoe, H. ; Norskov, J.K. *J. Catal.* **2009**, 268, 201-208.

[9] Huang, Y. ; Zhou, Z. ; Qi, Y. ; Li, X. ; Cheng, Z. ; Yuan, W. *Chem. Eng. J.* **2011**, 172, 444-451.

[10] Castillo-Villalon, P. ; Ramirez, J. ; Castaneda, R. *J. Catal.* **2012**, 294, 54-62.

[11] Rao, B.G. ; Ramakrishna Matte, H.S.S. ; Chaturbedy, P. ; Rao, C.N.R. *ChemPlusChem*, **2013**, 78, 419-422.

[12] Menoufy, M.F. ; Ahmed, H.S. ; Betiha, M.A. ; Sayed, M.A. *Fuel*, **2014**, 119, 106-110.

[13] Thakur, D.S. *J. Catal.* **1985**, 94, 310-312.

[14] Embaid, B.P. ; Biomorgi, J.G. ; Gonzalez-Jimenez, F. ; Perez-Zurita, M.J. ; Scott, C.E. *Appl. Catal. A: General*, **2011**, 400, 166-170.

[15] Raje, A.P. ; Dadyburjor, D.B. *Ind. Eng. Chem. Res.* **1993**, 32, 1637-1644.

[16] Diaz, Y. ; Sevilla, A. ; Monaco, A. ; Mendez, F.J. ; Rosales, P. ; Garcia, L. ; Brito, J.L. *Fuel*, **2013**, 210, 235-248.

[17] Zaera, F. ; Kollin, E.B. ; Gland, J.L. *Langmuir*, **1987**, 3(4), 555-557.

[18] Dos Santos, N. ; Dulot, H. ; Marchal, N. ; Vrinat, M. *Appl. Catal. A*, **2009**, 352, 114-123.

[19] Li, Z. ; Wang, G. ; Liu, Y. ; Gao, J. ; Xu, C. ; Liang, Y. ; Wang, X. *Fuel Proc. Technol.* **2013**,115, 1-10.

[20] Valencia, D. ; Olivares-Amaya, R. ; Aburto, J. ; Garcia-Cruz, I. *Catal. Lett.* **2013**, 143, 1354-1361.

Chapter 2

[1] Gentzis, T.; Parker, R. J.; McFarlane, R. A. *Fuel.* **2000**, 79, 1173-1184.

[2] Hong E.; and Watkinson A.P. *Heat Transf. Eng*. **2009**, 30, 786–793.

[3] Rabou, L.P.L.M.; Zwart, R.W.R.; Vreugdenhil B.J.; Bos L. *Energy Fuels.* **2009**, 23, 6189-6198.

[4] Frandsen, F.J.; Pedersen A.J.; Hansen J.; Madsen O.H.; Lundtorp K.; Mortensen L. *Energy Fuels.* **2009**, 23, 3490–3496.

[5] Parker, R.J.; McFarlane, R.A. *Energy Fuels.* **2000**, 14, 11-13.

[6] Falkler, T.J.; Stark, J.L. *Oil and Gas Journal.* **2004**, 102, 72-74.

[7] Eaton, P.E.; Williams, J., Delayed Coker Furnace Fouling Control – Laboratory Correlation to Field Experience. In *NACE*, paper 8670, **2008**, 1-7.

[8] Eaton, P.E.; Newman, B.; Gray, M. Kubis, A.; Derakhshesh, M.; Holt, C.; Mitlin, D. Furnace Coker Simulations in a Laboratory Apparatus. *PetroPhase Conference*, paper O30, **2010**.

[9] Eaton, P.E., Salt Hydrolysis in Crude & Bitumen Fouling. *AIChE,* Spring Meeting, paper 103d, **2006**.

[10] Panchal, C.B. Understanding the Mechanism of FeS induced Fouling in Upgrading. *AIChE,* Spring Meeting, paper 103f, **2006**.

[11] Watkinson, A.P.; Wilson, D.I. *Exp. Therm. and Fluid Sci.* **1997**, 14, 361-374.

[12] Srinivasan, M.; Watkinson, A. P. *Heat Transf. Eng.* **2005**, 26(1), 7-14.

[13] Wu, X.A.; Chung, K. *Energy Fuels* **2007**, 21, 1212-1216.

[14] Eaton, P. E. Method and Apparatus for Conducting Fouling Tests. US Patent #4,910,999, 1990.

[15] Waldner, P.; Pelton, A.D. *J. of Phase Equilib. and Diffus.* **2005**, 26(1), 23-38.

[16] Pareek, V.K.; Ramanarayanan, T.A.; Mumford, J.D. *Catal. Lett.* **1997**, 46, 223-228.

[17] Brons, G.; Yu, J.M. *Energy Fuels.* **1995**, 9, 641-647.

[18] Attar, A. *J. AIChE.* **1978**, 24(1), 106-115.

[19] Gray M.R.; Le, T.; McCaffrey, W.C. *Ind. Eng. Chem. Res.* **2001**, 40, 3317-3324.

[20] Piazza, R. ; Parola, A. *J. of Phys: Cond. Matt.* **2008**, 20, 1-19.

[21] Qu, D.R.; Zheng, Y.G.; Jing, H.M.; Yao, Z.M.; Ke, W. *Corrosion Science*, **2006**, 48, 1960-1985.

[22] Shi, Q.A.; Zhao, S.Q.; Xu, Z.M.; Chung, K.H.; Zhang, Y.H.; Xu, C.M. *Energy Fuels,* **2010**, 24, 4005-4011.

[23] Liu, P.; Shi, Q.A.; Chung, K.H.; Zhang, Y.H.; Pan, N.; Zhao, S.Q.; Xu, C.M. *Energ. Fuels,* **2010**, 24, 5089-5096.

[24] Babaiankibala, E.; Craig, H.L.; Rusk, G.L.; Blanchard, K.V.; Rose, T.J.; Uehlein, B.L.; Quinter, R.C.; Summers, M.A. *Materials Performance*, **1993**, 32, 50-55.

[25] Ohmi, T.; Nakagawa, Y.; Nakamura, M.; Ohki, A.; Koyama, T. *J. Vac. Sci. Tech.* **1996**, 14(4), 2505-2510.

[26] Cheng, S-Y.; Kuan, S-L.; Tsai, W-T. *Corr. Sci.* **2006**, 48, 634-649

[27] Davis, J.R. *Heat-Resistant Materials*. ASM International, Materials Park, OH, **1997**, 148-150, 159-166.

[28] Haynes, W.M. Ed. CRC Handbook of Chemistry and Physics, 91st Edition (Internet Version 2011), CRC Press/Taylor and Francis, Boca Raton, FL. **2011**, 5-4 – 5-42.

[29] Lee, H.G. *Chemical Thermodynamics for Metals and Materials.* Imperial College Press, London UK, **1999**, 279.

[30] Young, D. *High Temperature Oxidation and Corrosion of Metals.* Elsevier Ltd. Oxford, UK, **2008**, 326-331.

[31] Davis, J.R. *Stainless Steels.* ASM International, Materials Park, OH, **1997**, 10.

[32] Mitlin, D.; Misra, A.; Radmilovic, V.; Nastasi, M.; Hoagland, R.; Embury, D.J.; Hirth, J.P.; Mitchell, T.E. *Phil. Mag.* **2004**, 84(7), 719-736.

[33] Mitlin, D.; Misra, A.; Mitchell, T.E.; Hirth, J.P.; Hoagland, R.G. *Phil. Mag.* **2005**, 85(28), 3379-3392.

[34] Wiehe, I.A. *J. of Dispersion Sci. Technol.* **2004**, 25, 333-339.

[35] Wiehe, I.A.; Kennedy, R.J.; Dickakian, G. *Energy Fuels*, **2001**, 15, 1057-1058.

[36] Wiehe I.A.; Kennedy R.J. *Energy Fuels*, **2000**, 14, 60-63.

Chapter 3

[1] Gentzis, T.; Parker, R. J.; McFarlane, R. A. *Fuel,* **2000**, *79(10)*, 1173-1184.

[2] Ebrahimi, S. ; Moghaddas, J.S. ; Aghjeh, M.K.R. *Fuel*, **2008**, *87*, 1623-1627.

[3] Wiehe, I.A. *Ind. Eng. Chem. Res.* **1993**, *32*, 2447-2454.

[4] Reyniers, M.-F.S.G. ; Froment, G.F. *Ind. Eng. Chem. Res.* **1995**, *34*, 773-785.

[5] Acevedo, S. ; Ranaudo, M.A. ; Escobar, G. ; Gutierrez, L. ; Ortega, P. *Fuel*, **1995**, *74(4)*, 595-598.

[6] Brons, G.; Yu, J.M. *Energ. Fuel.* **1995**, *9*, 641-647.

[7] Watkinson, A.P.; Wilson, D.I. *Exp. Therm. and Fluid Sci.* **1997**, *14*, 361-374.

[8] Lemke, H.K. ; Stephenson, W.K. *Petrol. Sci. Technol.* **1998**, *16(3)*, 335-360.

[9] Crittenden, B.D. ; Kolaczkowski, S.T. ; Phillips, D.Z. *Chemical Reaction Fouling*. 91-103. In *Understanding Heat Exchanger Fouling and its Mitigation*: Proceedings of an International Conference on Understanding Heat Exchanger Fouling and Its mitigation. Castelvecchio Pascoli, Italy, 1997. Ed. Bott, T.R. ; Melo, L.F. ; Panchal, C.B. Somerscales, E.F.C. Begell House Publishers Inc. Redding Connecticut, USA, **1999**.

[10] Parker, R.J.; McFarlane, R.A. *Energ. Fuel.* **2000**, *14*, 11-13.

[11] Costulchi, A. ; Garciafigueroa, E. ; Mar, B. ; Garcia-Borquez, A. ; Lara, V.H. ; Bosch, P. *Fuel*, **2002**, *81*, 413-421.

[12] Wang, J. ; Anthony, E.J. *Chem. Engg. Sci.* **2003**, *58*, 157-162.

[13] Gentzis, T. ; Rahimi, P.M. *Fuel*, **2003**, *82*, 1531-1540.

[14] Hong, E. ; Watkinson, P. *Fuel*, **2004**, *83*, 1881-1887.

[15] Falkler, T.J.; Stark, J.L. *Oil and Gas J.* **2004**, *102*, 72-74.

[16] Srinivasan, M.; Watkinson, A. P. *Heat Transf. Eng.* **2005**, *26(1)*, 7-14.

[17] Eaton, P.E., Salt Hydrolysis in Crude & Bitumen Fouling. *AIChE,* Spring Meeting, paper 103d, **2006**.

[18] Panchal, C.B. Halpern, Y. ; Kuru, W.C. ; Miller, G. *Mechanisms of Iron Sulfide Formation in Refining Processes.* 1-8. In: Proceedings of the Engineering Foundation Conference. *Understanding of Heat Exchanger Fouling and its Mitigation.* Lucca, Italy, **1997**.

[19] Fan, Z. ; Watkinson, A.P. *Ind. Eng. Chem. Res.* **2006**, *45*, 6104-6110.

[20] Silva, C.C. ; Machado, J.P.S.E. ; Sobral-Santiago, A.V.C. ; de Sant'Ana, H.B. ; Farias, J.P. *J. Petrol. Sci. Engg.* **2007**, *59*, 219-225.

[21] Wu, X.A.; Chung, K. *Energ. Fuel.* **2007**, *21*, 1212-1216.

[22] Wiehe, I.A. *Process Chemistry of Petroleum Macromolecules*; CRC Press: Boca Raton, FL, **2008**, Vol. 121, 296-298.

[23] Eaton, P.E.; Williams, J., Delayed Coker Furnace Fouling Control – Laboratory Correlation to Field Experience. In *NACE*, paper 8670, **2008**, 1-7.

[24] Hong E.; and Watkinson A.P. *Heat Transf. Eng*. **2009**, *30*, 786–793.

[25] Wilson, D.I. ; Ishiyama, E.M. ; Paterson, W.R. ; Watkinson, A.P. *Ageing: Looking back and looking forward.* 221-230. In: Procedings of International Conference on Heat Exchanger Fouling and Cleaning VIII. Ed: Muller-Steinhagan, H. ; Malayeri, M.R. ; Watkinson, A.P. Schladming, Austria. **2009**.

[26] Fan, Z. ; Rahimi, P. ; McGee, R. ; Wen, Q. ; Alem, T. *Energy Fuels*, **2010**, *24*, 6110-6118.

[27] Eaton, P.E.; Newman, B.; Gray, M. Kubis, A.; Derakhshesh, M.; Holt, C.; Mitlin, D. Furnace Coker Simulations in a Laboratory Apparatus. *PetroPhase Conference*, paper O30, **2010**.

[28] Wang, W. ; Watkinson, A.P. *Iron sulphide and coke fouling from sour oils: Review and initial experiments.* 23-30. In: Proceedings of International Conference on Heat Exchanger Fouling and Cleaning. Ed: Malayeri, M.R. ; Muller-Steinhagen, H. ; Watkinson, A.P. Crete Island, Greece. **2011**.

[29] Stephenson, T. ; Kubis, A. ; Derakhshesh, M. ; Hazelton, M. ; Holt, C. ; Eaton, P. ; Newman, B. ; Hoff, A. ; Gray, M. ; Mitlin, D. *Energ. Fuel.* **2011**, *25*, 4540-4551.

[30] Derakhshesh, M. ; Eaton, P. ; Newman, B. ; Hoff, A. ; Mitlin, D. ; Gray, M.R. *Energ. Fuel.* **2013**, 27, 1856.

[31] Yang, M. ; Wood, Z. ; Rickard, B. ; Crittenden, B. ; Gough, M. ; Droegemueller, P. ; Higley, T. *Appl. Thermal Eng.* **2013**, 54, 516-520.

[32] Muller-Steinhagen, H. ; Malayeri, M.R. ; Watkinson, A.P. *Heat Trasf. Eng.* **2013**, 34(8-9), 653-654.

[33] Petkovic, B. ; Watkinson, A.P. *Heat Trasf. Eng.* **2014**, 35(3), 302-310.

[34] Wiehe, I.A. ; Kennedy R.J. *Energ. Fuel.* **2000**, 14, 60-63.

[35] Wiehe, I.A. ; Kennedy, R.J.; Dickakian, G. *Energ. Fuel.* **2001**, 15, 1057-1058.
[36] Wiehe, I.A. *J. Disper. Sci. Technol.* **2004**, *25*, 333-339.

[37] Mena-Cervantes, V.Y. ; Hernandez-Altamirano, R. ; Buenrostro-Gonzalez, E. ; Beltran, H.I. ; Zamudio-Rivera, L.S. *Fuel*, **2013**, 110, 293-301.

[38] Rana, M.S. ; Samano, V. ; Ancheyta, J. ; Diaz, J.A.I. *Fuel*, **2007**, 86, 1216-1231.

[39] Speight, J.G. *The Chemistry and Technology of Petroleum*. 4th Ed. **2007**, CRC Press, Boca Raton, FL, 521-597.

[40] Cheng, F. ; Chen, J. ; Guo, X. *Adv. Mater.* **2006**, 18, 2561-2564.

[41] Moses, P.G. ; Hinnemann, B. ; Topsoe, H. ; Norskov, J.K. *J. Catal.* **2009**, 268, 201-208.

[42] Huang, Y. ; Zhou, Z. ; Qi, Y. ; Li, X. ; Cheng, Z. ; Yuan, W. *Chem. Eng. J.* **2011**, 172, 444-451.

[43] Castillo-Villalon, P. ; Ramirez, J. ; Castaneda, R. *J. Catal.* **2012**, 294, 54-62.

[44] Rao, B.G. ; Ramakrishna Matte, H.S.S. ; Chaturbedy, P. ; Rao, C.N.R. *ChemPlusChem*, **2013**, 78, 419-422.

[45] Menoufy, M.F. ; Ahmed, H.S. ; Betiha, M.A. ; Sayed, M.A. *Fuel*, **2014**, 119, 106-110.

[46] Thakur, D.S. *J. Catal.* **1985**, 94, 310-312.

[47] Yu, Z. ; Fareid, L.E. ; Molijord, K. ; Blekkan, E.A. ; Walmsley, J.C. ; Chen, D. *Appl. Catal. B: Environ.* **2008**, 84, 482-489.

[48] Embaid, B.P. ; Biomorgi, J.G. ; Gonzalez-Jimenez, F. ; Perez-Zurita, M.J. ; Scott, C.E. *Appl. Catal. A: General*, **2011**, 400, 166-170.

[49] Raje, A.P. ; Dadyburjor, D.B. *Ind. Eng. Chem. Res.* **1993**, 32, 1637-1644.

[50] Diaz, Y. ; Sevilla, A. ; Monaco, A. ; Mendez, F.J. ; Rosales, P. ; Garcia, L. ; Brito, J.L. *Fuel*, **2013**, 210, 235-248.

[51] Zaera, F. ; Kollin, E.B. ; Gland, J.L. *Langmuir*, **1987**, 3(4), 555-557.

[52] Dos Santos, N. ; Dulot, H. ; Marchal, N. ; Vrinat, M. *Appl. Catal. A*, **2009**, 352, 114-123.

[53] Li, Z. ; Wang, G. ; Liu, Y. ; Gao, J. ; Xu, C. ; Liang, Y. ; Wang, X. *Fuel Proc. Technol.* **2013**,115, 1-10.

[54] Valencia, D. ; Olivares-Amaya, R. ; Aburto, J. ; Garcia-Cruz, I. *Catal. Lett.* **2013**, 143, 1354-1361.

[55] Bajus, M. ; Vesely, V. ; Baxa, J. ; Leclercq, P.A. ; Rijks, J.A. *Ind. Eng. Chem. Prod. Res. Dev.* **1981**, 20, 741-745.

[56] Sahu, D. Kunsru, D. *Can. J. Chem. Eng*. **1988**, 66, 808-816.

[57] Taylor, W.F. *Ind. Eng. Chem. Prod. Res. Dev.* **1976**, 15(1), 64-68.

[58] Zhang, L. ; Holt, CMB. ; Luber, E.J. ; Olsen, B.C. ; Wang, H. ; Danaie, M. ; Cui, X. ; Tan, X. ; Lui, V. ; Kalisvaart, P. ; Mitlin, D. *J. Phys. Chem. C*, **2011**, 115, 24381-24393.

[59] Ohmi, T.; Nakagawa, Y.; Nakamura, M.; Ohki, A.; Koyama, T. *J. Vac. Sci. Tech.* **1996**, *14(4)*, 2505-2510.

[60] Cheng, S-Y. ; Kuan, S-L.; Tsai, W-T. *Corr. Sci.* **2006**, *48*, 634-649.

[61] Li, H. ; Chen, W. *Oxid. Met.* **2012**, 78, 103-122.

[62] Gesmundo, F. ; Viani, F. ; Znamirowski, W. ; Godlewski, D. ; Bregani, F. *Mater. Corr.* **1992**, 43, 83-85.

[63] Orchard, J.P. ; Young, D.J. *J. Electrochem. Soc*. **1986**, 133, 1734-1741.

[64] Lobnig, R.E. ; Grabke, H.J. *Corr. Sci.* **1990**, 30, 1045-1071.

[65] Baxter, D.J. ; Natesan, K. *Oxid. Met*. **1989**, 31, 305-322.

[66] Wilson, D.F. ; Devereux, O.F. *J. Electrochem. Soc.* **1991**, 138, 2168-2176.

[67] Farrell, D. ; Roberts, L. NACE Conference, *Corrosion*, **2010**, paper 10358, 1-11.

[68] Gutzeit, J. *High Temperature Sulfidic Corrosion in Steels*, in Process Industries Corrosion-The Theory and Practice, NACE, **1986**, 367-372.

[69] Lai, G.Y. *High-Temperature Corrosion and Materials Applications*, ASM International, Ohio, **2007**, 201-231.

[70] Nguyen, M.T. ; Sengupta, D. ; Raspoet, G. ; Vanquickenborne, L.G. *J. Phys. Chem.* **1995**, 99, 11883-11888.

[71] Wang, W. ; Watkinson, A.P. *Deposition from a sour heavy oil under incipient coking conditions: Effects of surface material and temperature*. 9-17. In: Proceedings ofInternational Conference on Heat Exchanger Fouling and Cleaning. Budapest, Hungary. **2013**.

[72] Lacroix, M. ; Marrakchi, H. ; Calais, C. ; Breysse, M. ; Forquy, C. *Stud. Surf. Sci. Catal.* **1991**, 59, 277-285.

Chapter 4

[1] Wang, Q.H. ; Kalantar-zadeh, K. ; Kis, A. ; Coleman, J.N. ; Strano, M.S. *Nat. Nanotechnol.* **2012**, 7, 699.

[2] Chhowalla, M. ; Shin, H.S. ; Eda, G. ; Li, L.-J. ; Loh, K.P. ; Zhang, H. *Nat. Chem.* **2013**, 5, 263.

[3] Rapoport, L. ; Fleischer, N. ; Tenne, R. *J. Mater. Chem.* **2005**, 15, 1782.

[4] Le Mogne, T. ; Donnet, C. ; Martin, J.M. ; Tonck, A. ; Millard-Pinard, N. *J. Vac. Sci. Technol. A*. **1994**, 12(4), 1998.

[5] Wang, H.W. ; Skeldon, P. ; Thompson, G.E. *Surf. Coat. Technol.* **1997**, 91, 200.

[6] Barboza, A.P.M. ; Chacham, H. ; Oliveira, C.K. ; Fernandes, T.F.D. ; Ferreira, E.H.M. ; Archanjo, B.S. ; Batista, R.J.C. ; de Oliveira, A.B. ; Neves, B.R.A. *Nano Lett.* **2012**, 12, 2313.

[7] Zhang, H. ; Loh, K.P. ; Sow, C.H. ; Gu, H. ; Su, X. ; Huang, C. ; Chen, Z.K. *Langmuir*, **2004**, 20, 6914.

[8] Zhu, C. ; Zeng, Z. ; Li, H. ; Li, F. ; Fan, C. ; Zhang, H. *J. Am. Chem. Soc.* **2013**, 135, 5998.

[9] Li, H. ; Yin, Z. ; He, Q. ; Li, H. ; Huang, X. ; Lu, G. ; Fam, D.W.H. ; Tok, A.L.Y. ; Zhang, Q. ; Zhang, H. *Small*, **2012**, 8(1), 63.

[10] He, Q. ; Zeng, Z. ; Yin, Z. ; Li, H. ; Wu, S. ; Huang, X. ; Zhang, H. *Small*, **2012**, 8(19), 2994.

[11] Barreau, N. ; Bernede, J.C. *J. Phys. D: Appl. Phys.* **2002**, 35, 1197.

[12] Feng, J. ; Qian, X. ; Huang, C.-W. ; Li, J. *Nat. Photonics,* **2012**, 6, 866.

[13] Liu, C.-J. ; Tai, S.-Y. ; Chou, S.-W. ; Yu, Y.-C. ; Chang, K.-D. ; Wang, S. ; Chien, F.S.-S. ; Lin, J.-Y. ; Lin, T.-W. *J. Mater. Chem.* **2012**, 22, 21057.

[14] Tai, S.-Y. ; Liu, C.-J. ; Chou, S.-W. ; Chien, F.S.-S. ; Lin, J.-Y. ; Lin, T.-W. *J. Mater. Chem.* **2012**, 22, 24753.

[15] Shanmugam, M. ; Bansal, T. ; Durcan, C.W. ;Yu, B. *Appl. Phys. Lett.* **2012**, 100, 153901.

[16] Kibsgaard, J. ; Chen, Z. ; Reinecke, B.N. ; Jaramillo, T.F. *Nat. Mater.* **2012**, 11, 963.

[17] Hansen, L.P. ;Ramasse, Q.M. ; Kisielowski, C. ; Brorson, M. ; Johnson, E. ; Topsoe, H. ; Helveg, S. *Angew. Chem. Int. Ed.* **2011**, 50, 10153.

[18] Wilcoxon, J.P. *J. Phys. Chem. B.* **2000**, 104, 7334.

[19] Ho, W. ; Yu, J.C. ; Lin, J. ; Yu, J. ; Li, P. *Langmuir*, **2004**, 20, 5865.

[20] Han, W. ; Yuan, P. ; Fan, Y. ; Shi, G. ; Liu, H. ; Bai, D. ; Bao, X. *J. Mater. Chem.* **2012**, 22, 25340.

[21] Chu, X. ; Yao, G. ; Wee, A.T.S. ; Wang, X.-S. *Nanotechnology,* **2012**, 23, 375603.

[22] Zhong, X. ; Yang, H. ; Guo, S. ; Li, S. ; Guo, G. ; Niu, Z. ; Dong, Z. ; Lei, Y. ; Jin, J. ; Li, R. ;Ma, J. *J. Mater. Chem.* **2012**, 22, 13925.

[23] Merki, D. ; Fierro, S. ; Vrubel, H. ; Hu, X. *Chem. Sci.* **2011**, 2, 1262.

[24] Laursen, A.B. ; Kegnaes, S. ; Dahl, S. ; Chorkendorff, I. *Energy Environ. Sci.* **2012**, 5, 5577.

[25] Wang, T. ; Liu, L. ;Zhu, Z. ; Papakonstantinou, P. ; Hu, J. ; Liu, H. ; Li, M. *Energy Environ. Sci.* **2013**, 6, 625.

[26] Yan, Y. ; Xia, B. ; Qi, X. ; Wang, H. ; Xu, R. ; Wang, J.-Y. ; Zhang, H. ; Wang, X. *Chem. Commun.* **2013**, 49, 4884.

[27] Laursen, A.B. ; Vesborg, P.C.K. ; Chorkendorff, I. *Chem. Commun.* **2013**, 49, 4965.

[28] Huang, X. ; Zeng, Z. ; Bao, S. ; Wang, M. ; Qi, X. ; Fan, Z. ; Zhang, H. *Nat. Commun.* **2013**, 4, 1444.

[29] Liu, J. ; Zeng, Z. ; Cao, X. ; Lu, G. ; Wang, L.H. ; Fan, Q.L. ; Huang, W. ; Zhang, H. *Small*, **2012**, 8(22), 3517.

[30] van Schalkwijk, W.A. (Ed.) ; Scrosati, B. (Ed.), *Advances in Lithium-Ion Batteries*, Klumer Academic Publishers, New York USA, **2002**, 1-5.

[31] Gabano, J.P. (Ed.) *Lithium Batteries*, Academic Press, New York USA, **1983**, 1-12.

[32] Linden, D. (Ed.) ; Reddy, T.B. (Ed.) *Linden's Handbook of Batteries.* McGraw Hill, NewYork USA, **2011**, 27.1-26.28

[33] Harris, W.S. Ph.D. Thesis, UCRL-8381, University of California, Berkeley, **1958**, 1-37.

[34] Rudorff, W. *Angew. Chem.* 71, **1959**, 487.

[35] Rudorff, W. ; Sick, H.H. *Angew. Chem.* 71, **1959**, 127.

[36] Whittingham, M.S. ; Gamble Jr. F.R. *Mat. Res. Bull.* **1975**, 10, 363.

[37] Whittingham, M.S. *Science*. **1976**, 192, 1126.

[38] Whittingham, M.S. *J. Electrochem. Soc.* **1976**, 123(3), 315.

[39] Whittingham, M.S. *Prog. Solid St. Chem.* **1978**, 12, 41.

[40] Silbernagel, B.G. ; Whittingham, M.S. *J. Chem. Phys.* **1976**, 64(9), 3670.

[41] Farrington, G.C. ; Briant, J.L. *Science*, **1979**, 204, 1371.

[42] Dines, M.B. *Mat. Res. Bull.* **1975**, 10, 287.

[43] Goodenough, J.B. *Proc. R. Soc. Lond.* **1984**, A 393, 215.

[44] Xie, Y. ; Wu, C. *Dalton Trans.* **2007**, 45, 5235.

[45] Wang, Y. ; Li, H. ; He, P. ; Hosono, E. ; Zhou, H. *Nanoscale*, **2010**, 2, 1294.

[46] Chang, K. ; Chen, W. *Chem. Commun.* **2011**, 47, 4252.

[47] Kohandehghan, A. ; Kalisvaart, P. ; Kupsta, M. ; Zahiri, B. ; Amirkhiz, B.S. ; Li, Z. ; Memarzadeh, E.L. ; Bendersky, L.A. ; Mitlin, D. *J. Mater. Chem. A.* **2013**, 1, 1600-1612.

[48] Hwang, H. ; Kim, H. ; Cho, J. *Nano Lett.* **2011**, 11, 4826.

[49] Yang, Z. ; Zhang, J. ; Kintner-Meyer, M.C.W. ; Lu, X. ; Chio, D. ; Lemmon, J.P. ; Liu, J. *Chem. Rev.* **2011**, 111, 3577.

[50] Cui, L.-F. ; Hu, L. ; Choi, J.W. ; Cui, Y. *ACS Nano*, **2010**, 4(7), 3671.

[51] Xie, J. ; Yang, X. ; Zhou, S. ; Wang, D. *ACS Nano,* **2011**, 5(11), 9225.

[52] Haering, R.R. ; Stiles, J.A.R. ; Brandt, K. US Patent No. 4,224,390, Sept. 23, **1980**.

[53] Julien, C. ; Saikh, S.I. ; Nazri, G.A. *Mater. Sci. Eng.* **1992**, B15, 73.

[54] Miki, Y. ; Nakazato, D. ; Ikuta, H. ; Uchida, T. ; Wakihara, M. *J. Power Sources*, **1995**, 54, 508.

[55] Yufit, V. ; Nathan, M. ; Golodnitsky, D. ; Peled, E. *J. Power Sources.* **2003**, 122, 169.

[56] Murugan, A.V. ; Quintin, M. ; Delville, M.-H. ; Campet, G. ; Gopinath, C.S. ; Vijayamohanan, K. *J. Power Sources*, **2006**, 156, 615.

[57] Shembel, E. ; Apostolova, R. ; Kirsanova, I. ; Tysyachny, V. *J. Solid State Electrochem.* **2008**, 12, 1151.

[58] Kim, M.G. ; Jo, M. ; Hong, Y.-S.; Cho, J. *Chem. Commun.* **2008**, 219.

[59] Chen, H. ; Qiu, X. ; Zhu, W. ; Hagenmuller, P. *Electrochem. Commun.* **2002**, 4, 488.

[60] Xia, L. ; Li, S.-L. ; Ai, X.-P. ; Yang, H.-X. ; Cao, Y.-L. *Energy Environ. Sci.* **2011**, 4, 2845.

[61] Hong, Z. ; Zheng, X. ; Ding, X. ; Jiang, L. ; Wei, M. ; Wei, K. *Energy Environ. Sci.* **2011**, 4, 1886.

[62] Koksbang, R. ; Barker, J. ; Shi, H. ; Saidi, M.Y. *Solid State Ionics*, **1996**, 84, 1.

[63] Chen, Z. ; Dahn, J.R. *Electrochim. Acta*, **2004**, 49, 1079.

[64] Lu, Y. ; Das, S.K. ; Moganty, S.S. ; Archer, L.A. *Adv. Mater.* **2012**, 24, 4430.

[65] Lai, C.-H. ; Lu, M.-Y. ; Chen, L.-J. *J. Mater. Chem.* **2012**, 22, 19.

[66] Gao, M.-R. ; Xu, Y.-F. ; Jiang, J. ; Yu, S.-H. *Chem. Soc. Rev.* **2013**, 42, 2986.

[67] Huang, X. ; Zeng, Z. ; Zhang, H. *Chem. Soc. Rev.* **2013**, 42, 1934.

[68] Balendhran, S. ; Walia, S. ; Nili, H. ; Ou, J.Z. ; Zhuiykov, S. ; Kaner, R.B. ; Sriram, S. ; Bhaskaran, M. ; Kalantar-zadeh, K. *Adv. Funct. Mater.* **2013**, 23, 3952.

[69] Wang, Y. ; Li, H. ; He, P. ; Hosono, E. ; Zhou, H. *Nanoscale*, **2010**, 2, 1294.

[70] Manthiram, A. ; Murugan, A.V. ; Sarkar, A. ; Muraliganth, T. *Energy Environ. Sci.* **2008**, 1, 621.

[71] Balaya, P. *Energy Environ. Sci.* **2008**, 1, 645.

[72] Fan, X. ; Zhang, H. ; Du, N. ; Wu, P. ; Xu, X. ; Li, Y. ; Yang, D. *Nanoscale*, **2012**, 4, 5343.

[73] Lim, A.-H. ; Shim, H.-W. ; Seo, S.-D. ; Lee, G.-H. ; Park, K.-S. ; Kim, D.-W. *Nanoscale,* **2012**, 4, 4694.

[74] Derrien, G. ; Hassoun, J. ; Panero, S. ; Scrosati, B. *Adv. Mater*. **2007**, 19, 2336.

[75] Ding, S. ; Lou, X.W. *Nanoscale*, **2011**, 3, 3586.

[76] Pabakar, S.J.R. ; Hwang, Y.-H. ; Bae, E.-G. ; Shim, S. ; Kim, D. ; Lah, M.S. ; Sohn, K.-S. ; Pyo, M. *Adv. Mater*. **2013**, 25, 3307.

[77] Sun, D.S. ; Schlogl, R. *Chem. Sus. Chem.* **2010**, 3, 136.

[78] Song, R. ; Song, H. ; Zhou, J. ; Chen, X. ; Wu, B. ; Yang, H.Y. *J. Mater. Chem.* **2012**, 22, 12369.

[79] Frackowiak, E. ; Gautier, S. ; Gaucher, H. ; Bonnamy S. ; Beguin F. *Carbon*, **1999**, 37, 61.

[80] Landi, B.J. ; Ganter, M.J. ; Cress, C.D. ; DiLeo, R.A. ; Raffaelle, R.P. *Energy Environ. Sci.* **2009**, 2, 638.

[81] Chen, J. ; Wang, J.Z. ; Minett, A.I. ; Liu, Y. ; Lynam, C. ; Liu, H. ; Wallace, G. *Energy Environ. Sci.* **2009**, 2, 393.

[82] Pan, D. ; Wang, S. ; Zhao, B. ; Wu, M. ; Zhang, H. ; Wang, Y. ; Jiao, Z. *Chem. Mater.* **2009**, 21, 3136.

[83] Wang, G. ; Shen, X. ; Yao, J. ; Park, J. *Carbon*, **2009**, 47, 2049.

[84] Yoo, E. ; Kim, J. ; Hosono, E. ; Zhou, H.S. ; Kudo, T. ; Honma, I. *Nano Lett.* **2008**, 8(8), 2277.

[85] Bhardwaj T. ; Antic, A. ; Pavan, B. ; Barone, V. ; Fahlman, B.D. *J. Am. Chem. Soc.* **2010**, 132, 12556.

[86] Pumera, M. *Energy Environ. Sci.* **2011**, 4, 668.

[87] Zu, C.-X. ; Li, H. *Energy Environ. Sci.* **2011**, 4, 2614.

[88] Li, Z. ; Xu, Z. ; Tan, X. ; Wang, H. ; Holt, C.M.B. ; Stephenson, T. ; Olsen, B.C. ; Mitlin, D. *Energy Environ. Sci.* **2013**, 6, 871.

[89] Wu, P. ; Du, N. ; Zhang, H. ; Yu, J. ; Qi, Y. ; Yang, D. *Nanoscale,* **2011**, 3, 746.

[90] Choi, B.G. ; Chang, S.-J. ; Lee, Y.B. ; Bae, J.S. ; Kim, H.J. ; Huh, Y.S. *Nanoscale*, **2012**, 4, 5924.

[91] Das, S.K. ; Darmakolla, S. ; Bhattacharyya, A.J. *J. Mater. Chem.* **2010**, 20, 1600.

[92] Han, H. ; Song, T. ; Bae, J.-Y. ; Nazar, L.F. ; Kim, H. ; Paik, U. *Energy Environ. Sci.* **2012**, 4,4532.

[93] Yang, Z. ; Du, G. ; Meng, Q. ; Guo, Z. ; Yu, X. ; Chen, Z. ; Guo, T. ; Zeng, R. *J. Mater. Chem.* **2012**, 22, 5848.

[94] Zhu, G.-N. ; Wang, Y.-G. ; Xia, Y.-Y. *Energy Environ. Sci.* **2012**, 5, 6652.

[95] Xia, F. ; Hu, X. ; Sun, Y. ; Luo, W. ; Huang, Y. *Nanoscale*, **2012**, 4, 4707.

[96] Bhaskar, A. ; Deepa, M. ; Rao, T.N. *Appl. Mater. Inferfaces*. **2013**, 5, 2555.

[97] Sun, Y. ; Hu, X. ; Yu, J.C. ; Li, Q. ; Luo, W. ; Yuan, L. ; Zhang, W. ; Huang, Y. *Energy Environ. Sci.* **2011**, 4, 2870.

[98] Huang, X.H. ; Tu, J.P. ; Zhang, C.Q. ; Chen, X.T. ; Yuan, Y.F. ; Wu, H.M. *Electrochim. Acta,* **2007**, 52, 4177.

[99] Zou, Y. ; Wang, Y. *Nanoscale*, **2011**, 3, 2615.

[100] Liu, H. ; Yang, W. *Energy Environ. Sci.* **2011**, 4, 4000.

[101] Zhou, X. ; Yin, Y.-X. ; Wan, L.-J. ; Guo, Y.-G. *Chem. Commun.* **2012**, 48, 2198.

[102] Memarzadeh, E.L. ; Kalisvaart, W.P. ; Kohandehghan, A. ; Zahiri, B. ; Holt, C.M.B. ; Mitlin, D. *J. Mater. Chem.* **2012**, 22, 6655.

[103] Ji, L. ; Zhang, X. *Energy Environ. Sci.* **2010**, 3, 124.

[104] Szczech, J.R. ; Jin, S. *Energy Environ. Sci.* **2011**, 4, 56.

[105] Du, C. ; Gao, C. ; Yin, G. ; Chen, M. ; Wang, L. *Energy Environ. Sci.* **2011**, 4, 1037.

[106] Nguyen, H.T. ; Zamfir, M.R. ; Duong, L.D. ; Lee, Y.H. ; Bondavalli, P. ; Pribat, D. *J. Mater. Chem.* **2012**, 22, 24618.

[107] Seo, J.-W. ; Jang, J.-T. ; Park, S.-W. ; Kim, C. ; Park, B. ; Cheon, J. *Adv. Mater.* **2008**, 20, 4269.

[108] Luo, B. ; Fang, Y. ; Wang, B. ; Zhou, J. ; Song, H. ; Zhi, L. *Energy Environ. Sci.* **2012**, 5, 5226.

[109] Ji, X. ; Nazar, L.F. *J. Mater. Chem.* **2010**, 20, 9821.

[110] Cai, K. ; Song, M.-K. ; Cairns, E.J. ; Zhang, Y. *Nano Lett.* **2012**, 12, 6474.

[111] Arico, A.S. ; Bruce, P. ; Scrosati, B. ; Tarascon, J.-M. ; Schalkwijk, W.V. *Nat. Mater.* **2005**, 4, 366.

[112] Tarascon, J.-M. ; Armand, M. *Nature*, **2001**, 414, 359.

[113] Whittingham, M.S. *Chem. Rev.* **2004**, 104, 4271.

[114] Marom, R. ; Amalraj, S.F. ; Leifer, N. ; Jacob, D. ; Aurbach, D. *J. Mater. Chem.* **2011**, 21, 9938.

[115] Cabana, J. ; Monconduit, L. ; Larcher, D. ; Palacin M.R. *Adv. Energ. Mater.* **2010**, 22, E170.

[116] Liu, X.H. ; Huang, J.Y. *Energy Environ. Sci.* **2011**, 4, 3844.

[117] Etacheri, V. ; Marom, R. ; Elazari, R. ; Salitra, G. ; Aurbach, D. *Energy Environ. Sci.* **2011**, 3243.

[118] Scrosati, B. ; Hassoun, J. ; Sun, Y.-K. *Energy Environ. Sci.* **2011**, 4, 3287.

[119] Manthiram, A. *J. Phys. Chem. Lett.* **2011**, 2, 176.

[120] Liwen, J. ; Lin, Z. ; Alcoutlabi, M. ; Zhang, X. *Energy Environ. Sci.* **2011**, 4, 2682.

[121] Wu, H.B. ; Chen, J.S. ; Hng, H.H. ; Lou, X.W. *Nanoscale*, **2012**, 4, 2526.

[122] Dickinson, R.G. ; Pauling, L. *J. Amer. Chem. Soc.* **1923**, 45, 1466.

[123] Bell, R.E. ; Herfert, R.E. *J. Am. Chem. Soc.* **1957**, 79(13), 3351.

[124] Traill, R.J. *Can. Mineral*, **1963**, 7, 524.

[125] Wildervanck, J.C. ; Jellinek, F. *Z. Anorg. Allg. Chem.* **1964**, 328, 309.

[126] Takeuchi, Y. ; Nowacki, W. *Schweiz. Mineral. Petrogr. Mitteil.* **1964**, 44, 105.

[127] Wickman, F.E. ; Smith, D.K. *Am. Mineral.* **1970**, 55, 1843.

[128] Wilson, J.A. ; Yoffe, A.D. *Advan. Phys.* **1969**, 18, 193.

[129] Connell, G.A.N. ; Wilson, J.A. ; Yoffe, A.D. *J. Phys. Chem. Solids*, **1969**, 30, 287.

[130] Newberry, R.J.J. *Am. Mineral.* **1979**, 64, 758.

[131] Schonfeld, B. ; Huang, J.J. ; Moss, S.C. *Acta Cryst.* **1983**, B39, 404.

[132] Bronsema, K.D. ; De Boer, J.L. ; Jellinek, F. *Z. Anorg. Allg. Chem.* **1986**, 540/541, 15.

[133] Fleischauer, P.D. ; Lince, J.R. ; Bertrand, P.A. ; Bauer, R. *Langmuir*, **1989**, 5, 1009.

[134] Didziulis, S.V. ; Lince, J.R. ; Shuh, D.K ; Durbin, T.D. ; Yarmoff, J.A. *J. Electron Spec. Rel. Phenom.* **1992**, 60, 175.

[135] Wypych, F. ; Schollhorn, R. *J. Chem. Soc. Chem. Commun.* **1992**, 19, 1386.

[136] Rovira, C. ; Whangbo, M.-H. *Inorg. Chem.* **1993**, 32, 4094.

[137] Goodenough, J.B. ; Dutta, G. ; Manthiram, A. *Phys. Rev. B.* **1991**, 43, 10170.

[138] Guay, D. *Chem. Mater.* **1994**, 6, 614.

[139] El Beqqali, O. ; Zorkani, I. ; Rogemond, F. ; Chermette, H. ; Ben Chaabane, R. ; Gamoudi, M.; Guillaud, G. *Synth. Met.* **1997**, 90, 165.

[140] Wypych, F. ; Weber, Th. ; Prins, R. *Chem. Mater.* **1998**, 10, 723.

[141] Wypych, F. ; Solenthaler, C. ; Prins, R. ; Weber, Th. *J. Solid State Chem.* **1999**, 144, 430.

[142] Benavente, E. ; Santa Ana, M.A. ; Mendizabal, F. ; Gonzalez, G. *Coordin. Chem. Rev.* **2002**, 224, 87.

[143] Mattheiss, L.F. *Phys. Rev. B.* **1973**, 8, 3719.

[144] Lu, P. ; Wu, X. ; Guo, W. ; Zeng, X.C. *Phys. Chem. Chem. Phys.* **2012**, 14, 13035.

[145] Zhou, Y. ; Yang, P. Zu, H. ; Gao, F. ; Zu, X. *Phys. Chem. Chem. Phys.* **2013**, 15, 10385.

[146] Py, M.A. ; Haering, R.R. *Can. J. Phys.* **1983**, 61, 76.

[147] Pauling, L. *J. Am. Chem. Soc.* **1931**, 53, 1367.

[148] Hultgren, R. *Phys. Rev.* **1932**, 40, 891.

[149] Selwyn, L.S. ;McKinnon, W.R. ; von Sacken, U. ; Jones, C.A. *Solid State Ionics.* **1987**, 22, 337.

[150] Papageorgopoulos, C.A. ; Jaegermann, W. *Surf. Sci.* **1995**, 338, 83.

[151] Imanishi, N. ; Toyoda, M. ; Takeda, Y. ; Yamamoto, O. *Solid State Ionics.* **1992**, 58, 333.

[152] Gonzalez, G. ; Santa Ana, M.A. ; Benavente, E. ; Donoso, J.P. ; Bonagamba, T.J. ; Mello, N.C. ; Panepucci, H. *Solid State Ionics*, **1996**, 85, 225.

[153] Dungey, K.E. ; Curtis, M.D. ; Penner-Hahn, J.E. *Chem. Mater.* **1998**, 10, 2152.

[154] Zak, A. ; Feldman, Y. ; Lyakhovitskaya, V. ; Leitus, G. ; Popovitz-Biro, R. ; Wachtel, E. ; Cohen, H. ; Reich, S. ; Tenne, R. *J. Am. Chem. Soc.* **2002**, 124, 4747.

[155] Tonti, D. ; Pettenkofer, C. ; Jaegermann, W. *J. Phys. Chem. B.* **2004**, 108, 16093.

[156] Chen, J. ; Tao, Z.-L. ; Li, S.-L. *Angew. Chem, Int. Ed.* **2003**, 42, 2147.

[157] Julien, C.M. *Mater. Sci. Eng.* **2003**, R40, 47.

[158] Kim, Y. ; Goodenough, J.B. *J. Phys. Chem. C.* **2008**, 112, 15060.

[159] Feng, C. ; Ma, J. ; Li, H. ; Zeng, R. ; Guo, Z. ; Liu, H. *Mat. Res. Bull.* **2009**, 44, 1811.

[160] Chrissafis, K. ; Zamani, M. ; Kambas, K. ; Stoemenos, J. ; Economou, N.A. ; Samaras, I. ; Julien, C. *Mat. Sci. Eng.* **1989**, B3, 145.

[161] Li, Y. ; Wu, D. ; Zhou, Z. ; Cabrera, C.R. ; Chen, Z. *J. Phys. Chem. Lett.* **2012**, 3, 2221.

[162] Yang, D. ; Sandoval, S.J. ; Divigalpitiya, W.M.R. ; Irwin, J.C. ; Frindt, R.F. *Phys. Rev. B.* **1991**, 43(14), 12053.

[163] Zubavichus, Y.V. ; Slovokhotov, Y.L.; Schilling, P.J. ; Tittsworth, R.C. ; Golub, A.S. ; Protzenko, G.A. ; Novikov, Y.N. *Inorg. Chim. Acta*, **1998**, 280, 211.

[164] Heising, J. ; Kanatzidis, G. *J. Am. Chem. Soc.* **1999**, 121, 11720.

[165] Dahn, J.R. ; Zheng, T. ; Liu, Y. ; Xue, J.S. *Science*, **1995**, 270, 590.

[166] Mulhern, P.J. *Can. J. Phys.* **1989**, 67, 1049.

[167] Hayes, W.M. (Ed.) ; Lide, D.R. (Ed.). *CRC Handbook of Chemistry and Physics, Internet Version,* **2012***,* 92nd Ed. CRC Press: Boca Raton, Florida, pp. 9-50, 12-11.

[168] Du, G. ; Guo, Z. ; Wang, S. ; Zeng, R. ; Chen, Z. ; Liu, H. *Chem. Comm.* **2010**, 46, 1106.

[169] Chang, K. ; Chen, W. ; Ma, L. ; Li, H. ; Li, H. ; Huang, F. ; Xu, Z. ; Zhang, Q. ; Lee, J.-Y. *J. Mater. Chem.* **2011**, 21, 6251.

[170] Chang, K. ; Chen, W. *ACS Nano*, **2011**, 5(6), 4720.

[171] Wang, Q. ; Li, J. *J. Phys. Chem. C.* **2007**, 111, 1675.

[172] Das, S.K. ; Mallavajula, R. ; Jayaprakash, N. ; Archer, L.A. *J. Mater. Chem.* **2012**, 22, 12988.

[173] Li, H. ; Li, W. ; Ma, L. ; Chen, W. ; Wang, J. *J. Alloys and Compounds,* **2009**, 471, 442.

[174] Ding, S. ; Zhang, D. ; Chen, J.S. ; Lou, X.W. *Nanoscale.* **2012**, 4, 95.

[175] Ding, S. ; Chen, J.S. ; Lou, X.W. *Chem. Eur. J.* **2011**, 17, 13142.

[176] Kwon, J.-H. ; Ahn, H.-J. ; Jeon, M.-S. ; Kim, K.-W. ; Ahn, I.-S. ; Ahn, J.-H. ; Wang, G. ; Ryu, H.-S. *Res. Chem. Intermed.* **2010**, 36, 749.

[177] Fang, X. ; Guo, X. ; Mao, Y. ; Hua, C. ; Shen, L. ; Hu, Y. ; Wang, Z. ; Wu, F. ; Chen, L. *Chem. Asian J.* **2012**, 7, 1013.

[178] Fang, X. ; Yu, X. ; Liao, S. ; Shi, Y. ; Hu, Y.S. ; Wang, Z. ; Stucky, G.D. ; Chen, L. *Micropor. Mesopor. Mat.* **2012**, 151, 418.

[179] Fang, X. ; Hua, C. ; Guo, X. ; Hu, Y. ; Wang, Z. ; Gao, X. ; Wu, F. ; Wang, J. ; Chen, L. *Electrochim. Acta.* **2012**, 81, 155.

[180] Xiao, J. ; Choi, D. ; Cosimbescu, L. ; Koech, P. ; Liu, J. ; Lemmon, J.P. *Chem. Mater.* **2010**, 22, 4522.

[181] Xiao, J. ; Wang, X. ; Yang, X.Q. ; Xun, S. ; Liu, G. ; Koech, P.K. ; Liu, J. ; Lemmon, J.P. *Adv. Funct. Mater.* **2011**, 21, 2840.

[182] Zhou, X. ; Wan, L.-J. ; Guo, Y.-G. *Nanoscale*, **2012**, 4, 5868.

[183] Rauh, R.D.; Abraham, K.M.; Pearson, G.F.; Surprenant, J.K.; Brummer, S.B. *J. Electrochem. Soc.* **1979**, 126, 523.

[184] Yamin, H. ; Peled, E. *J. Power Sources,* **1983**, 9, 281.

[185] Liang, C. ; Dudney, N.J. ; Howe, J.Y. *Chem. Mater.* **2009**, 21, 4724.

[186] Ji, X. ; Lee, K.T. ; Nazar, L.F. *Nat. Mater.* **2009**, 8(6), 500.

[187] Zhang, B. ; Qin, X. ; Li, G.R. ; Gao, X.P. *Energy Environ. Sci.* **2010**, 3, 1531.

[188] Gao, X.-P. ; Yang, H.-X. *Energy Environ. Sci.* **2010**, 3, 174.

[189] Ellis, B.L. ; Lee, K.T. ; Nazar, L.F. *Chem. Mater.* **2010**, 22, 691.

[190] Chen, J.-J. ; Zhang, Q. ; Shi, Y.-N. ; Qin L.-L. ; Cao, Y. ; Zheng, M.-S. ; Dong, Q.-F. *Phys. Chem. Chem. Phys.* **2012**, 14, 5376.

[191] Park, M.S. ; Yu, J.-S. ; Kim, K.J. ; Jeong, G. ; Kim, J.-H. ; Jo, Y.-N. ; Hwang, U. ; Kang, S. ; Woo, T. ; Kim, Y.-J. *Phys. Chem. Chem. Phys.* **2012**, 14, 6796.

[192] Dorfler, S. ; Hagen, M. ; Althues, H. ; Tubke, J. ; Kaskel, S. ; Hoffmann, M.J. *Chem. Commun.* **2012**, 48, 4097.

[193] Ahn, W. ; Kim, K.-B. ; Jung, K.-N. ; Shin, K.-H. ; Jin, C.-S. *J. Power Sources*, **2012**, 202, 394.

[194] Enyashin, A.N. ; Ivanovskii, A.L. *Semicond.* **2007**, 41(1), 81.

[195] Deepak, F.L. ; Jose-Yacaman, M. *Isr. J. Chem.* **2010**, 50, 426.

[196] Pan, H. ; Zhang, Y.-W. *J. Mater. Chem.* **2012**, 22, 7280.

[197] Enyashin, A. ; Gemming, S.; Seifert, G. *Eur. Phys. J. Special Topics.* **2007**, 149, 103.

[198] Weiss, W. ; Bohne, W. ; Rohrich, J. ; Strub, E. ; Bloeck, U. ; Sieber, I. ; Ellmer, K. ; Mientus, R. ; Prosch, F. *J. Appl. Phys.* **2004**, 95(12), 7665.

[199] Chan, Y. ; Hill, J.M. *Nanoscale Res. Lett.* **2011**, 6, 203.

[200] Kibsgaard, J. ; Lauritsen, J.V. ; Laegsgaard, E. ; Clausen, B.S. ; Topsoe, H. ; Besenbacher, F. *J. Am. Chem. Soc.* **2006**, 128, 13950.

[201] Enyashin, A.N. ; Bar-Sadan, M. ; Sloan, J. ; Houben, L. ; Seifert, G. *Chem. Mater.* **2009**, 21, 5627.

[202] Tuxen, A. ; Kibsgaard, J. ; Gobel, H. ; Laegsgaard, E. ; Topsoe, H. ; Lauritsen, J.V. ; Besenbacher, F. *ACS Nano.* **2010**, 4(8), 4677.

[203] Castro-Guerrero, C.F. ; Deepak, F.L. ; Ponce, A. ; Cruz-Reyes, J. ; Valle Granados, M.D. ; Fuentes-Moyado, S. ; Galvan, D.H. ; Jose Yacaman, M. *Catal. Sci. Technol.* **2011**, 1, 1024.

[204] Kochubei, D.I. ; Rogov, V.A. ; Babenko, V.P. ; Bogdanov, S.V. ; Zaikovskii, V.I. *Kinet. Catal.* **2003**, 44, 135.

[205] Balke, N. ; Jesse, S. ; Morozovska, A.N. ; Eliseev, E. ; Chung, D.W. ; Kim, Y. ; Adamczyk, L. ; Garcia, R.E. ; Dudney, N. ; Kalinin S.V. *Nature Nanotech.* **2010**, 5, 749.

[206] Mao, Y. ; Duan, H. ; Xu, B. ; Zhang, L. ; Hu, Y. ; Zhao, C. ; Wang, Z. ; Chen, L. ; Yang, Y. *Energy Environ. Sci.* **2012**, 5, 7950.

[207] Wang, Y.-X. ; Huang, L. ; Sun, L.-C. ; Xie, S.-Y. ; Xu, G.-L. ; Chen, S.-R. ; Xu, Y.-F. ; Li, J. T. ; Chou, S.-L. ; Dou, S.-X. ; Sun, S.-G. *J. Mater. Chem.* **2012**, 22, 4744.

[208] Elazari, R. ; Salitra, G. ; Garsuch, A. ; Panchenko, A. ; Aurbach, D. *Adv. Mater.* **2011**, 23, 5641.

[209] Su, Y.-S. ; Manthiram, A. *Chem. Comm.* **2012**, 48, 8817.

[210] Li, X. ; Cao, Y. ; Qi, W. ; Saraf, L.V. ; Xiao, J. ; Nie, Z. ; Mietek, J. ; Zhang, J.-G. ; Schwenzer, B. ; Liu, J. *J. Mater. Chem.* **2011**, 21, 16603.

[211] Jamnik, J. ; Maier, J. *Phys. Chem. Chem. Phys.* **2003**, 5, 5215.

[212] Yang, Y. ; McDowell, M.T. ; Jackson, A. ; Cha, J.J. ; Hong, S.S. ; Cui, Y. *Nano Lett.* **2010**, 10, 1486.

[213] Li, Y. ; Tan, B. ; Wu, Y. *Nano Lett.* **2008**, 8, 265.

[214] Qie, L. ; Chen, W.-M. ; Wang, Z.-H. ; Shao, Q.-G. ; Li, X. ; Yuan, L.-X. ; Hu, X.-L. ; Zhang, W.-X. ; Huang, Y.-H. *Adv. Mater.* **2012**, 24, 2047.

[215] Laruelle, S. ; Grugeon, S. ; Poizot, P. ; Dolle, M. ; Dupont, L. ; Tarascon, J.-M. *J. Electrochem. Soc.* **2002**, 149(5), A627.

[216] Dedryvere, R. ; Laruelle, S. ; Grugeon, S. ; Poizot, P. ; Gonbeau, D. ; Tarascon, J.-M. *Chem. Mater.* **2004**, 16, 1056.

[217] Shi, Y. ; Guo, B. ; Corr, S.A. ; Shi, Q. ; Hu, Y.-S. ; Heier, K.R. ; Chen, L. ; Seshardri, R. ; Stucky, G.D. *Nano Lett.* **2009**, 9(12), 4215.

[218] Balaya, P. ; Li, H. ; Kienle, L. ; Maier, J. *Adv. Funct. Mater.* **2003**, 13(8), 621.

[219] Zhai, C. ; Du, N. ; Zhang, H. ; Yu, J. ; Wu, P. ; Xiao, C. ; Yang, D. *Nanoscale*, **2011**, 3, 1798.

[220] Bindumadhavan, K. ; Srivastava, S.K. ; Mahanty, S. *Chem. Commun,* **2013**, 49, 1823.

[221] Marschilok, A. ; Lee, C.-Y. ; Subramanian, A. ; Takeuchi, K.J. ; Takeuchi, E.S. *Energy Environ. Sci.* **2011**, 4, 2943.

[222] Zhou, G. ; Wang, D.-W. ; Hou, P.-X. ; Li, W. ; Li, N. ; Liu, C. ; Li, F. ; Cheng, H.-M. *J. Mater. Chem.* **2012**, 22, 17942.

[223] Park, S.-K. ; Yu, S.-H. ; Woo, S. ; Quan, B. ; Lee, D.-C. ; Kim, M.K. ; Sung, Y.-E. ; Piao, Y. *Dalton Trans.* **2013**, 42, 2399.

[224] Lee, S.W. ; Gallant, B.M. ; Byon, H.R. ; Hammond, P.T. ; Shao-Horn, Y. *Energy Environ. Sci.* **2011**, 4, 1972.

[225] Cao, X. ; Shi, Y. ; Shi, W. ; Rui, X. ; Yan, Q. ; Kong, J. ; Zhang, H. *Small,* **2013**, 9(20), 3433.

[226] Xi, J. ; Long, M.L. ; Tang, L. ; Wang, D. ; Shuai, Z. *Nanoscale,* **2012**, 4, 4348.

[227] Jia, X. ; Campos-Delgado, J. ; Terrones, M. ; Meunier, V. ; Desselhaus, M.S. *Nanoscale*, **2011**, 3, 86.

[228] Zhou, X. ; Wan, L.-J. ; Guo, Y.-G. *Chem. Commun.* **2013**, 49, 1838.

[229] Chang, K. ; Geng, D. ; Li, X. ; Yang, J. ; Tang, Y. ; Cai, M. ; Li, R. ; Sun, X. *Adv. Funct. Mater.* **2013**, 3, 839.

[230] Wang, H. ; Holt, C.M.B. ; Li, Z. ; Tan, X. ; Amirkhiz, B.S. ; Xu, Z. ; Olsen, B.C. ; Stephenson, T. ; Mitlin, D. *Nano Research*, **2012**, 5, 605-617.

[231] Hummers, W.S. ; Offeman, R.E. *J. Am. Chem. Soc.* **1958**, 80(6), 1339.

[232] Chen, W. ; Zhu, Z. ; Li, S. ; Chen, C. ; Yan, L. *Nanoscale*, **2012**, 4, 2124.

[233] Malik, S. ; Vijayaraghavan, A. ; Erni, R. ; Arida, K. ; Khalakhan, I. ; Hill, J.P. *Nanoscale*, **2010**, 2, 2139.

[234] Xu, Z. ; Li, Z. ; Tan, X. ; Holt, C.M.B. ; Zhang, L. ; Shalchi-Amirkhiz, B. ; Mitlin, D. *RSC Advances*, **2012**, 2, 2753.

[235] Ma, Y. ; Dai, Y. ; Guo, M. ; Niu, C. ; Huang, B. *Nanoscale*, **2011**, 3, 3883.

[236] Jiang, H. ; Zhao, T. ; Yan, C. ; Ma, J. ; Li, C. *Nanoscale*, **2010**, 2, 2195.

[237] Cao, F.-F. ; Guo, Y.-G. ; Wan, L.-J. *Energy Environ. Sci.* **2011**, 4, 1634.

[238] Jung, H.-G. ; Myung, S.-T. ; Yoon, C.S. ; Son, S.-B. ; Oh, K.H. ; Amine, K. ; Scrosati, B. ; Sun, Y.-K. *Energy Environ. Sci.* **2011**, 4, 1345.

[239] Lei, D. ; Zhang, M. ; Qu, B. ; Chen, L. ; Wang, Y. ; Zhang, E. ; Xu, Z. ; Li, Q. ; Wang, T. *Nanoscale,* **2012**, 4, 3422.

[240] Liu, H. ; Su, D. ; Zhou, R. ; Sun, B. ; Wang, G. ; Qiao, S.Z. *Adv. Energy Mater.* **2012**, 2, 970.

[241] Saravanan, K. ; Ananthanarayanan, K. ; Balaya, P. *Energy Environ. Sci.* **2010**, 3, 939.

[242] Srolovitz, D.J. ; Safran, S.A. ; Homyonfer, M. ; Tenne, R. *Phys. Rev. Lett.* **1995**, 74(10), 1779.

[243] Xiong, Y. ; Xie, Y. ; Li, Z. ; Li, X. ; Zhang, R. *Chem. Phys. Lett.* **2003**, 382, 180.

[244] Alexandrou, I. ; Sano, N. ; Burrows, A. ; Meyer, R.R. ; Wang, H. ; Kirkland, A.I. ; Kiely, C.J. ; Amaratunga, G.A.J. *Nanotech.* **2003**, 14, 913.

[245] Bar-Sadan, M. ; Enyashin, A.N. ; Gemming, S. ; Popovitz-Biro, R. ; Hong, S.Y. ; Prior, Y. ; Tenne, R. ; Seifert, G. *J. Phys. Chem. B.* **2006**, 110, 25399.

[246] Chang, L. ; Yang, H. ; Fu, W. ; Zhang, J. ; Yu, Q. ; Zhu, H. ; Chen, J. ; Wei, R. ; Sui, Y. ; Pang, X. ; Zou, G. *Mater. Res. Bull.* **2008**, 43, 2427.

[247] Li, T. ; Galli, G. *J. Phys. Chem. C.* **2007**, 111, 16192.

[248] Frey, G.L. ; Tenne, R. *J. Mater. Res.* **1998**, 13(9), 1998, 2412.

[249] Seifert, G. ; Terrones, H. ; Terrones, M. ; Jungnickel, G. ; Frauenheim, T. *Phys. Rev. Lett.* **2000**, 85(1), 146.

[250] Tenne, R. ; Rao, C.N.R. *Phil. Trans. R. Soc. Lond. A.* **2004**, 362, 2099.

[251] Tenne, R. ; Seifert, G. *Annu. Rev. Mater. Res.* **2009**, 39, 387.

[252] Zibouche, N. ; Kuc, A. ; Heine, T. *Eur. Phys. J. B.* **2012**, 85(49), 1.

[253] Hassanien, A. ; Tokumoto, M. ; Mrzel, A. ; Mihailovic, D. ; Kataura, H. *Physica E.* **2005**, 29, 684.

[254] Hassanien, A. ; Leintschnig, G. ; Mrzel, A. ; Tokumoto, M. ; Kataura, H. *Surf. Interface Anal.* **2006**, 38, 1530.

[255] Kibsgaard, J. ; Tuxen, A. ; Levisen, M. ; Laegsgaard, E. ; Gemming, S. ; Seifert, G. ; Lauritsen, J.V. ; Besenbacher, F. *Nano Lett.* **2008**, 8(11), 3928.

[256] Heising, J. ; Kanatzidis, M.G. *J. Am. Chem. Soc.* **1999**, 121, 638.

[257] Li, Q. ; Newberg, J.T. ; Walter, E.C. ; Hemminger, J.C. ; Penner, R.M. *Nano Lett.* **2004**, 4(2), 277.

[258] Li, Y. ; Zhou, Z. ; Zhang, S. ; Chen, Z. *J. Am. Chem. Soc.* **2008**, 130, 16739.

[259] Brivio, J. ; Alexander, D.T.L. ; Kis, A. *Nano Lett.* **2011**, 11, 5148.

[260] Wang, Z. ; Li, H. ; Liu, Z. ; Shi, Z. ; Lu, J. ; Suenaga K. ; Joung, S.-K. ; Okazaki, T. ; Gu, Z. ; Zhou, J. ; Gao, Z. ; Li, G. ; Sanvito, S. ; Wang, E. ; Iijima, S. *J. Am. Chem. Soc.* **2010**, 132, 13840.

[261] Matte, H.S.S.R. ; Gomathi, A. ; Manna, A.K. ; Late, D.J. ; Datta, R. ; Pati, S.K. ; Rao, C.N.R. *Angew. Chem. Int. Ed.* **2010**, 49, 4059.

[262] Balendhran, S. ; Ou, J.Z. ; Bhaskaran, M. ; Sriram, S. ; Ippolito, S. ; Vasic, Z. ; Kats, E. ; Bhargava, S. ; Zhuiykov, S. ; Kalatar-zadeh, K. *Nanoscale*, **2012**, 4, 461.

[263] Remskar, M. ; Mrzel, A. ; Skraba, Z. ; Jesih, A. ; Ceh, M. ; Demsar, J. ; Stadelmann, P. ; Levy, F. ; Mihailovic, D. *Science.* **2001**, 292, 479.

[264] Terrones, H. ; Terrones, M. *New J. Phys.* **2003**, 5, 126.1.

[265] Zelenski, C.M. ; Dorhout, P.K. *J. Am. Chem. Soc.* **1998**, 120, 734.

[266] Jia, X. ; Chen, Z. ; Suwarnasarn, A. ; Rice, L. ; Wang, X. ; Sohn, H. ; Zhang, Q. ; Wu, B.M. ; Wei, F. ; Lu, Y. *Energy Environ. Sci.* **2012**, 5, 6845.

[267] Hsu, W.K. ; Chang, B.H. ; Zhu, Y.Q. ; Han, W.Q. ; Terrones, H. ; Terrones, M. ; Grobert, N. ; Cheetham, A.K. ; Kroto, H.W. ; Walton, D.R.M. *J. Am. Chem. Soc.* **2000**, 122, 10155.

[268] Feldman, Y. ; Frey, G.L. ; Homyonfer, M. ; Lyakhovitskaya, V. ; Margulis, L. ; Cohen, H. ; Hodes, G. ; Hutchison, J.L. ; Tenne, R. *J. Am. Chem. Soc.* **1996**, 118, 5362.

[269] German, C.R.S. ; Santiago, P. ; Ascencio, J.A. ; Pal, U. ; Perez-Alvarez, M. ; Rendon, L. ; Mendoza, D. *J. Phys. Chem. B.* **2005**, 109, 17488.

[270] Shi, Y. ; Wan, Y. ; Liu, R. ; Tu, B. ; Zhao, D. *J. Am. Chem. Soc.* **2007**, 129, 9522.

[271] Adeogun, A. ; Afzaal, M. ; O'Brien, P. *Chem. Vap. Deposition*. **2006**, 12, 597.

[272] Zhang, J. ; Soon, J.M. ; Loh, K.P. ; Yin, J. ; Ding, J. ; Sullivian, M.B. ; Wu, P. *Nano Lett.* **2007**, 7(8), 2370.

[273] Lee, Y.H. ; Zhang, X.-Q. ; Zhang, W. ; Chang, M.-T. ; Lin, C.-T. ; Chang, K. D. ; Yu, Y.-C. ; Wang, J.T.-W. ; Chang, C.-S. ; Li, L.-J. ; Lin, T.-W. *Adv. Mater.* **2012**, 24, 2320.

[274] Remskar, M. ; Mrzel, A. ; Virsek, M. ; Godec, M. ; Krause, M. ; Kolitsch, A. ; Singh, A. ; Seabaugh, A. *Nanoscale Res. Lett.* **2011**, 6(26), 1.

[275] Fleischauer, P.D. *Thin Solid Films*, **1987**, 154, 309.

[276] Wu, H. ; Yang, R. ; Song, B. ; Han, Q. ; Li, J. ; Zhang, Y. ; Fang, Y. ; Tenne, R. ; Wang, C. *ACS Nano.* **2011**, 5(2), 1276.

Appendix A

[1] Gray, M.R. Fundamentals of Oilsands Upgrading. Custom Courseware,Winter term **2011**, Chemical and Materials Engineering.

[2] Ohmi, T. ; Nakagawa, Y. ; Nakamura, M. ; Ohki, A. ; Koyama, T. J. Vac. Sci. Technol. A. **1996**, 14(4), 2505-2510.

APPENDIX A

Corrosion-Fouling Supporting Information

A.1 Schematic diagram of the delayed coking process

Figure A1 presents a schematic diagram of the delayed coking process. This particular schematic is of the Canadian Natural Resources Limited, Horizon system and shows the use of a bitumen feed.[1] The feed is deposited into the coker factionator. The resid from the fractionator is fed into the coker heater where it is heated to a temperature in excess of 550 °C to start the delayed coking process. After heating, the feed is then directed into the coke drums where coke precipitates from the solution. Light material is removed from the drum and recycled into the fractionator. The coke settles to the bottom of the drum, and is cleaned out once the drum is full. Steam is injected into the bottom of the coke drum to improve settling by the entrainment of lighter material to the top of the drum.

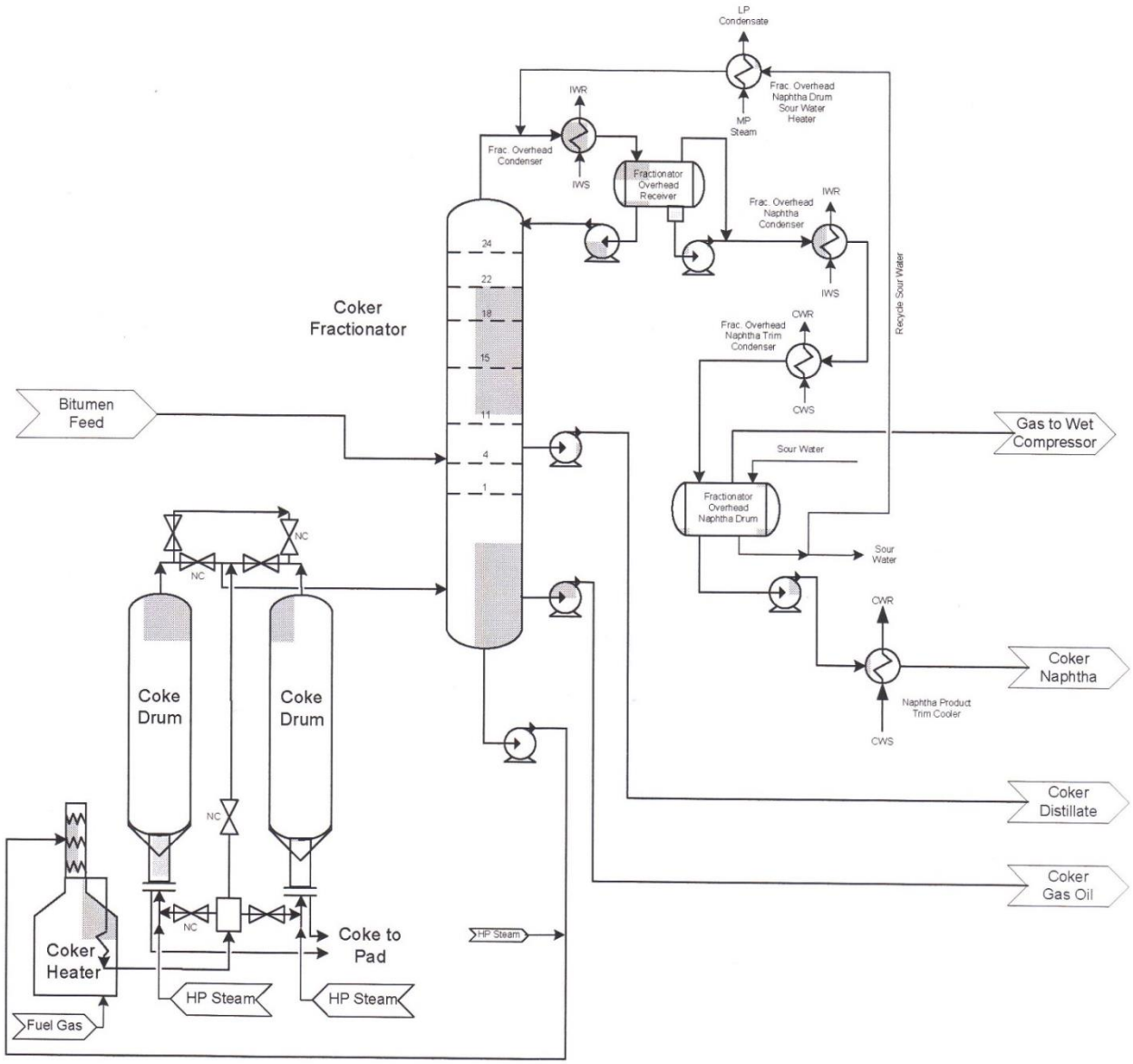

Figure A1: Schematic diagram of the delayed coking process.[1]

A.2 Fouling factor derivation

The derivation for the fouling factor is shown here in Figures A2 and A3. Figure A2 shows the derivation considering a plane wall with thermal conduction in one direction, and Figure A3 shows the derivation considering a radial system. These two scenarios are considered to convince the reader that it is possible to arrive at the same fouling factor formulas regardless of the manner in which the derivation is conducted.

For the derivation, the following simplifying assumptions were considered; 1) For the plane wall case, the "back" of the wall (which corresponds to the centre of the wire), is adiabatic. ie: there is thermal conduction only in one direction. 2) The wire temperature is equivalent to the surface temperature in both cases. ie: The temperature gradient across the foulant layer is considered to be zero. This assumption is considered valid for thin foulant layers, such as the ones considered in this thesis. 3) The A_{fouled} term was calculated from observations of the fouled wire diameters, measured after the respective fouling run. The fouled area was calculated considering it as a smooth cylinder. This assumption likely underestimates the actual heat transfer surface area in the fouled state as it does not consider surface roughness. However, it is also recognized that sufficiently small pores are not likely to contribute to the overall heat transfer surface area, as the material inside them should be in thermal equilibrium with their immediate surroundings.

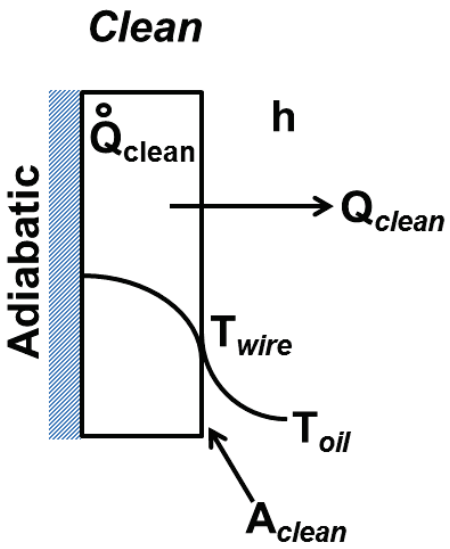

$$R_{cond} = \frac{\Delta T}{Q} = \frac{L}{kA}$$

$$R_{conv} = \frac{\Delta T}{Q} = \frac{1}{hA}$$

Analogous to:

$$R_e = \frac{\Delta V}{I} = \frac{L}{\sigma A}$$

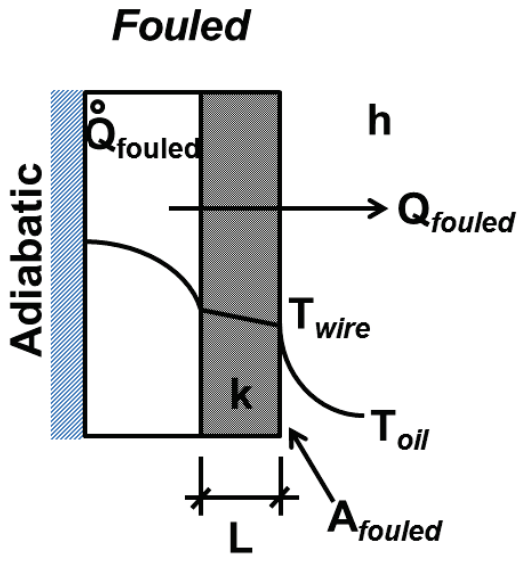

$$Q_{clean} = U_{clean} A_{clean} (T_{wire} - T_{oil})_{clean}$$

$$Q_{fouled} = U_{fouled} A_{fouled} (T_{wire} - T_{oil})_{fouled}$$

$$\frac{1}{U_{clean}} = \frac{1}{h} = \frac{A_{clean}(T_{wire} - T_{oil})_{clean}}{Q_{clean}}$$

$$\frac{1}{U_{fouled}} = \frac{1}{h} + \frac{L}{k} = \frac{A_{fouled}(T_{wire} - T_{oil})_{fouled}}{Q_{fouled}}$$

$$FFF = \frac{1}{U_{fouled}} - \frac{1}{U_{clean}} = \frac{1}{h} + \frac{L}{k} - \frac{1}{h} = \frac{A_{fouled}(T_{wire} - T_{oil})_{fouled}}{Q_{fouled}} - \frac{A_{clean}(T_{wire} - T_{oil})_{clean}}{Q_{clean}}$$

Figure A2: Derivation of final fouling factor (FFF) considering that the system is simplified to a plane wall condition.

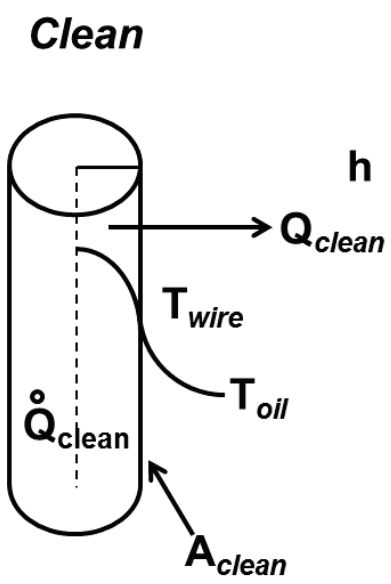

$$R_{cond} = \frac{\Delta T}{Q} = \frac{\ln(\frac{r_2}{r_1})}{2\pi kL}$$

$$R_{conv} = \frac{\Delta T}{Q} = \frac{1}{2\pi rLh}$$

Analogous to:

$$R_e = \frac{\Delta V}{I} = \frac{L}{\sigma A}$$

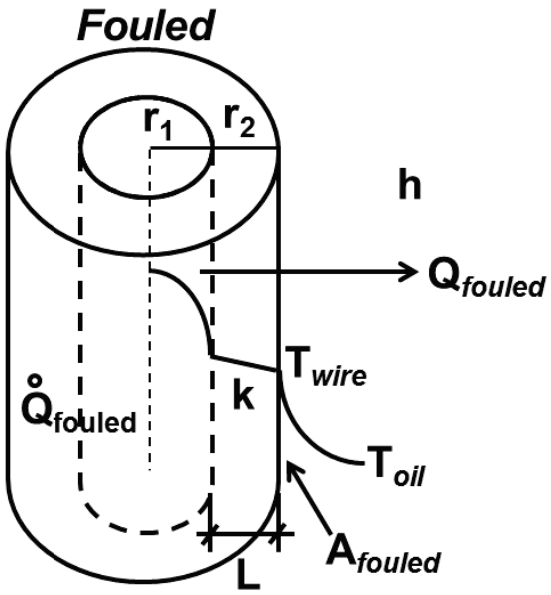

$$Q_{clean} = U_{clean} A_{clean} (T_{wire} - T_{oil})_{clean} \qquad Q_{fouled} = U_{fouled} A_{fouled} (T_{wire} - T_{oil})_{fouled}$$

$$\frac{1}{U_{clean}} = \frac{1}{h} = \frac{A_{clean}(T_{wire} - T_{oil})_{clean}}{Q_{clean}} \qquad \frac{1}{U_{fouled}} = \frac{1}{h} + \frac{r}{k}\ln(\frac{r_2}{r_1}) = \frac{A_{fouled}(T_{wire} - T_{oil})_{fouled}}{Q_{fouled}}$$

$$FFF = \frac{1}{U_{fouled}} - \frac{1}{U_{clean}} = \frac{1}{h} + \frac{r}{k}\ln(\frac{r_2}{r_1}) - \frac{1}{h} = \frac{A_{fouled}(T_{wire} - T_{oil})_{fouled}}{Q_{fouled}} - \frac{A_{clean}(T_{wire} - T_{oil})_{clean}}{Q_{clean}}$$

Figure A3: Derivation of final fouling factor (FFF) considering a radial system.

The derivations in Figures A2 and A3 show that the fouling factor is simply a consideration of the heat transfer of the system. Furthermore, it is shown that the fouling factor in its most basic form is simply the difference between the inverse of the overall heat transfer coefficients in the fouled and clean states. In both cases, expressions for the heat being transferred out of the wire in the clean and fouled states are the starting point. ie: Q_{clean} and Q_{fouled}. The overall heat transfer coefficients in the clean and fouled states are then U_{clean} and U_{fouled}. It is here that it is useful to consider that the inverse of the heat transfer coefficient (the fouling factor) is defined as the thermal resistance to heat transfer. Expressions for the thermal resistance to conduction (R_{cond}) and convection (R_{conv}) are given in both Figures A2 and A3. These are shown to be analogous to the resistance to electrical conduction in a current carrying wire. ie: The inverse of electrical conductivity (σ) is analogous to the inverse of thermal conductivity (k).

In this way, the inverse of thermal conduction is defined as thermal resistance, and it is here that we arrive at an expression for the fouling factor in the clean and fouled states. As is seen in both Figures, the parameters that are used to evaluate the fouling factor are all measurable. However, it is useful to point out that the Q_{clean} and Q_{fouled} terms are evaluated using the Joule heating law for a current carrying wire. Here, the product of voltage and current yields the power (or heat) output of the wire. ie; $P = VI$. Calculating the difference in thermal resistance between the fouled and clean states, we can see from the equations that this expression is equivalent to the thickness of the foulant layer

divided by its thermal conductivity. In this way, the fouling factor can be evaluated for the system.

In Figures A2 and A3, the final fouling factor (FFF) is evaluated, which takes into consideration the fouled surface area (A_{fouled}). This calculation is cumbersome, as the final surface area can only be evaluated after the fouling run when the fouled diameter of the wire is measured and fouled surface area is subsequently calculated. For a faster evaluation of the fouling factor, one can consider the heat transfer surface area as constant, and in this way, the fouling factor (FF) can be plotted continuously versus fouling time. This is shown in Figure 2-1, and while less accurate, is useful in obtaining a rapid determination of the overall shape of the fouling factor curve with time. Comparing Figures 2-1 and 3-3, it can be seen that the FF and FFF have similar asymptotic shapes, however the FF is, of course, calculated to be a much smaller estimate.

A.3 Wire temperature determination

The wire temperature was a calculated value that was determined using ex-situ temperature calibration plots shown here in Figure A4.

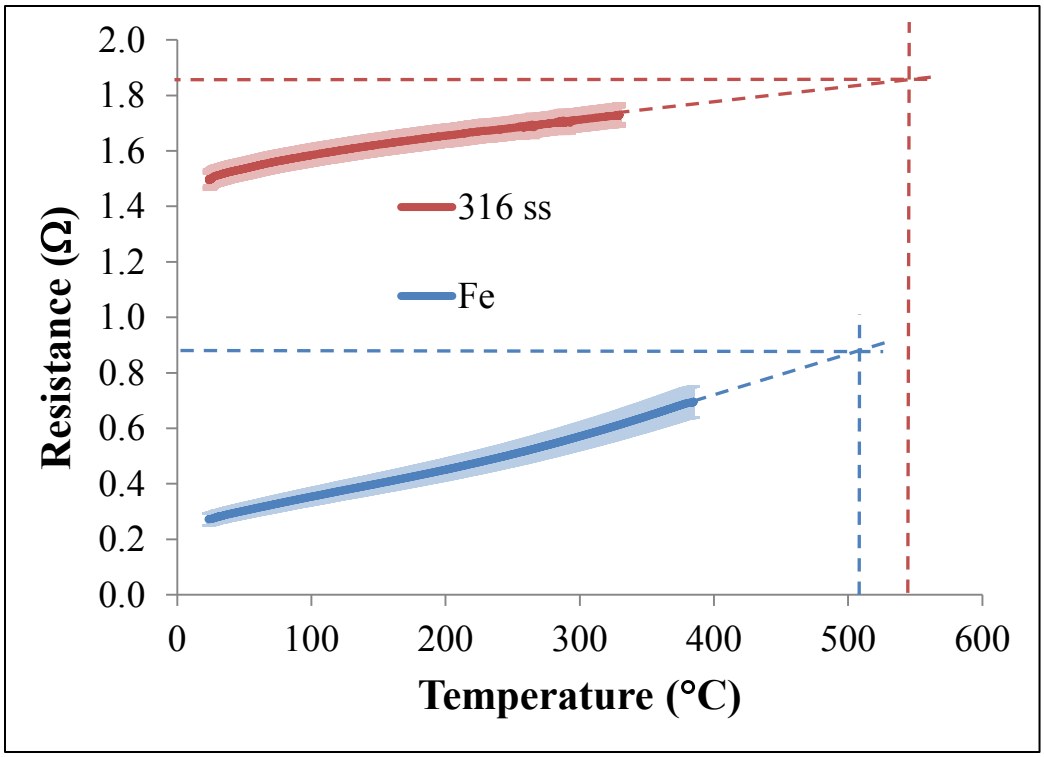

Figure A4: Graph of resistance versus temperature for pure iron and 316 stainless steel wires used in this thesis. Error bars are shown as one standard deviation of the average between multiple runs.

A probe was removed from the fouling reactor and a wire was mounted in it. The probe was then inserted into a quartz tube furnace. Pure nitrogen was flowed at a rate of 100 sccm through the tube to minimize oxidation during the temperature calibration. A constant 0.2 A of current was sent through the wires to facilitate electrical measurements. The temperature of the tube furnace was then ramped

up at its lowest setting of 1 °C/min. Voltage and current measurements were logged with time and temperature. To facilitate the measurement of temperature with time, electronics from the fouling reactor including a multiplexor and a computer with custom data logging software were used. A k-type thermocouple was inserted into the tube and placed as close as possible to the wire in the probe to measure temperature. In this way, the resistance versus temperature plot shown in Figure A4 was generated for both types of wires. The resistance was calculated using Ohm's law (R = V/I).

Unfortunately, the maximum service temperature of the probe was approximately 400 °C. Going over this temperature would damage the probe, and so extrapolation along the last known trajectory of the plot was used to evaluate the wire temperature during fouling. Resistance values for 316 stainless steel and iron at the start of fouling (once the wires had reached 5 A constant current) are shown on the y-axis of the plot at approximately 1.85 Ω and 0.89 Ω respectively. The corresponding respective starting wire temperatures of 540 °C and 508 °C are also shown.

A.4 Wire resistance, temperature, foulant thickness and fouling factor

Figures A5a-d show plots of wire resistance with fouling time, wire temperature with fouling time, fouling factor with fouling time, and finally, fouling factor with fouling time to 1400 minutes respectively. These plots illustrate the excellent correlation between all of the aforementioned fouling parameters. The shape of the fouling factor curve is dominated by foulant thickness, and the rate at which foulant forms on the wire surface. This, in turn, causes the temperature to increase concomitantly with the resistance of the wire. All of these parameters taken together, produce curves that are asymptotic in nature.

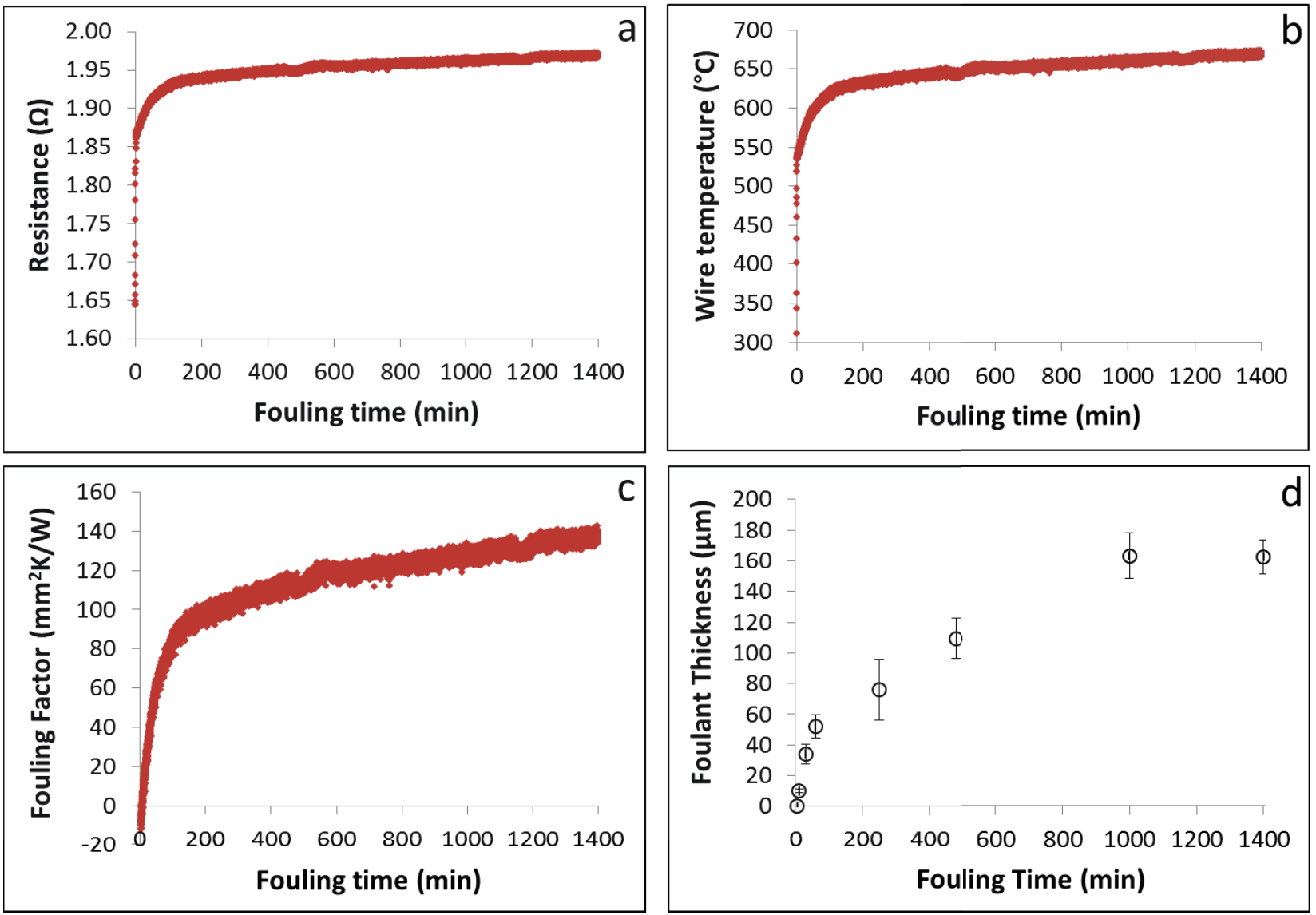

Figure A5: Fouling parameter plots versus fouling time. (a) Wire resistance. (b) Wire temperature. (c) Fouling factor. (d) Foulant thickness.

A.5 Ellingham Diagram

The Ellingham diagram provides a great deal of useful information and is shown in Figure A6.[2] It shows the relative thermodynamic stability of various metals in equilibrium with their oxides as a function of temperature. A dotted line

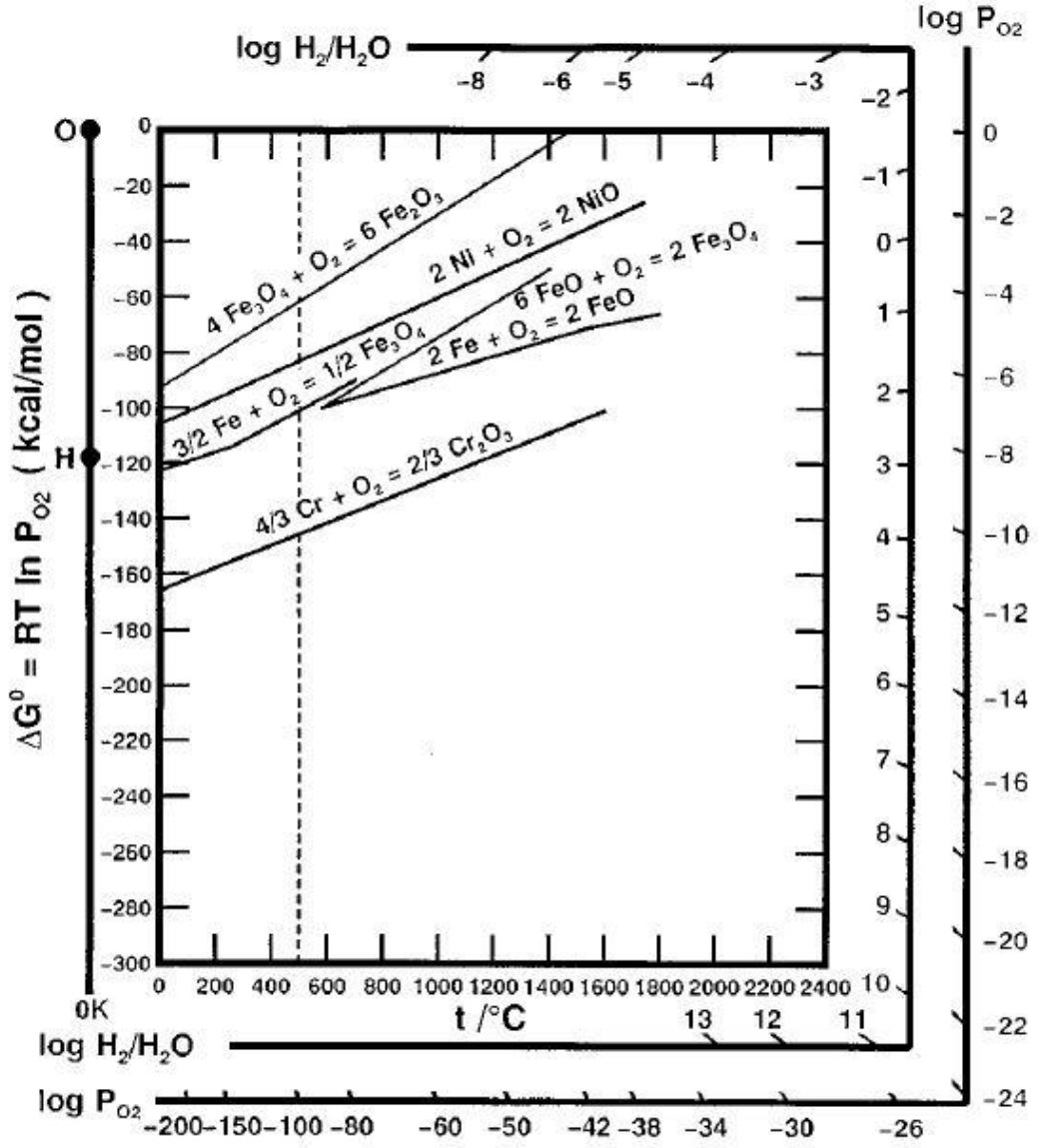

Figure A6: Ellingham diagram for metal oxides.[2]

has been drawn on this particular diagram at 500 °C. The intersection of this line with the plotted line for chromium gives the Gibbs free energy of reaction (approximately -147 kcal/mol in this case). Furthermore, if one constructs a line between the "O" on the y-axis, and the intersection of the dotted line with the chromium plot, one can get an estimate of the partial pressure of oxygen required to stabilize this reaction at equilibrium. In this case $\log(P_{O2})$ is seen to equal approximately -38, meaning that the partial pressure of oxygen required is 10^{-38} atm. The implication of this information is that if the partial pressure of oxygen is above this value, chromium metal will be expected to oxidize.

The plot can also be used to estimate the stratification of oxides at the surface of an oxidized sample of 316 stainless steel. From the Ellingham diagram, we expect a surface layer of chromia, with mixed iron and nickel oxide spinels underneath. In the samples analyzed in this thesis, it is likely that the mixed iron and nickel oxide spinels convert to sulfides in the subsurface of the wire.

A.6 SEM image processing for coke : sulfide ratio

It was recognized that all of the SEM micrographs obtained for fouled wire cross sections showed differences in contrast between the coke and the sulfide phases. Typically, the sulfide was seen as a light gray phase, and the coke appeared black. This difference offered a unique opportunity to characterize the coke:sulfide ratio using digital image processing software. A graph of this data for 316 stainless steel is shown here in Figure A7.

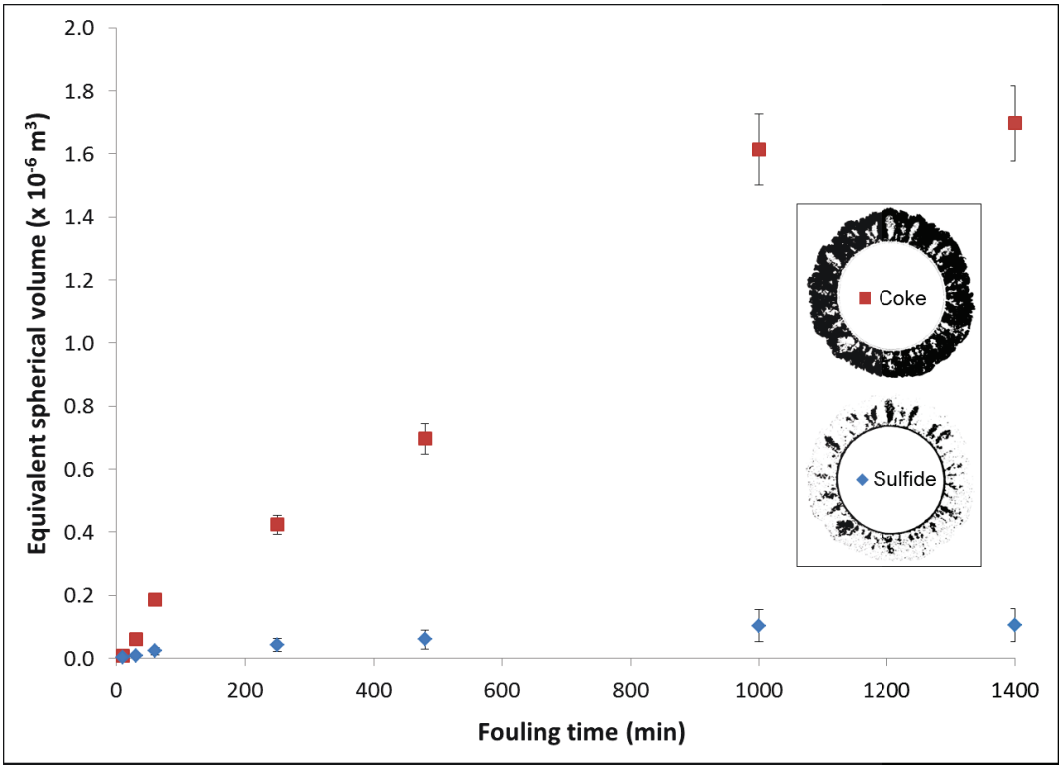

Figure A7: Graph of equivalent spherical volume of coke and sulfide phases versus fouling time as determined from the fouled wire cross sections of 316 stainless steel. Error bars are shown as one standard deviation of the average between multiple samples.

Gwyddion version 2.30 software was used for the image processing. Contrast masks were applied to the images and the relative areas of each phase were then calculated. The legend depicts a sample of the masks that were used (this particular wire was fouled for 60 minutes). First the coke phase was preferentially measured by masking the sulfide phase. The legend shows the coke phase of the wire cross section as black, and the sulfide as white. In a similar manner, the area of the sulfide phase was also calculated. This allowed for an estimation of the relative amounts of coke and sulfide, plotted with fouling time. Equivalent spherical volume (ESV) was calculated from the area using the relation ESV = (4/3)*PI*sqrt(Area/PI)^3. It can be seen from the Figure, that the coke and sulfide phases form rapidly at the onset of fouling and begin to attenuate at the longer times. This is particularly true for the sulfide phase, which is seen to attenuate much faster than the coke phase.

This is likely due to the manner in which the sulfide phase forms. Corrosive sulfide species such as H_2S must diffuse to the surface of the wire and react with iron. As the foulant thickness increases, diffusion to the surface of the wire becomes more difficult over the longer distance, and the formation of sulfide diminishes as a result. In contrast, the coke phase continues to form at the hot coke-oil interface. The rate of coke formation diminishes as a result of the increasing coke : sulfide ratio. ie: There is less sulfide in contact with coke to catalyze organic fouling reactions at the longer fouling durations.

A.7 References

[1] Gray, M.R. *Fundamentals of Oilsands Upgrading*. Custom Courseware, Winter term **2011**, Chemical and Materials Engineering.

[2] Ohmi, T. ; Nakagawa, Y. ; Nakamura, M. ; Ohki, A. ; Koyama, T. *J. Vac. Sci. Technol. A*. **1996**, 14(4), 2505-2510.

APPENDIX B

Nanocomposite MoS_2-CNT Electrodes for Lithium Ion Batteries

B.1 Nanocomposite MoS_2-CNT electrodes for LIBs

The material presented in Appendix B represents the portion of my own research that was devoted to the fabrication of nanocomposite MoS_2 lithium ion batteries (LIBs). During this work I also attempted to characterize the lithiation mechanism of MoS_2. There is a large body of literature focusing on MoS_2-CNT nanocomposite materials for lithium ion batteries, however the CNTs were simply mechanically mixed with MoS_2 to form the nanocomposite. Nobody had ever tried to grow a CNT forest from a current collector, and deposit MoS_2 onto it, which offers a number of advantages.

My thinking behind this method was that each nanotube would be well anchored to the substrate and provide good ohmic contact and hence good electrical conductivity to the MoS_2 active material coating. In this way, I would improve the cycle life and coulombic efficiency of the electrode. Unfortunately this research was only met with limited success as I was unable to deposit pure MoS_2 using physical vapour deposition (PVD). It was decided that using MoS_2 in our PVD vacuum chamber would contaminate it with sulfur. Had I been able to deposit MoS_2 onto my nanotube forests directly, the project would have been met with more success. However I was relegated to depositing molybdenum metal using PVD and then trying to convert it to MoS_2 using chemical vapour deposition (CVD), which is a difficult reaction considering that molybdenum oxides are quite thermodynamically stable. Furthermore, the concentration of H_2S gas that I was able to use (for safety reasons) for the CVD process was far

too low to affect a good conversion. The result was CNTs coated with a molybdenum oxysulfide. Furthermore, the CVD step was found to partially oxidize the titanium nitride diffusion barrier underneath the CNT forest. This resulted in partial lithiation of the substrate (since TiO_2 is active towards lithiation), and electrochemical data that was difficult to interpret.

For these reasons, this data is included in an Appendix and not in the main body of the thesis. It was my feeling that the overall quality of the data was unsatisfactory. This was brought about by the aforementioned problems in my synthesis technique that begot questionable results. Nonetheless, this body of work still supports the claims made in Chapter 4. ie: MoS_2 decomposes on initial lithiation and does not reform.

B.2 Synthesis of MoS_2-CNT nanocomposite electrodes

In this work, the working electrode was constructed in the following manner. A 316 stainless steel current collector was polished to a mirror finish using standard metallographic techniques, with silicon carbide grinding paper, and finally 0.05 micron alumina slurry and a napping cloth. A 50 nm adhesion layer of titanium was deposited using PVD on the polished current collector prior to the titanium nitride diffusion barrier. 150 nm of titanium nitride (TiN) was then deposited using reactive sputtering at 250 °C. The sputtering was conducted using an ATC Orion planar magnetron sputtering system. The chamber was evacuated to 5×10^{-8} Torr prior to sputtering. A working pressure of 4 mTorr was

used for all sputtering steps. The sputtering gas was research grade argon, which was mixed with nitrogen at a ratio of 10:3 for reactive sputtering. A sputtering power of 10 W was applied to the titanium target and the total sputtering time was approximately 90 minutes.

After the deposition of the TiN, 4 nm of pure nickel was deposited. This layer was used as the catalyst layer for the growth of vertically aligned carbon nanotubes from the current collector surface. After this step, the current collector was inserted into a Tystar CVD furnace for carbon nanotube growth. The current collector was inserted at 500 °C and ramped to 750 °C at a rate of 10 °C/min. The 5 min growth of CNTs was conducted at 750 °C in a flow of 15 vol% ethylene and 10 vol% hydrogen gas with the balance argon with a total flow rate of 3300 sccm. The furnace was then cooled to 450 °C and the samples were removed. This created a CNT forest on the surface of the current collector onto which molybdenum metal was then deposited.

Molybdenum was sputtered to a planar thickness of 150 nm on the CNT forest, and subsequently sulfided by CVD using H_2S gas. After the deposition of the molybdenum, the current collector was inserted into a 150 mm quartz tube furnace and subjected to a 5 hour CVD sulfidation process at 750 °C with a gas mixture of 10 vol% hydrogen, 0.5 vol% H_2S and the balance argon flowing at 50 sccm. This entire process created a nanocomposite electrode in which MoS_2 was finely dispersed onto the surfaces of a carbon nanotube forest which had

physically grown from the surface of the current collector. This ensured good ohmic contact and electrical conduction to the active material. Figure B1 shows the results of the CNT growth on the current collector and the subsequent sputtering of molybdenum metal.

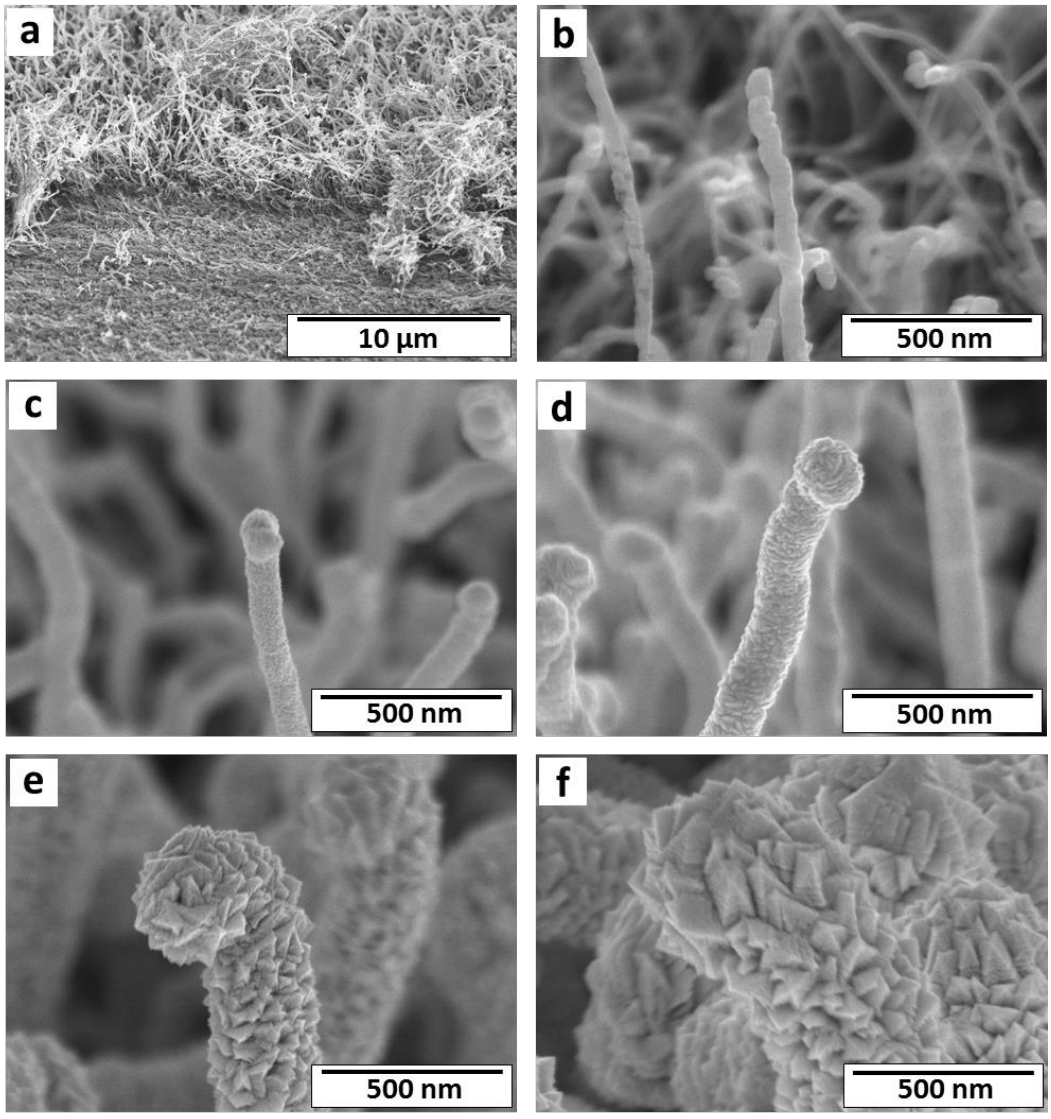

Figure B1: SEM micrographs of a multi-walled carbon nanotube forest grown on a 316 stainless steel current collector. (a) Low magnification SEM of a location where the CNTs were scrapped off using a razor blade. (b) MWCNT prior to molybdenum deposition. (c) MWCNT after deposition of 50 nm of molybdenum. (d) After 150 nm molybdenum. (e) After 300 nm molybdenum. and (f) After 500 nm molybdenum.

Figure B1a shows a low magnification SEM image of a portion of the current collector that had been scrapped with a razor blade. The fact that the CNTs tore off along their length was a good indication that they were well connected to the substrate and that good ohmic contact had been achieved by the CNT growth step. Figure B1b shows a high magnification image of a bare multi-walled CNT (MWCNT) prior to the deposition of molybdenum metal by sputtering. Figures B1c-f show high magnification images of MWCNTs after various amounts of molybdenum had been sputtered onto them. A planar thickness of 150 nm was chosen for the sulfidation step as it was observed to have the most conformal coating that penetrated deeply into the CNT forest.

Figure B2 shows a series of SEM micrographs of the MWCNTs after the sulfidation step to convert the molybdenum into molybdenum disulfide. Figure B2a shows a high magnification image of a MWCNT coated in 150 nm of molybdenum metal. Figures B2c-d show MWCNTs after the sulfidation step, where the molybdenum had been converted to a mixture of MoS_2, molybdenum oxide, and unconverted metal. It was found that the final product was always a mixture of the sulfide, oxide, and unconverted metal, as the concentration of H_2S gas was not high enough to effect a conversion to pure sulfide. For safety reasons the maximum CVD gas concentration that I was able to use was 0.5 vol% H_2S, which was only partially effective at producing MoS_2.

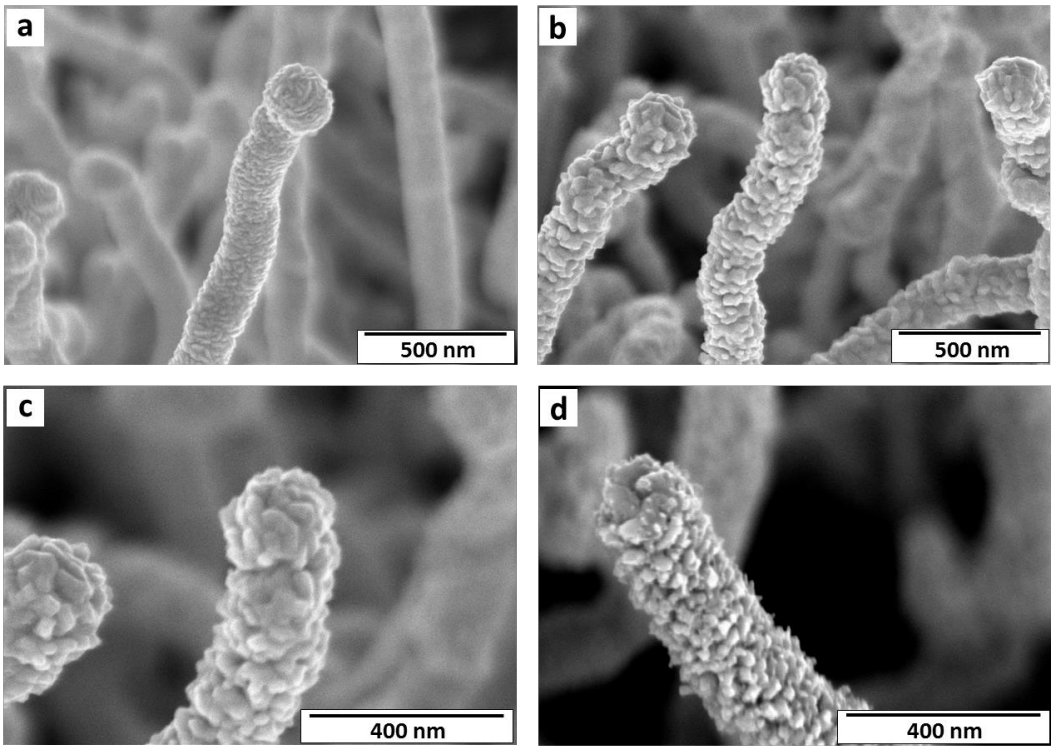

Figure B2: SEM micrographs of MWCNTs coated in molybdenum metal and then subjected to a CVD step for sulfidation. (a) MWCNT coated in 150 nm of molybdenum metal. (b-d) After sulfidation.

Figure B3 shows XRD scans of the electrode after various steps in the synthesis process, highlighting the oxidation of the titanium nitride diffusion barrier. These scans were completed on substrates that had bare titanium nitride deposited on them, and were included in each of the subsequent processing steps to evaluate the effect on the diffusion barrier which is vital to the battery function. After reactive sputtering of the titanium nitride, one can see from the XRD scan that a very high quality polycrystalline TiN layer had been successfully created as indicated by the indexed TiN pattern included in the Figure. Also evident is the fact that the titanium nitride diffusion barrier survived the CNT growth step,

despite the high temperature of that process. Although there is some reduction in crystallinity, as seen by peak broadening, the layer is still intact. Unfortunately, the titanium nitride did not survive the sulfidation process, as is seen by the topmost XRD spectrum.

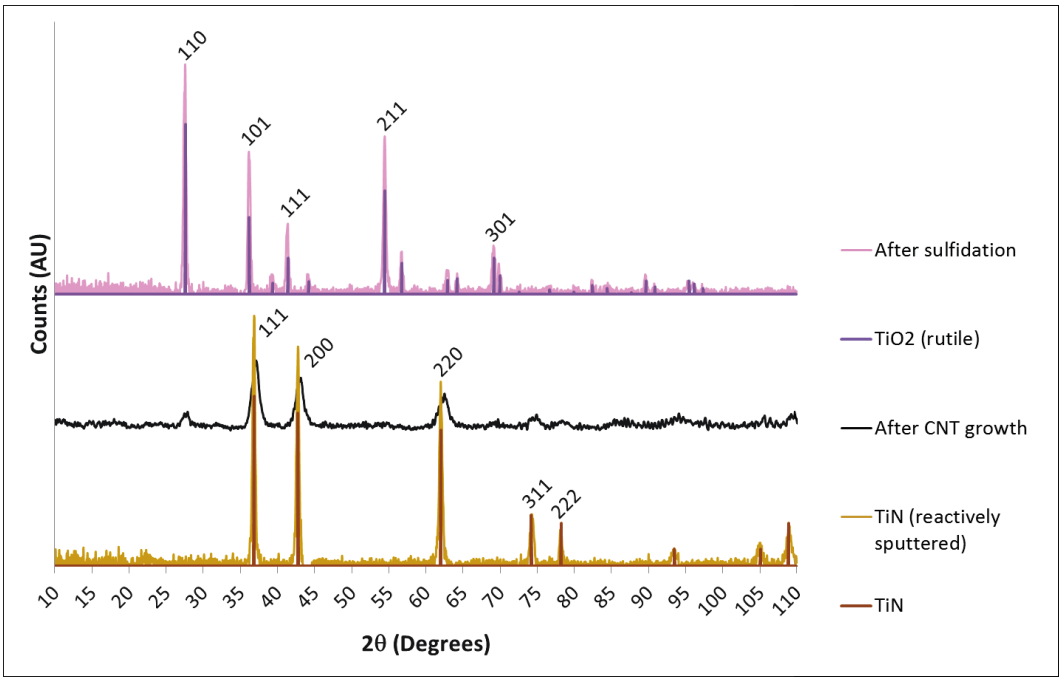

Figure B3: XRD scans of the titanium nitride diffusion barrier layer after each step of the electrode fabrication process.

At this point, a large portion of the nitride had converted to oxide (the rutile phase of TiO_2) and was therefore rendered active towards lithiation. The topmost scan is shown in conjunction with the theoretical indices for rutile. The colouration of each scan is indicative of the colour of the TiN coating after each subsequent processing step. As-deposited TiN appeared dark golden brown.

After the CNT growth step, the layer darkened due to the deposition of amorphous carbon on the surface. After sulfidation, the TiN layer had oxidized to the rutile phase of TiO_2 and appeared pink in colour. As will be shown in the subsequent electrochemical characterization, the oxidation of the diffusion barrier was the primary failure mechanism for these LIBs. This meant that the substrate was active towards lithiation during cycling, and that interpretation of the resulting electrochemical data became difficult due to the high number of active phases present. Furthermore, it was impossible to accurately estimate the active material mass. Additionally, the cyclic lithiation of the substrate led to the eventual delamination of the CNTs from the surface, and a loss in electrical connectivity to the active material. As a result, the cycle life of these batteries was poor. The final result of these combined effects was that my research efforts were frustrated in this area. Obviously, the direct PVD of MoS_2 onto the CNTs would have alleviated these difficulties, and remains an area of future study.

B.3 Characterization of MoS_2-CNT nanocomposite electrode

Figure B4a shows bright field TEM micrographs and accompanying EDX elemental maps for a fragment of a MWCNT that has been subjected to the aforementioned procedures for making the nanocomposite. This scan was conducted using a JEOL 2200 FS TEM with an accelerating voltage of 200 kV. Figure B4b shows the EDX elemental maps overlaid on the TEM micrograph. As expected, the coating is a combination of molybdenum oxide and molybdenum disulfide. The carbon scan shows that the underlying carbon nanotube was also detectable by EDX. The oxide to sulfide conversion was extremely difficult to complete under the experimental conditions used.

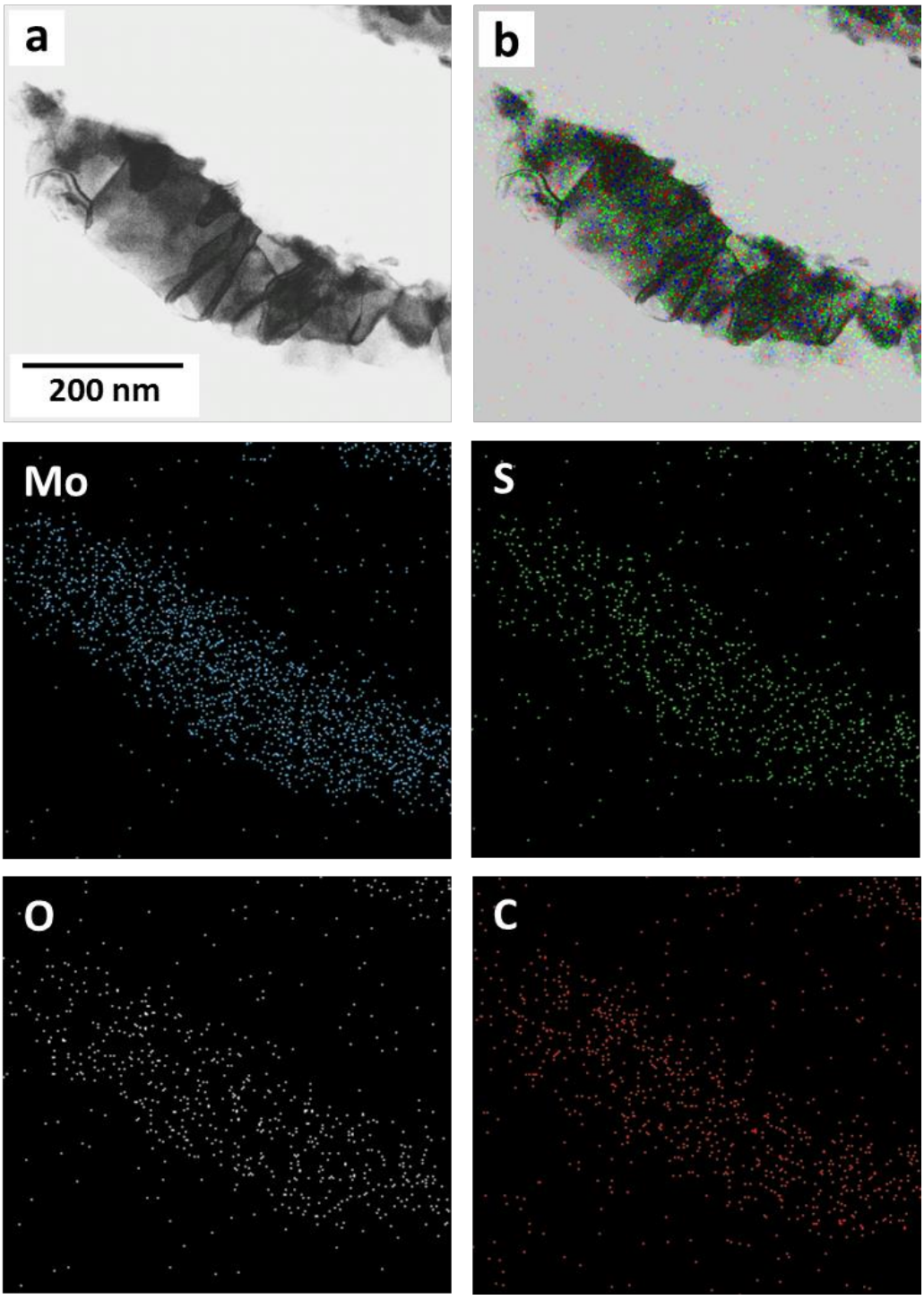

Figure B4: Bright field TEM micrographs and accompanying EDX elemental maps of a fragment of a MWCNT coated in a combination of molybdenum disulfide and molybdenum oxide. (a) BF TEM micrograph. (b) BF TEM micrograph overlaid with EDX elemental maps.

Figure B5 shows some high angle annular dark field (HAADF) TEM micrographs and accompanying electron energy loss spectroscopy (EELS) elemental maps for a MWCNT partially coated in MoS_2. The software for signal collection was Digital Micrograph (Gatan inc.). Figure B5a shows a higher magnification portion of Figure B5b, where the EELS scan was taken. The EELS elemental maps confirm that the MWCNT was at least partially coated with MoS_2. However there are regions in which molybdenum was detected, and sulfur was not, indicating that the conversion reaction was not complete. Comparing this scan with the information presented in Figure B4, other phases, such as unconverted molybdenum metal, and molybdenum oxide were likely present. As we will see, the presence of such extraneous phases, made the interpretation of electrochemical data difficult.

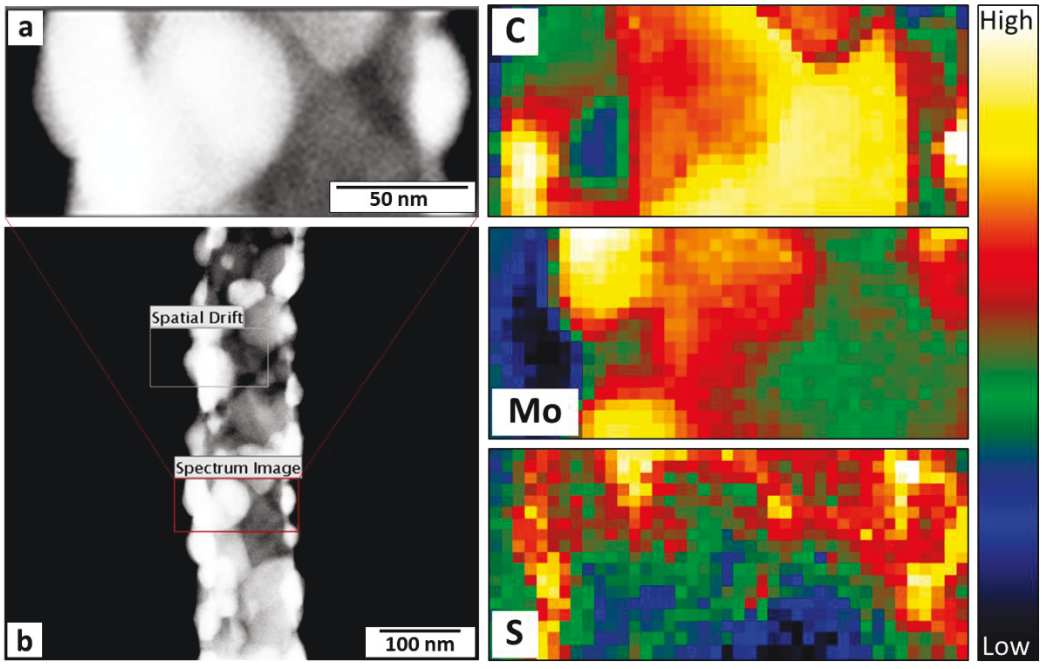

Figure B5: HAADF TEM images and corresponding EELS elemental maps of a coated MWCNT fragment. (a) Higher magnification HAADF TEM image of (b) showing where the EELS maps were taken.

Electron energy loss spectroscopy (EELS) was performed using a JEOL 2200 FS TEM with a 200 kV accelerating voltage. An in-column Ω filter in scanning mode (STEM) with a nominal analytical beam size of 0.5 nm was used. The standard procedure of pre-edge background subtraction and integration on the edge was used for the data extraction from the recorded EELS spectra. For each elemental map, a thickness profile was calculated from the low loss EELS spectrum to check for possible artifacts due to the large variation in sample thickness. Mo-M, C-K, and S-L edges were used for elemental mapping. We used multiple linear least squares (MLLS) fitting of EELS spectra for separating the respective edges.

Figure B6 shows bright field and dark field TEM micrographs and an accompanying SAED pattern highlighting the presence of residual molybdenum metal after the sulfidation step. The SAED has been indexed to bcc molybdenum. The position of the aperture for the dark field image is circled in the SAED pattern. These micrographs were collected using a JEOL 2010 TEM with an accelerating voltage of 200 kV.

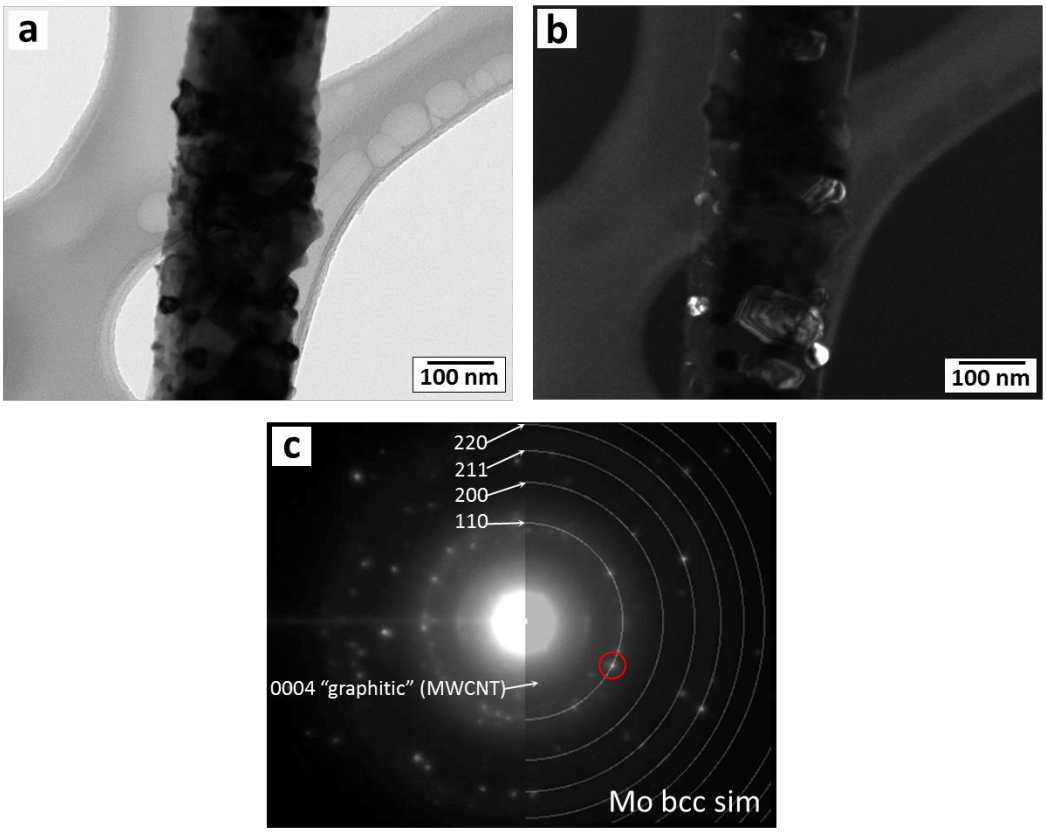

Figure B6: TEM micrographs and accompanying SAED pattern of a fragment of a MWCNT after sulfidation. (a) Bright field TEM. (b) Dark field TEM. (c) SAED pattern indexed to bcc molybdenum. The location of the aperture for the dark field image is circled in (c).

Figure B7 shows bright field and dark field TEM micrographs, as well as a high resolution TEM (HRTEM) micrograph and accompanying SAED pattern for a fragment of a MWCNT after sulfidation. The SAED pattern has been indexed to the hcp phase of MoS_2, and the location of the aperture for the dark field imaged is circled. The dark field image indicates that only a portion of the deposited molybdenum metal was converted to the sulfide phase. The bright spots on the dark field image indicate that the edges of molybdenum particles had been converted, but the reaction was incomplete.

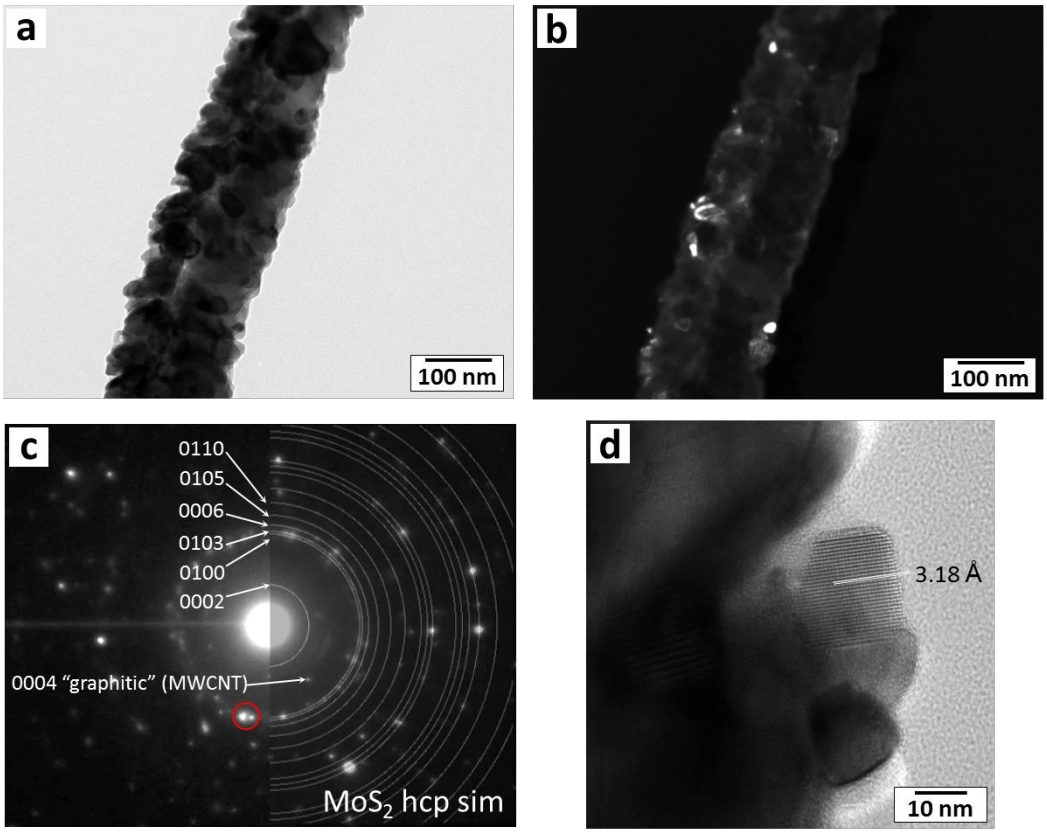

Figure B7: TEM micrographs and SAED pattern of a fragment of a MWCNT after sulfidation. (a) Bright field TEM micrograph. (b) Dark field TEM micrograph. (c) SAED pattern indexed to hcp molybdenum disulfide. The location of the aperture for the dark field image is circled. (d) HRTEM image showing measurement of the a-lattice parameter for an MoS_2 crystal.

A faint graphitic signal is detected from the MWCNTs in the SAED pattern in Figure B7c. In Figure B7d, a measurement of the lattice spacing on the HRTEM image is shown to agree very well with the a-lattice parameter for 2H-MoS_2 (3.16 Å).

Figure B8 shows an XRD pattern of a sulfided MoS_2-CNT nanocomposite electrode highlighting the presence of MoS_2. While there are a myriad of other phases that were detected, the principle peak for 2H-MoS_2 was detected in the sulfided sample, indicating that at least partial sulfidation was achieved. Furthermore, the experimental pattern shows evidence of residual molybdenum metal which was not converted. There is also a faint signal from the MWCNTs that occurs at approximately 25° 2θ, as expected.

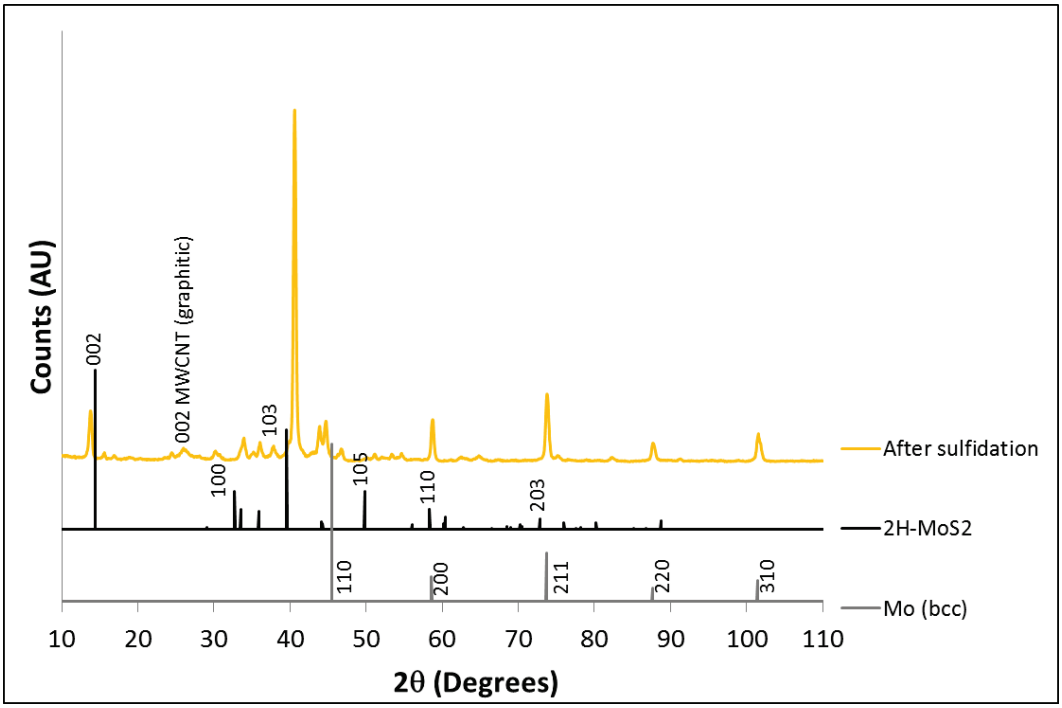

Figure B8: XRD spectrum of a MoS_2-CNT nanocomposite electrode after sulfidation. Theoretical spectra for 2H-MoS_2 and bcc molybdenum metal are also shown.

B.4 Coin cell assembly

Figure B9 shows a schematic of the order in which the coin cells were assembled for electrochemical testing. 2032 coin cells were used for the experiments, and all components were purchased from MTI Corporation. The MoS_2-CNT working electrode was inserted into the bottom of the positive battery cap. Three drops of electrolyte were then dripped onto its surface using a 100 μL micropipette. The composition of the electrolyte was a standard 1.0 M lithium hexaflourophosphate ($LiPF_6$) mixed with a 1:1:1 ratio of ethylene carbonate, dimethyl carbonate, and diethyl carbonate. The battery separator was then laid onto the surface of the working electrode and three more drops of electrolyte were added.

The separator was a Celgard tri-layer of polypropylene-polyethylene-polypropylene, and was 25 μm thick. The lithium foil counter (and reference) electrode was then placed on top of this, ensuring it was aligned directly on top of the working electrode and in the centre of the cap. Two 316 stainless steel spacers were then added, followed by a Belleville washer, which ensured that the components remained in compression. The negative cap was then placed onto the assembly and the coin cell was inserted into a pneumatic battery press and sealed using a pressure of 100 psig. At this point the open circuit voltage (OCV) was measured to ensure that the battery was not shorted out. Typical OCV values for MoS_2 coin cells ranged between 2.0-2.4 V versus Li/Li^+. Prior to electrochemical

testing, the battery was allowed to equilibrate for a period of 24 hours to ensure electrolyte penetration throughout the separator membrane and active material.

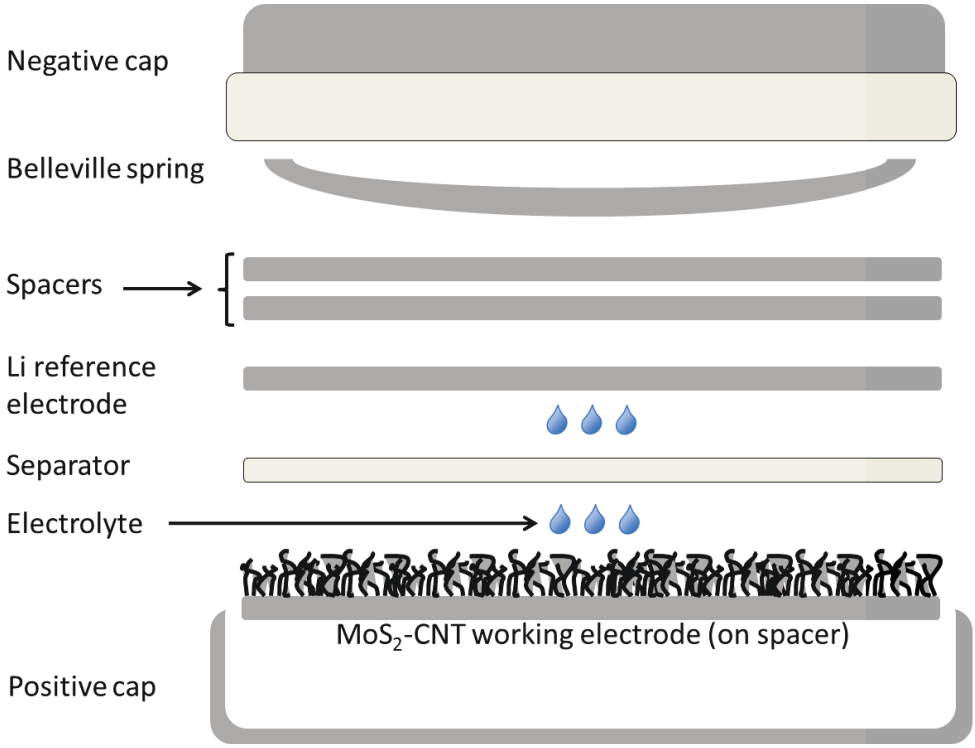

Figure B9: Schematic diagram showing a cross section of the coin cell assembly method.

B.5 Charge/discharge schematic for MoS_2-CNT coin cell

The charge/discharge behaviour of a typical MoS_2-CNT lithium ion battery is depicted in Figure B10. Here, the working electrode is shown as a nanocomposite of MoS_2 and carbon nanotubes. The flow of electrons and ions during charge and discharge is shown qualitatively. Also, the "anode" and "cathode" notation is shown as oxidation and reduction respectively.

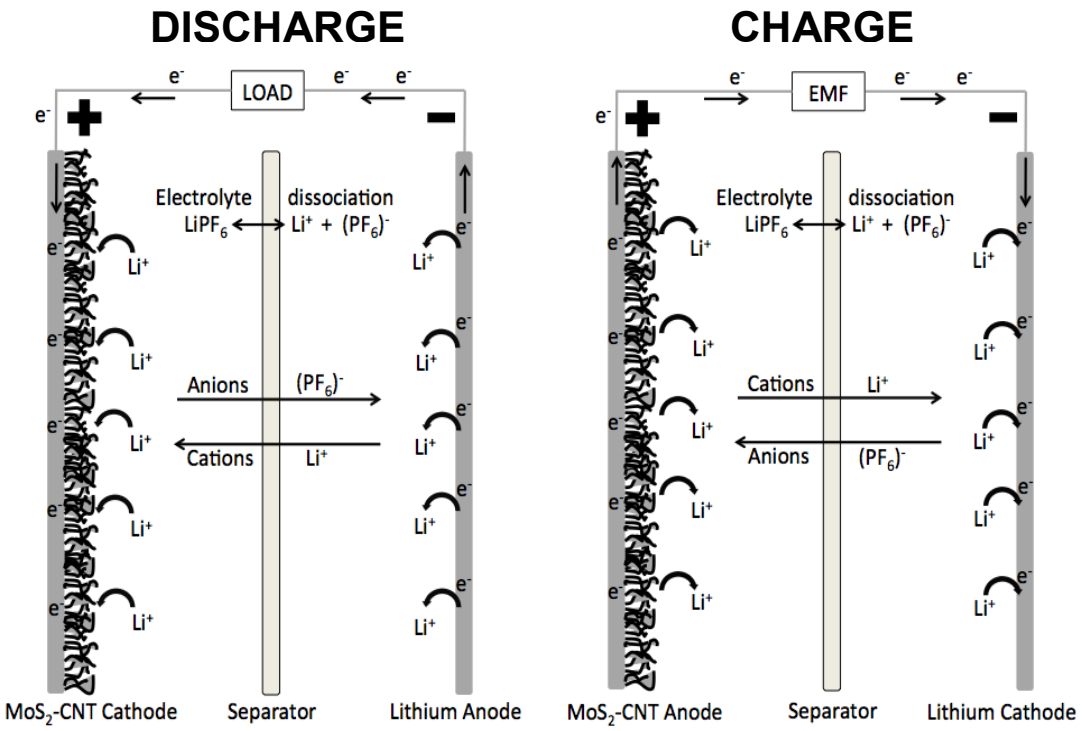

Figure B10: Charge/discharge behaviour of a typical MoS_2-CNT half-cell. The working electrode is shown as a nanocomposite of carbon nanotubes and MoS_2.

B.6 Electrochemical characterization

Figure B11 shows a voltage-capacity curve for an MoS_2-CNT LIB coin cell, showing the first five discharge and charge cycles. Here, a shift in the lithiation behaviour of MoS_2 is seen as a drastic change between the first discharge curve (labeled "1") and the other four. This is consistent with the theory that MoS_2 actually decomposes after the first lithiation cycle and never re-forms. Instead the battery continues to function as a lithium-sulfur system.

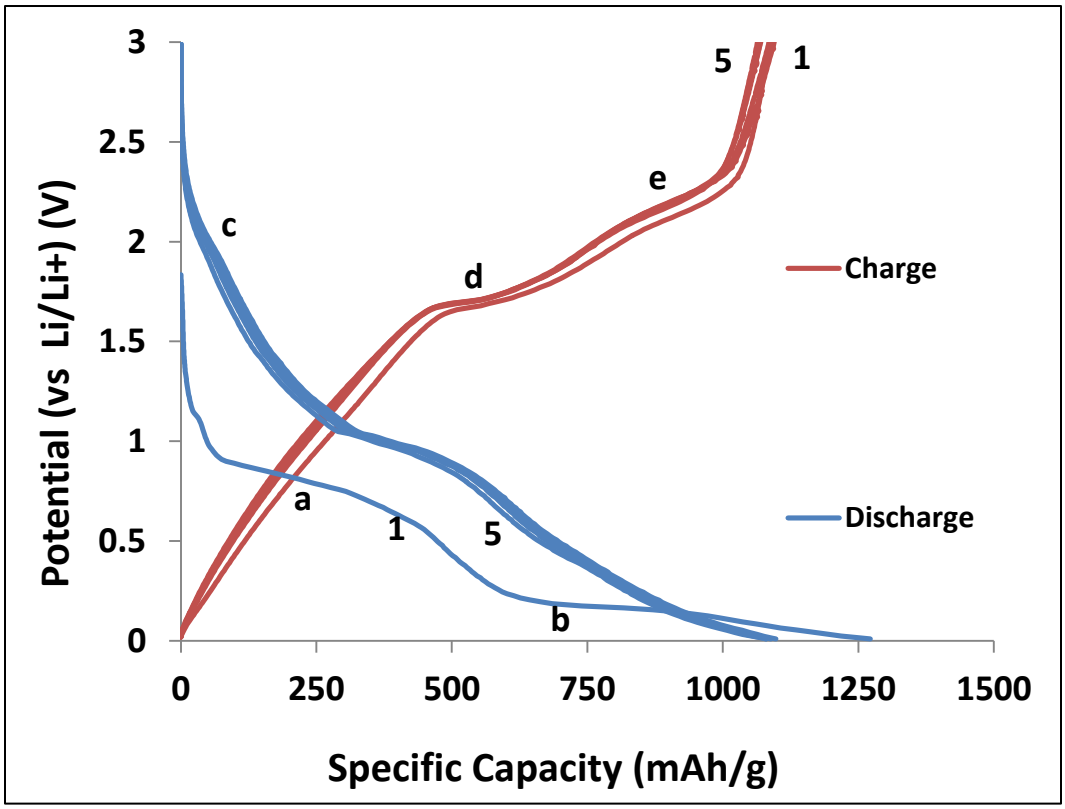

Figure B11: Voltage-capacity curve for an MoS_2-CNT coin cell during charge and discharge in the voltage range of 0-3 V vs Li/Li+. The scan rate was 10 mV/s.

Further evidence of this is seen by comparing the voltage position of the plateaus of the first discharge curve with subsequent discharge curves. On the first discharge curve, plateaus are seen at approximately 0.9 V and 0.2 V which are akin to the voltages of the first and second lithiation steps for MoS_2 discussed in Chapter 4. These are labelled as plateaus (a) and (b) respectively. The first plateau is indicative of the 2H to 1T phase transformation of MoS_2, and the second plateau is attributed to the decomposition of MoS_2 to Li_2S and molybdenum metal. Subsequent discharge curves show a weak plateau (c) forming at approximately 2 V, which is indicative of sulfur lithiation to Li_2S. Furthermore, re-charge plateaus at (d) 1.7 V, and (e) 2.3 V appear, which are attributed to the delithiation steps of Li_2S to elemental sulfur. To construct this plot it was necessary to estimate the active material mass, which included the CNTs and MoS_2 after sulfidation. The reversible capacity was approximately 1100 mAh/g, which agrees well with commonly reported capacity values for MoS_2 nanocomposite electrodes. This means that the active mass was accurately estimated and that this particular sample underwent minimal substrate lithiation, at least in the first five cycles.

Figure B12 shows a cyclic voltammogram that was collected on an MoS_2-CNT nanocomposite LIB coin cell. The results are consistent with those discussed in Chapter 4. The incomplete sulfidation of the molybdenum metal, and the oxidation of the titanium nitride diffusion barrier made electrochemical measurements difficult to interpret. However, the following general trends are

evident in the scan. For this voltammogram, a scan rate of 1 mV/s was used. In the first cathodic sweep, the peak at approximately 1.9 V is attributed to the lithiation of residual elemental sulfur left over from the sulfidation process. The peak at approximately 1.4 V is attributed to the lithiation of the substrate. The peaks around 1.0 V and 0.4 V are attributed to the first and second lithiation steps of MoS_2 forming Li_2S and molybdenum metal. These peaks become much smaller by the 10^{th} cycle, indicating that MoS_2 has been consumed and has not reformed.

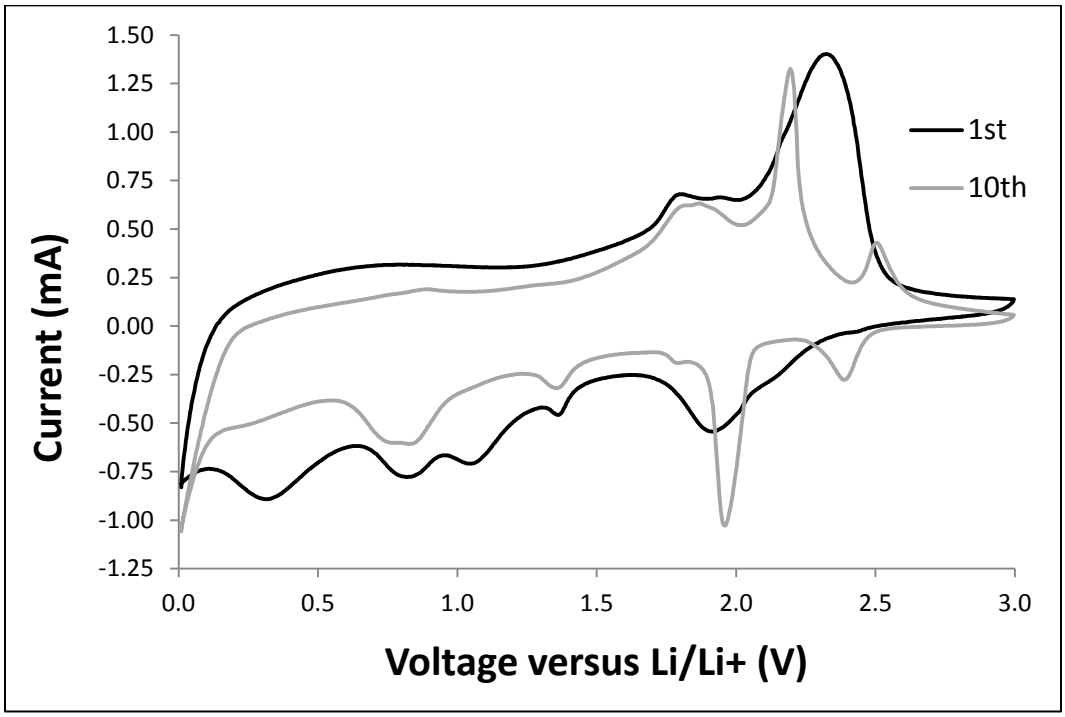

Figure B12: Cyclic voltammogram of an MoS_2-CNT LIB coin cell showing the 1^{st} and the 10^{th} scans. Scan rate was 1 mV/s.

In the first anodic sweep, there is a broad doublet at just below 2.0 V, which is attributed to the delithiation of unconverted MoS_2. The intensity of this

feature decreases with cycling, indicating that the material responsible is being consumed. The large anodic peak at approximately 2.4 V is attributed to the delithiation of Li_2S, forming elemental sulfur. After the 10^{th} anodic sweep, this peak has shifted down in voltage slightly, but remains strong.

By the 10^{th} cathodic sweep, the peak at approximately 2.0 V has strengthened significantly, and is attributed to the lithiation of sulfur to Li_2S. All other cathodic peaks are observed to weaken, as the MoS_2 in the system is converted to Li_2S and molybdenum metal and does not reform. There is a small anodic and cathodic peak around 2.5 V that are likely attributable to the stepwise delithiation of Li_2S, and lithiation of sulfur respectively.